

A high precision measurement of the neutron magnetic form factor using the CLAS detector.

Analysis Note

Version 1.3

J.Lachniet<sup>1,2,3</sup>, G.P.Gilfoyle<sup>4</sup>, B.Quinn<sup>2</sup>, M.F.Vineyard<sup>5</sup>,  
and W.K.Brooks<sup>6</sup>

<sup>1</sup>*Carnegie Mellon University, Pittsburgh, Pennsylvania 15213*

<sup>2</sup>*Old Dominion University, Norfolk, Virginia 23529*

<sup>3</sup>*Arete Associates, Arlington, VA 22202*

<sup>4</sup>*University of Richmond, Richmond, Virginia 23173*

<sup>5</sup>*Union College, Schenectady, NY 12308*

<sup>6</sup>*Universidad Técnica Federico Santa María, Casilla 110-V  
Valparaíso, Chile*

## Abstract

The neutron magnetic form factor  $G_M^n$  has been extracted from the ratio of quasi-elastic e-n to e-p scattering from a deuterium target using the CLAS detector. The measurement covers the range 0.5 to 4.8 (GeV/c)<sup>2</sup> in four-momentum transfer squared. High precision was achieved by use of the ratio technique, with which many uncertainties cancel. A dual-cell target was used, featuring a deuterium cell and a hydrogen cell, which allowed a simultaneous *in-situ* calibration of the neutron detection efficiency. Neutrons were detected using the CLAS Time-of-Flight system and the Forward Electromagnetic Calorimeter. Data were taken at two different electron beam energies, allowing up to four semi-independent measurements of  $G_M^n$  to be made at each value of  $Q^2$ . The data were compared to previous measurements, and with several theoretical and phenomenological models. It is found that for  $Q^2 > 1$  (GeV/c)<sup>2</sup> the standard dipole parametrization gives a good representation of the data over a wide range of  $Q^2$ .

# Contents

<b>1</b>	<b>Introduction</b>	<b>1</b>
1.1	Electromagnetic Form Factors . . . . .	1
1.1.1	Electron-Nucleon scattering in the Single Photon Exchange Approximation . . . . .	1
1.1.2	Interpretation of Elastic Form Factors . . . . .	4
1.1.3	Models and Theoretical Predictions . . . . .	5
1.2	Previous $G_M^n$ measurements . . . . .	13
1.3	Experimental technique . . . . .	13
<b>2</b>	<b>Experiment Analysis</b>	<b>16</b>
2.1	Event Reconstruction . . . . .	16
2.2	Run Selection . . . . .	16
2.3	Neutron Detection Efficiency Measurement . . . . .	18
2.3.1	Electron Identification . . . . .	18
2.3.2	$\pi^+$ Identification . . . . .	20
2.3.3	Neutron selection . . . . .	21
2.3.4	Efficiency Measurement in the Forward Calorimeter . . . . .	22
2.3.5	Efficiency Measurement in the Time of Flight system . . . . .	30
2.4	Proton Detection Efficiency Measurement . . . . .	37
2.4.1	Electron Identification . . . . .	37
2.4.2	Proton Identification . . . . .	38
2.4.3	Efficiency calculation . . . . .	39
2.5	Momentum Corrections . . . . .	39
2.6	Quasi-elastic ratio measurement . . . . .	45
2.6.1	Quasi-elastic electron selection . . . . .	45
2.6.2	Quasi-elastic $D(e, e'p)$ selection . . . . .	45
2.6.3	Quasi-elastic $D(e, e'n)$ selection . . . . .	46
2.6.4	Rejection of unreconstructed proton tracks . . . . .	46
2.6.5	Acceptance matching and fiducial cuts . . . . .	49
2.6.6	Efficiency corrections and Ratio calculation . . . . .	53
2.7	Corrections to Quasi-elastic ratio . . . . .	57
2.7.1	Uncalibrated SC paddles . . . . .	57
2.7.2	Losses due to Fermi motion of the target . . . . .	57

2.7.3	Quasi-elastic event generator . . . . .	61
2.7.4	Fermi Loss Corrections . . . . .	66
2.7.5	Radiative Corrections . . . . .	82
2.7.6	Nuclear Corrections . . . . .	86
<b>3</b>	<b>Experiment Results</b>	<b>96</b>
3.1	$G_M^n$ extraction from ratio . . . . .	96
3.2	Systematic Errors . . . . .	99
3.2.1	Systematic error due to uncertainty in Proton cross-section . .	99
3.2.2	Systematic error due to uncertainty in $G_E^n$ . . . . .	100
3.2.3	Other sources of systematic error . . . . .	104
3.2.4	Combined systematic error . . . . .	131
<b>4</b>	<b>Conclusions</b>	<b>135</b>
4.1	Comparison to previous measurements . . . . .	135
4.1.1	Comparison to theoretical predictions and fits . . . . .	136
	<b>Bibliography</b>	<b>140</b>
<b>A</b>	<b>Measured <math>G_M^n</math> values and errors</b>	<b>143</b>
<b>B</b>	<b>EC neutron detection efficiency fits</b>	<b>148</b>
B.1	2.6 GeV beam energy . . . . .	148
B.2	4.2 GeV beam energy . . . . .	155
<b>C</b>	<b>SC neutron detection efficiency fits</b>	<b>162</b>
C.1	2.6 GeV beam energy . . . . .	162
C.2	4.2 GeV beam energy . . . . .	173
<b>D</b>	<b>Kinematics of quasi-elastic scattering</b>	<b>184</b>
<b>E</b>	<b>Response to Analysis Review Committee 1</b>	<b>187</b>
<b>F</b>	<b>Response to Analysis Review Committee 2</b>	<b>210</b>

# Chapter 1

## Introduction

### 1.1 Electromagnetic Form Factors

Neutrons and protons are fundamental building blocks of the visible matter in the universe. If the proton and neutron were simple, structureless Dirac particles like the electron, they would have a magnetic moment given by:

$$\mu_N = \frac{q}{m} |\vec{s}| \quad (1.1)$$

where  $q, m,$  and  $\vec{s}$  are the nucleon's charge, mass and spin respectively (using natural units  $\hbar = c = 1$ ). In particular, the proton magnetic moment should be equal in magnitude to  $\mu_N$ , where  $\mu_N = \frac{e}{2M_p}$ , and the neutron magnetic moment should vanish. Otto Stern's measurement of the proton magnetic moment in 1933, which showed that the proton magnetic moment was  $\mu_p = 2.79\mu_N$ , indicated that the proton was not a structureless Dirac particle. Subsequent measurement of the neutron magnetic moment ( $\mu_n = -1.91\mu_N$ ) confirmed the non-Dirac nature of the neutron. Beginning in the 1950s, electron scattering experiments by Hofstadter and others showed evidence of charge and magnetization distributions inside the proton. Form factors, called  $G_E^p$  and  $G_M^p$  were introduced to parametrize the proton internal structure revealed in the electron scattering experiments.

#### 1.1.1 Electron-Nucleon scattering in the Single Photon Exchange Approximation

From the Feynman rules for quantum electrodynamics (QED), the amplitude for electron-nucleon scattering in the single-photon exchange approximation is given by:

$$-iM = j^\mu \frac{-ig_{\mu\nu}}{q^2} J^\nu \quad (1.2)$$

In this expression,  $j^\mu$  is the electron transition current,  $J^\nu$  is the proton transition current and  $g_{\mu\nu}$  is the metric tensor. This is illustrated in Fig 1.1 for an electron of

initial(final) momentum  $k(k')$  and a nucleon of initial(final) momentum  $p(p')$ . The four-momentum transferred in the reaction is  $q = k - k'$ .

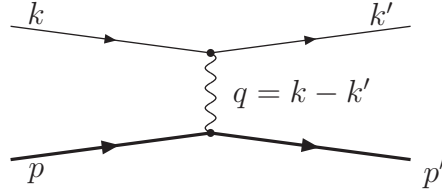


Figure 1.1: Elastic electron-nucleon scattering in the single-photon exchange approximation

The electron is an elementary spin- $\frac{1}{2}$  particle. The form of its transition current is known:

$$j^\mu = -e\bar{u}_e(k')\gamma^\mu u_e(k)e^{iq\cdot x} \quad (1.3)$$

In this expression,  $u_e(k)$  and  $\bar{u}_e(k')$  are Dirac spinors representing the incident and scattered electron, and the  $\gamma^\mu$  are the usual Dirac matrices.

The nucleon is a composite particle, with non-trivial internal structure, so the simple form of Eqn 1.3 must be replaced with a more complicated form:

$$J^\mu = -e\bar{u}(p')\Gamma^\mu u(p)e^{iq\cdot x} \quad (1.4)$$

$\Gamma^\mu$  must be constructed such that  $J^\mu$  transforms like a 4-vector. The ingredients available to construct such an expression for  $\Gamma^\mu$  are functions of  $p, p', q$  and combinations of Dirac gamma matrices. It can be shown that the most general nucleon current, subject to the requirements of current conservation, parity conservation and Lorentz invariance, can be written as:

$$J^\mu = e\bar{u}(p') \left[ F_1(Q^2)\gamma^\mu + \frac{\kappa}{2M}F_2(Q^2)i\sigma^{\mu\nu}q_\nu \right] u(p)e^{iq\cdot x} \quad (1.5)$$

where  $\kappa$  is the nucleon anomalous magnetic moment,  $M$  is the nucleon mass and  $F_1$  and  $F_2$  are scalar functions of  $Q^2$  (with  $Q^2 = -q^2$ ) called the Dirac and Pauli form factors respectively. The form factors parametrize our ignorance of the details of the internal structure of the nucleon.

Long wavelength photons ( $Q^2 \rightarrow 0$ ) do not resolve the interior structure of the nucleon, so in that limit, the nucleon current must reduce to that of a point particle of appropriate charge and magnetic moment. This requirement fixes the values of the form factors at  $Q^2 = 0$ :

$$F_1^p(0) = 1, \quad F_2^p(0) = 1 \quad (1.6)$$

$$F_1^n(0) = 0, \quad F_2^n(0) = 1. \quad (1.7)$$

The superscripts label the isospin state of the nucleon.

With this expression for the nucleon electromagnetic current, the cross section for elastic electron-nucleon scattering can be calculated (in the lab frame, where the nucleon is initially at rest):

$$\frac{d\sigma}{d\Omega} = \sigma_{Mott} \left[ \left( F_1^2 + \frac{\kappa^2 Q^2}{4M^2} F_2^2 \right) + \frac{Q^2}{2M^2} (F_1 + \kappa F_2)^2 \tan^2\left(\frac{\theta}{2}\right) \right], \quad (1.8)$$

where  $\theta$  is the electron scattering angle, and  $\sigma_{Mott}$  is the Mott cross section (using natural units,  $\hbar = c = 1$ ):

$$\sigma_{Mott} = \frac{\alpha^2 E' \cos^2(\frac{\theta}{2})}{4E^3 \sin^4(\frac{\theta}{2})} \quad (1.9)$$

Eqn 1.8 is inconvenient due to the  $F_1 F_2$  term. If the so-called Sachs' form factors are defined as:

$$G_E \equiv F_1 - \frac{\kappa Q^2}{4M^2} F_2 \quad (1.10)$$

$$G_M \equiv F_1 + \kappa F_2, \quad (1.11)$$

then Eqn 1.8 can be rewritten as:

$$\frac{d\sigma}{d\Omega} = \sigma_{Mott} \left( G_E^2 + \frac{\tau}{\epsilon} G_M^2 \right) \left( \frac{1}{1 + \tau} \right) \quad (1.12)$$

In this equation,  $\tau = \frac{Q^2}{4M^2}$  and  $\epsilon = (1 + 2(1 + \tau) \tan^2(\frac{\theta}{2}))^{-1}$ . The Sachs' form factors  $G_E$  and  $G_M$  are known as the *electric* and *magnetic* form factors, respectively. The  $Q^2 = 0$  limit of these form factors can be found by combining Eqn 1.11, Eqn 1.6 and Eqn 1.7, giving:

$$G_E^p(0) = 1, \quad G_M^p(0) = \mu_p \quad (1.13)$$

$$G_E^n(0) = 0, \quad G_M^n(0) = \mu_n, \quad (1.14)$$

where  $\mu_p$  and  $\mu_n$  are the proton and neutron magnetic moment ( $\mu_p = 1 + \kappa_p$ ,  $\mu_n = \kappa_n$ ), respectively.

Early measurements of the elastic form factors showed that  $G_E^p$  could be parameterized using the so-called dipole form:

$$G_D(Q^2) = \frac{1}{(1 + Q^2/\Delta)^2} \quad (1.15)$$

where  $\Delta = 0.71$  (GeV/c)<sup>2</sup>. Furthermore the other elastic form factors, with the exception of  $G_E^n$ , were found to be well approximated by scaling  $G_E^p$ :

$$G_E^p(Q^2) \approx G_D(Q^2) \quad (1.16)$$

$$G_M^p(Q^2) \approx \mu_p G_D(Q^2) \quad (1.17)$$

$$G_M^n(Q^2) \approx \mu_n G_D(Q^2) \quad (1.18)$$

It is a standard practice when showing form factor data to scale the data points to the dipole. The dipole does not describe  $G_E^n$ , which is frequently parametrized using the Galster fit:

$$G_E^n(Q^2) = \frac{\mu_n \tau G_D}{1 + \eta \tau} \quad (1.19)$$

where  $\tau = Q^2/4M_n^2$  and  $\eta = 5.6$ .

### 1.1.2 Interpretation of Elastic Form Factors

The introduction of the Sachs' form factors removed the interference term from the cross section, simplifying experimental analysis. The Sachs' form factors also have a somewhat more direct physical interpretation. In the non-relativistic region  $Q^2 \ll M_N^2$ , the Sachs' form factors can be interpreted as Fourier transforms of the charge and magnetization distributions:

$$G_E(Q^2) = \int \rho(r) e^{i\vec{q}\cdot\vec{r}} d^3r \quad (1.20)$$

The dipole form  $G_D(Q^2)$  discussed in the previous section corresponds to an exponential fall-off in the spatial charge and magnetization distributions.

The integrand in the equation can be expanded in powers of  $q$  to obtain the RMS charge radius of the nucleon:

$$G_E = \int \rho(r) \left\{ 1 - \frac{1}{2}(qr)^2 \cos^2 \theta + \dots \right\} r^2 \sin \theta dr d\theta d\phi \quad (1.21)$$

Differentiating with respect to  $\vec{q}^2$  and taking the limit  $q^2 \rightarrow 0$  gives:

$$\langle r^2 \rangle = -6 \left. \frac{dG_E(q)}{dq^2} \right|_{q^2=0} \quad (1.22)$$

At higher  $Q^2$ , this simple interpretation is complicated by relativistic effects. However, a simple connection between the form factors and the electromagnetic structure of the nucleon still exists in a special reference frame, called the Breit, or "Brick Wall" frame. In this frame, defined by the condition  $\mathbf{p} = -\mathbf{p}'$ , where no energy is transferred to the nucleon, it can be shown that the form factors are related to the charge and magnetic moment distributions in the nucleon in momentum-space [1].

In this frame,

$$J^0(Q^2) = \rho(Q^2) = 2MeG_E(Q^2) \quad (1.23)$$

$$J^1(Q^2) \pm iJ^2(Q^2) = \mp 2|\mathbf{q}| eG_M(Q^2). \quad (1.24)$$

so that there is a connection between the components of the nucleon current 4-vector and the elastic form factors.

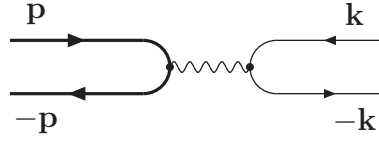


Figure 1.2: Elastic electron-nucleon scattering in the Breit frame

The measurement of the elastic form factors of the nucleon is a topic of great interest. The elastic form factors encode fundamental information about hadron structure, and the nucleon is the only hadron for which precise form factor measurements are possible. Hence, the elastic form factors provide the most stringent test for models of the transverse structure of hadrons.

### 1.1.3 Models and Theoretical Predictions

#### 1.1.3.1 IJL model

The model of Iachello, Jackson and Lande [2] uses isospin symmetry to relate the proton and neutron form factors, which are decomposed into linear combinations of isoscalar and isovector terms [3]:

$$G_M^p(Q^2) = (F_1^{is} + F_1^{iv}) + (F_2^{is} + F_2^{iv}) \quad (1.25)$$

$$G_E^p(Q^2) = (F_1^{is} + F_1^{iv}) + \frac{Q^2}{4M^2}(F_2^{is} + F_2^{iv}) \quad (1.26)$$

$$G_M^n(Q^2) = (F_1^{is} - F_1^{iv}) + (F_2^{is} - F_2^{iv}) \quad (1.27)$$

$$G_E^n(Q^2) = (F_1^{is} - F_1^{iv}) + \frac{Q^2}{4M^2}(F_2^{is} - F_2^{iv}) \quad (1.28)$$

The virtual-photon/nucleon interaction is modeled as a combination of a direct photon-nucleon coupling, described by a dipole form factor of the form  $g(Q^2) = (1 + \gamma Q^2)^{-2}$ , and VMD pole terms for isoscalar ( $\omega$  and  $\phi$ ) and isovector ( $\rho$ ) meson couplings. The model interactions are illustrated in Fig 1.3.

The meson-nucleon coupling parameters and the direct coupling parameters were obtained by fitting to the form factor data available at the time. The model was found to give an adequate description of the proton form factors, and successfully predicted the fall-off of the ratio  $\frac{\mu_p G_E^p}{G_M^p}$  recently observed in polarization-transfer measurements at Jefferson Lab [4, 5].

The prediction of the IJL model for  $G_M^n$  is shown (scaled to the dipole) in Fig 1.5.

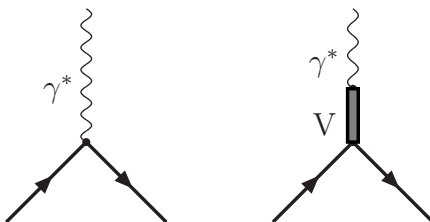


Figure 1.3: Photon-Nucleon interactions in the IJL model

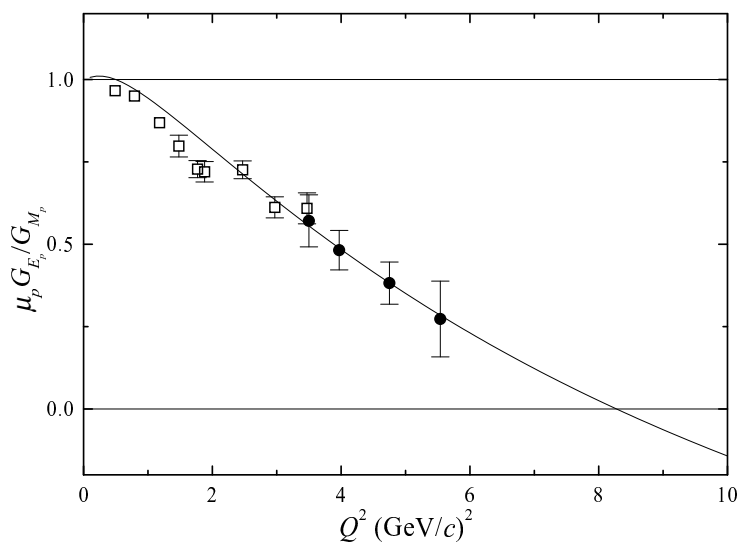


Figure 1.4: The prediction of the IJL model for  $\frac{\mu_p G_E^p}{G_M^p}$ , compared to recent data from JLab. The open squares are from [4], the filled circles from [5]

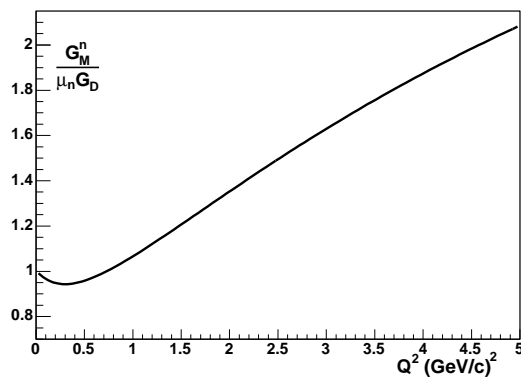


Figure 1.5: The prediction of the IJL model for  $G_M^n$ , scaled to the dipole

### 1.1.3.2 Lomon/GK fit

The Gari-Krümpelmann model [6] attempts to model the nucleon form factors in a manner which incorporates the VMD model at low  $Q^2$  and perturbative QCD at high  $Q^2$ . The Dirac and Pauli form factors are decomposed into isoscalar and isovector parts, as described in Section 1.1.3.1. As in the IJL model, the isoscalar and isovector form factors are modeled as being due to a photon/vector-meson/nucleon interaction and a direct photon-nucleon coupling (see Fig 1.3):

$$F_1^{iv}(Q^2) = \left[ \frac{m_\rho^2}{m_\rho^2 + Q^2} \frac{g_\rho}{f_\rho} + \left( 1 - \frac{g_\rho}{f_\rho} \right) \right] F_1(Q^2) \quad (1.29)$$

$$\kappa_V F_2^{iv}(Q^2) = \left[ \frac{m_\rho^2}{m_\rho^2 + Q^2} \frac{\kappa_\rho g_\rho}{f_\rho} + \left( \kappa_V - \frac{\kappa_\rho g_\rho}{f_\rho} \right) \right] F_2(Q^2) \quad (1.30)$$

$$F_1^{is}(Q^2) = \left[ \frac{m_\omega^2}{m_\omega^2 + Q^2} \frac{g_\omega}{f_\omega} + \left( 1 - \frac{g_\omega}{f_\omega} \right) \right] F_1(Q^2) \quad (1.31)$$

$$\kappa_S F_2^{is}(Q^2) = \left[ \frac{m_\omega^2}{m_\omega^2 + Q^2} \frac{\kappa_\omega g_\omega}{f_\omega} + \left( \kappa_S - \frac{\kappa_\omega g_\omega}{f_\omega} \right) \right] F_2(Q^2) \quad (1.32)$$

The  $\phi$  meson is taken to be completely decoupled from the nucleon, in accord with the Zweig rule. The  $F_1$  and  $F_2$  terms are chosen to satisfy the meson-dynamics prediction [7] of a monopole type dependence at low  $Q^2$ :

$$F_1 \sim F_2 \sim \frac{\Lambda_1^2}{\Lambda_1^2 + Q^2} \quad (1.33)$$

with  $\Lambda_1 \sim 0.8 GeV$ . At large  $Q^2$ , perturbative QCD makes predictions for the  $Q^2$  dependence of the form factors [8]:

$$F_1 \sim \left[ \frac{1}{Q^2 \log(Q^2/\Lambda_{QCD}^2)} \right]^2 \quad (1.34)$$

$$F_2 \sim \frac{F_1}{Q^2} \quad (1.35)$$

To interpolate between these two limiting  $Q^2$  regimes, Gari and Krümpelmann use intrinsic form factors of the form:

$$F_1(Q^2) = \frac{\Lambda_1^2}{\Lambda_1^2 + \tilde{Q}^2} \frac{\Lambda_2^2}{\Lambda_2^2 + \tilde{Q}^2} \quad (1.36)$$

$$F_2(Q^2) = \frac{\Lambda_1^2}{\Lambda_1^2 + \tilde{Q}^2} \left[ \frac{\Lambda_2^2}{\Lambda_2^2 + \tilde{Q}^2} \right]^2 \quad (1.37)$$

where

$$\tilde{Q}^2 = Q^2 \frac{\log(\frac{\Lambda_2^2 + Q^2}{\Lambda_{QCD}^2})}{\log(\frac{\Lambda_2^2}{\Lambda_{QCD}^2})} \quad (1.38)$$

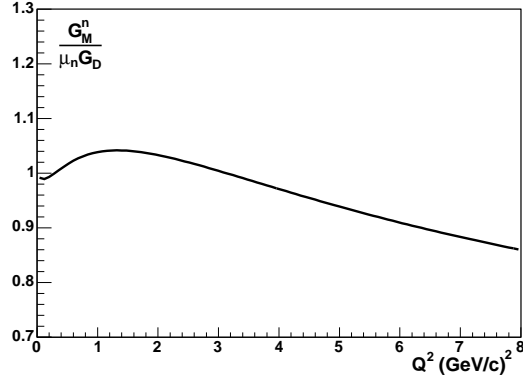


Figure 1.6: The  $G_M^n$  prediction of the Lomon's extended GK model, scaled to the dipole

Lomon [9, 10] extended the GK model by including  $\phi$  coupling to the nucleon, adding the  $\rho'(1450)$  and replacing the  $\rho$  pole term with a dispersion relation term [11]. The meson-nucleon coupling constants and cut-off scale factors ( $\Lambda_1, \Lambda_2, \Lambda_{QCD}$ ) were determined by fitting to the world data on  $G_M^p, G_E^p, G_M^n, G_E^n$  and the recent JLab results for  $\frac{\mu_p G_M^p}{G_E^p}$ . The  $G_M^n$  values generated by the best-fit parameters [10] are shown in Fig 1.6.

### 1.1.3.3 Miller model

The model of Miller [12] treats the nucleon as a relativistic bound state of three constituent quarks surrounded by a pion cloud. Poincaré invariance is imposed using light-front dynamics, in which fields are quantized at a fixed light-cone time  $\tau = x^0 + x^3 \equiv x^+$ . The advantage of using the light-cone for form-factor calculations is that light-cone boost operators are independent of interactions (the initial and final state nucleons in elastic scattering are connected by a boost operator). The model uses a relativistic quark model first proposed by [13] and [14]. Quark effects are dominant at large  $Q^2$ . Pion cloud effects, important at low  $Q^2$ , are implemented using a cloudy-bag approach. The results of Miller's Light Front Cloudy Bag model (LFCBM) for  $G_M^n$  are shown in Fig 1.7.

### 1.1.3.4 Wagenbrunn model

The model of Wagenbrunn *et al.* [15] uses a constituent quark model in which the interaction between two quarks is modeled by single Goldstone boson exchange [16]. Poincaré invariance is obtained by using the “point-form”, a third variety of relativistic dynamics, in which the fields are quantized on the surface of a hyperboloid  $t^2 - \vec{x}^2 = \kappa^2$ . The results of the point-form CQM are shown in Fig. 1.8.

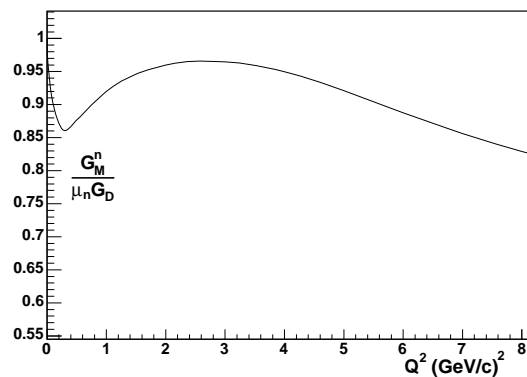


Figure 1.7: The  $G_M^n$  prediction of the Miller model, scaled to the dipole

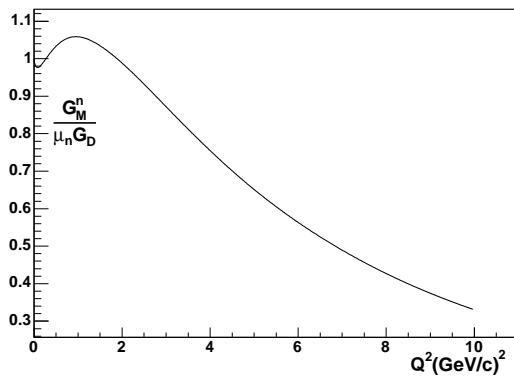


Figure 1.8: The  $G_M^n$  prediction of the Wagenbrunn model, scaled to the dipole

### 1.1.3.5 Lattice-based calculation

Isvector and isoscalar form factors can be defined as linear combinations of the standard form factors:

$$G^v = G_p - G_n \quad (1.39)$$

$$G^s = G_p + G_n \quad (1.40)$$

The QCDSF collaboration [17] have made quenched lattice calculations of the isovector and isoscalar form factors. Present computer power does not allow the calculations to be performed at realistic quark masses, so the calculations were performed with quark masses 5-10 times higher than the physical value. Three different values of the lattice spacing were used. Ashley *et al.* [18] use results obtained from chiral perturbation theory to perform the extrapolation down to physical values of the quark masses. All of the electromagnetic form factors are assumed to have a dipole form:

$$G(Q^2) = \frac{G(0)}{(1 + Q^2/\Lambda)^2} \quad (1.41)$$

At each value of the pion mass and lattice spacing, the QCDSF form factor result was fitted with a dipole form. The dipole mass ( $\Lambda$  in Eqn 1.41) is fitted as a function of the pion mass, using a functional form determined from chiral perturbation theory, as shown in Fig 1.9. The value of the isovector and isoscalar dipole mass determined from this extrapolation are used to calculate  $G_M^n$ , with the results shown in Fig 1.10. A range of values is shown.

### 1.1.3.6 Kelly Fit

Kelly [19] fit a selection of world data with a function of the form:

$$G_M^n(Q^2) = \frac{\sum_{k=0}^n a_k \tau^k}{1 + \sum_{k=1}^{n+2} b_k \tau^k} \quad (1.42)$$

where  $\tau = Q^2/4M_p^2$  and the  $a_k, b_k$  are coefficients of the fit. This form contains only even powers of  $Q$  in the denominator, ensuring that  $\langle r^2 \rangle$  is finite, and the degree of the polynomial in the denominator is higher than the numerator, ensuring the  $Q^{-4}$  behavior predicted by pQCD at large  $Q^2$ . The results of the fit are shown in Fig 1.11.

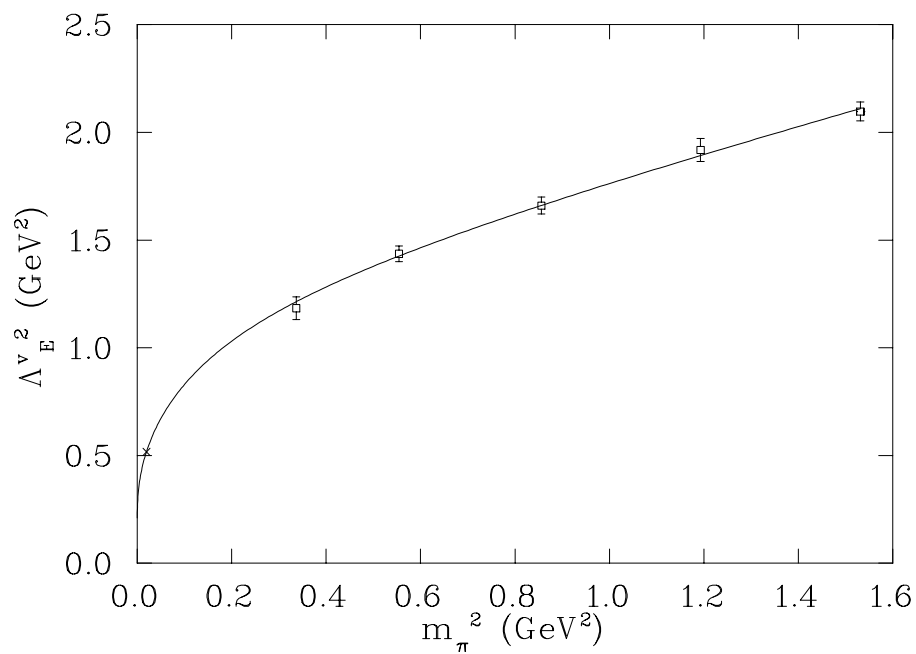


Figure 1.9: Fits to values of the isovector dipole mass, as a function of  $m_\pi^2$ . The lattice calculations are indicated by the open boxes, and the extrapolated value at the physical pion mass is shown with the x.

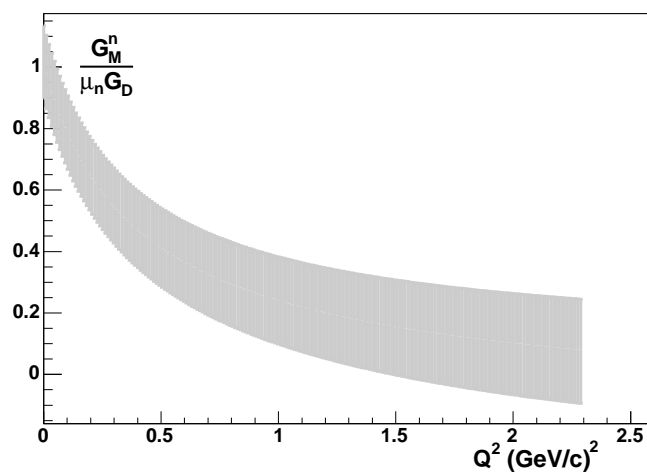


Figure 1.10: The range of  $G_M^n$  values (scaled to the dipole) predicted from the lattice calculations of Ashley et al [18].

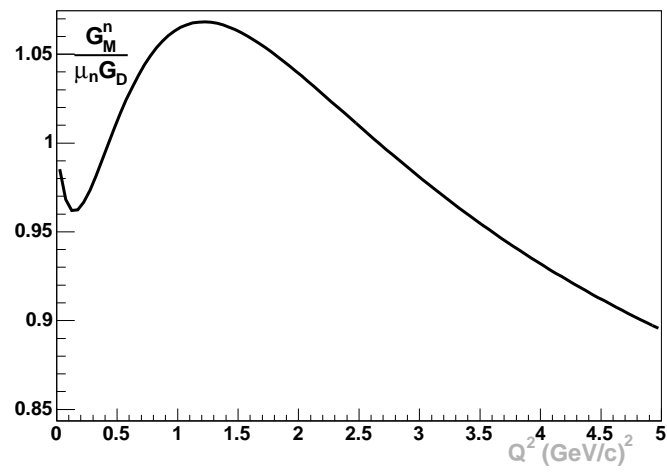


Figure 1.11: Results of the fit by Kelly to world  $G_M^n$  data.

## 1.2 Previous $G_M^n$ measurements

The lack of a free neutron target complicates measurements of the neutron form factors. The deuteron is the simplest target nucleus, and most previous  $G_M^n$  measurements have used deuteron targets. For inclusive e-d scattering, used in Ref [20–24], a longitudinal-transverse separation of the scattering cross section must be made, followed by a subtraction of the proton contribution. This subtraction introduces significant model dependence due to the choice of deuteron model and treatment of final state interactions. The proton-subtraction error is avoided in exclusive quasi-elastic measurements where the neutron in  $D(e, e'n)p$  is also observed [25–27]. The price that is paid for removing the proton subtraction uncertainty is that this method requires knowledge of the neutron detection efficiency. Anti-coincidence measurements of  $d(e, e'NOT - p)$  where the *absence* of a scattered proton is required have also been performed [28].

Most recent unpolarized measurements of  $G_M^n$  measure the ratio of the cross section ratio for  $D(e, e'n)p$  to  $D(e, e'p)n$  scattering [29–31]. Taking this ratio reduces the sensitivity to the nucleon structure and radiative corrections. This is the same technique used in the present e5 analysis. As with the  $D(e, e'n)p$  exclusive measurements, this technique requires accurate determination of the neutron detection efficiency. Fig 1.12 shows the world data on  $G_M^n$  from unpolarized electron-deuteron experiments.

Neutron form factor information, typically at lower values of  $Q^2$ , can also be extracted from measurements on polarized targets. Recent  $G_M^n$  results from measurements using polarized targets are shown in Fig 1.13. Typically, a polarized  $^3\text{He}$  target is used. The  $^3\text{He}$  nucleus is dominated by a spatially symmetric S-wave state in which the two proton spins cancel, so that the  $^3\text{He}$  spin is carried by the neutron. Spin-dependent response functions can be extracted from the  $^3\text{He}(e, e')$  cross section, which under the right kinematic configuration contains terms proportional to  $G_M^n$ .

## 1.3 Experimental technique

The value of  $G_M^n$  was extracted from a measurement of the ratio of quasi-elastic e-n to e-p scattering from a deuterium target:

$$R = \frac{\frac{d\sigma}{d\Omega}(D(e, e'n))}{\frac{d\sigma}{d\Omega}(D(e, e'p))} \quad (1.43)$$

This ratio is nearly equal to the ratio of the *free nucleon* e-n to e-p cross sections:

$$R = a(Q^2) \frac{\frac{G_{En}^2 + \tau G_{Mn}^2}{1 + \tau} + 2\tau G_{Mn}^2 \tan^2(\frac{\Theta}{2})}{\frac{G_{Ep}^2 + \tau G_{Mp}^2}{1 + \tau} + 2\tau G_{Mp}^2 \tan^2(\frac{\Theta}{2})} \quad (1.44)$$

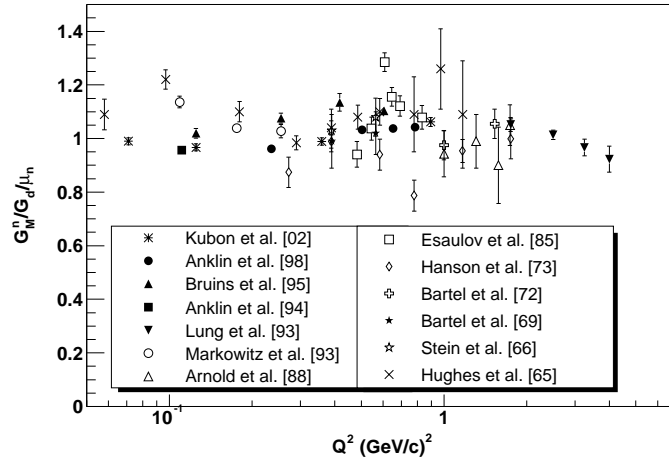


Figure 1.12: World data on  $G_M^n$  from unpolarized electron-deuteron measurements. The figure is from [32]

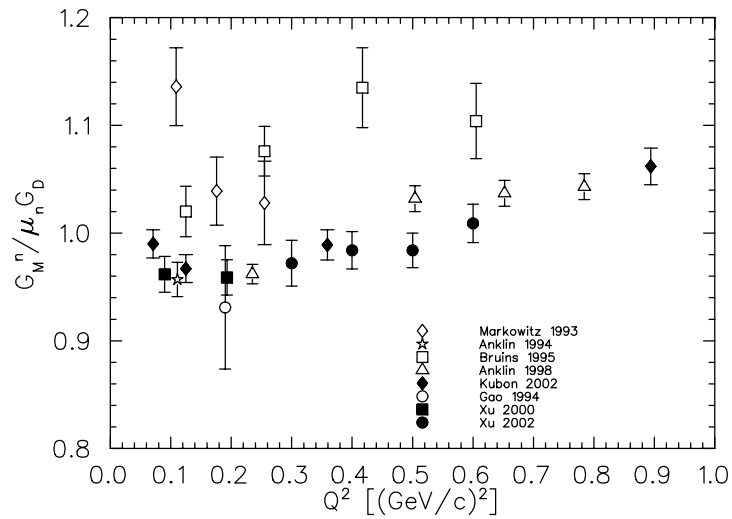


Figure 1.13: World data on  $G_M^n$  from polarized target measurements. The figure is from [32]

Deviations from this “free ratio” assumption are parametrized by the factor  $a(Q^2)$ , which can be calculated from deuteron models, and are small at large  $Q^2$ . Once the model corrections have been applied to  $R$ , the results of previous measurements of the elastic proton scattering cross section and the neutron electric form factor can be used to extract  $G_M^n$ . The ratio method has several advantages. It is insensitive to the luminosity, electron acceptance, reconstruction efficiency and trigger efficiency. The dominant contribution to radiative corrections in elastic electron-nucleon scattering comes from additional photons which couple to the electron, so when the ratio is taken, the radiative corrections very nearly cancel. Sensitivity to the details of the deuteron wave function are also reduced by taking the ratio.

Use of the ratio model requires making an exclusive measurement of e-n scattering, and so requires an accurate measurement of the neutron detection efficiency. Accurate matching of the scattered neutron and proton acceptance is also required. The e5 running period used a dual-cell target, containing collinear deuterium and hydrogen cells. Use of the hydrogen cell allows a simultaneous *in-situ* measurement of the neutron detection efficiency. The ratio method also requires information on the other three form factors, or more precisely, the proton elastic scattering cross section and  $G_E^n$ . The proton cross section has been well measured in the past, and as only the total elastic cross section is needed for the proton, two-photon exchange issues (relevant to the extraction of the proton form factors from elastic scattering data) are not important. While the uncertainties on  $G_E^n$  are large,  $G_E^n$  is small compared to the other form factors, and its contribution to the value of the ratio diminishes as  $Q^2$  becomes larger.

# Chapter 2

## Experiment Analysis

### 2.1 Event Reconstruction

The analysis of the e5 data was performed with a modified version of the CLAS reconstruction software, derived from the “release-4-3” code. The detectors were calibrated (EC timing and energy, SC timing and energy, DC drift time to drift distance conversion) using the standard packages. A set of special “road files” generated for the e5 target and magnetic field configurations was used as an input template to the RECSIS event reconstruction code. RECSIS returned particle charge, momentum, and position values for charged particles in the drift chamber. Details of the tracking code can be found in [33]. Information from other detector packages, such as hit locations and times in the EC and SC, were matched to the DC tracks by the SEB package. The SEB package was modified to write summary information to a MySQL database after processing each file. The reconstructed events were written to BOS files, along with some of the raw event information, to the JLab tape silo.

### 2.2 Run Selection

Files were selected for analysis by examining two quantities recorded in the cooking database, the ratio of protons to electrons originating in the hydrogen target cell, and the ratio of time-based tracks to hit based tracks. The cuts were selected to remove files in which either of these quantities differed too much from the average. Files selected for analysis were required to satisfy:

$$0.9 < \frac{N_p}{N_e} < 1.2 \quad E_{beam} = 4.2GeV \quad (2.1)$$

$$0.85 < \frac{N_p}{N_e} < 1.0 \quad E_{beam} = 2.6GeV \quad (2.2)$$

where  $N_p$  is the number of protons and  $N_e$  is the number of electrons.

These cuts are illustrated in Fig. 2.1 and Fig. 2.2.

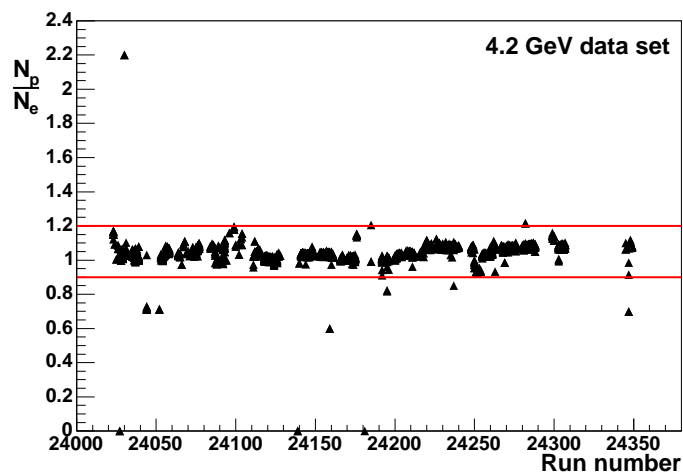


Figure 2.1: The ratio of the number of protons to the number of electrons for events originating in the hydrogen target versus run number. The data are from the 4.2 GeV beam energy data set. The cuts applied are shown in red.

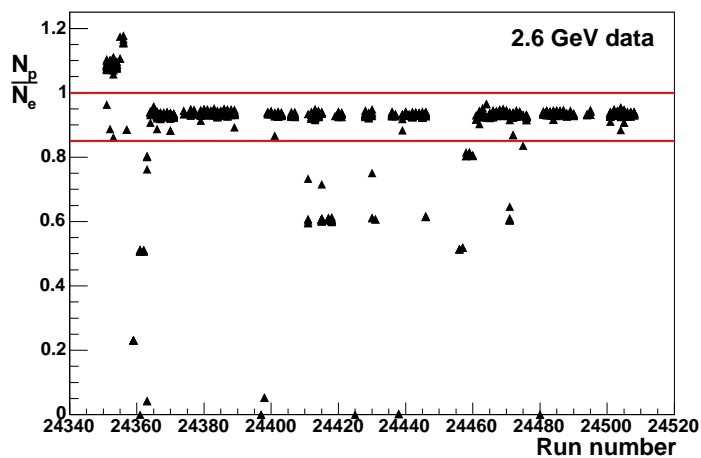


Figure 2.2: The ratio of the number of protons to the number of electrons for events originating in the hydrogen target versus run number. The data are from the 2.6 GeV beam energy data set. The cuts applied are shown in red.

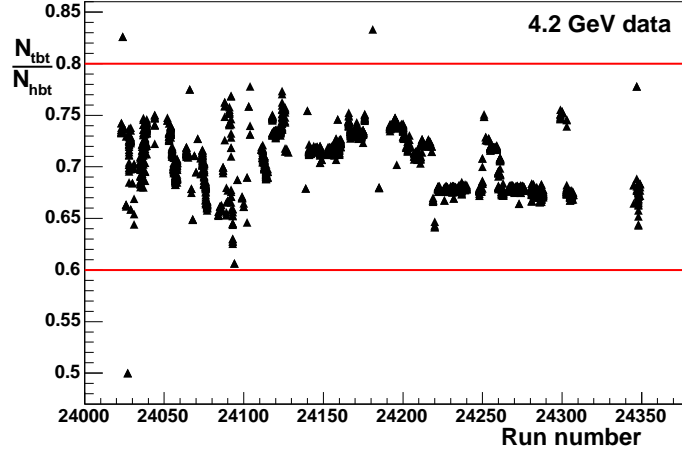


Figure 2.3: The ratio of the number of time-based tracks to the number of hit-based tracks versus run number. The data are from the 4.2 GeV beam energy data set. The cuts applied are shown in red.

Files selected for analysis were also required to satisfy:

$$0.6 < \frac{N_{tbt}}{N_{hbt}} < 0.8 \quad E_{beam} = 4.2 GeV \quad (2.3)$$

$$0.75 < \frac{N_{tbt}}{N_{hbt}} < 0.85 \quad E_{beam} = 2.6 GeV \quad (2.4)$$

where  $N_{tbt}$  is the number of time-based tracks, and  $N_{hbt}$  is the number of hit-based tracks. These cuts are illustrated in Fig. 2.3 and Fig. 2.4.

## 2.3 Neutron Detection Efficiency Measurement

The hydrogen cell of the e5 target allows for an *in-situ* measurement of the neutron detection efficiency of the EC and SC detector systems. The reaction  $ep \rightarrow e\pi^+(n)$  on protons in the hydrogen cell is used as a source of tagged neutrons. Candidate events are selected which have one negative track and one positive track.

### 2.3.1 Electron Identification

Events with well identified electrons were selected according to the following criteria:

1. Vertex Cut

The  $z$ -component of the electron vertex position determined by tracking must satisfy  $-3.0 < v_z < 3.0$  cm. This cut ensures that the electron originated in the hydrogen cell of the target, and removes some of the contamination from events in the target entrance/exit windows.

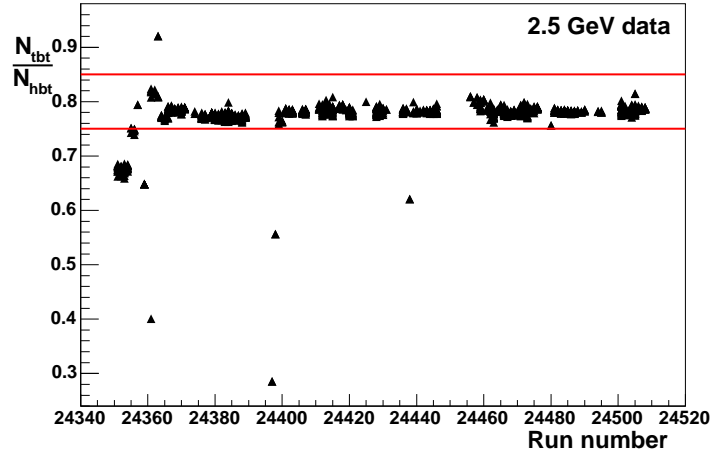


Figure 2.4: The ratio of the number of time-based tracks to the number of hit-based tracks versus run number. The data are from the 2.6 GeV beam energy data set. The cuts applied are shown in red.

## 2. EC fiducial cut

The location of the electron hit on the EC face plane must be at least 10 cm away from any of the three edges of the EC. This cut removes events in which energy from the electron shower leaks out the sides of the calorimeter (95% of the shower is concentrated within 4 cm transverse to the incident track [34]).

## 3. EC minimum energy deposit

The energy deposited in the inner layer of the EC is required to satisfy  $EC_{inner} > 50$  MeV. This cut rejects minimum ionizing particles (MIP) by requiring an energy deposit larger than a MIP would make in traversing the inner layer.

## 4. EC energy/momentum match

The sampling fraction of the EC has been parameterized in terms of the incident electron momentum:

$$f(p) = \frac{0.23p + 0.071p^2 - 0.032p^3}{p} \quad p < 1.0 \text{ GeV}/c \quad (2.5)$$

$$(2.6)$$

$$f(p) = 0.272 \quad p > 1.0 \text{ GeV}/c \quad (2.7)$$

The electron energy determined from the track momentum measured in the DC and the energy deposited in the EC must satisfy the relation:

$$-0.2 < E - \frac{E_{dep}}{f(p)} < 0.15 \text{ GeV}/c \quad (2.8)$$

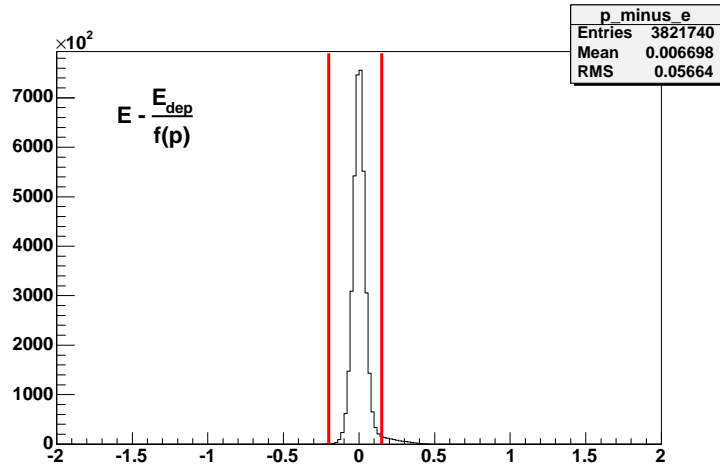


Figure 2.5: The difference between electron energy determined from tracking and sampling-fraction corrected energy deposited in EC. The cut values are shown in red. The data is a sample of the 2.6 GeV data set.

This cut is illustrated for a sample of the 2.6 GeV data set in Fig 2.5.

#### 5. CC hit and photo-electron cut

A hit in the CC, correlated with the DC track, was required, with a minimum of 1.0 for the estimated number of photo-electrons produced, based on the ADC response. This cut is illustrated in Fig 2.6.

### 2.3.2 $\pi^+$ Identification

Positive tracks were identified as  $\pi^+$  by comparing the particle velocity measured from a combination of tracking and time-of-flight information to the velocity expected for a  $\pi^+$  of the measured momentum.

The particle velocity was determined from:

$$\beta_{track} = \frac{l_{\pi}}{c\Delta t} \quad (2.9)$$

where  $l_{\pi}$  is the track length of the  $\pi^+$  candidate measured by the DC, and

$$\Delta t = t_{\pi} - t_0 \quad (2.10)$$

where  $t_{\pi}$  is the time reported by the SC for the particle, and  $t_0$  is the event start time, found from:

$$t_0 = t_{electron} - \frac{l_{electron}}{c}. \quad (2.11)$$

where  $t_{electron}$  is the electron time reported by the SC and  $l_{electron}$  is the electron track length (from the vertex to the SC plane) determined from tracking.

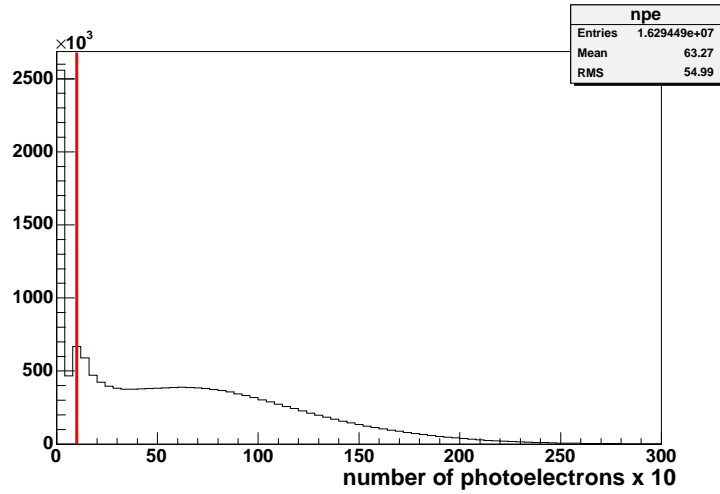


Figure 2.6: The horizontal axis shows 10 times the estimated number of photoelectrons produced in the CC. The cut is shown in red. The data is a sample of the 2.6 GeV data set.

The particle velocity can also be determined from its measured momentum and an assumption regarding its species:

$$\beta_{\pi} = \frac{|\vec{p}|}{\sqrt{\vec{p}^2 + M_{\pi}^2}} \quad (2.12)$$

A cut was placed on the difference of these two  $\beta$  values, which required:

$$-0.04 < \Delta\beta < 0.04. \quad (2.13)$$

This cut is illustrated in Fig 2.7.

A CC veto was applied, rejecting any  $\pi^+$  candidate track that had an associated hit in the Cerenkov detector.

### 2.3.3 Neutron selection

Once the event had been identified as having a good electron and  $\pi^+$ , the missing mass in the event was calculated. The 4-momentum of the initial state particles was known:

$$e_{in} = E_0(1, 0, 0, 1) \quad (2.14)$$

$$P = (M_p, 0, 0, 0) \quad (2.15)$$

where  $e_{in}$  is the incoming electron 4-momentum ( $E_0$  is the incident beam energy), and  $P$  is the 4-momentum of the target proton. The final-state was assumed to be composed of an electron,  $\pi^+$  and neutron. The electron and  $\pi^+$  4-momenta were known

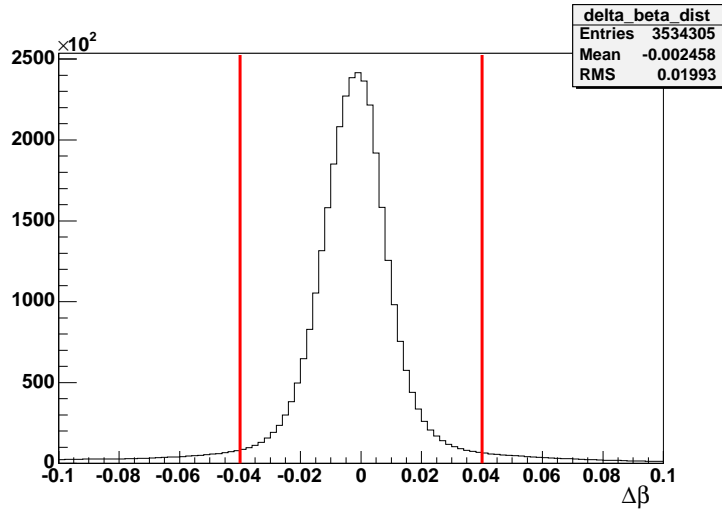


Figure 2.7: The distribution of the difference between  $\beta$  determined from path length and time-of-flight and  $\beta$  determined from the measured momentum and the assumption that the particle is a  $\pi^+$ . The cuts are shown in red. The data is from the 2.6 GeV data set.

from tracking, so the neutron 4-momentum could be determined from conservation of 4-momentum:

$$X_n = e_{in} + P - e_{out} - \pi_{out} \quad (2.16)$$

where  $X_n$  is the neutron 4-momentum and  $e_{out}, \pi_{out}$  are the momentum of the scattered electron and pion. The missing mass was found from:

$$MM = \sqrt{X^2} \quad (2.17)$$

The missing mass for each event was required to satisfy:

$$0.9 < MM < 0.95 \text{ GeV}/c^2 \quad (2.18)$$

The missing mass cut is illustrated in Fig 2.8.

## 2.3.4 Efficiency Measurement in the Forward Calorimeter

### 2.3.4.1 Neutron selection and sector-wise efficiency measurement

The direction of the neutron in the  $ep \rightarrow e\pi^+(n)$  reaction was determined from Eqn 2.16. A ray was drawn from the electron- $\pi^+$  vertex position to a plane parallel to the EC face. If the point-of-intersection lay outside the triangle defined by the EC face, the event was dropped. An additional fiducial cut required that the point-of-intersection lie more than 60 cm from any EC edge was enforced. In the cases where the reconstructed neutron was expected to intersect the fiducial region of one

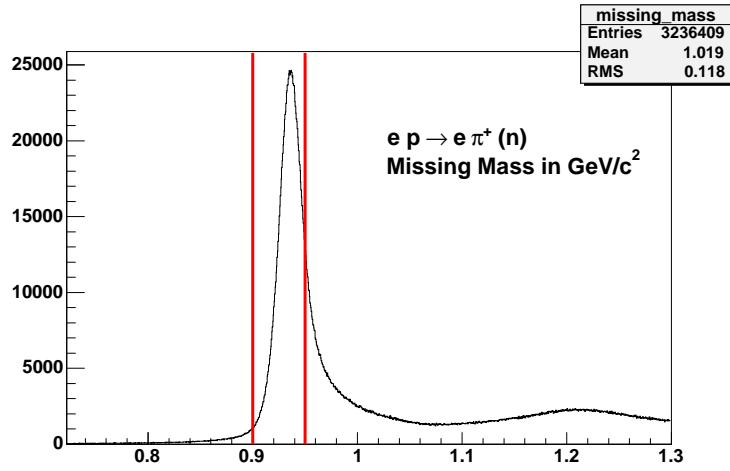


Figure 2.8: Missing mass in the  $ep \rightarrow e\pi^+(n)$  reaction. The neutron selection cut is shown in red. The data is from the 2.6 GeV data set.

of the EC modules, the EC module was searched for neutral hits (hits which have no associated charged tracks) in the vicinity of the expected point-of-intersection. A cut rejecting neutral hits found more than 30 cm (as measured in the EC plane) from the expected point-of-intersection was applied. This cut is illustrated in Fig 2.9.

In the case where a neutral hit was found which satisfied the  $\Delta R$  cut, an additional cut required at least 15 MeV of energy deposited in the calorimeter.

An event in which a good electron and  $\pi^+$  were found, and for which the expected point-of-intersection was within the EC fiducial region was labeled a *reconstructed* event. A reconstructed event which contained a neutron hit which satisfied the  $\Delta R$  cut and the minimum energy deposited cut was labeled a *found* event. The events were binned in neutron momentum and the detection efficiency in each momentum bin was calculated as:

$$\eta_i = \frac{f_i}{r_i} \quad (2.19)$$

where  $\eta_i$  is the efficiency in the  $i^{\text{th}}$  momentum bin, and  $f_i$  and  $r_i$  are the number of found and reconstructed neutron events in the  $i^{\text{th}}$  momentum bin, respectively. The distribution of accepted neutrons in each momentum bin follows a binomial distribution (in each trial, the neutron is either found or not found), with the probability of success being the efficiency at that momentum. The variance on  $r$  for the binomial distribution is given by:

$$V = \left(\frac{r}{r-1}\right) r \left(\frac{f}{r}\right) \left(1 - \frac{f}{r}\right) \quad (2.20)$$

where  $r$  is the number of trials (the number of reconstructed neutrons) and  $f$  is the number of successes (the number of found neutrons). The estimate for the efficiency

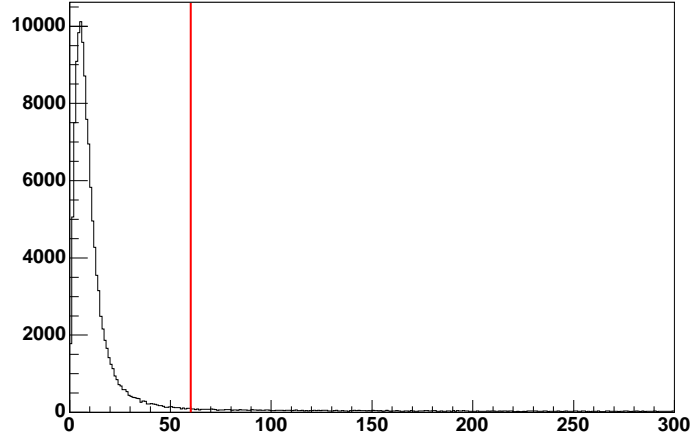


Figure 2.9: The distribution of the distance  $\Delta R$  between the expected point-of-intersection and the observed hit location for neutron candidate events in the EC. The cut applied is shown in red. The data is a sample from the 2.6 GeV dataset.

is  $\frac{f}{r}$ , so the estimate on the error on the efficiency in the  $i^{\text{th}}$  bin is given by:

$$\sigma_i = \sqrt{\left(\frac{f_i}{r_i}\right) \frac{1 - \frac{f_i}{r_i}}{r_i - 1}} \quad (2.21)$$

Fig 2.10 and Fig 2.11 show plots of the neutron detection efficiency in each of the six EC modules, for the 2.6 GeV and 4.2 GeV data sets. Fig 2.12 shows a comparison of the neutron detection efficiency integrated over all six EC modules measured in each data set.

### 2.3.4.2 Efficiency parameterization in the EC

The neutron detection efficiency in each sector was parameterized as a function of the neutron momentum with polynomials of the form:

$$\eta(p) = a_0 + a_1 p + a_2 p^2 + a_3 p^3 \quad (2.22)$$

for  $p < p_t$ , and:

$$\eta(p) = f \quad (2.23)$$

for  $p \geq p_t$ .  $p_t$  was a parameter of the fit, and the parameter  $f$  was determined by requiring that  $\eta(p)$  be continuous at  $p = p_t$ . The fit parameters were obtained using a maximum likelihood method. The following terms will be used in the description of the fitting procedure:

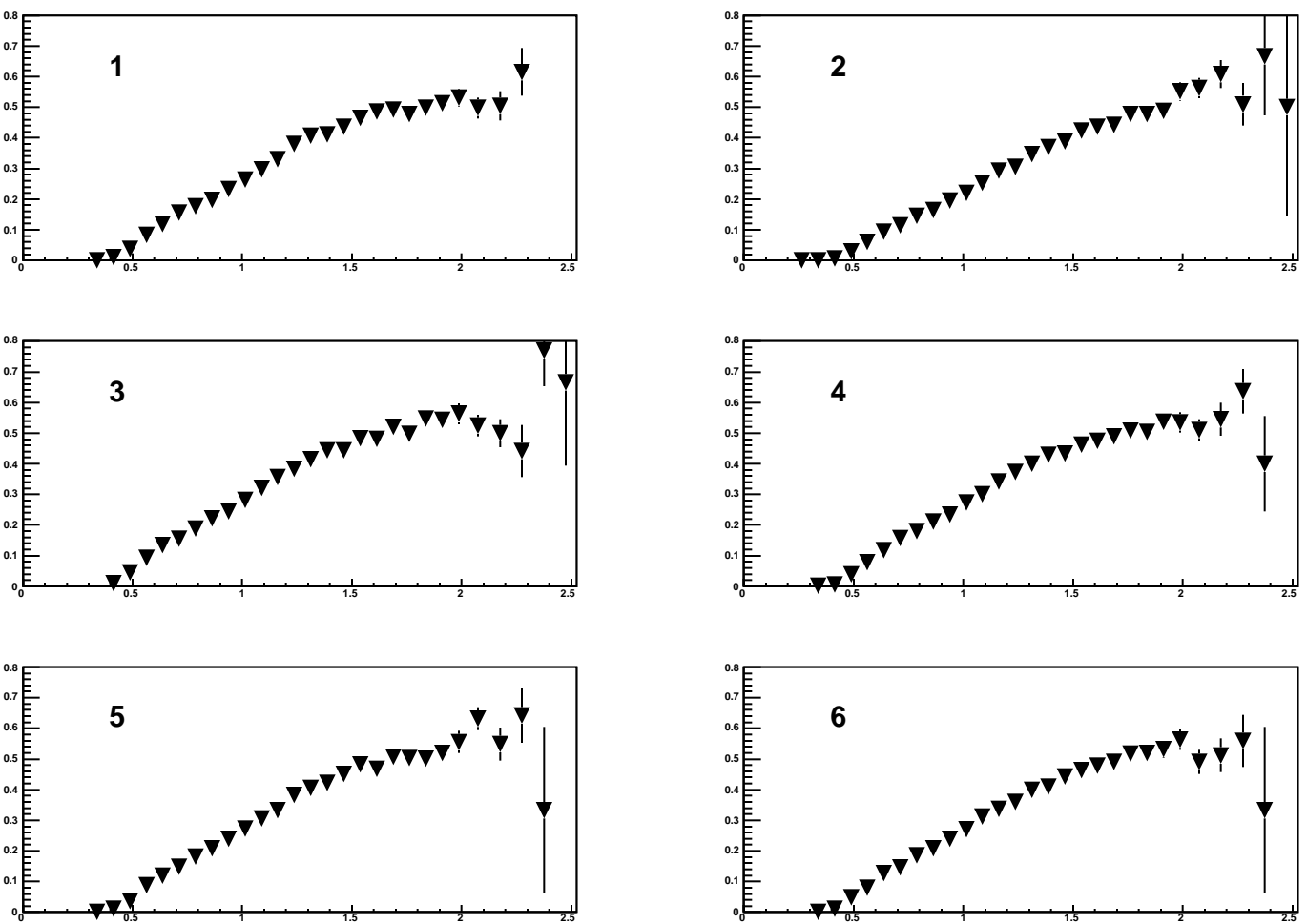


Figure 2.10: EC Neutron detection efficiency, binned in neutron momentum, for each sector in the 2.6 GeV dataset. The sectors numbers are indicated in each panel. The horizontal axis in each panel is the neutron momentum in GeV/c.

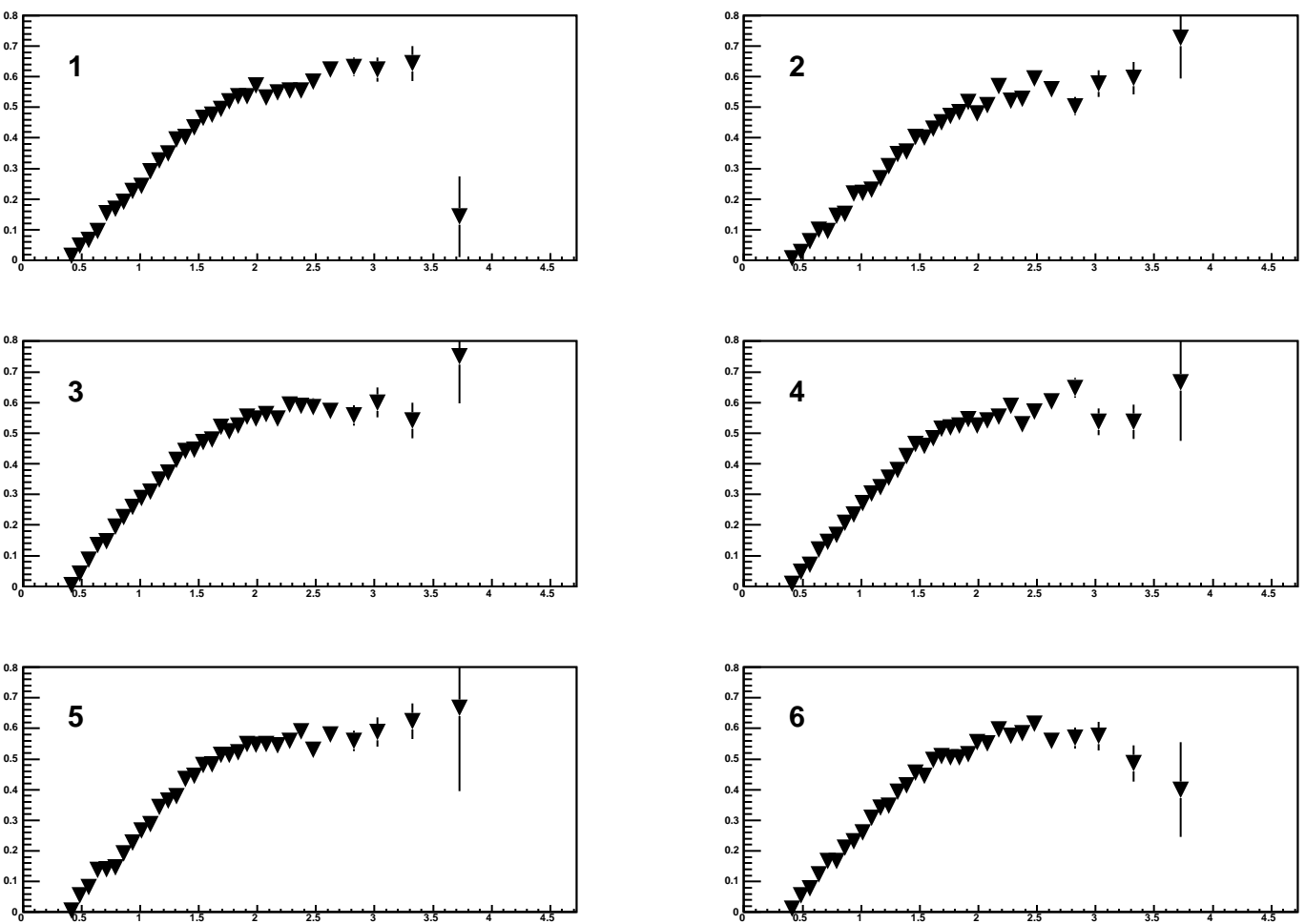


Figure 2.11: EC Neutron detection efficiency, binned in neutron momentum, for each sector in the 4.2 GeV dataset. The sectors numbers are indicated in each panel. The horizontal axis in each panel is the neutron momentum in GeV/c.

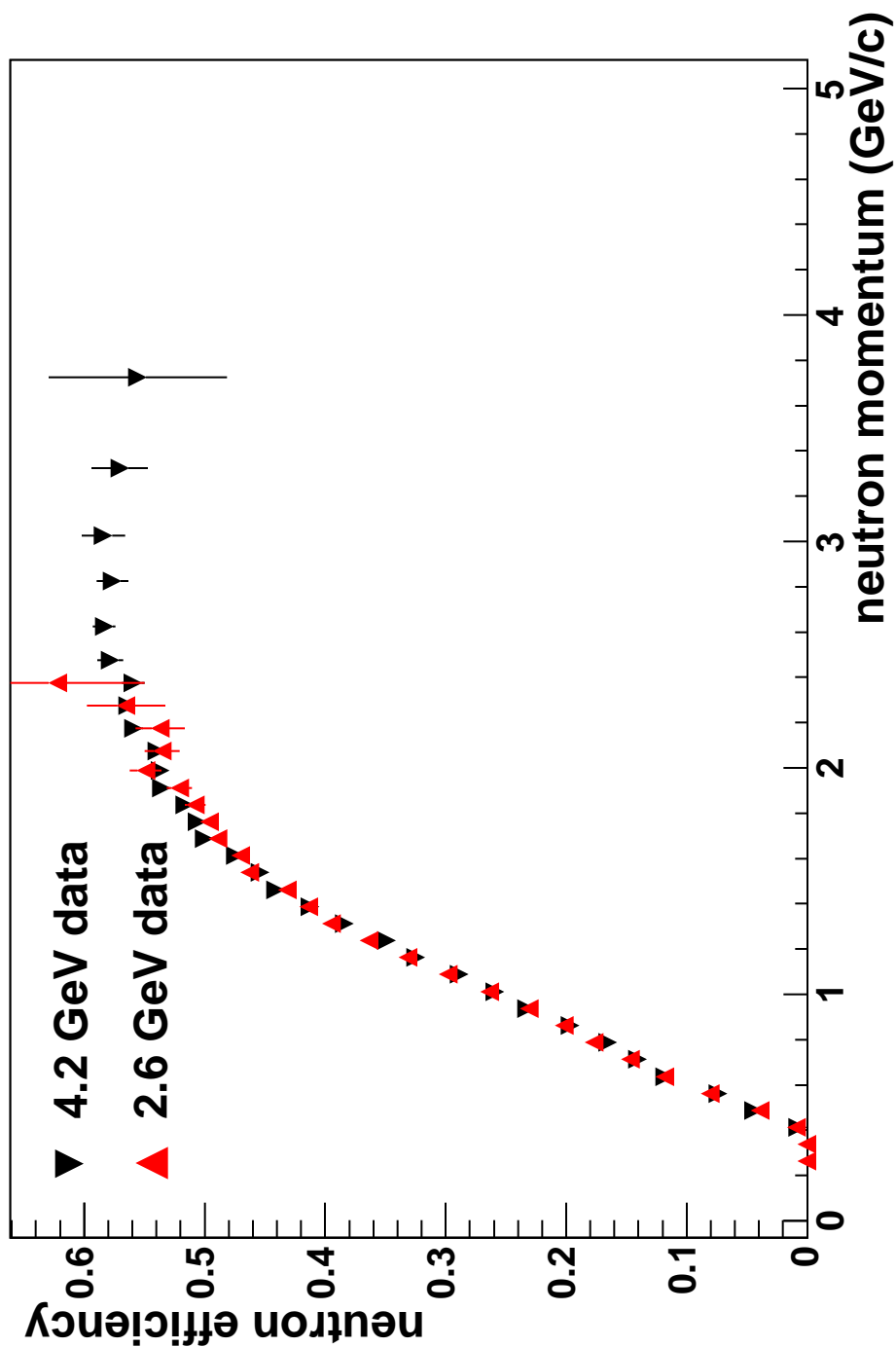


Figure 2.12: A comparison of the neutron detection efficiency in the EC, as measured at two different beam energies. In this figure, the efficiency has been integrated over all six sectors

$r_i$  = number of entries in  $i^{\text{th}}$  momentum bin of the reconstructed neutron histogram

$f_i$  = number of entries in  $i^{\text{th}}$  momentum bin of the found neutron histogram

$\eta_i$  = efficiency in  $i^{\text{th}}$  momentum bin, defined above.

It is assumed that the number of found  $i$  neutrons expected to be seen in the  $i^{\text{th}}$  momentum bin is:

$$\mu_i = \eta_i r_i. \quad (2.24)$$

From the Poisson distribution, the probability to see  $f_i$  counts when  $\mu_i$  counts are expected is:

$$P_i = \frac{\mu_i^{f_i}}{f_i!} e^{-\mu_i} \quad (2.25)$$

The probability to observe the entire found neutron distribution is then given by the product of the probability of observing  $f_i$  counts in each bin:

$$P = \prod_i \frac{\mu_i^{f_i}}{f_i!} e^{-\mu_i} \quad (2.26)$$

The parameters in the function  $\eta(p)$  are chosen such that  $P$  is maximized. Consider the (negative) natural log of  $P$ :

$$-\ln P = - \sum_i \{f_i \ln \mu_i - \ln f_i! - \mu_i\} \quad (2.27)$$

The second term,  $\sum_i \ln f_i!$ , does not depend on any of the parameters, so it can be treated as a constant. The 5 parameters for  $\eta(p)$  are then obtained by minimizing:

$$-\ln P = - \sum_i \{f_i \ln \mu_i - \mu_i\} + \text{constant} \quad (2.28)$$

This minimization procedure was performed, using MINUIT, in each of six sectors. In an effort to account for any possible dependence of the neutron detection efficiency on the position of the neutron hit on the EC face, the EC face was subdivided into smaller units. Each of the three EC views is composed of 36 strips. This division segments the EC face into  $36^2 = 1296$  triangular *pixels*. Sets of 12 adjacent strips in each view were collected together in software to reduce the number of divisions per view to 3. These 3 *superstrips* divide the EC face into  $3^2 = 9$  *superpixels*, as illustrated in Fig 2.13.

The uncertainty on the fit at a given momentum was found from the error matrix returned by MINUIT:

$$\sigma_\eta^2 = \sum_{i,j} \epsilon_{ij} \frac{\partial \eta}{\partial a_i} \frac{\partial \eta}{\partial a_j} \quad (2.29)$$

where  $\eta$  is the value of the fitted function function,  $a_i$  is the  $i^{\text{th}}$  parameter of the fit, and  $\epsilon_{ij}$  are the values of the error matrix returned by MINUIT. The results of

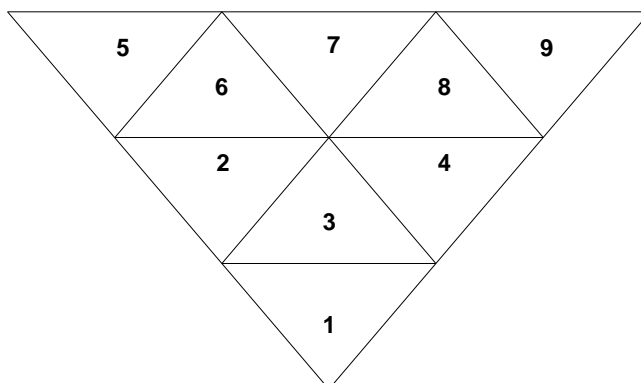


Figure 2.13: Division of the EC face into 9 superpixels. Pixel 1 is located nearest the beam line.

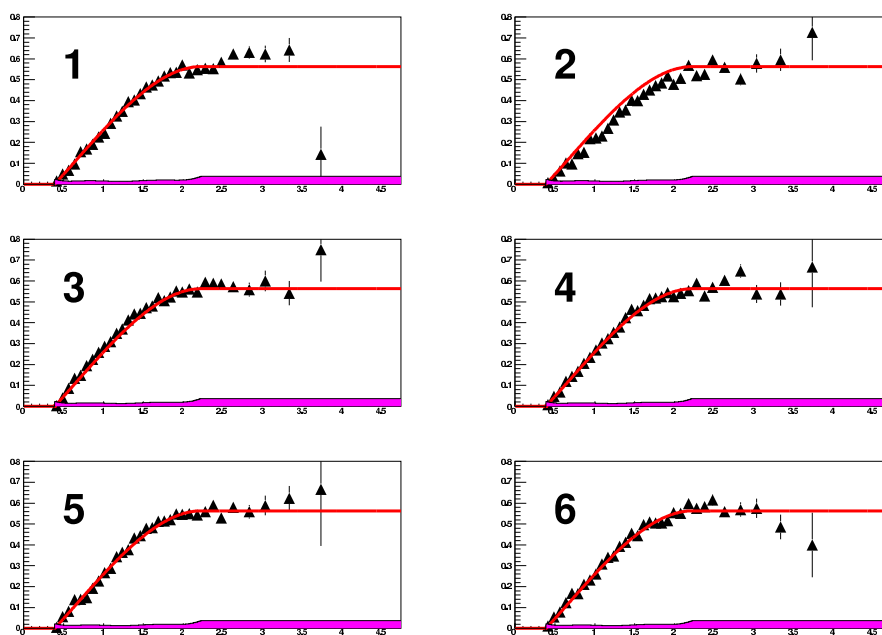


Figure 2.14: The sector-based fits to the EC neutron detection efficiency for the 4.2 GeV data are shown in red. The uncertainty on the fit, scaled up by a factor of 10, is shown by the magenta band. The horizontal axis shows the neutron momentum in GeV/c.

the sector-based fits for the 4.2 GeV data are shown in Fig 2.14. Similar results are obtained in the 2.6 GeV case.

The efficiency function on each superpixel,  $\eta_{sp}$ , was taken to be the product of the efficiency function for that sector multiplied by a scale factor:

$$\eta_{sp}(p) = \alpha \eta_{sector}(p) \quad (2.30)$$

The scale factor  $\alpha$  for each superpixel was found by minimizing the function:

$$\chi^2 = \sum_i \left( \frac{\epsilon_i - \alpha \eta(p_i)}{\sigma_i} \right)^2 \quad (2.31)$$

In this equation,  $\epsilon_i$  is the measured efficiency in the  $i^{th}$  momentum bin for that superpixel,  $\eta(p_i)$  is the efficiency function for the sector evaluated at the center of the  $i^{th}$  momentum bin and  $\sigma_i$  is the error on the measured efficiency in the  $i^{th}$  momentum bin for that superpixel. The value of the scale factor is given by:

$$\alpha = \frac{\sum \frac{\epsilon_i \eta(p_i)}{\sigma_i^2}}{\sum \frac{\eta(p_i)^2}{\sigma_i^2}} \quad (2.32)$$

The uncertainty on the scale factor is given by:

$$\sigma_\alpha^2 = \sum \sigma_i^2 \left( \frac{\partial \alpha}{\partial \epsilon_i} \right)^2 \quad (2.33)$$

$$= \frac{1}{\sum \frac{\eta(p_i)^2}{\sigma_i^2}} \quad (2.34)$$

Appendix B contains plots of the measured efficiency and efficiency fits for each of the nine superpixels in each of the six sectors for the 2.6 GeV and 4.2 GeV data sets. The values of the scale factor and error on the scale factor are indicated on the plots.

## 2.3.5 Efficiency Measurement in the Time of Flight system

### 2.3.5.1 Neutron selection and sector-wise efficiency measurement

The direction of the neutron in the  $ep \rightarrow e\pi^+(n)$  reaction was determined from Eqn 2.16. A ray was drawn from the electron- $\pi^+$  vertex position to each of the planes parallel to the four SC panels in the sector into which the neutron was moving. The point-of-intersection of the neutron in each plane was calculated, and the plane which had the shortest vertex to point-of-intersection distance was used to determine the SC panel hit. This was done to resolve paddle-overlap issues near the panel edges. The point-of-intersection was required to be located on one of the SC paddles in the struck

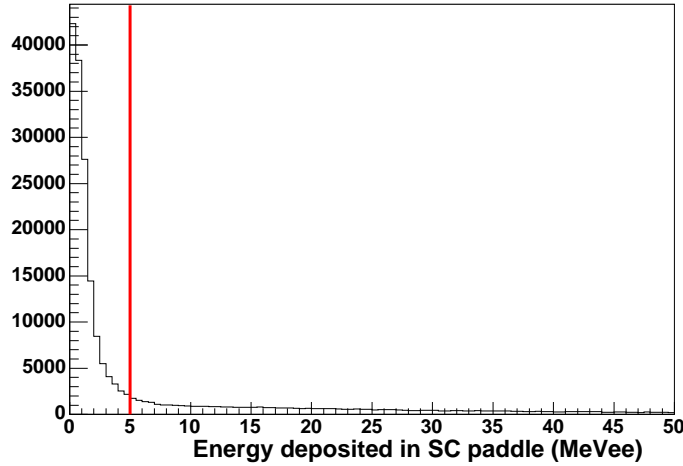


Figure 2.15: The energy deposited in the SC by candidate neutron events. The cut applied is shown in red. Only events with energy greater than 5 MeVee were considered for further analysis. The data shown are a sample from the 2.6 GeV data set.

panel. An additional fiducial cut required that the expected point-of-intersection to be more than 10 cm from either of the two ends of the paddle. In the cases where the reconstructed neutron was expected to intersect the fiducial region of one of the SC panels, that SC panel was searched for neutral hits uncorrelated with any charged track. Events which had SC hits on paddles other than the expected paddle or one of the two paddles adjacent to the expected paddle were rejected. In the case where the neutron was expected to strike a paddle at the edge of a panel, the edge paddles in the adjacent panel were searched as well.

Because generating an SC hit requires an interaction in only a single scintillator, the photon background is higher in the SC than in the EC. Photon rejection was accomplished by cuts on energy deposited and timing. Fig 2.15 shows a plot of the distribution of energy deposited in candidate SC neutron events. A large spike of very low energy events is seen. A cut requiring  $E_{dep} > 5$  MeVee (MeV, electron equivalent) was applied to reject low energy photon background. Because the same  $E_{min}$  cut was applied to SC neutrons in the quasi-elastic analysis, the exact location of this cut could be chosen somewhat arbitrarily.

After rejecting the low energy events, a timing cut was applied. The expected time-of-flight of the neutron was calculated from:

$$t_{expected} = \frac{|\vec{v} - \vec{x}|}{\beta c} \quad (2.35)$$

where  $\vec{v}$  is the electron- $\pi^+$  vertex position and  $\vec{x}$  is the location of the expected point-of-intersection of the neutron at the SC paddle. The measured neutron time-of-flight

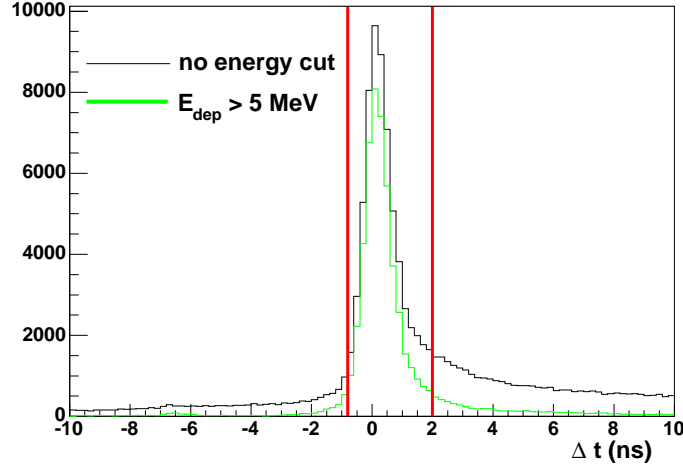


Figure 2.16: The  $\Delta t$  distribution for candidate neutron events in the SC. The black curve shows  $\Delta t$  before application of the  $E_{dep}$  cut. The green curve shows  $\Delta t$  after the  $E_{dep}$  cut. The cuts applied are shown in red. The data shown are a sample from the 2.6 GeV data set.

was calculated from:

$$t_{measured} = t_{sc} - t_0 \quad (2.36)$$

where  $t_{sc}$  is the hit time reported by the SC and  $t_0$  is the event start time defined in Eqn 2.11. A cut was applied requiring

$$-0.8 < \Delta t < 2.0ns \quad (2.37)$$

where  $\Delta t = t_{measured} - t_{expected}$ . The effect of the timing cut is illustrated in Fig 2.16

The events were binned in neutron momentum and the efficiency and uncertainties were calculated as in Eqns 2.19 and 2.21. Fig 2.17 and Fig 2.18 show plots of the neutron detection efficiency in each of the six SC sectors (integrated over all paddles), for the 2.6 GeV and 4.2 GeV data sets. Fig 2.19 shows a comparison of the neutron detection efficiency integrated over all six SC modules measured in each data set.

### 2.3.5.2 Efficiency parameterization in the SC

The neutron detection efficiency in each sector was parameterized as a function of the neutron momentum with a polynomial of the form:

$$\eta(p) = a_0 + a_1p + a_2p^2 + a_3p^3 \quad (2.38)$$

for  $p < p_t$  and:

$$\eta(p) = f \quad (2.39)$$

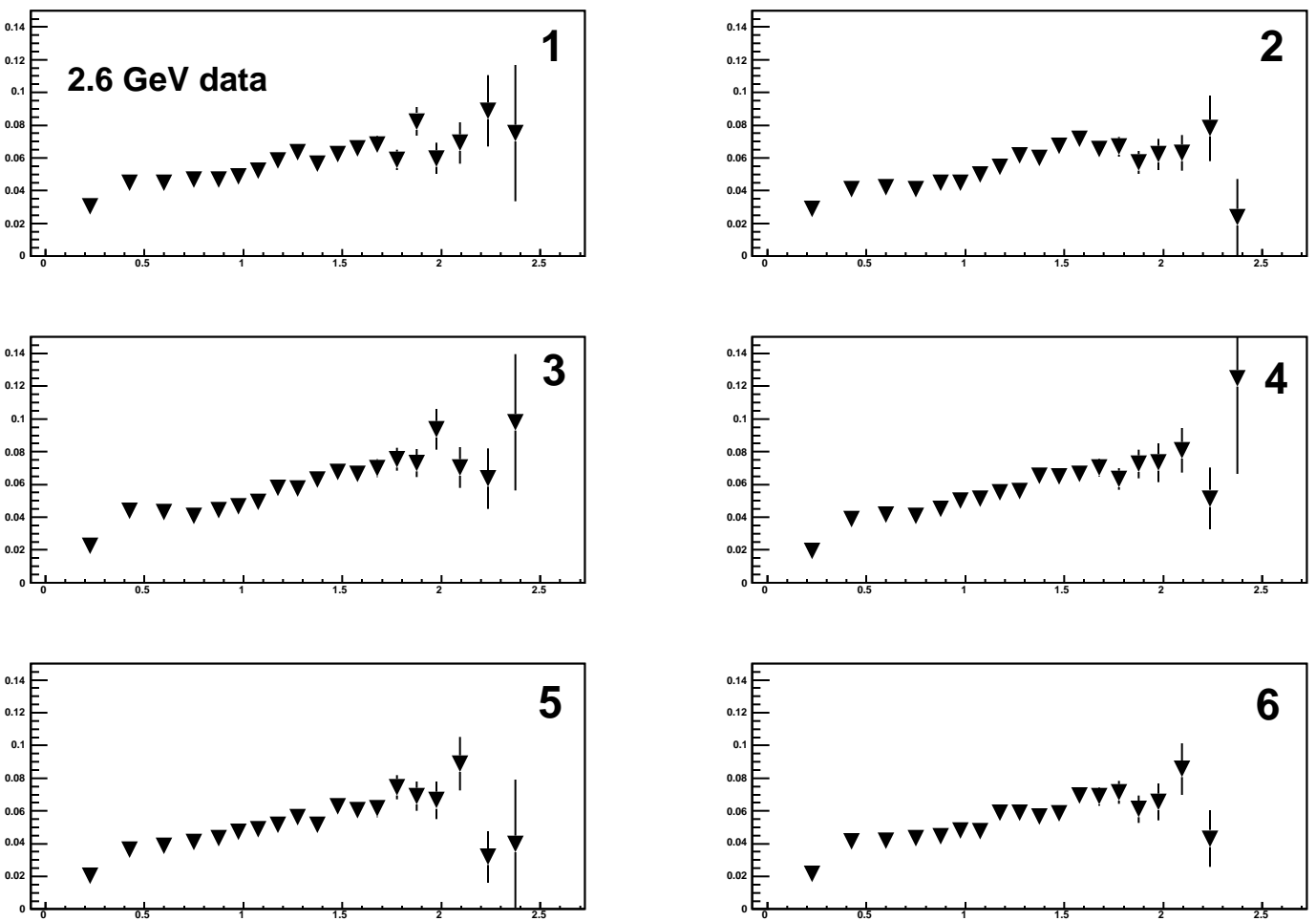


Figure 2.17: SC Neutron detection efficiency, binned in neutron momentum, for each sector in the 2.6 GeV data set. The horizontal axis in each panel is the neutron momentum in GeV/c.

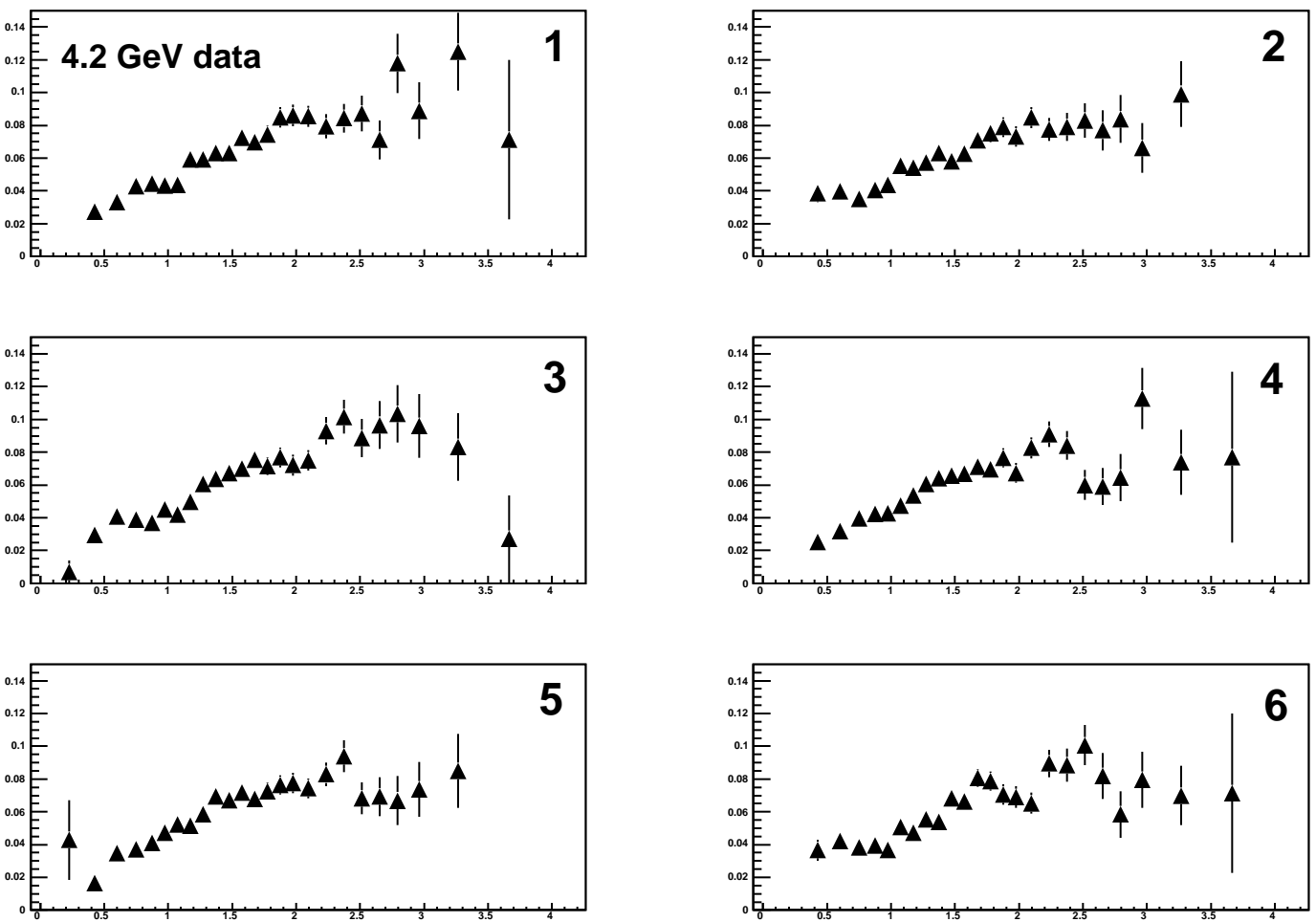


Figure 2.18: SC Neutron detection efficiency, binned in neutron momentum, for each sector in the 4.2 GeV data set. The horizontal axis in each panel is the neutron momentum in GeV/c.

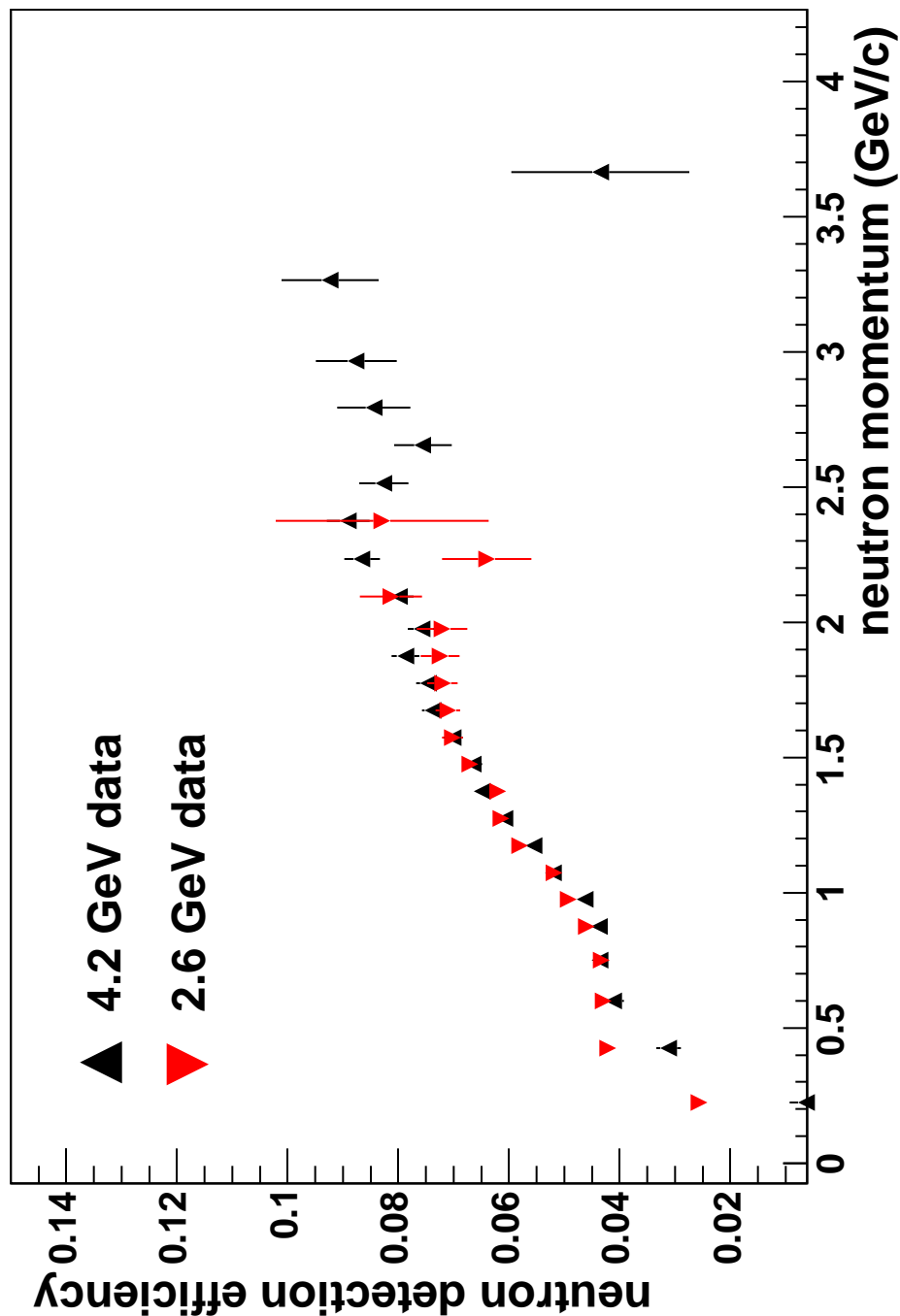


Figure 2.19: A comparison of the neutron detection efficiency in the SC, as measured at two different beam energies. In this figure, the efficiency has been integrated over all six sectors

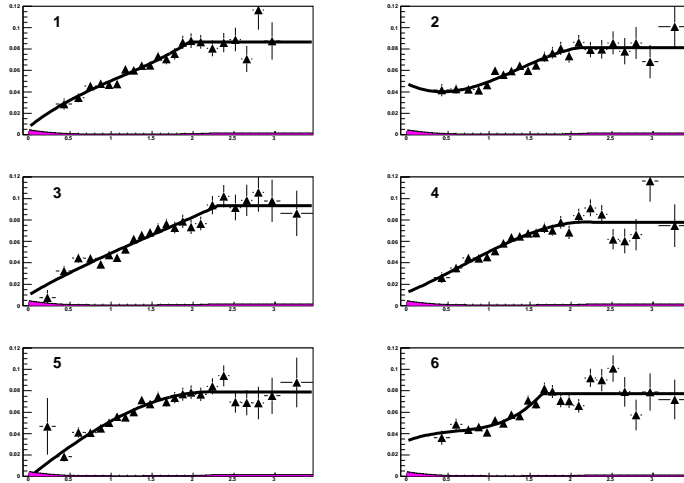


Figure 2.20: The sector-based fits to the SC neutron detection efficiency for the 4.2 GeV data are shown. The uncertainty on the fit is shown by the magenta band. The horizontal axis in each panel shows the neutron momentum in GeV/c.

for  $p \geq p_t$ .  $p_t$  was a parameter of the fit, and  $f$  was determined by requiring  $\eta(p)$  to be continuous at  $p_t$ .

The global efficiency histogram in each sector (containing data from all paddles in the sector) was fitted by this polynomial form using a least-squares fit over the momentum range  $0.0 < p < 1.8$  GeV/c for the 2.6 GeV data set, and  $0.0 < p < 2.8$  GeV/c for the 4.2 GeV data set. The uncertainty on the fit at a given momentum was found from the error matrix returned by MINUIT:

$$\sigma_\eta^2 = \sum_{i,j} \epsilon_{ij} \frac{\partial \eta}{\partial a_i} \frac{\partial \eta}{\partial a_j} \quad (2.40)$$

where  $\eta$  is the value of the fitted function,  $a_i$  is the  $i^{\text{th}}$  parameter of the fit, and  $\epsilon_{ij}$  are the values of the error matrix returned by MINUIT. The fits and associated errors for each of the six sectors in the 4.2 GeV data is shown in Fig 2.20.

In an effort to account for possible paddle-by-paddle variations in the neutron detection efficiency, the efficiency on each paddle,  $\eta_p$ , was taken to be the product of the efficiency function for that sector multiplied by a scale factor:

$$\eta_{\text{paddle}}(p) = \alpha \eta_{\text{sector}}(p). \quad (2.41)$$

The scale factor  $\alpha$  for each paddle was found by minimizing the function:

$$\chi^2 = \sum_i \left( \frac{\epsilon_i - \alpha \eta(p_i)}{\sigma_i} \right)^2 \quad (2.42)$$

In this equation,  $\epsilon_i$  is the measured efficiency in the  $i^{th}$  momentum bin for that paddle,  $\eta(p_i)$  is the efficiency function for the sector evaluated at the center of the  $i^{th}$  momentum bin and  $\sigma_i$  is the error on the measured efficiency in the  $i^{th}$  momentum bin for that paddle. The equation for the value of the scale factor and its error are the same as in the EC case.

Appendix C contains plots of the measured efficiency and efficiency fits for each paddle in each of the six sectors for the 2.3 GeV and 4.2 GeV data sets. Badly-performing paddles were rejected by requiring:

$$0.8 \leq \alpha \leq 1.2 \quad (2.43)$$

Paddles which failed to satisfy this requirement were switched off in software. Paddles with less than 4 data points (for example, sector 4, paddle 29 in Fig C.4) were switched off in software. This cut defined the high-paddle number cut-off. For the 4.2 GeV data, the high-paddle cut-off is 25 or 26 depending on sector, while the cut-off in the 2.6 GeV data set is paddle number 27 or 28 depending on sector.

## 2.4 Proton Detection Efficiency Measurement

The hydrogen cell of the e5 target allows for an *in-situ* measurement of the proton detection efficiency in the SC detector system. Elastic  $ep$  scattering is used as a proton source. Candidate events were selected which had one negative track, and not more than one positive tracks.

### 2.4.1 Electron Identification

The electron selection criteria described in Section 2.3.1 were applied. Once the event was identified as having a good electron, the mass of the recoiling hadronic system was calculated. The 4-momentum of the initial state particles was known:

$$e_{in} = E_0(1, 0, 0, 1) \quad (2.44)$$

$$P = (M_p, 0, 0, 0) \quad (2.45)$$

where  $e_{in}$  is the incoming electron 4-momentum ( $E_0$  is the incident beam energy), and  $P$  is the 4-momentum of the target proton. The final state was taken to be an electron and a recoiling hadronic system. The scattered electron 4-momentum was known from tracking, so the recoil 4-momentum could be determined from conservation of 4-momentum:

$$X_h = e_{in} + P - e_{out} \quad (2.46)$$

where  $X_h$  is the 4-momentum of the hadronic system and  $e_{out}$  is the scattered electron 4-momentum. The square of the invariant mass of the hadronic system was found from:

$$W^2 = X_h^\mu X_{h,\mu}. \quad (2.47)$$

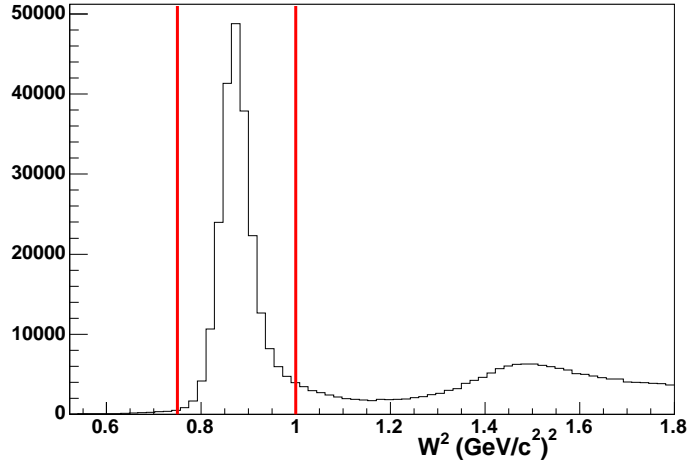


Figure 2.21: The  $W^2$  distribution in candidate  $ep$  elastic events (events with an electron and zero or one charged track). The cuts applied are shown in red. The data shown are a sample of the 2.6 GeV data set.

Elastic events were selected by applying a cut that required

$$0.75 < W^2 < 1.0(\text{GeV}/c^2)^2 \quad (2.48)$$

The distribution of  $W^2$  and the cuts applied are illustrated in Fig. 2.21.

For events which passed the  $W^2$  cut (labeled *reconstructed* events), the paddle the proton was expected to hit was calculated by *swimming* the proton from the electron-beamline vertex position through the mini-torus and main torus magnetic fields out to the SC. The point-of-intersection of the proton in each SC plane was calculated, and the plane which had the shortest vertex to point-of-intersection distance was used to determine the SC panel hit. The point-of-intersection was required to be located on one of the SC paddles in the struck panel. An additional fiducial cut required that the expected point-of-intersection to be more than 10 cm from either of the two ends of the paddle. In those cases where the proton was expected to intersect the SC fiducial region, the SC was searched for hits correlated with a positively-charged track.

## 2.4.2 Proton Identification

Elastic events in which a positive track is found were subjected to a cut requiring the coplanarity of the positive track and the electron. For elastic scattering, the electron and proton azimuthal angles should be  $180^\circ$  apart. Fig 2.22 shows the  $|\Delta\phi|$  distribution for events which passed the  $W^2$  cut. A cut requiring

$$178^\circ < |\Delta\phi| < 182^\circ \quad (2.49)$$

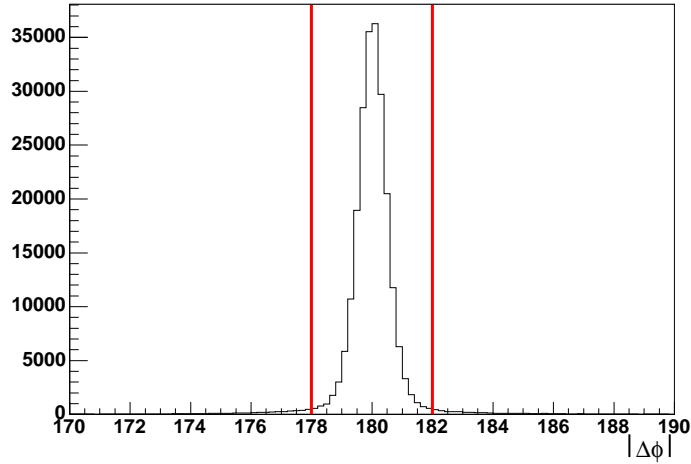


Figure 2.22: The  $\Delta\phi$  distribution for candidate  $ep$  elastic events which passed the  $W^2$  cut. The horizontal axis is in degrees. The cuts applied are shown in red. The data shown are a sample from the 2.6 GeV data set.

was applied.

The SC paddle which the proton hit was required to be the paddle predicted, or one of the two adjacent paddles.

### 2.4.3 Efficiency calculation

Because of the one-to-one relationship between proton scattering angle and proton momentum for elastic scattering, each SC paddle was illuminated by a narrow range of proton momenta. As such, no momentum dependent fitting was attempted. The efficiency on each paddle was calculated by integrating the found and reconstructed protons over the small momentum range covered by the paddle. The errors assigned were binomial, as described in Eqn 2.21. Figs 2.23 and 2.24 show plots of the average proton detection efficiency on each SC paddle in each of the six sectors for the 2.6 and 4.2 GeV data sets.

## 2.5 Momentum Corrections

Fig 2.25 shows  $W^2$  measured in  $ep$  elastic scattering as a function of electron azimuthal angle. Because of uncertainties in the magnetic field map used to reconstruct tracks in the drift chamber, the  $W^2$  determination is flawed, leading to mis-located centroids and strong  $\phi$  dependence in some sectors.

Elastic scattering from the proton target is used to derive a multiplicative correc-

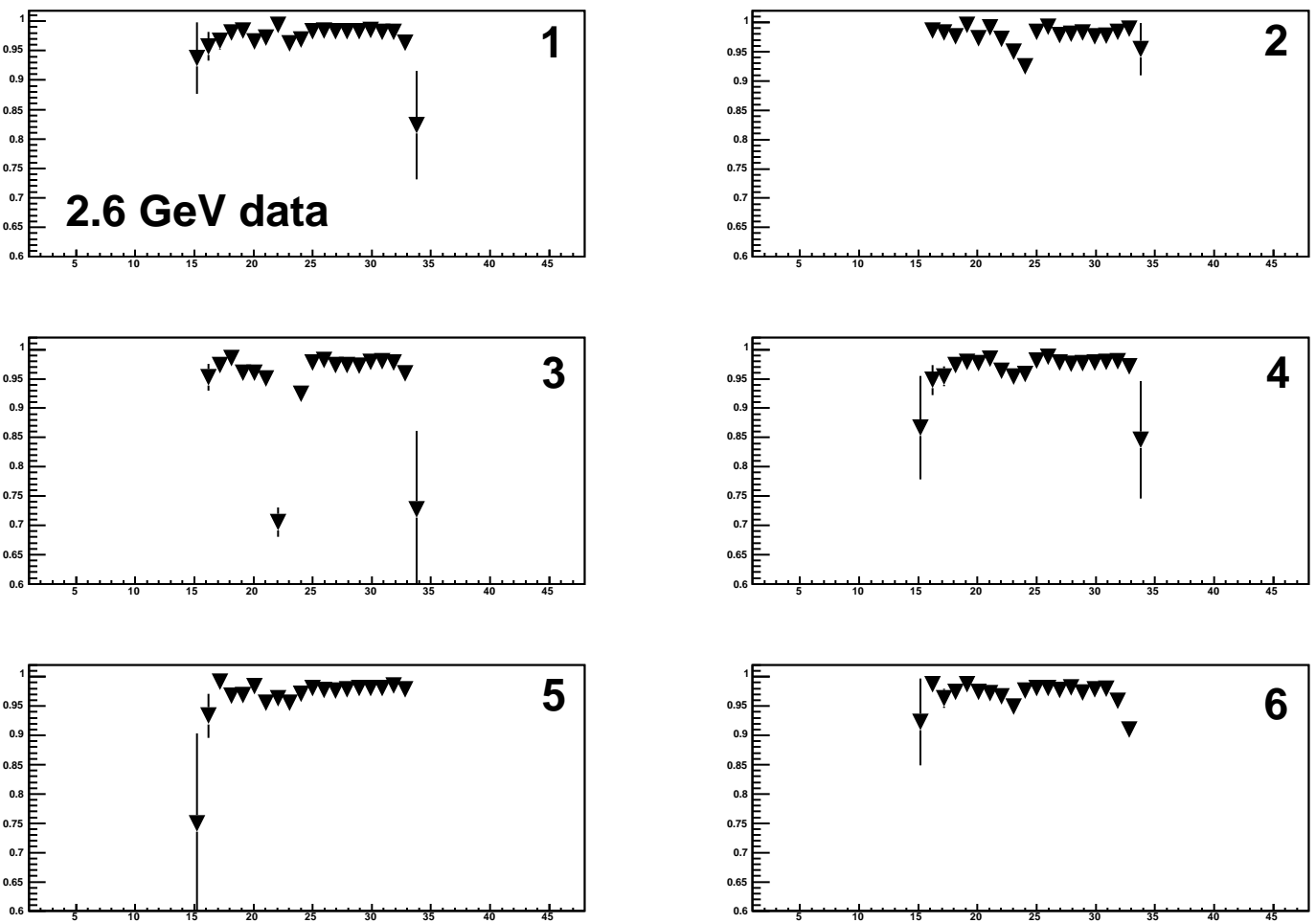


Figure 2.23: Average proton detection efficiency in the SC for the 2.6 GeV data set. The horizontal axis in each panel shows SC paddle number. The sector numbers are indicated in each panel.



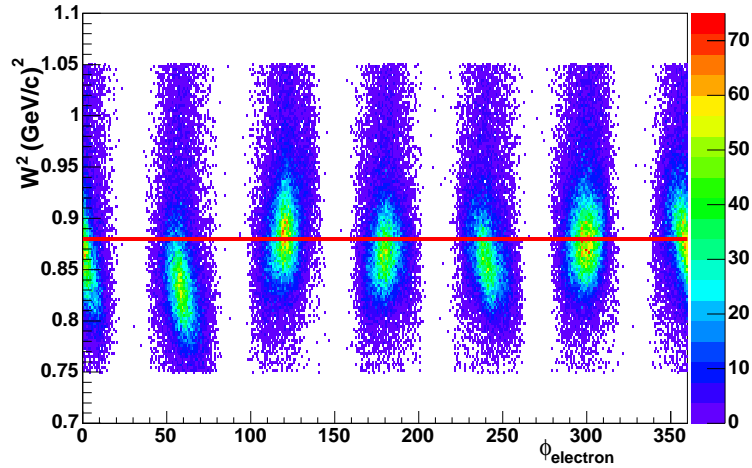


Figure 2.25:  $W^2$  as measured in ep elastic scattering in the 4.2 GeV data set, as a function of electron azimuthal angle. The red line shows the square of the proton mass.

tion to the electron momentum. Conservation of 4-momentum gives:

$$b^\mu + t^\mu = e^\mu + W^\mu \quad (2.50)$$

where  $b^\mu$  is the 4-momentum of the incident beam,  $t^\mu$  is the 4-momentum of the target proton,  $e^\mu$  is the 4-momentum of the scattered electron and  $W^\mu$  is the 4-momentum of the recoiling proton. These vectors have the following values:

$$b^\mu = E_0(1, \hat{z}) \quad (2.51)$$

$$t^\mu = (M_p, 0, 0, 0) \quad (2.52)$$

$$e^\mu = E(1, \hat{e}) \quad (2.53)$$

where  $E_0$  is the incident beam energy,  $E$  is the scattered electron energy and  $\hat{e}$  is the scattered electron direction. The proton invariant mass-squared is found from:

$$W^\mu = e^\mu - b^\mu - t^\mu \quad (2.54)$$

$$= e^\mu - a^\mu \quad (2.55)$$

where  $a^\mu \equiv b^\mu + t^\mu$ .

$$W^2 = (e^\mu - a^\mu)(e_\mu - a_\mu) \quad (2.56)$$

$$= a^2 - 2a^\mu e_\mu \quad (2.57)$$

The mass of the electron has been neglected. The assumption is made that tracking has correctly measured the *direction* of the scattered electron, but that its *energy*

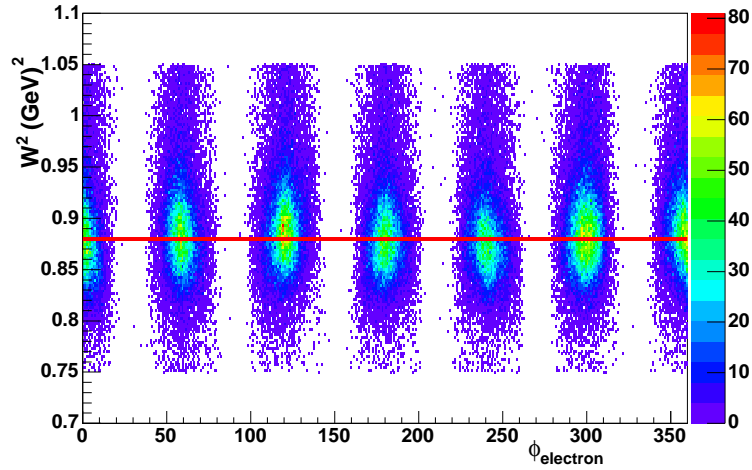


Figure 2.26:  $W^2$  as measured in ep elastic scattering in the 4.2 GeV data set, as a function of electron azimuthal angle, after momentum corrections. The red line shows the square of the proton mass.

may have been mismeasured, so that  $e^\mu$  is replaced by  $\alpha e^\mu$ . A sample of ep elastic events, selected according to the same criteria used in the proton detection efficiency measurement was used to find optimal values for  $\alpha$ . The data in each sector was subdivided in  $\theta$  and  $\phi$  bins. In each bin,  $\alpha$  was determined by minimizing:

$$\chi^2 = \sum_i \left( \frac{W_i^2 - M_p^2}{\sigma_i} \right)^2 \quad (2.58)$$

All events in each bin were weighted evenly. Setting  $\frac{d\chi^2}{d\alpha} = 0$  gives:

$$\alpha = \frac{\sum (a^\mu e_\mu) (a^2 - M_p^2)}{2 \sum (a^\mu e_\mu)^2} \quad (2.59)$$

The results of this procedure are illustrated in Fig 2.26, which shows  $W^2$  as a function of electron azimuthal angle *after* application of the corrections. Notice the reduced  $\phi$  dependence and improved centroid location.

Table 2.1 shows the centroid location in each of the six sectors for the 4.2 GeV data set before and after applying the correction. Table 2.2 shows the centroid locations for the 2.6 GeV data set.

Table 2.1: Comparison of uncorrected and corrected centroid values for  $W^2$  determination from elastic ep scattering in the 4.2 GeV data set. Centroid locations are given in  $\text{GeV}^2$

sector	uncorrected centroid	corrected centroid
1	0.8731	0.8784
2	0.8323	0.8697
3	0.8819	0.8838
4	0.8669	0.8763
5	0.8606	0.8734
6	0.8766	0.8809

Table 2.2: Comparison of uncorrected and corrected centroid values for  $W^2$  determination from elastic ep scattering in the 2.6 GeV data set. Centroid locations are given in  $\text{GeV}^2$

sector	uncorrected centroid	corrected centroid
1	0.8730	0.8793
2	0.8431	0.8790
3	0.8810	0.8825
4	0.8717	0.8793
5	0.8714	0.8792
6	0.8805	0.8821

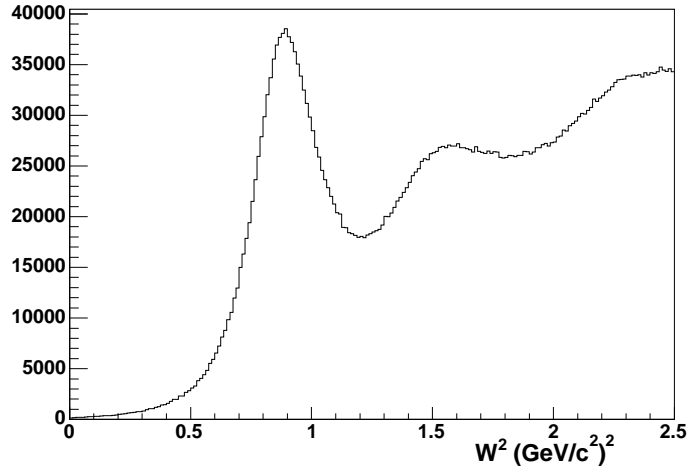


Figure 2.27:  $W^2$  in  $(\text{GeV}/c^2)^2$  for candidate  $D(e, e'n)$  and  $D(e, e'p)$  events after application of electron-based cuts. A quasi-elastic peak is clearly seen, along with a substantial inelastic background. Data from the 4.2 GeV running period is shown.

## 2.6 Quasi-elastic ratio measurement

### 2.6.1 Quasi-elastic electron selection

The cooked files containing all events seen in e5 were filtered down to a smaller set of files containing only  $D(e, e'n)$  and  $D(e, e'p)$  candidates by applying a few cuts based on the electron observed in each event. Events were required to have an electron which satisfied all of the electron selection criteria described in Section 2.4.1. Events which contained any negatively charged tracks in addition to the electron, or more than one positively charged track were discarded. Events in which the z-component of the electron vertex position was outside the deuterium target ( $-12.5 \leq z \leq -8.25$  cm) were discarded. After application of these cuts a substantial inelastic background remained, as shown in Fig 2.27.

### 2.6.2 Quasi-elastic $D(e, e'p)$ selection

To remove the inelastic background, an additional set of cuts were applied to the proton candidates. A  $Q^2$  dependent cut in the  $W^2, \theta_{pq}$  plane ( $\theta_{pq}$  is the angle between the virtual photon direction and the direction of the scattered nucleon at the vertex) was used to isolate events in the quasi-elastic region. The cuts are shown in Fig 2.28 and Fig 2.30 for protons which satisfied the EC fiducial cut described in Section 2.6.5, and in Fig 2.29 and Fig 2.31 for protons which satisfied the SC fiducial cuts described in Sec 2.6.5. The allowed  $W^2$  region is  $0.5 \leq W^2 \leq 1.2(\text{GeV}/c^2)^2$  in all  $Q^2$  bins. The maximum allowed  $\theta_{pq}$  varies from bin to bin and is summarized in Table 2.3 and

Table 2.3:  $Q^2$ -dependent  $\theta_{pq}$  cuts for EC protons in the 4.2 GeV data.

$Q^2$ range	$\theta_{pq}^{maximum}$
1.5,1.75	3.5
1.75,2.0	3.0
2.0,2.5	2.75
2.5,3.0	2.5
3.0,4.5	2.25

Table 2.4:  $Q^2$ -dependent  $\theta_{pq}$  cuts for SC protons in the 4.2 GeV data.

$Q^2$ range	$\theta_{pq}^{maximum}$
1.0,1.5	4.5
1.5,2.0	4.0
2.0,2.5	3.5
2.5,3.0	3.0
3.0,4.5	2.5

Table 2.4 for the 4.2 GeV data, and in Table 2.5 and Table 2.6 for the 2.6 GeV data.

### 2.6.3 Quasi-elastic $D(e, e'n)$ selection

In the  $D(e, e'n)$  channel the same electron selection criteria and  $Q^2$ -dependent cuts in the  $W^2, \theta_{pq}$  plane used in the  $D(e, e'p)$  channel were applied. To suppress accidentals in the SC, a cut requiring that the energy deposited in an SC paddle exceed 5 MeVee was applied. This is the same energy deposited cut that was applied in the SC neutron detection efficiency calibration.

### 2.6.4 Rejection of unreconstructed proton tracks

The energy-deposited spectrum of protons (from the  $D(e, e'p)$  reaction) traversing the SC array is shown in Fig 2.32. The energy-deposited spectrum of quasi-elastic neutron candidates in the SC is shown in Fig 2.33. The peak near  $E_{dep} \approx 0$  is most likely caused by low energy photons, and is excluded by the  $E_{min} > 5$  MeVee cut

Table 2.5:  $Q^2$ -dependent  $\theta_{pq}$  cuts for EC protons in the 2.6 GeV data.

$Q^2$ range	$\theta_{pq}^{maximum}$
1.25,1.75	3.5
1.75,2.0	3.0
2.0,2.25	2.75
2.25,2.5	3.0

Table 2.6:  $Q^2$ -dependent  $\theta_{pq}$  cuts for SC protons in the 2.6 GeV data.

$Q^2$ range	$\theta_{pq}^{maximum}$
0.5,0.75	6.0
0.75,1.0	5.0
1.0,1.5	4.0
1.5,2.5	3.5

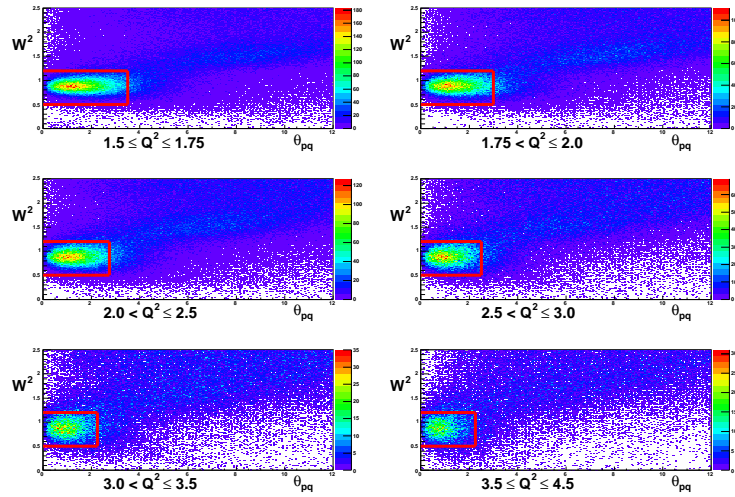


Figure 2.28: Quasi-elastic proton selection cuts for EC protons in the 4.2 GeV data set. Events outside the red box are discarded. In each  $Q^2$  bin, the horizontal axis is  $\theta_{pq}$  (the angle between the virtual photon direction and the scattered proton direction) in degrees and the vertical axis is  $W^2$  in  $(GeV/c^2)^2$

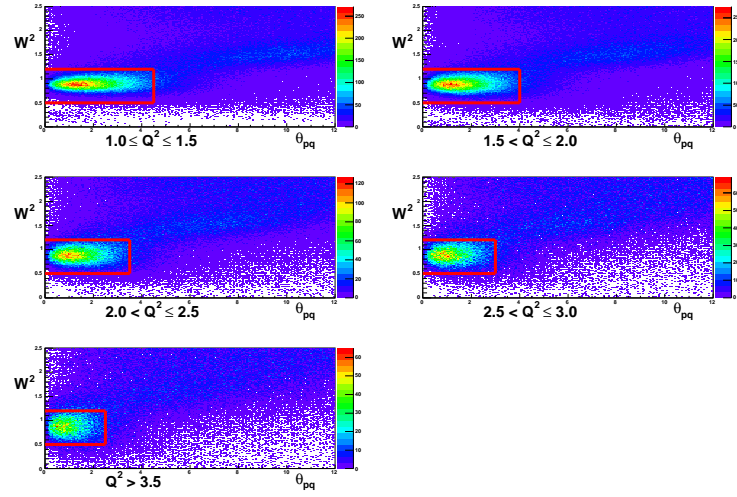


Figure 2.29: Quasi-elastic proton selection cuts for SC protons in the 4.2 GeV data set. Events outside the red box are discarded. In each  $Q^2$  bin, the horizontal axis is  $\theta_{pq}$  (the angle between the virtual photon direction and the scattered proton direction) in degrees and the vertical axis is  $W^2$  in  $(\text{GeV}/c^2)^2$

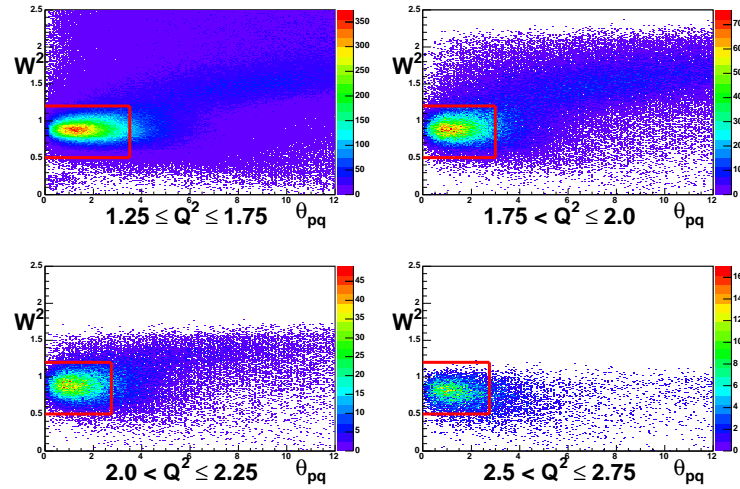


Figure 2.30: Quasi-elastic proton selection cuts for EC protons in the 2.6 GeV data set. Events outside the red box are discarded. In each  $Q^2$  bin, the horizontal axis is  $\theta_{pq}$  (the angle between the virtual photon direction and the scattered proton direction) in degrees and the vertical axis is  $W^2$  in  $(\text{GeV}/c^2)^2$

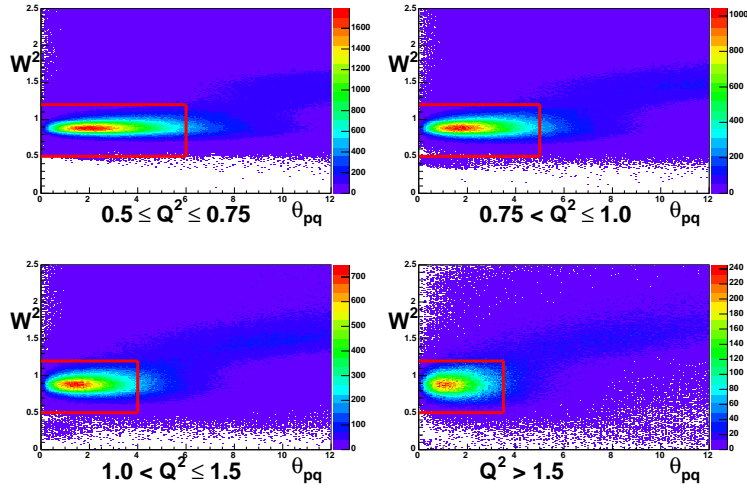


Figure 2.31: Quasi-elastic proton selection cuts for SC protons in the 2.6 GeV data set. Events outside the red box are discarded. In each  $Q^2$  bin, the horizontal axis is  $\theta_{pq}$  (the angle between the virtual photon direction and the scattered proton direction) in degrees and the vertical axis is  $W^2$  in  $(GeV/c^2)^2$

applied to neutrons in both the calibration and quasi-elastic reactions. A second peak in the neutron distribution is seen in the region of  $E_{dep} \approx 12$  MeV. This second peak is unexpected, and occurs at approximately the energy that would be expected for protons.

A sample of events in the region of this peak ( $8 < E_{dep} < 14$  MeV) were inspected visually using the event-display program CED. While some looked normal, others appeared to have partial positive tracks in the sector opposite the electron, as shown in Figs 2.34, 2.35, and 2.36. All of these partial tracks were missing data in one or more DC superlayers, and were not reconstructed by the tracking algorithm. The unreconstructed proton tracks were rejected by counting the number of active DC wires, in each DC region, inside a  $\pm 5^\circ$  window around the expected proton trajectory. SC neutron candidate events that had an energy deposited in the area around the expected proton energy were rejected if they also had either: 1) 7 active wires in Region 1 and 9 or more active wires in either Region 2 or Region 3, or 2) more than 9 active wires in Region 2 and Region 3 were rejected. The effect of this cut is illustrated in Fig 2.37.

## 2.6.5 Acceptance matching and fiducial cuts

To ensure that the  $\sigma_n/\sigma_p$  ratio is measured correctly, it is necessary to take some care that the range of solid angle over which the neutrons are accepted is the same as that over which the protons are accepted. A common fiducial region was enforced by applying an identical fiducial cut to proton and neutron candidate events. In

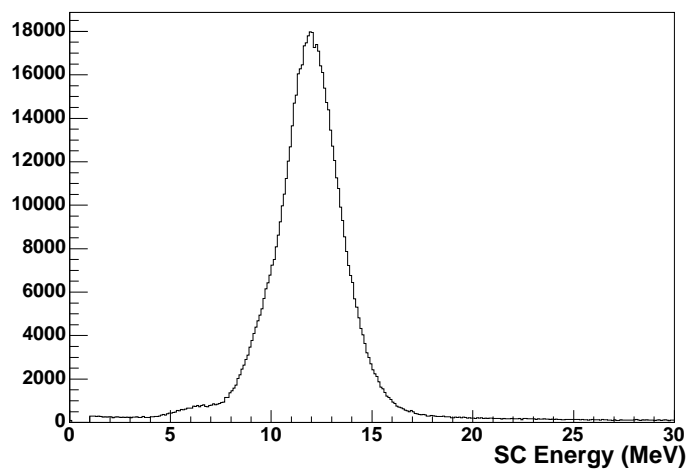


Figure 2.32: Energy deposited in the SC by protons from the  $D(e, e'p)$  reaction

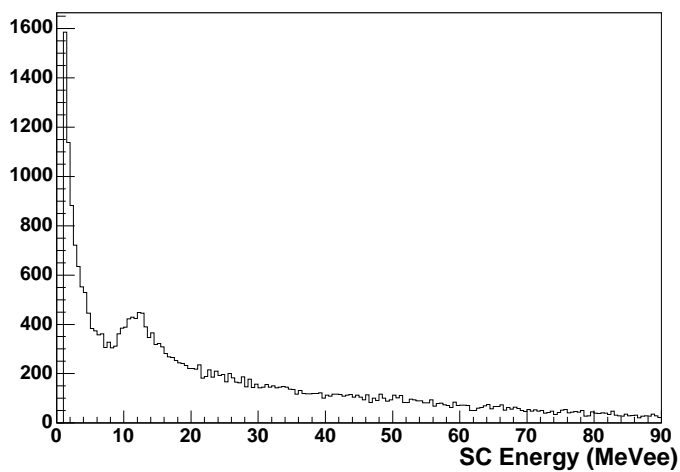


Figure 2.33: Energy deposited in the SC by quasi-elastic neutron candidates.

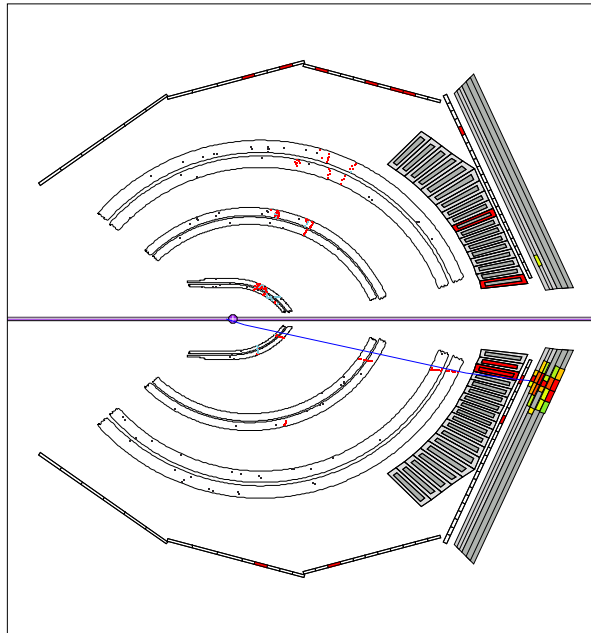


Figure 2.34: CED representation of an unreconstructed proton event.

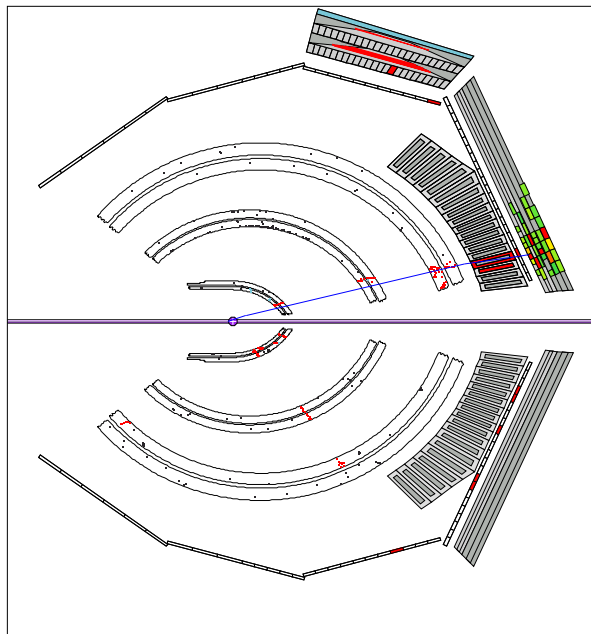


Figure 2.35: CED representation of an unreconstructed proton event.

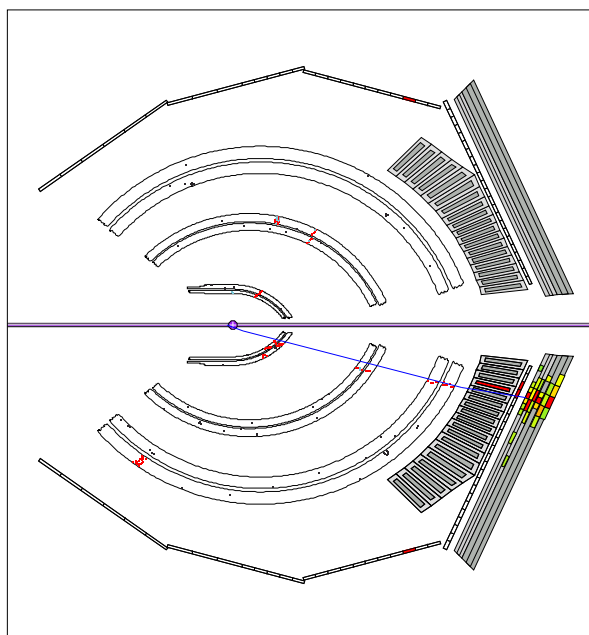


Figure 2.36: CED representation of an unreconstructed proton event.

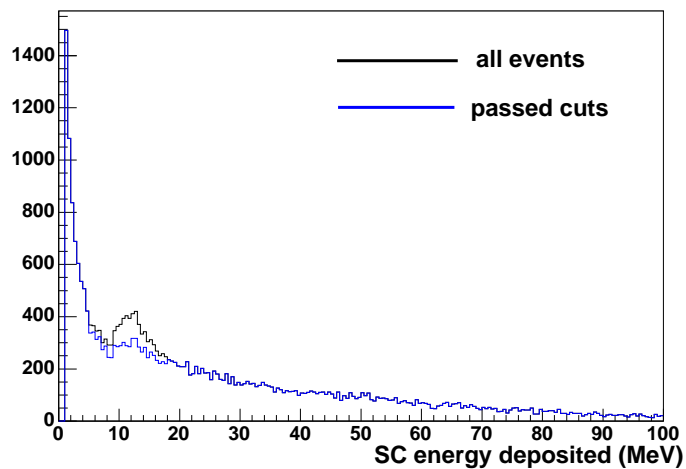


Figure 2.37: SC energy deposit spectrum for candidate neutral events before and after applying DC wire-based unreconstructed proton rejection cut.

each event, the expected nucleon 3-momentum (assuming a stationary target) was determined from the electron kinematics. The possibility that the struck nucleon was a neutron was considered first. This neutron was traced out to either the EC or SC plane, depending on which analysis was being performed. If this expected neutron failed to intersect a good SC paddle (a paddle with neutron detection efficiency greater than 1% and whose neighbors also had efficiency greater than 1%), or a good EC pixel (a pixel with neutron detection efficiency greater than 5%), the event was discarded for the SC or EC analysis, respectively. Next, the possibility that the struck nucleon was a proton was considered. A proton with the expected nucleon 3-momentum was swum through the magnetic field out to the SC plane, where it was required to strike an SC paddle whose efficiency was greater than 85%, and whose neighboring paddles also had efficiency greater than 85%. Events which failed this cut were also discarded for both the SC and EC analysis. The struck nucleon was required to satisfy the .AND. of both of these conditions: expected neutron went into allowed region, expected proton went into allowed region. The double particle-tracking used to evaluate the fiducial cut is illustrated in Fig 2.38. The distribution of events in the  $\theta_{expected}, \phi_{expected}$  plane for the EC neutron analysis of the 4.2 GeV data is shown in Fig 2.39.

## 2.6.6 Efficiency corrections and Ratio calculation

### 2.6.6.1 Event-by-event efficiency corrections

Events which satisfy the quasi-elastic selection cuts and the fiducial cuts are filled into two histograms, binned in  $Q^2$ , one for neutron events and one for proton events. The entries to these histograms were weighted by the reciprocal of the detection efficiency of the detector element in which they were found: EC pixel or SC paddle for neutrons, SC paddle for protons. Any events which are found in poorly performing detector elements (EC neutron detection efficiency below 5%, SC neutron detection efficiency below 1%, proton detection efficiency below 85%) are discarded. The average efficiency correction, binned in  $Q^2$ , for the detectors are shown in Fig 2.40, Fig 2.41 and Fig 2.42.

### 2.6.6.2 Statistical Error Analysis for Neutron Histograms

The contents of each of the  $Q^2$  bins in the neutron histogram are:

$$b_i = \sum_{j=1}^{N_i} \frac{1}{\alpha_j \eta_j} \quad (2.60)$$

where  $b_i$  is the entry in the  $i^{th}$   $Q^2$  bin,  $N_i$  is the number of events seen in the  $i^{th}$   $Q^2$  bin,  $\alpha_j$  is the scale factor on the detector element in which the  $j^{th}$  event was found (SC paddle or EC superpixel), and  $\eta_j$  is the value of the efficiency fit evaluated at

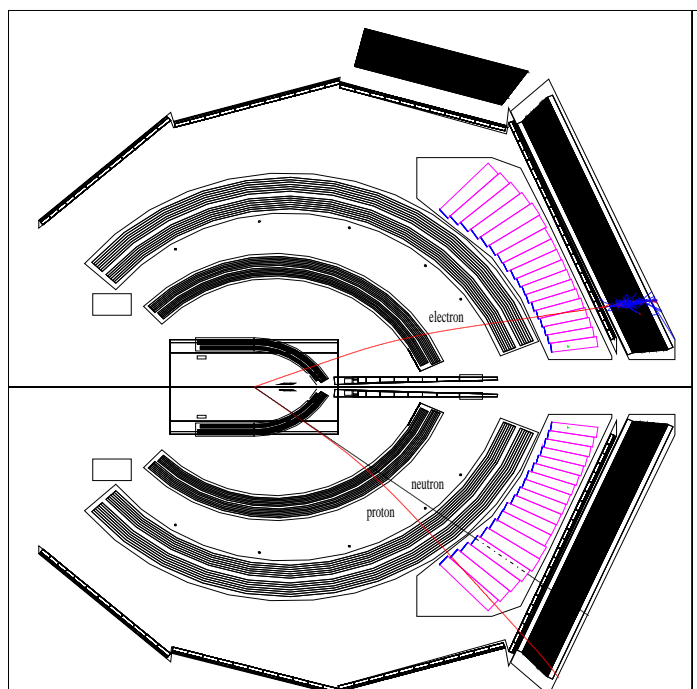


Figure 2.38: An illustration of the acceptance matching technique. From the scattered electron (inbending red track) kinematics, the 3-momentum of a stationary target nucleon was determined. This nucleon was required to strike the active region of the acceptance if it were either a neutron (black track) or a proton (outbending red track). This illustration shows an acceptable event from the 4.2 GeV EC neutron measurement.

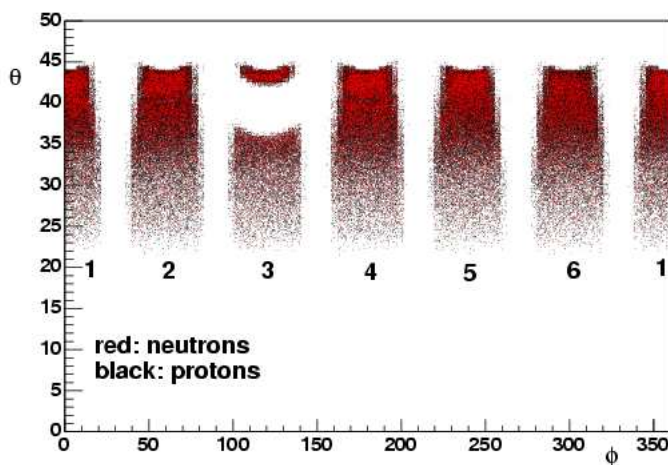


Figure 2.39: The distribution of neutron and proton events in the  $\theta_{expected}, \phi_{expected}$  plane for the EC neutron analysis of the 4.2 GeV data. The gap in sector 3 is caused by a dead TOF paddle and its adjacent paddles which were switched off in software.

momentum  $p_j$ . In each  $Q^2$  bin, only a limited number of detector elements contribute. For the purpose of determining the statistical error on  $b_i$ , the expression for the bin content can be rewritten as:

$$b_i = \sum_{k=1}^{N_d} \frac{n_k}{\alpha_k} f_k \quad (2.61)$$

where the index  $k$  denotes the detector element in which the neutron was detected (SC paddle or EC superpixel),  $N_d$  is the number of active detector elements in the  $i^{\text{th}}$   $Q^2$  bin,  $n_k$  is the number of counts seen in the  $k^{\text{th}}$  detector element,  $\alpha_k$  is the scale factor for the  $k^{\text{th}}$  detector element, and

$$f_k = \left\langle \frac{1}{\eta(p)} \right\rangle \quad (2.62)$$

is the reciprocal of the efficiency parameterization associated with the  $k^{\text{th}}$  detector element, averaged over the momentum range covered by the  $i^{\text{th}}$   $Q^2$  bin.

The uncertainty on  $b_i$  can then be written as:

$$\sigma_{b_i}^2 = \sum_{k=1}^{N_d} \left\{ \sigma_{n_k}^2 \left( \frac{\partial b_i}{\partial n_k} \right)^2 + \sigma_{\alpha_k}^2 \left( \frac{\partial b_i}{\partial \alpha_k} \right)^2 + \sigma_{f_k}^2 \left( \frac{\partial b_i}{\partial f_k} \right)^2 \right\} \quad (2.63)$$

The  $\sigma_{f_k}$  term is small compared to the others and will be neglected. Setting  $\sigma_{n_k}^2 = n_k$  gives:

$$\sigma_{b_i}^2 = \sum_{k=1}^{N_d} \left\{ n_k \left( \frac{f_k}{\alpha_k} \right)^2 + \sigma_{\alpha_k}^2 \left( \frac{n_k f_k}{\alpha_k^2} \right)^2 \right\} \quad (2.64)$$

$$= \sum_{k=1}^{N_d} \frac{n_k f_k^2}{\alpha_k^2} \left( 1 + \frac{n_k \sigma_{\alpha_k}^2}{\alpha_k^2} \right) \quad (2.65)$$

### 2.6.6.3 Statistical Error Analysis for Proton Histograms

The contents of each of the  $Q^2$  bins in the proton histogram are:

$$b_i = \sum_{j=1}^{N_i} \frac{1}{\epsilon_j} \quad (2.66)$$

where  $b_i$  is the entry in the  $i^{\text{th}}$   $Q^2$  bin,  $N_i$  is the number of events seen in the  $i^{\text{th}}$   $Q^2$  bin and  $\epsilon_j$  is the proton efficiency on the  $j^{\text{th}}$  paddle. As in the neutron case, only a few SC paddles are active in a given  $Q^2$  bin, so that the bin contents can be rewritten as:

$$b_i = \sum_{k=1}^{N_d} \frac{n_k}{\epsilon_k} \quad (2.67)$$

where the index  $k$  denotes the SC paddle in which the proton was detected,  $N_d$  is the number of SC paddles active in the  $i^{\text{th}}$   $Q^2$  bin,  $n_k$  is the number of protons found in paddle  $k$ , and  $\epsilon_k$  is the detection efficiency of the  $k^{\text{th}}$  paddle. Recall that for proton detection, the detection efficiency on each SC paddle is taken to be momentum *independent*. The uncertainty on  $b_i$  is then given by:

$$\sigma_{b_i}^2 = \sum_{k=1}^{N_d} \left\{ \sigma_{n_k}^2 \left( \frac{\partial b_i}{\partial n_k} \right)^2 + \sigma_{\epsilon_k}^2 \left( \frac{\partial b_i}{\partial \epsilon_k} \right)^2 \right\} \quad (2.68)$$

$$= \sum_{k=1}^{N_d} \left\{ \frac{n_k}{\epsilon_k^2} + \frac{\sigma_{\epsilon_k}^2 n_k^2}{\epsilon_k^4} \right\} \quad (2.69)$$

$$= \sum_{k=1}^{N_d} \frac{n_k}{\epsilon_k^2} \left( 1 + \frac{\sigma_{\epsilon_k}^2 n_k}{\epsilon_k^2} \right) \quad (2.70)$$

where we have set  $\sigma_{n_k}^2 = n_k$ . The uncertainty on the efficiency  $\sigma_{\epsilon_k}$  is taken to be the binomial uncertainty on the appropriate bin in the efficiency histogram.

#### 2.6.6.4 Statistical Error Analysis for Ratio Histograms

The  $\sigma_n/\sigma_p$  ratio histogram was constructed by dividing the neutron and proton histograms bin-by-bin, so that the contents of each bin in the ratio histogram are:

$$R_i = \frac{b_i^{\text{neutron}}}{b_i^{\text{proton}}} \quad (2.71)$$

where  $b_i^{\text{neutron}}$  is the efficiency-weighted number of neutron events found in the  $i^{\text{th}}$   $Q^2$  bin and  $b_i^{\text{proton}}$  is the efficiency-weighted number of proton events found in the  $i^{\text{th}}$   $Q^2$  bin. The uncertainty on each bin in the ratio histogram is given by the usual propagation of errors formula:

$$\frac{\sigma_R^2}{R^2} = \frac{\sigma_n^2}{n^2} + \frac{\sigma_p^2}{p^2} \quad (2.72)$$

where  $R$  is the value of the ratio histogram in that bin,  $n$  is the weighted number of neutron entries in that bin and  $p$  is the weighted number of proton entries in that bin ( $n$  and  $p$  correspond to  $b_i^{\text{neutron}}$  and  $b_i^{\text{proton}}$  in Eqn 2.71).

#### 2.6.6.5 Uncorrected Ratio Histograms

The  $\sigma_n/\sigma_p$  ratio histograms from the 4.2 GeV data set are shown in Fig 2.43 and the ratio histograms from the 2.6 GeV data set are shown in Fig 2.44. Note that a comparison of the  $\sigma_n/\sigma_p$  ratio at two different beam energies is not appropriate. There are beam energy dependent terms in the elastic cross section, so even if identical values of  $G_M^n$  were determined at the two beam energies, identical values of  $\sigma_n/\sigma_p$  would not be found. Notice that the EC and SC ratio values at low  $Q^2$  values in

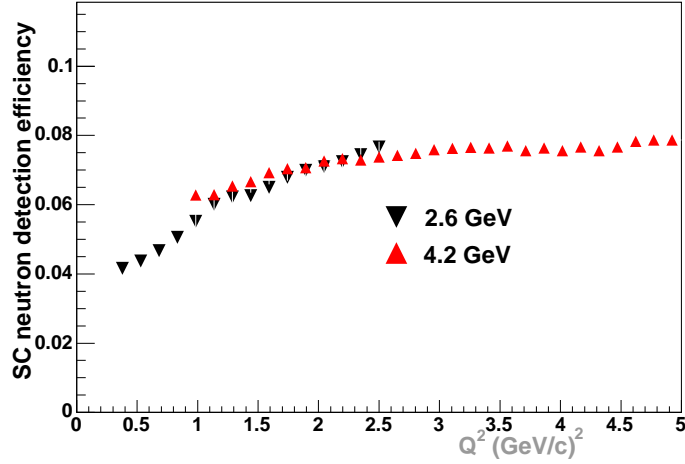


Figure 2.40: The average efficiency correction applied to SC neutrons, binned in  $Q^2$  for the two beam energy settings.

each of these plots do not agree. Additional corrections need to be applied to the measured ratio before  $G_M^n$  can be extracted.

## 2.7 Corrections to Quasi-elastic ratio

### 2.7.1 Uncalibrated SC paddles

The calibration reaction  $ep \rightarrow e\pi^+(n)$  fully illuminates the EC face, allowing the calibration of all the EC pixels. The reaction does not fully illuminate the range of SC paddles where quasi-elastically scattered neutrons are found. A glance at Appendix C will show that the calibration reaction provides calibration data on paddles numbered as high as 25 in the 4.2 GeV data, and as high as 28 in the 2.6 GeV data. Neutron candidates scattered from the  $D_2$  target can be found at higher paddle number than the calibration cut-off. Fig 2.45 shows a plot of the number of neutron candidates in each SC paddle for the 4.2 GeV data set. The neutron population extends up to paddle number 30. The proton calibration reaction  $ep \rightarrow ep$  illuminates the same set of paddles as the quasi-elastic reaction, so there is no uncalibrated paddle problem for protons.

### 2.7.2 Losses due to Fermi motion of the target

If the target nucleon were stationary, there would be a one-to-one relation between  $Q^2$  and nucleon scattering angle, and all of the uncalibrated paddles could be switched off in software and all of the calibrated paddles used. When the target nucleon is in motion, as it is in the deuterium nucleus, the one-to-one relationship between

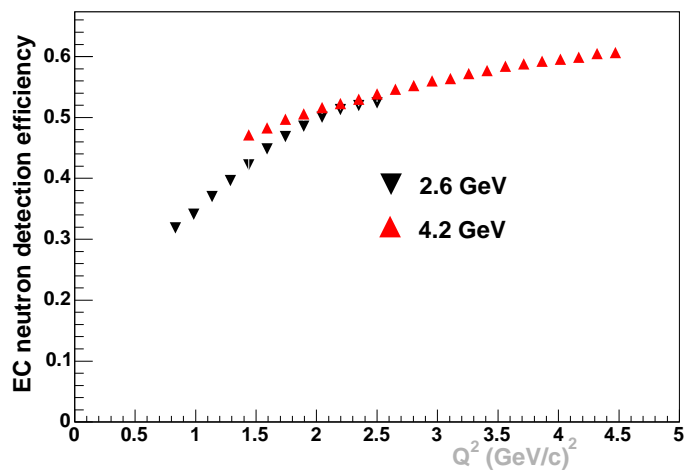


Figure 2.41: The average efficiency correction applied to EC neutrons, binned in  $Q^2$  for the two beam energy settings.

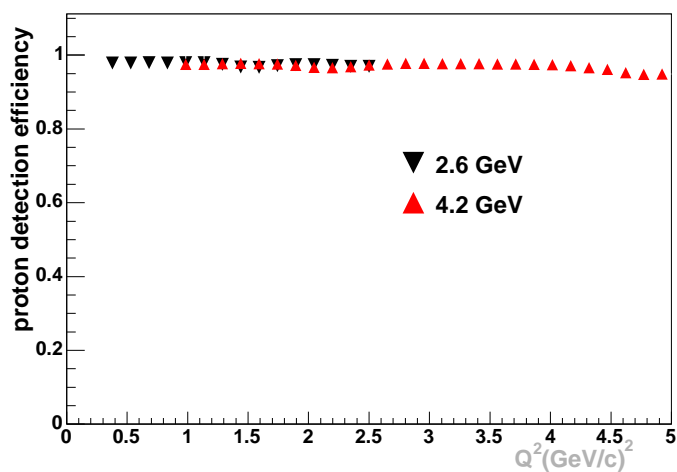


Figure 2.42: The average efficiency correction applied to protons, binned in  $Q^2$  for the two beam energy settings.

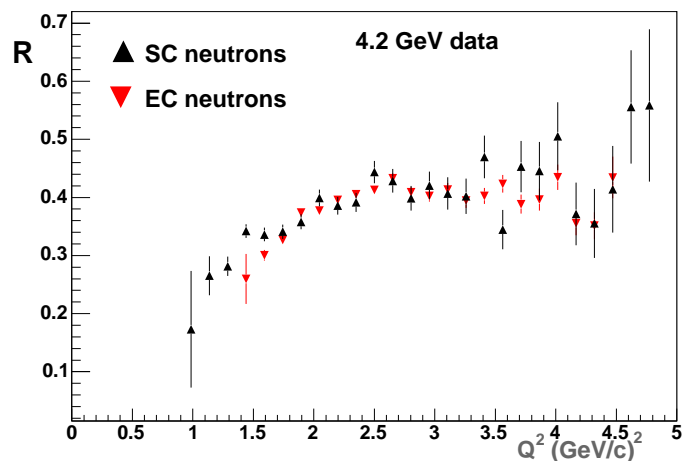


Figure 2.43: The  $\sigma_n/\sigma_p$  ratio  $R$ , as measured in the 4.2 GeV data set for both EC neutrons (red triangles) and SC neutrons (black triangles), binned in  $Q^2$ .

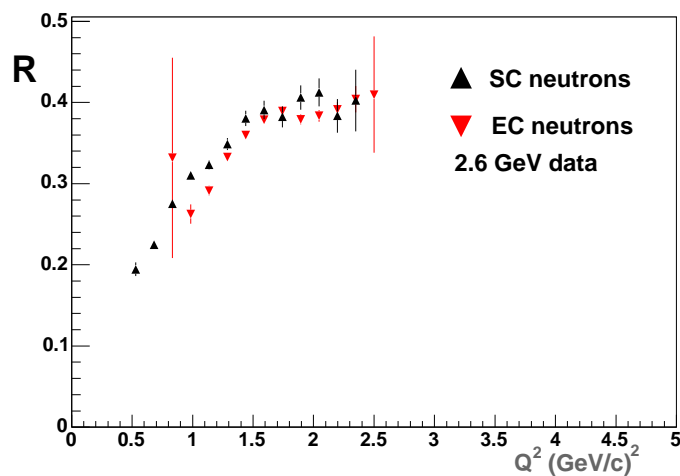


Figure 2.44: The  $\sigma_n/\sigma_p$  ratio  $R$ , as measured in the 2.6 GeV data set for both EC neutrons (red triangles) and SC neutrons (black triangles), binned in  $Q^2$ .

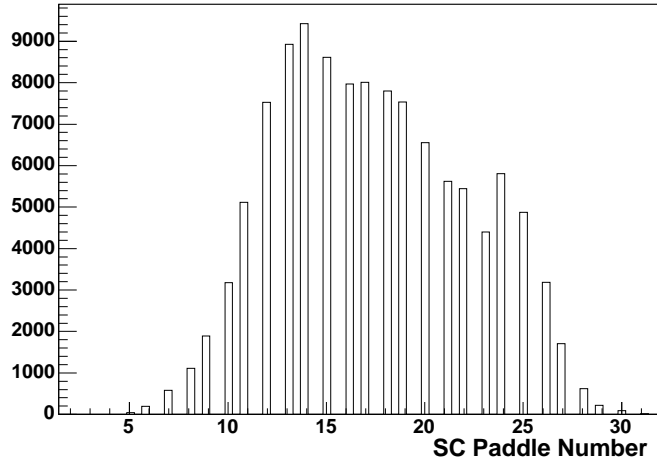


Figure 2.45: Neutron candidate events from the D<sub>2</sub> target, binned by SC paddle number, from the 4.2 GeV data set.

$Q^2$  and scattering angle in elastic scattering is broken. Simply switching off the uncalibrated paddles will give an incorrect measure of the  $\frac{\sigma_n}{\sigma_p}$  ratio at low  $Q^2$  (low  $Q^2$  corresponds to high SC paddle numbers) because of the effects of the target Fermi motion. Neutrons which, based on the electron kinematics, would be expected to strike a paddle near the edge of the calibrated region, may in fact strike uncalibrated paddles due to the additional effect of the Fermi motion. Such a neutron would not be counted, incorrectly lowering the cross-section ratio. A similar loss is not suffered by the protons, because the calibrated proton paddles cover the range of the quasi-elastic reaction. Note that there is no corresponding Fermi induced migration of neutrons *into* the acceptance, due to the requirement that acceptable events must have a predicted nucleon location *inside* the acceptance.

A similar effect is seen in the EC, where neutrons which are expected to strike near the edge of the EC can be moved out of the EC acceptance by Fermi effects. Again, a similar problem is not seen for the protons because the angular coverage of the SC is significantly larger than that of the EC.

This phenomena of particles migrating out of the acceptance due to Fermi effects can be removed in two ways. A fiducial cut which restricts the expected nucleon location to regions of the acceptance sufficiently far away from the edge that Fermi effects are not large enough to move the nucleon out of the acceptance could be applied. Such a cut would have the effect of raising the value of the minimum  $Q^2$  accessible to the measurement. Alternatively, a Monte-Carlo calculation could be used to estimate the fraction of nucleons expected to be removed from the acceptance by Fermi effects. We have developed a Monte Carlo code to study this effect and also tested our approach using the standard CLAS simulation package GSIM.

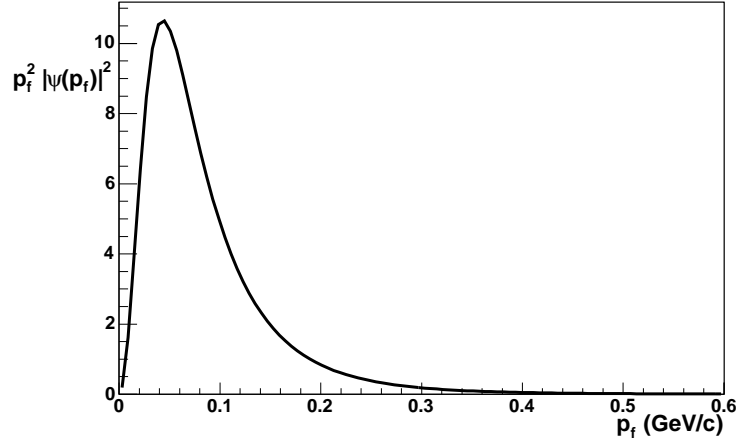


Figure 2.46: The Hulthen distribution for the nucleon Fermi momentum in the deuteron.

### 2.7.3 Quasi-elastic event generator

The angular distribution of neutrons and protons quasi-elastically scattered from the deuteron was simulated using the Hulthen model of the deuteron wave function. The Hulthen model prediction for the nucleon Fermi momentum distribution is shown in Fig 2.46.

Equation 1.8 gives the elastic electron-nucleon scattering cross-section in terms of the Lorentz invariant  $Q^2$  and the energy of the incident electron beam for a nucleon at rest. This equation was used to evaluate quasi-elastic scattering from a moving nucleon in a deuteron (off-shell effects were neglected). To do this, it was first necessary to transform from the lab frame, in which both the electron and the nucleon are in motion, to the nucleon rest frame. Fig 2.47 shows the effect of the boost to the nucleon rest frame on the electron beam energy for a 4.2 GeV incident beam, binned in the magnitude of the Fermi momentum and the cosine of the angle between the Fermi momentum and the incident electron.

The lab frame and rest frame cross sections are related by:

$$\frac{d\sigma}{d\Omega_l} = \frac{d\sigma}{d\Omega_r} \frac{d\Omega_r}{d\Omega_l} \quad (2.73)$$

$$= \frac{d\sigma}{d\Omega_r} \frac{\sin \theta_r}{\sin \theta_l} \frac{d\theta_r}{d\theta_l} \quad (2.74)$$

where the subscripts  $l, r$  denote the lab frame and rest frame respectively.

Equation 2.73 was integrated over polar angle:

$$\int_{d\theta_l} \frac{d\sigma}{d\theta_l} d\theta_l = \int_{d\theta_r} \frac{d\sigma}{d\theta_r} \frac{\sin \theta_r}{\sin \theta_l} \frac{d\theta_r}{d\theta_l} d\theta_r \quad (2.75)$$

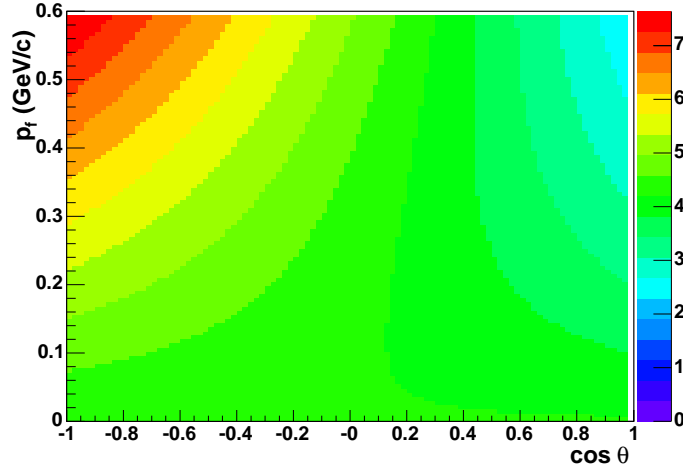


Figure 2.47: The horizontal axis shows the cosine of the angle between the momenta of the incident 4.2 GeV electron and the moving nucleon (the angle in the lab frame). The vertical axis shows the magnitude of the Fermi momentum in GeV/c. The color z-axis shows the energy of the incident electron in the nucleon rest frame, in GeV.

The integration on the left in Eqn 2.75 is over an angular range roughly covering the CLAS acceptance: full azimuthal coverage, 14 to 52 degrees in polar angle for the 4.2 GeV incident beam energy, 12 to 52 degrees in polar angle for the 2.6 GeV incident beam energy. The integration on the right is over the equivalent angular range in the rest frame. The kinematic relations between the lab frame and the rest frame are derived in Appendix D. The Brash parameterization of the form factors is used in evaluation of the integral on the right. The integrated lab-frame cross-section was determined for a range of  $p_f$ ,  $\cos\theta_f$  values. Fig 2.48 shows the integrated cross-section as a function of the magnitude of the Fermi momentum and the cosine of the angle between the incident electron and the Fermi momentum in the lab frame for electron-neutron scattering, and Fig 2.49 shows the same for the electron-proton case. The electron-neutron and electron-proton elastic scattering cross-sections as a function of scattering angle in the rest frame are shown in Fig 2.50. Note that the cross-section peaks for large Fermi momentum nucleons in the  $\cos\theta_{pq} \approx 1$  region, where the electron beam energy in the nucleon rest frame is smallest.

Each cell in Fig 2.48 and Fig 2.49 was multiplied by the value of the Hulthen function (shown in Fig 2.46) at the appropriate momentum. This generated a two-dimensional histogram for which the relative weighting of the cells should give the relative probability for quasi-elastic scattering at those values of  $p_f$  and  $\cos\theta$ . Fig 2.51 and Fig 2.52 show the weight tables for electron-neutron and electron-proton scattering, respectively.

The kinematics of quasi-elastic scattering are treated using a spectator approximation in which the deuteron is composed of two on-shell nucleons, one moving with

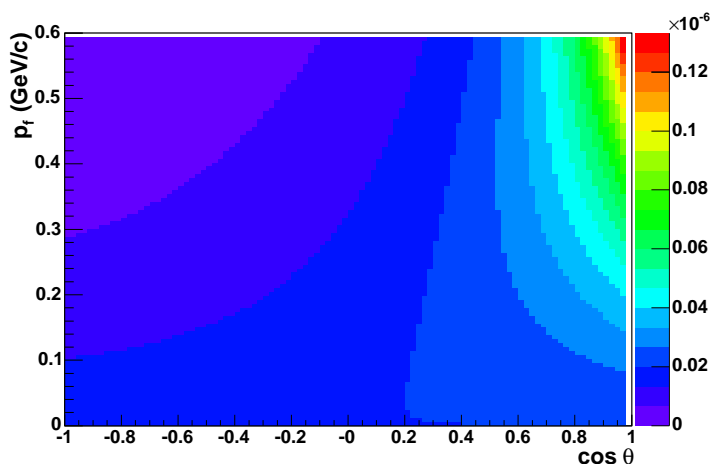


Figure 2.48: Electron-Neutron Scattering: The horizontal axis shows the cosine of the angle between the incident 4.2 GeV electron and the moving nucleon (the angle in the lab frame). The vertical axis shows the magnitude of the Fermi momentum in GeV/c. The color z-axis shows the integrated electron-neutron scattering cross section (in the nucleon rest frame) in units of  $1/\text{GeV}^2$ .

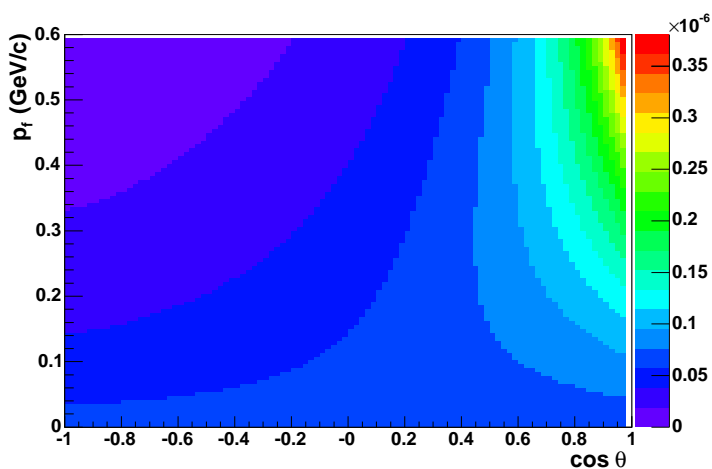


Figure 2.49: Electron-Proton Scattering: The horizontal axis shows the cosine of the angle between the incident 4.2 GeV electron and the moving nucleon (the angle in the lab frame). The vertical axis shows the magnitude of the Fermi momentum in GeV/c. The color z-axis shows the integrated electron-proton scattering cross section (in the nucleon rest frame) in units of  $1/\text{GeV}^2$ .

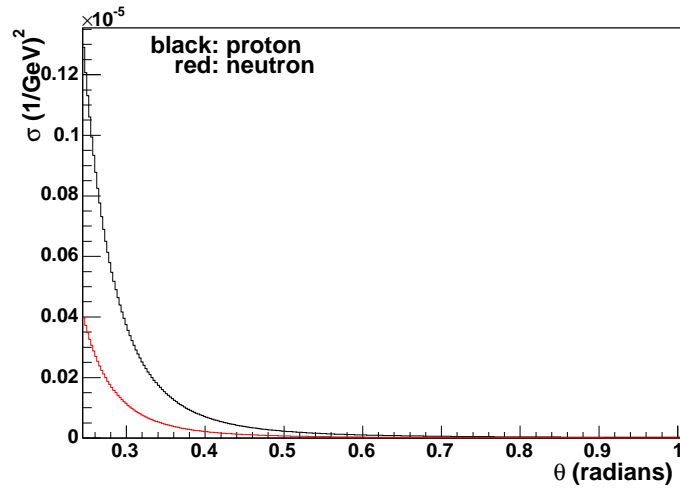


Figure 2.50: The cross-section for elastic electron-proton (black curve) and electron-neutron (red curve) as a function of scattering angle (in radians). The Brash parameterization [35] of the form factors was used. Notice the suppressed zero on the horizontal axis. As  $\theta \rightarrow 0$ ,  $\sigma \rightarrow 0$  for the e-n case, and  $\sigma \rightarrow \infty$  for the e-p case. An incident beam energy of 4.2 GeV was used to generate this figure.

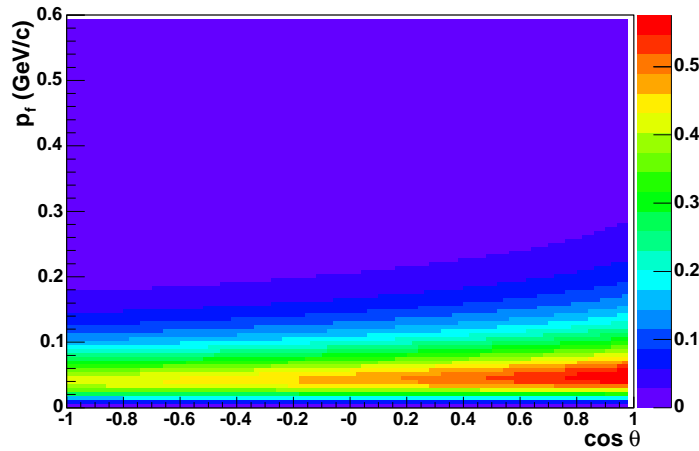


Figure 2.51: Electron-Neutron Scattering: The horizontal axis shows the cosine of the angle between the incident 4.2 GeV electron and the moving nucleon (the angle in the lab frame). The vertical axis shows the magnitude of the Fermi momentum in GeV/c. The color z-axis shows the product of the integrated cross-section and the Hulthen distribution for the electron-neutron case.

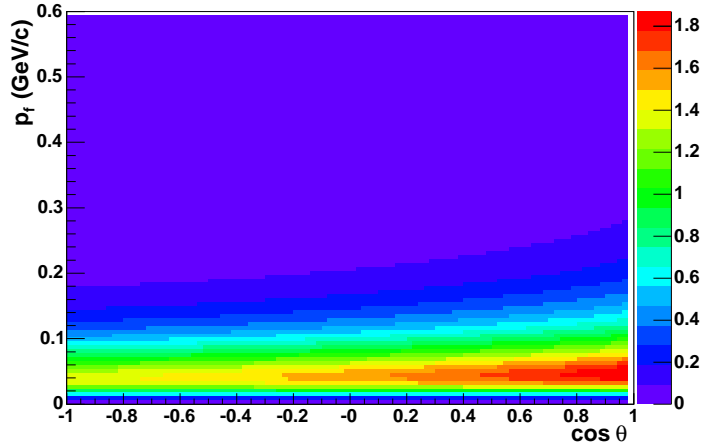


Figure 2.52: Electron-Proton Scattering: The horizontal axis shows the cosine of the angle between the incident 4.2 GeV electron and the moving nucleon (the angle in the lab frame). The vertical axis shows the magnitude of the Fermi momentum in GeV/c. The color z-axis shows the product of the integrated cross-section and the Hulthen distribution for the electron-proton case.

Fermi momentum  $\vec{p}_f$ , the other moving with momentum  $-\vec{p}_f$ . The virtual photon interacts with one of the moving nucleons and the other is unaffected. For simplicity, the nucleons are taken to have the same mass,  $M_N = (1/2)(M_{neutron} + M_{proton})$ . Conservation of energy in the lab frame gives:

$$E_0 + M_D = E_S + E_I + E' \quad (2.76)$$

$$= \sqrt{p_f^2 + M_N^2} + \sqrt{p_I^2 + M_N^2} + E' \quad (2.77)$$

where  $M_D$  is the deuteron mass,  $E_0$  is the incident electron beam energy,  $E_S$  is the energy of the spectator nucleon in the final state,  $E_I$  is the energy of the interacting nucleon in the final state,  $E'$  is the energy of the scattered electron,  $p_f$  is the magnitude of the Fermi momentum and  $p_I$  is the magnitude of the momentum of the interacting nucleon in the final state. Since the virtual photon interacts with only the one nucleon,

$$\vec{p}_I = \vec{p}_f + \vec{q} \quad (2.78)$$

where  $\vec{q}$  is the three-momentum transferred by the virtual photon.

Conservation of momentum in the lab frame gives:

$$E_0 \hat{z} + \vec{p}_f = E' \hat{e} + p_I \hat{n} \quad (2.79)$$

where  $\hat{z}$  is the direction of the incident electron,  $\hat{e}$  is the direction of the scattered electron, and  $\hat{n}$  is the direction of the scattered nucleon (the spectator nucleon has momentum  $-\vec{p}_f$  in the initial and final states).

To generate a quasi-elastic scattering event (either e-n or e-p), a pair of values  $(p_f, \cos \theta)$  are generated randomly, weighted according to the histogram shown in Fig 2.51 for neutrons or Fig 2.52 for protons. The  $\phi$  value for the Fermi momentum is chosen randomly in the range 0 to  $2\pi$ . A rest frame electron scattering angle is chosen randomly according to the distributions shown in Fig 2.50 (with the azimuthal angle taken randomly between 0 and  $2\pi$ ). The rest frame scattering angle is transformed to the lab frame angle using the kinematic relations in Appendix D. This fixes  $\hat{e}$ , the direction of the scattered electron. The solution now proceeds iteratively. A first guess for  $E'$  is made, taking  $E'$  to be equal to the value for an electron *elastically* scattered at the selected scattering angle. With this choice for  $E'$ , Eqn 2.79 can be solved for the scattered nucleon momentum:

$$\vec{p}_I = E_0 \hat{z} + \vec{p}_f - E' \hat{e} \quad (2.80)$$

The value of  $p_I$  determined from the momentum equation is used to derive a new value of  $E'$  from Eqn 2.77. This procedure is iterated until  $|\Delta E'| \leq 0.0001$ , which is usually accomplished in 3 or fewer iterations.

The event generator produces 3-momentum vectors for the scattered electron and scattered nucleon. From the incident and scattered electron 3-momenta,  $W^2$  can be calculated, as well as the virtual photon direction. Fig 2.53 shows a 2-dimensional histogram of event generator output, plotting  $W^2$  vs  $\theta_{pq}$  (the angle between the virtual photon direction and the scattered nucleon direction).

## 2.7.4 Fermi Loss Corrections

The quasi-elastic event generator was used to produce a set of simulated e-n and e-p events. The electron-nucleon vertex position was chosen randomly along the beamline in the z-range of the deuterium target cell,  $-12.5 \leq z \leq -8.25$  cm. The electron was tracked through the magnetic field and was required to strike the active region of the EC.

### 2.7.4.1 SC Fermi Loss Correction

In either the e-n or e-p case, two histograms were filled. In the first, events in which the nucleon would be *expected* to be found inside the SC acceptance (i.e. to strike an SC paddle whose detection efficiency exceeded the minimum efficiency cut of 0.5% for neutrons or 85% for protons) were binned in  $Q^2$ . The expected nucleon location was calculated using only information taken from the electron kinematics (the only information which would be available in the real data). A second histogram, also binned in  $Q^2$  was filled with events where the scattered nucleon would *actually*

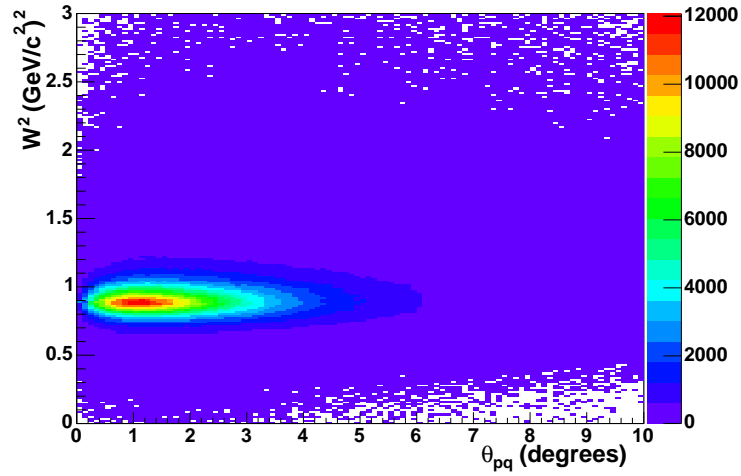


Figure 2.53: Quasi-elastic event generator output. The horizontal axis shows  $\theta_{pq}$  (the angle between the virtual photon direction and the scattered nucleon direction) in degrees. The vertical axis shows  $W^2$  in  $(\text{GeV}/c^2)^2$ . The figure was produced using an incident beam energy of 4.2 GeV and covers  $0.9 \leq Q^2 \leq 4.5 \text{ GeV}/c^2$ .

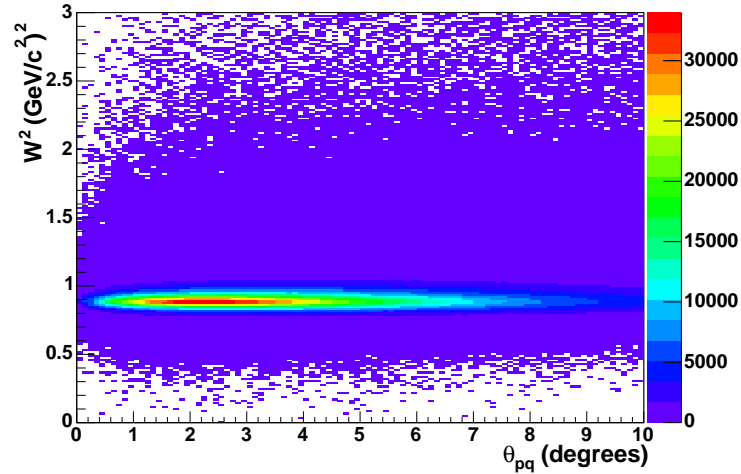


Figure 2.54: Quasi-elastic event generator output. The horizontal axis shows  $\theta_{pq}$  (the angle between the virtual photon direction and the scattered nucleon direction) in degrees. The vertical axis shows  $W^2$  in  $(\text{GeV}/c^2)^2$ . The figure was produced using an incident beam energy of 2.6 GeV and covers  $0.4 \leq Q^2 \leq 2.5 \text{ GeV}/c^2$ .

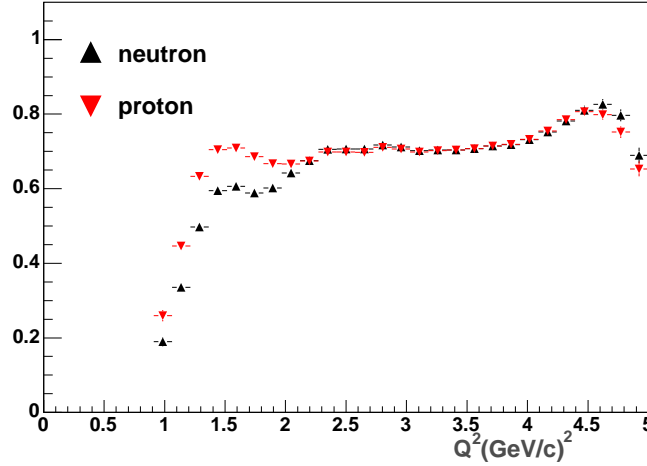


Figure 2.55: The fraction of nucleons scattered at the indicated  $Q^2$  which scattered into the SC acceptance and satisfied the  $\theta_{pq}$  cuts, as determined by the simulation. The black points show the neutron fraction, the red points show the proton fraction. An incident beam energy of 4.2 GeV was used to generate these points.

be found inside the acceptance and satisfy the  $\theta_{pq}$  cuts. This determination used the information about the scattered nucleon 3-momentum from the event generator, information that is *not* available in the real data. The ratio of these two histograms gives the fraction of nucleons that are lost due to the effects of Fermi motion moving the scattered nucleons outside the acceptance. Fig 2.55 shows plots of the loss factor for both neutrons and protons in the 4.2 GeV data set, and Fig 2.56 shows the same for the 2.6 GeV data.

To correct for the effects of the Fermi loss, each  $Q^2$  bin in the e-n/e-p ratio histogram is multiplied by the correction factor determined by the Fermi loss histograms:

$$R_{corrected}^{SC}(Q^2) = \frac{f_{proton}^{SC}(Q^2)}{f_{neutron}^{SC}(Q^2)} R_{observed}^{SC}(Q^2) = f_{fermi}^{SC}(Q^2) R_{observed}^{SC}(Q^2) \quad (2.81)$$

where  $f_{proton}^{SC}$ ,  $f_{neutron}^{SC}$  are taken from the histograms in Fig 2.55 or Fig 2.56. The correction factor for the 4.2 GeV data is shown in Fig 2.57 and for the 2.6 GeV data in Fig 2.58.

#### 2.7.4.2 EC Fermi Loss Correction

The Fermi loss correction for the EC was simulated in a fashion analogous to the SC. Two histograms were filled. In the first, events in which the *expected* nucleon satisfied the acceptance matching cuts (the expected neutron intersects the EC and the expected proton strikes an active SC paddle) were binned in  $Q^2$ . In the second,

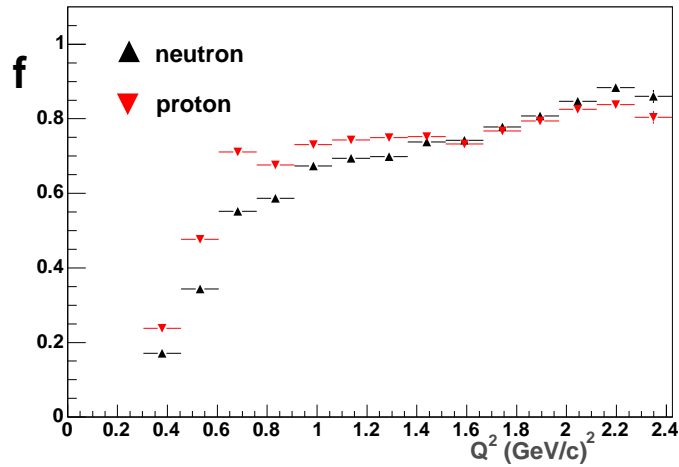


Figure 2.56: The fraction of nucleons scattered at the indicated  $Q^2$  which scattered into the SC acceptance and satisfied the  $\theta_{pq}$  cuts, as determined by the simulation. The black points show the neutron fraction, the red points show the proton fraction. An incident beam energy of 2.6 GeV was used to generate these points.

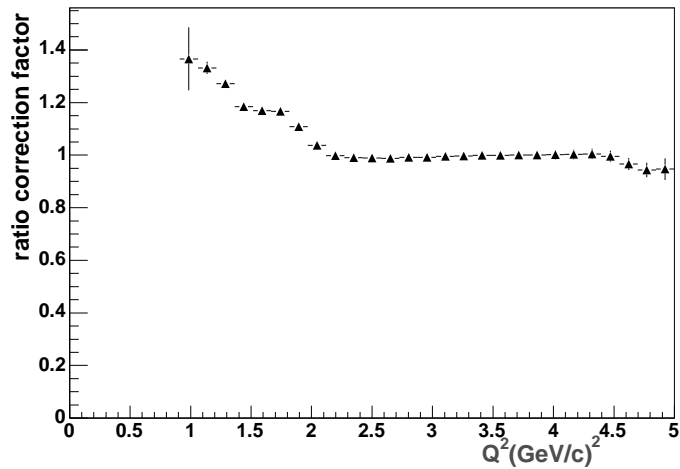


Figure 2.57: The correction factor to the e-n/e-p ratio for Fermi loss in the SC, for the 4.2 GeV data.

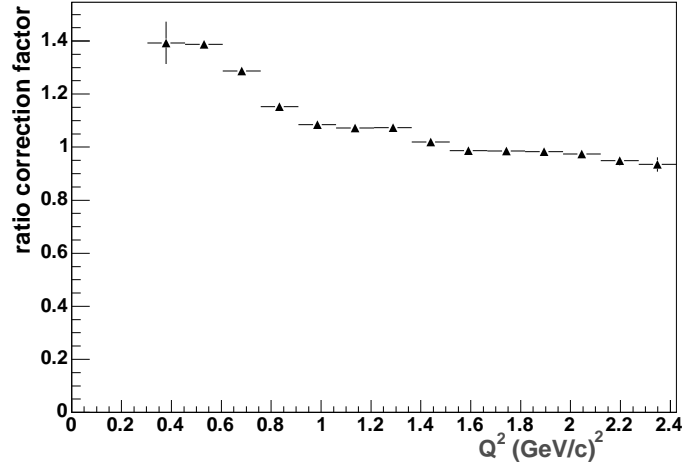


Figure 2.58: The correction factor to the e-n/e-p ratio for Fermi loss in the SC, for the 2.6 GeV data.

events in which the *real* nucleon was found in the acceptance (EC for neutrons, active SC paddle for protons) and satisfied the  $\theta_{pq}$  cut were binned in  $Q^2$ . Fig 2.59 shows the loss factor for protons and neutrons in the 4.2 GeV data set, and Fig 2.60 shows the same for the 2.6 GeV data. The correction to the e-n/e-p ratio for the EC measurement is shown in Fig 2.61 for the 4.2 GeV data, and in Fig 2.62 for the 2.6 GeV data. The Fermi loss correction for the EC is similar to the SC case:

$$R_{corrected}^{EC}(Q^2) = \frac{f_{proton}^{EC}(Q^2)}{f_{neutron}^{EC}(Q^2)} R_{observed}^{EC}(Q^2) = f_{fermi}^{EC}(Q^2) R_{observed}^{EC}(Q^2) \quad (2.82)$$

where  $f_{proton}^{EC}$ ,  $f_{neutron}^{EC}$  are taken from the histograms in Fig 2.59 or Fig 2.60. The correction factor for the 4.2 GeV data is shown in Fig 2.61 and for the 2.6 GeV data in Fig 2.62.

The effect of applying the Fermi loss corrections to the  $\sigma_n/\sigma_p$  ratio histograms are shown in Fig 2.63 for the 4.2 GeV data and in Fig 2.64. Notice that the corrections have removed most of the disagreement between the EC and SC values at low  $Q^2$  in each of the plots. The effect of the Fermi corrections is even more striking when its effect on  $G_M^n$  is considered in Section 3.1.

### 2.7.4.3 Comparison with GSIM

We have performed a study of the Fermi correction to the  $e - n/e - p$  ratio  $R$  at 2.6 GeV using the program GSIM. The code is the CLAS Collaboration standard simulation package and this study provides an additional cross-check on the Fermi correction. The procedure is the following.

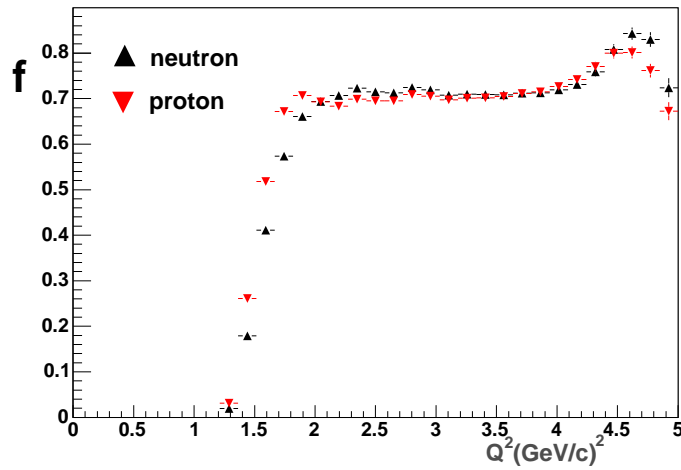


Figure 2.59: The fraction of nucleons scattered at the indicated  $Q^2$  which scattered into the EC acceptance and satisfied the  $\theta_{pq}$  cuts, as determined by the simulation. The black points show the neutron fraction, the red points show the proton fraction. An incident beam energy of 4.2 GeV was used to generate these points.

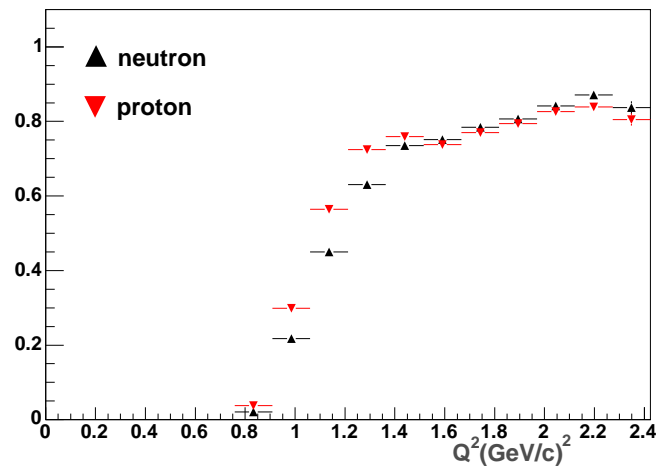


Figure 2.60: The fraction of nucleons scattered at the indicated  $Q^2$  which scattered into the EC acceptance and satisfied the  $\theta_{pq}$  cuts, as determined by the simulation. The black points show the neutron fraction, the red points show the proton fraction. An incident beam energy of 2.6 GeV was used to generate these points.

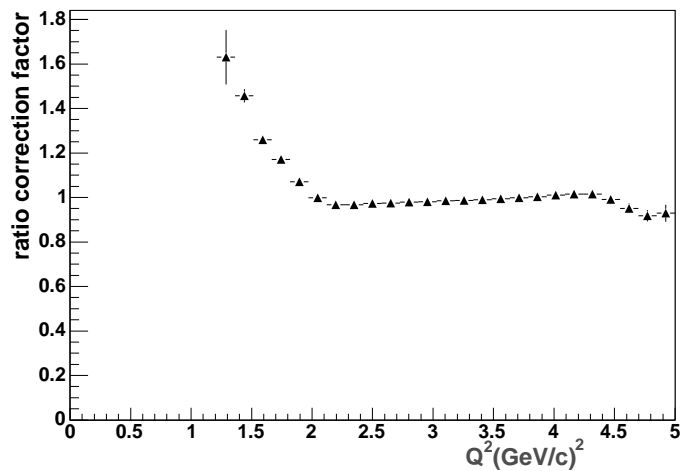


Figure 2.61: The correction factor to the e-n/e-p ratio for Fermi loss in the EC, for the 4.2 GeV data.

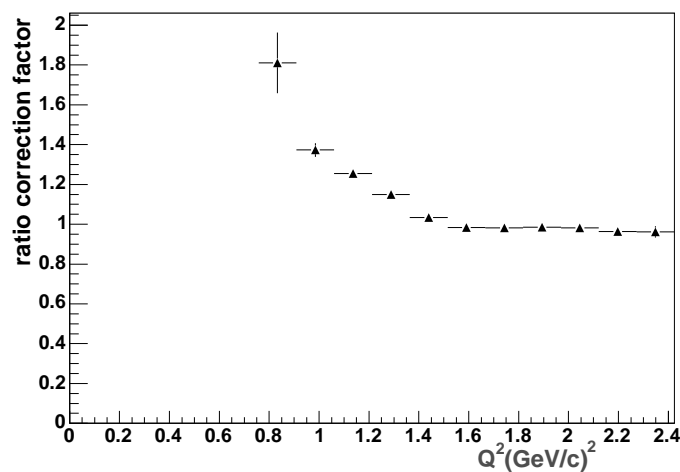


Figure 2.62: The correction factor to the e-n/e-p ratio for Fermi loss in the EC, for the 2.6 GeV data.

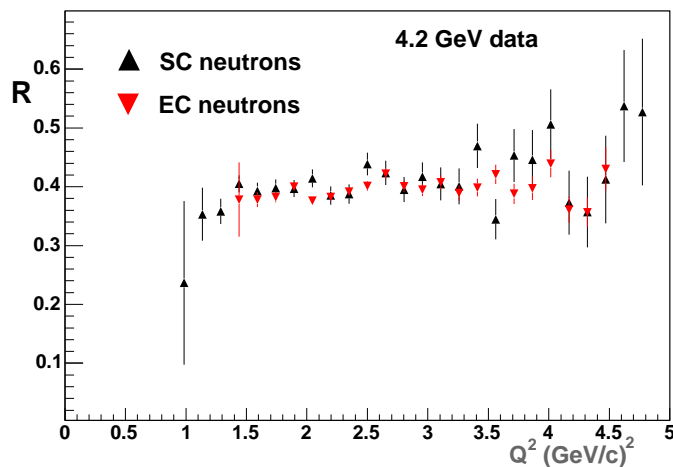


Figure 2.63: The  $\sigma_n/\sigma_p$  ratio  $R$ , as measured in the 4.2 GeV data set for both EC neutrons (red triangles) and SC neutrons (black triangles), binned in  $Q^2$ . The Fermi loss corrections have been applied.

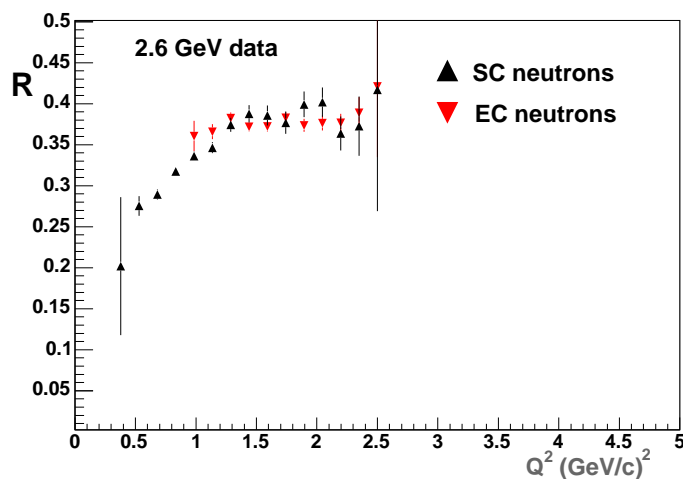


Figure 2.64: The  $\sigma_n/\sigma_p$  ratio  $R$ , as measured in the 2.6 GeV data set for both EC neutrons (red triangles) and SC neutrons (black triangles), binned in  $Q^2$ . The Fermi loss corrections have been applied.

1. Generate simulated  $ep \rightarrow e + X$  data using CELEG/GSIM. From these Monte Carlo ‘data’, we extract the simulated neutron detection efficiency of the EC and SC using the same algorithms that were applied to the real data.
2. Generate simulated  $ep \rightarrow ep$  elastic data and extract the simulated proton detection efficiency in the EC and SC, again using the same algorithms that were applied to the real data.
3. Generate a simulated, quasi-elastic data set with Fermi motion effects included using the quasielastic event generator QUEEG described in section 2.7.3. Using the detector efficiency results from steps 1 and 2 above, we determine the value for  $R$  with Fermi effects turned on.
4. Set the Fermi momentum distribution in QUEEG to  $f(p) = \delta(0)$  and generate a new, simulated data set. Analyze these data with the detector efficiency results from steps 1 and 2 above to determine the value of  $R$  with the Fermi effects turned off.
5. The ratio of  $R$  from step 3 and step 4 will be the Fermi correction with a set of calibration and production data points entirely generated by GSIM.

We now describe the details of the simulation. Calibration events (steps 1-2 above) were generated for the extraction of the detection efficiencies using the CLAS Collaboration standard event generator CELEG with inputs shown in Table 2.7. Simulated events for the quasielastic deuteron data were created with the program QUEEG described in section 2.7.3 using, for example, the following command

```
queeg -o queegsim.dat -E 2.558 -I 2250. -N 1000000 -F 0.5
```

where the output file (-o) is `queegsim.dat`, the beam energy (-E) is 2.558 GeV, the CLAS torus current (-I) is 2250 A, the number of events (-N) is 1000000, and the fraction of neutrons (-F) is 0.5. The events generated by CELEG and QUEEG were passed to GSIM and run with, for example, the following command

```
gsim_bat -ffread ffreed_gsim -kine 1 -mcin pde.out.$JOBID.bos
        -bosout pde.gsim.bos.A00
```

where the control parameters are in the file (-ffread) `ffread_gsim` and shown in Table 2.8, the input data from the event generator is a BOS file (-kine 1) with name taken from the -mcin flag, and the output file (-bosout) is `pde.gsim.bos.A00`. Finally, to simulate the effect of the finite resolution of CLAS the program GPP was used to process the outputs from GSIM using the following command

```
gpp -opde.gsim.bos.A00.gpp -a1.0 -b1.25 -c1.5 pde.gsim.bos.A00
```

Table 2.7: CELEG input card for calibration event generation

BEAM	ELECTRON	0.00000	0.00000	4.23200	0.00000
TARGET	PROTON	0.00000	0.00000	0.00000	0.00000
W RANGE		0.10000	3.0000	0.00000	0.00000
Q2 RANGE		0.80000	5.00000	0.00000	0.00000
X CUTS		0.00000	99.00000	0.00000	0.00000
Y CUTS		0.00000	99.00000	0.00000	0.00000
Q2 CUTS		0.80000	5.00000	0.00000	0.00000
W CUTS		0.10000	3.0000	0.00000	0.00000
NU CUTS		0.00000	99.00000	0.00000	0.00000
EP CUTS		0.00000	99.00000	0.00000	0.00000
THETAP CUTS		5.000	75.00000	0.00000	0.00000
E PHI ANG YES		0.00000	360.00000	0.00000	0.00000
MULT RANGE		0.00000	99.00000	0.00000	0.00000
DECAY	NO	0.00000	0.00000	0.00000	0.00000
EDIT	NO	13.00000	0.00000	0.00000	0.00000
FERMI	NO	1.00000	0.00000	0.00000	0.00000
FIX_TGT	YES				
EVENTS		100000.0	0.00000	0.00000	0.00000
VERTEX	YES	0.00000	0.00000	3.00000	0.00000
ELASTIC	YES	0.00000	0.00000	0.00000	0.00000
DEEP IN	NO	0.00000	0.00000	0.00000	0.00000
DEL1232	NO	0.00000	0.00000	0.00000	0.00000
DEL1620	NO	0.00000	0.00000	0.00000	0.00000
DEL1700	NO	0.00000	0.00000	0.00000	0.00000
DEL1900	NO	0.00000	0.00000	0.00000	0.00000
DEL1905	NO	0.00000	0.00000	0.00000	0.00000
DEL1910	NO	0.00000	0.00000	0.00000	0.00000
DEL1920	NO	0.00000	0.00000	0.00000	0.00000
DEL1930	NO	0.00000	0.00000	0.00000	0.00000
DEL1950	NO	0.00000	0.00000	0.00000	0.00000
N1440	NO	0.00000	0.00000	0.00000	0.00000
N1520	NO	0.00000	0.00000	0.00000	0.00000
N1535	NO	0.00000	0.00000	0.00000	0.00000
N1650	NO	0.00000	0.00000	0.00000	0.00000
N1675	NO	0.00000	0.00000	0.00000	0.00000
N1680	NO	0.00000	0.00000	0.00000	0.00000
N1700	NO	0.00000	0.00000	0.00000	0.00000
N1710	NO	0.00000	0.00000	0.00000	0.00000
N1720	NO	0.00000	0.00000	0.00000	0.00000
LAM1405	NO	0.00000	0.00000	0.00000	0.00000
LAM1520	NO	0.00000	0.00000	0.00000	0.00000
LAM1600	NO	0.00000	0.00000	0.00000	0.00000
LAM1670	NO	0.00000	0.00000	0.00000	0.00000
LAM1690	NO	0.00000	0.00000	0.00000	0.00000
LAM1800	NO	0.00000	0.00000	0.00000	0.00000
LAM1820	NO	0.00000	0.00000	0.00000	0.00000
LAM1830	NO	0.00000	0.00000	0.00000	0.00000
LAM1890	NO	0.00000	0.00000	0.00000	0.00000
LAM2110	NO	0.00000	0.00000	0.00000	0.00000
SIG1385	NO	0.00000	0.00000	0.00000	0.00000
SIG1660	NO	0.00000	0.00000	0.00000	0.00000
SIG1670	NO	0.00000	0.00000	0.00000	0.00000
SIG1750	NO	0.00000	0.00000	0.00000	0.00000
SIG1775	NO	0.00000	0.00000	0.00000	0.00000
SIG1915	NO	0.00000	0.00000	0.00000	0.00000
SIG1940	NO	0.00000	0.00000	0.00000	0.00000
SIG2030	NO	0.00000	0.00000	0.00000	0.00000
USER	NO	0.00000	0.00000	0.00000	0.00000
PRESCALE	NO				
FLSEED	YES				
LIST	NO				
DATAOUT	NO	gg.lund			
HISTOUT	NO	gg.rzdat			
BOSOUT	YES	celeg.evt			

Table 2.8: GSIM input card for calibration and quasielastic event simulation

```

MLIST
CUTS 5.e-3 5.e-3 5.e-3 5.e-3 5.e-3
CCCUTS 1.e-3 1.e-3 1.e-3 1.e-3 1.e-3
DCCUTS 1.e-4 1.e-4 1.e-4 1.e-4 1.e-4
ECCUTS 1.e-4 1.e-4 1.e-4 1.e-4 1.e-4
SCCUTS 1.e-4 1.e-4 1.e-4 1.e-4 1.e-4
TARGET 'e5a'
VERT_E5 4

RUNG 10
AUTO 1
MAGTYPE 3
MAGSCALE 0.8744 0.75
KINE 1
TRIG 200000
NOGEOM 'PTG' 'ST'
NOMCDATA 'ALL'
SAVE 'ALL' 5
STOP
END

```

where the output file (-o) is `pde.gsim.bos.A00.gpp`, the scale factors for the drift chamber timing resolution are 1.0 (-a), 1.25 (-b), and 1.5 (-c), and the output file is `pde.gsim.bos.A00`.

We now discuss the detection efficiencies determined from the GSIM simulations. The proton detection efficiency was extracted from the CELEG simulations with the same analysis code that was used to process the data. The results for the SC are shown in Figure 2.65 for a beam energy of 2.6 GeV and summed over all sectors (black points) along with the CLAS measured results for all sectors (red points). Compare this plot with Fig 2.23 for the measured efficiency in each sector. The real and simulated efficiencies both have high ( $\gtrsim 0.97$ ) efficiency for most paddles. The change in the proton efficiency at paddle 23 in the simulated results is associated with different scintillator panels. This difference between the two SC panels in GSIM does not appear in the data and is observed in GSIM simulations at 4.2 GeV. The neutron detection efficiency was also extracted from the CELEG simulations again with the same code used to analyze the real data. The results for the EC are shown in Figure 2.66 for 2.6 GeV. Compare this result with Figure 2.12 for the CLAS measured efficiency for both beam energies. Notice the difference in shape. The simulated neutron efficiency rises more rapidly as a function of neutron momentum for  $p_n \lesssim 1.0$  GeV/c. There is a dip in the simulated efficiency at  $p_n \approx 1.2$  GeV/c and a slow rise for  $p_n = 1.4 - 2.4$  GeV/c differing from the CLAS measured neutron efficiency. The dip at  $p_n \approx 1.2$  GeV/c has been observed in other CELEG/GSIM simulations we performed at a beam energy of 4.2 GeV even though those neutrons illuminate different parts of CLAS. Because the dip appears at the same momentum in both simulations, it is likely a feature in GSIM or CELEG and not our analysis code. We used the same function to fit the EC neutron detection efficiency that was used in the analysis of the real data. The fits were of lower quality because of the different shape of the simulated neutron detection efficiency. The results for the SC neutron detection efficiencies are shown in Figure 2.67 for 2.6 GeV. Compare this

## Average Efficiency vs Paddle Number, all sectors

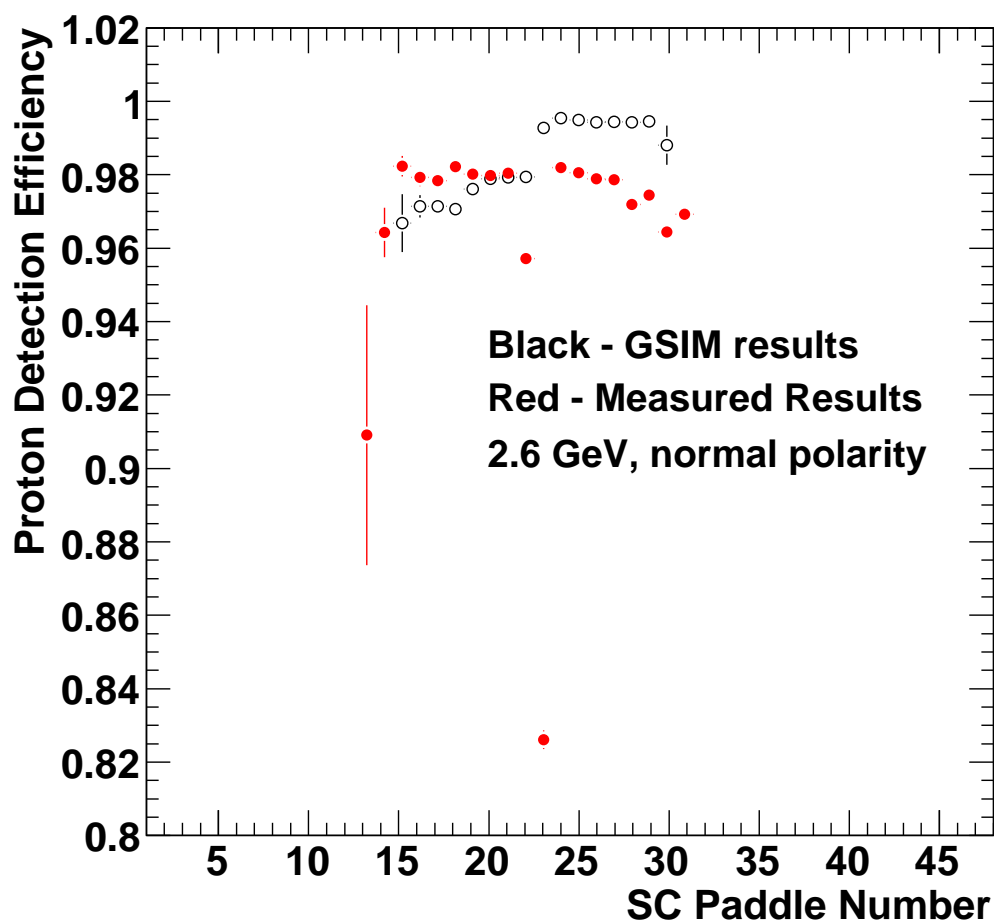


Figure 2.65: Proton detection efficiency in the SC measured in CLAS (red points) and extracted from GSIM (black points).

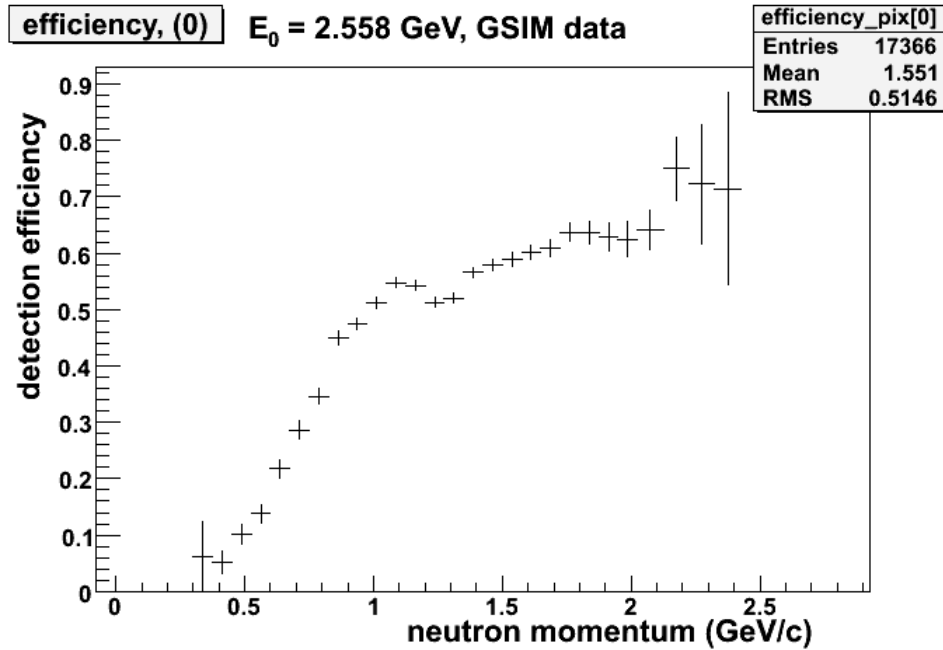


Figure 2.66: Neutron detection efficiency in the EC from GSIM.

figure with Figure 2.19 for the CLAS measured efficiency for both beam energies. Notice again the shape of the simulated efficiency differs from the measured one. The maximum efficiency from the GSIM simulation is about one-fifth to one-quarter of the measured one and there is more structure in the simulated efficiency spectrum. Again, we used the same function to fit the SC neutron detection efficiency that was used in the analysis of the real data. In this case, the fitting procedure failed for many paddles so we were unable to complete the full, sector-by-sector and paddle-by-paddle analysis of the SC neutron simulation without altering either the simulation or our analysis procedures. We dealt with this issue below by using the SC neutron efficiency averaged over all sectors and paddles in the Fermi correction simulation.

To determine the Fermi correction to the EC data from our simulation, we start with the neutron and proton detection efficiencies extracted from the GSIM simulation. We then calculate the value of  $R$  with the Fermi motion turned on (using QUEEG) and the value of  $R$  with the Fermi motion turned off. The ratio of these two calculations ( $R$  with Fermi motion on and off) is the correction. The results are shown in Figure 2.68. Compare this figure with Figure 2.62. For Figure 2.62 we used the same event generator (QUEEG), and only considered the geometric acceptance of the EC in the simulation (the detection efficiencies were measured from the calibration data). The GSIM simulation has more structure than the real data. There is a small dip at  $Q^2 \approx 1.5 (GeV/c)^2$  followed by a more rapid rise at lower  $Q^2$ . The GSIM simulation is in qualitative agreement with our previous calculation; the correction factor is about unity for  $Q^2 \gtrsim 1.3 (GeV.c)^2$  and increases at lower  $Q^2$ .

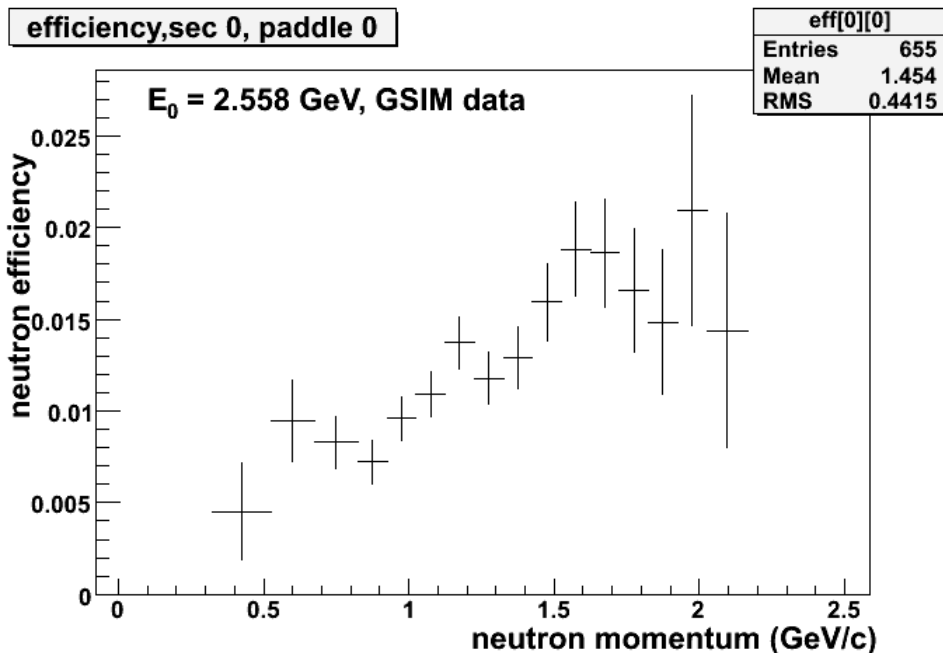


Figure 2.67: Neutron detection efficiency in the SC from GSIM.

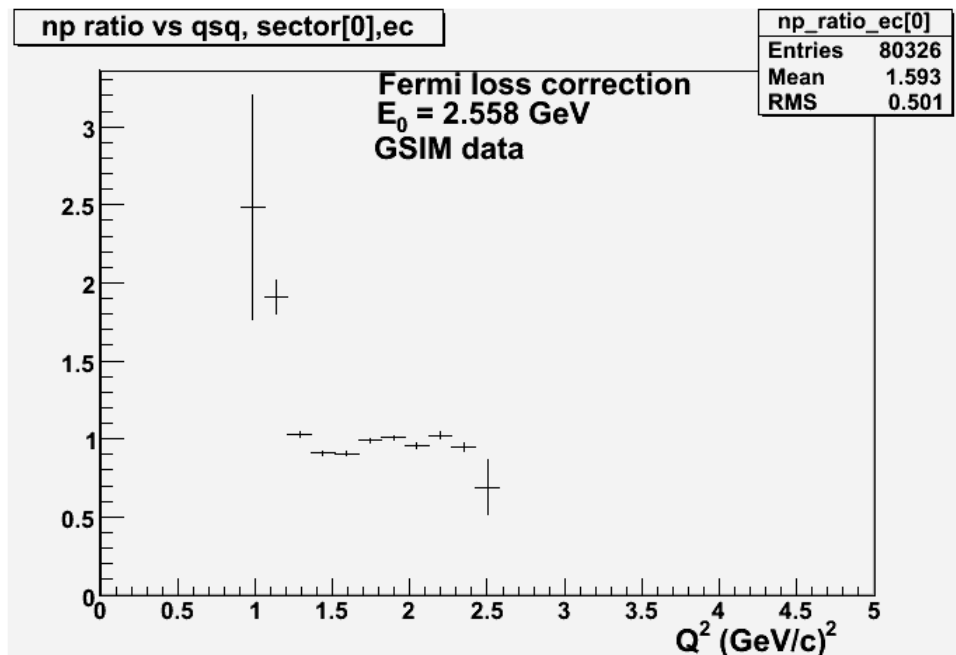


Figure 2.68: Fermi-loss correction from GSIM for EC neutrons at 2.6 GeV beam energy.

Obtaining quantitative agreement at lower  $Q^2$  would require a deeper investigation of the neutron simulation in GSIM that is beyond the scope of this work. We intend to publish initially the results for  $Q^2 > 1 \text{ GeV}^2$  because we have consistent overlaps in that range for the SC and EC while we only have the SC data for  $Q^2 < 1 \text{ GeV}^2$ . The low  $Q^2$  data are the subject of an ongoing study that includes the 2.6-GeV, reversed torus field data. The GSIM simulation will be studied more in that project. See also Section E item 1 of the Appendix.

We have investigated the Fermi correction to the SC with GSIM and studied our choice of the parameterization of the SC neutron detection efficiency for the low  $Q^2$  data at 2.6 GeV. In our standard procedure the SC neutron calibration spectra are fitted with a third-order polynomial in the region of the neutron momentum  $p_n$  where the detection efficiency is increasing and then with a plateau above some minimum value of  $p_n$ . The position of the low- $p_n$  end of the plateau is varied in the fit and the function is required to be continuous across the full range of the data. The results for the standard fit in the GSIM simulation at 2.6 GeV are shown in Figure 2.69 (black points). The simulated results again show more structure than ones where we used detection efficiencies based on our CLAS calibration data (compare with Figure 2.58). To study the impact of our choice of the parameterization we fixed the value of the coefficient of the third-order term in the polynomial to zero and redid the calibration fits in the Fermi correction calculation. The results are also shown in Figure 2.69 (red points). For  $Q^2 > 1 \text{ GeV}^2$ , the two calculations are consistent within the Monte Carlo statistical uncertainties, but start to diverge in the range  $Q^2 \lesssim 1 \text{ GeV}^2$ . This is due to the effect of the shape of the simulated SC neutron detection efficiency that does not appear in the CLAS measured SC neutron detection efficiency. Recall Figure 2.19 (SC neutron detection efficiency measured in CLAS) and Figure 2.67 (GSIM calculation of the SC neutron detection efficiency). The spectra have some similar features, but the simulated neutron detection efficiency has a dip at  $p_n \approx 0.9 \text{ GeV}$  that has a large effect on the fit to the neutron detection efficiency used in the Fermi correction. In Figure 2.70 we reproduce the GSIM SC neutron efficiency (recall Figure 2.67) and plot the fit results for the standard function (third-order polynomial with a plateau; the red curve) and the results for the fit using a second-order polynomial and a plateau (blue curve). The third-order polynomial reproduces the dip at  $p_n \approx 0.9 \text{ GeV}$  and is changing more rapidly for  $p_n \lesssim 1.2 \text{ GeV}$  than the second-order polynomial fit. This difference between the two fits is in a neutron momentum range that corresponds to  $Q^2 \lesssim 1 \text{ GeV}^2$  where the Fermi corrections diverge in Figure 2.69. Exploring the reason for this difference between the GSIM simulation and the measured efficiency is beyond the scope of this analysis. As mentioned above we intend to initially publish the results for  $Q^2 > 1 \text{ GeV}^2$  because we have consistent overlaps in that range for the SC and EC while we only have the SC data for  $Q^2 < 1 \text{ GeV}^2$ .

We also investigated the effect of the uncertainty in the electron polar angle on the Fermi corrections. The uncertainty in the angular position of the electron is about 1 mrad for the polar angle and 4 mrad for the azimuthal angle [36]. We

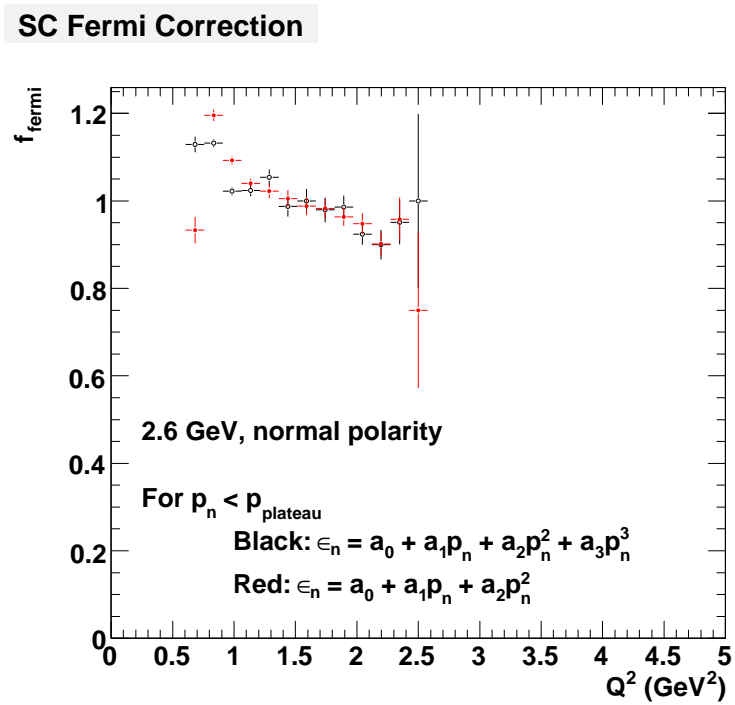


Figure 2.69: Comparison of the Fermi correction for the simulated, 2.6-GeV, SC data with different parameterizations.

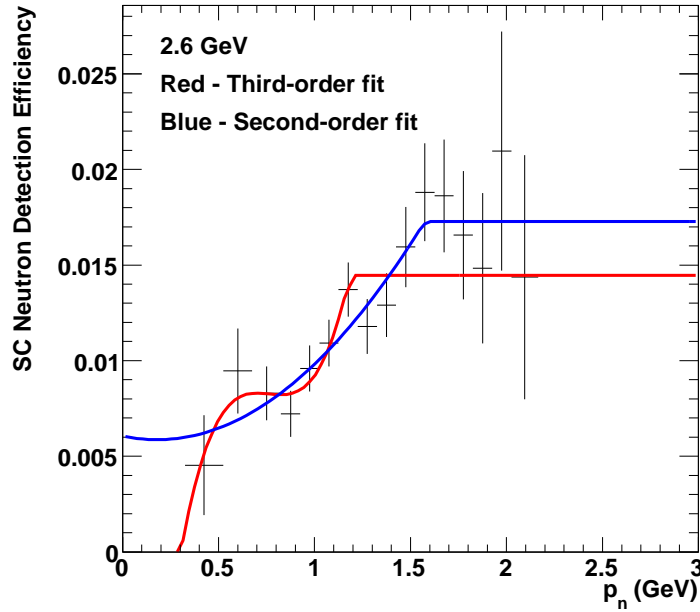


Figure 2.70: Comparison of the simulated SC neutron detection efficiency fits using a third-order polynomial with a plateau (red curve) and a second-order polynomial with a plateau (blue curve).

assumed (conservatively) a 4 mrad width for the polar angle and randomly smeared the electron polar and azimuthal angles by this amount. The results for the EC and SC at each beam energy (2.6 GeV and 4.2 GeV) are shown in Figures 2.71-2.74. In each figure the left-hand panel shows the standard Fermi correction (black points) and the same calculation after adding the smearing to the electron angle (red points). The right-hand panel in each figure shows the fractional difference  $\Delta f_{fermi}/f_{fermi}$  between each of those calculations. The size of the smearing effect is small and consistent with zero within the uncertainties in each case. In Section 3.2.3.12 we assign a systematic uncertainty of 0.6% on the Fermi correction factor due to this effect.

### 2.7.5 Radiative Corrections

If diagrams beyond the lowest order Born term, containing more than a single virtual or real photon, are considered, the scattering cross section is modified from its single photon value by a multiplicative factor:  $\sigma = \sigma_0(1 + \delta)$ , where  $\sigma_0$  is the single photon exchange cross-section, and  $\delta$  is due to the effect of higher-order diagrams. Various schemes for computing the correction factor  $(1 + \delta)$  have been put forward.

The traditional Mo and Tsai [37] approach to radiative corrections was developed for use in *inclusive* scattering, and cannot properly be applied to the scattering

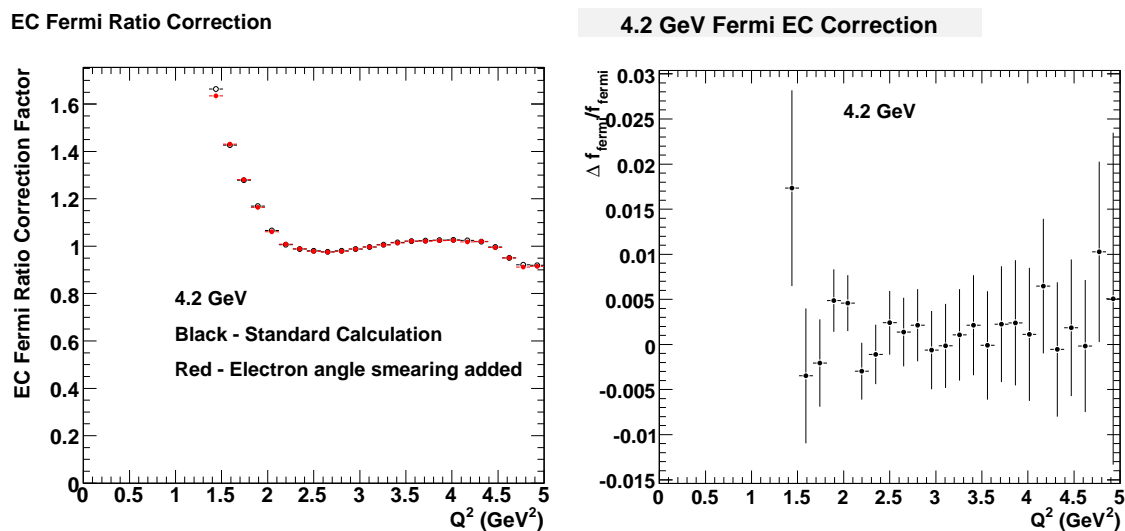


Figure 2.71: Effect of electron angle smearing on EC, 4.2-GeV Fermi correction.

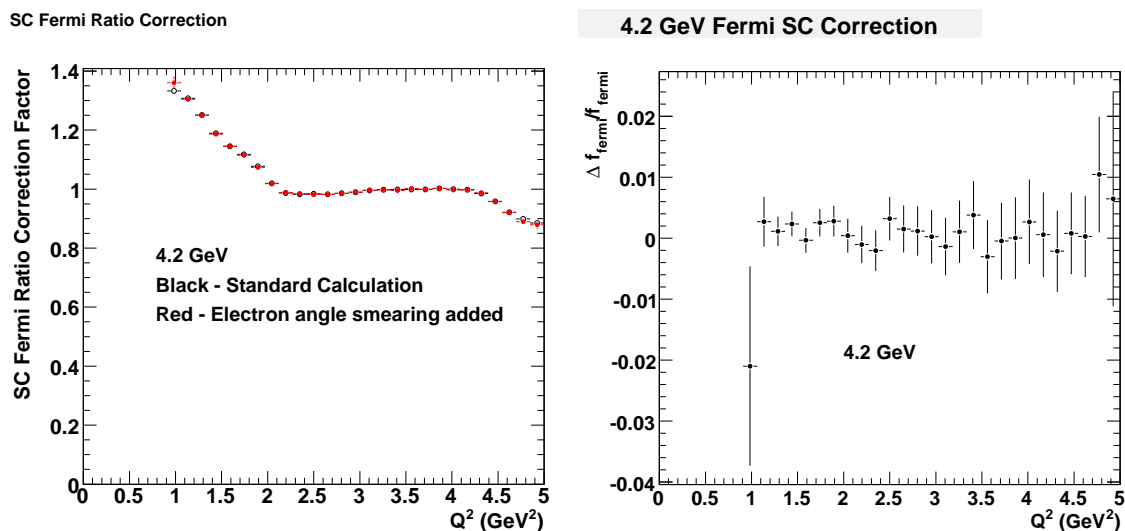


Figure 2.72: Effect of electron angle smearing on SC, 4.2-GeV Fermi correction.

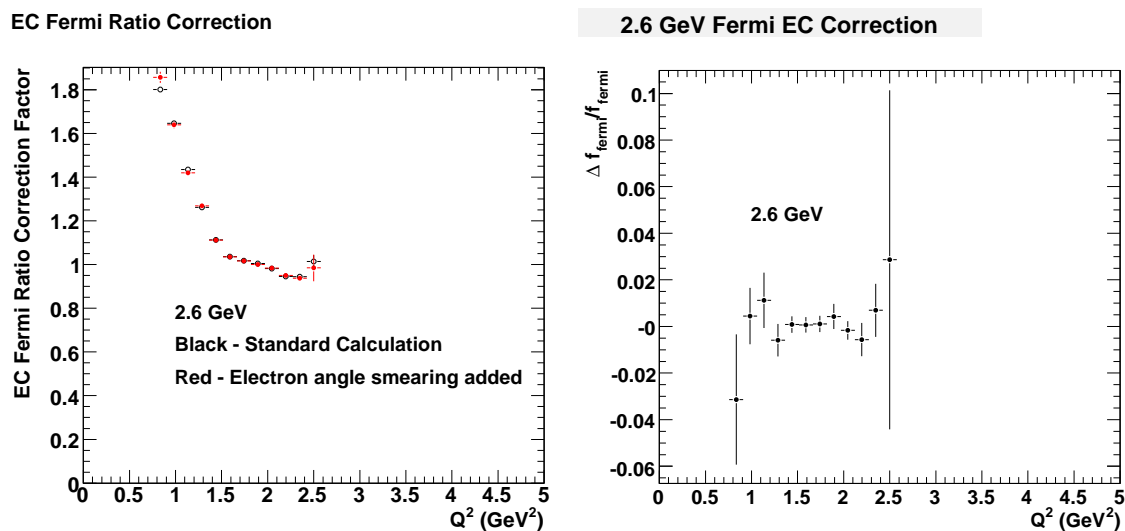


Figure 2.73: Effect of electron angle smearing on EC, 2.6-GeV Fermi correction.

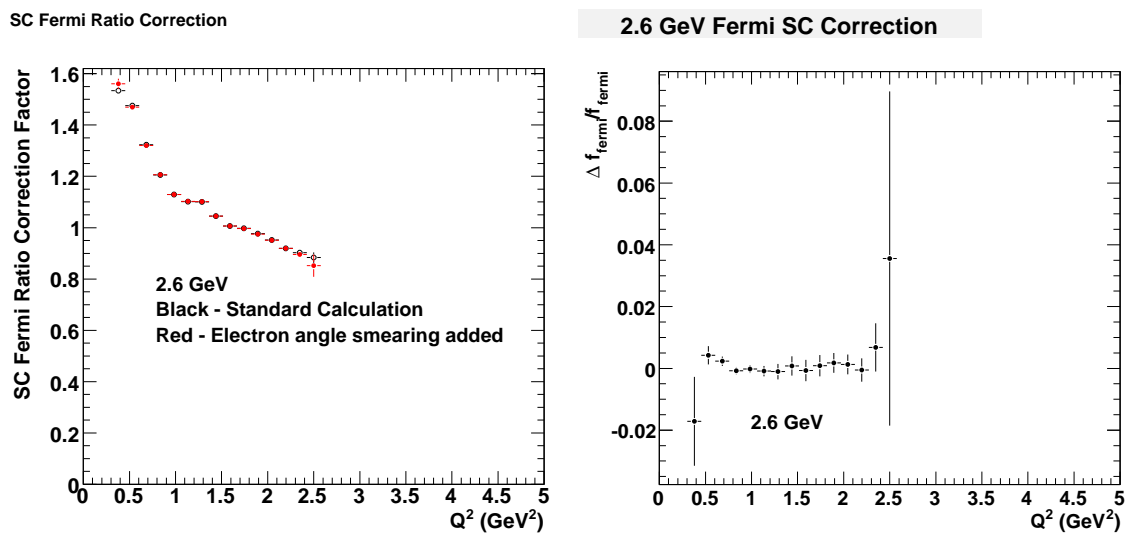


Figure 2.74: Effect of electron angle smearing on SC, 2.6-GeV Fermi correction.

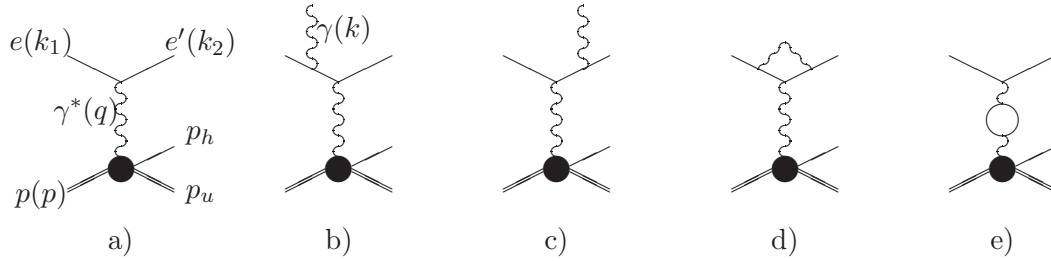


Figure 2.75: Feynman diagrams contributing to the Born and the next-order cross sections. a) Born process, b) and c) Bremsstrahlung, d) Vertex correction, and e) Vacuum polarization.  $p_h$  is the momentum of the detected hadron,  $p_u$  is the momentum of the undetected hadron.

measurement from which  $G_M^n$  is extracted. The measurement of the quasi-elastically scattered hadron, in addition to the electron, reduces the phase space allowed for the radiated photon. In addition, only two structure functions contribute in the case of exclusive scattering, while for unpolarized inclusive scattering, four structure functions can contribute.

The radiative corrections for this analysis were performed using the approach of Afanasev *et al.* [38], which was originally developed for exclusive pion electroproduction. The model includes, in addition to the Born term, diagrams for initial and final state electron Bremsstrahlung, electron vertex correction, and vacuum polarization. The diagrams included are shown in Fig 2.75. Note that two-photon exchange diagrams are not included.

Afanasev *et al.* wrote a computer code EXCLURAD to numerically evaluate the radiative corrections. The EXCLURAD code generates the ratio of the radiated cross section at a given value of  $Q^2, W, \cos \theta_{pq}, \phi_{pq}$  to the PWIA result ( $\theta_{pq}, \phi_{pq}$  are the polar and azimuthal angles between the virtual photon direction and the direction of the detected hadron). For the  $G_M^n$  analysis, the reactions of interest are  $D(e, e'p)n$  and  $d(e, e'n)p$ , not pion production on a proton target. To accommodate the change in final state hadron species, the EXCLURAD code was modified. The masses of the target, detected and undetected final state hadrons were changed to values appropriate for deuteron breakup. The DEEP code of Van Orden *et al.* [39], a relativistic deuteron model, was installed to calculate response functions at the deuteron-virtual photon vertex.

The EXCLURAD/DEEP code was used to generate surfaces in  $\cos \theta_{pq}$  and  $\phi_{pq}$  at a variety of  $Q^2$  points, as shown in Fig 2.76. At each  $Q^2$  value, this surface is integrated over the range of  $\cos \theta_{pq}$  accepted for that  $Q^2$  (see previous section) and over the full range of  $\phi_{pq}$  (Monte Carlo studies and analysis of the quasi-elastic data both confirm the full  $\phi_{pq}$  coverage of the detector). The calculation at each  $Q^2$  point is performed twice, once for the case where the detected hadron is the proton, once

Table 2.9: Radiative correction values for 2.6 GeV data.

$Q^2$	$1 + \delta_n$	$1 + \delta_p$	$f_{rad}$
1	0.7956	0.7957	0.9999
2.35	0.8273	0.8273	1.0000
2.45	0.8421	0.8424	0.9996
2.55	0.8568	0.8583	0.9983

Table 2.10: Radiative correction values for 4.2 GeV data.

$Q^2$	$1 + \delta_n$	$1 + \delta_p$	$f_{rad}$
4.0	0.82691	0.82691	1.0000
5.0	0.85310	0.85310	1.0000

for the case where the detected hadron is the neutron. Note that while the radiative correction factor ( $1 + \delta$ ) may be as large as 1.3 for either of the two final states, what is required for the  $G_M^n$  analysis is the ratio of the  $D(e, e'p)n$  and  $D(e, e'n)p$  corrections:

$$f_{radiative}(Q^2) = \frac{1 + \delta_n(Q^2)}{1 + \delta_p(Q^2)} \quad (2.83)$$

where the subscript indicates either the correction to the cross section ratio (*radiative*), or the hadron species (n,p). The corrections to the two hadron species, while individually large in some cases, are numerically close to each other. This is shown in Fig 2.77. The ratio of the curves in Fig 2.77 is shown in Fig 2.78. The radiative correction factors  $1 + \delta_n$ ,  $1 + \delta_p$  and  $f_{radiative}$  are shown for several  $Q^2$  points in Table 2.9 for the 2.6 GeV data and in Table 2.10 for the 4.2 GeV data. The largest radiative correction value seen in the two tables is 0.9983. The radiative correction at each value of  $Q^2$  was taken to be exactly unity, with a systematic uncertainty of 0.17% assigned at each value of  $Q^2$ .

### 2.7.6 Nuclear Corrections

The quantity of interest in this analysis is the ratio of e-n/e-p scattering from *free* nucleons. What is measured is the quasi-elastic e-n/e-p ratio from nucleons bound in the deuteron. This quantity is related to the measured ratio by a correction factor:

$$R_{corrected}(Q^2) = f_{nuclear}(Q^2)R_{observed}(Q^2) \quad (2.84)$$

The correction factor  $f_{nuclear}(Q^2)$  must be determined by theoretical calculation. It would be ideal to perform this calculation in a fully relativistic framework, starting from a Lagrangian. Such an approach would automatically include a proper relativistic treatment of the nuclear dynamics and electromagnetic current. However, a fully relativistic treatment is not available. In practice, electron scattering from nuclei is usually treated by taking the nuclear initial state as the solution to a bound-state

$$E=4.232 \text{ GeV}, W=2.417 \text{ GeV}, Q^2=4.0 \text{ GeV}^2$$

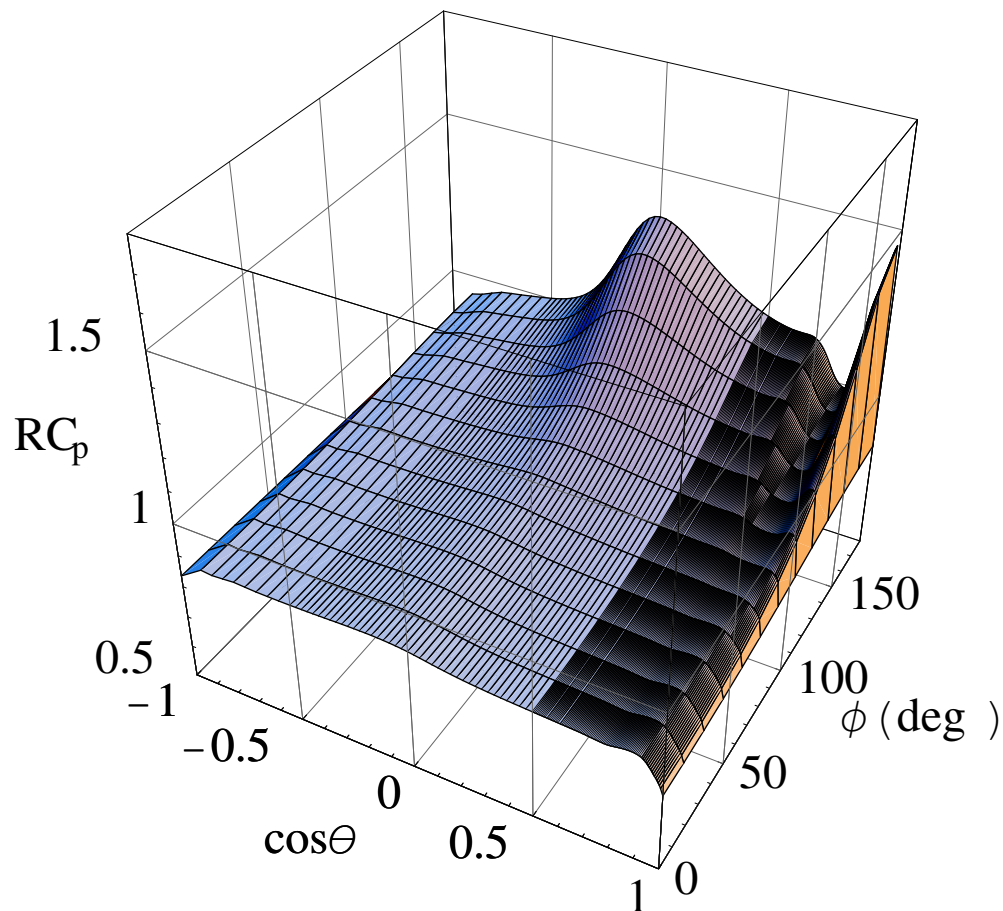


Figure 2.76: Radiative correction for quasi-elastic  $D(e, e'p)n$  scattering as a function of  $\cos\theta_{pq}$  and  $\phi_{pq}$ . The figure was made using an incident beam energy of 4.23 GeV, and shows the correction for scattering at  $Q^2 = 4.0 \text{ GeV}^2$

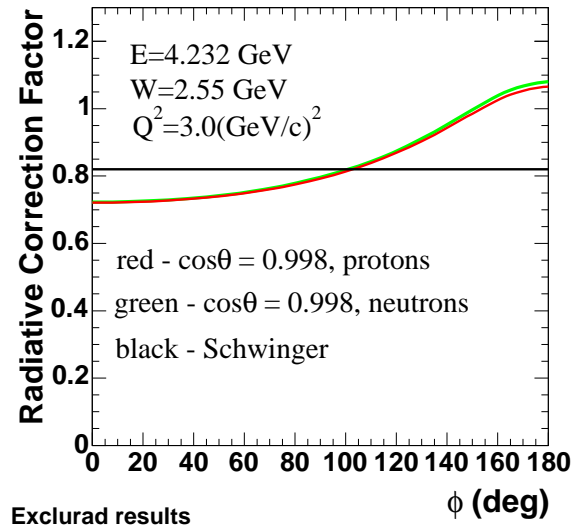


Figure 2.77: A comparison of the radiative correction factor for  $D(e, e'p)n$  and  $D(e, e'n)p$ , as a function of  $\phi_{pq}$ . The curves shown were generated for a beam energy of 4.232 GeV and  $Q^2$  of 3.0 (GeV/c)<sup>2</sup>. Also shown for comparison are the results of the Schwinger model [40], which calculates the correction for inclusive scattering off a fixed potential.

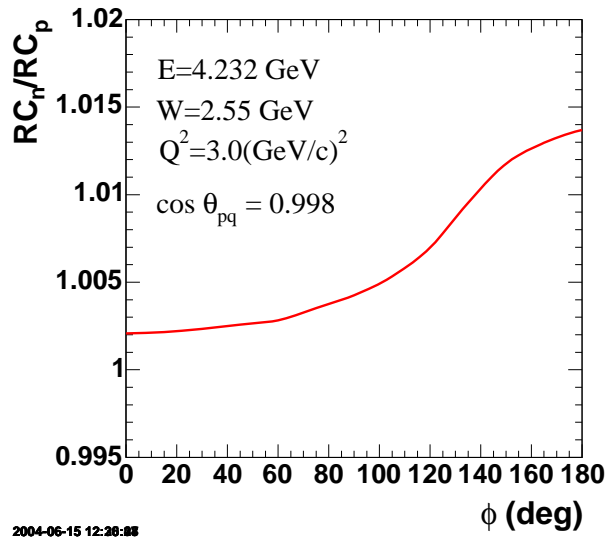


Figure 2.78: The ratio of the  $D(e, e'p)n$  and  $D(e, e'n)p$  radiative correction curves shown in Fig. 2.77. When averaged over  $\phi_{pq}$ , this curve gives the radiative correction to the quasi-elastic ratio at  $Q^2 = 3.0(\text{GeV}/c)^2$ .

Schrodinger equation, and the final state is calculated using optical potentials or a multiple-scattering approach. The electromagnetic current is subjected to a non-relativistic reduction in this case. The theoretical calculations for this analysis were carried out by Jeschonnek [41], using the procedure described in [42], [43], [44], and by Arenhövel [45].

For relativistic scattering, the cross-section in the lab frame can be written as [46]:

$$\begin{aligned} \left( \frac{d\sigma^5}{d\epsilon' d\Omega_e d\Omega_N} \right)_{fi}^h &= \frac{m_N m_f p_N}{8\pi^3 m_i} \sigma_{Mott} f_{rec}^{-1} \\ &\quad \left[ (v_L R_{fi}^L + v_T R_{fi}^T + v_{TT} R_{fi}^{TT} + v_{TL} R_{fi}^{TL}) \right. \\ &\quad \left. + h (v_{T'} R_{fi}^{T'} + v_{TL'} R_{fi}^{TL'}) \right], \end{aligned} \quad (2.85)$$

where  $m_i$ ,  $m_N$  and  $m_f$  are the masses of the target nucleus, the ejectile nucleon and the residual system,  $p_N$  and  $\Omega_N$  are the momentum and solid angle of the ejectile,  $\epsilon'$  is the energy of the detected electron and  $\Omega_e$  is its solid angle. The helicity of the electron is denoted by  $h$ . The Mott cross section is (setting  $\hbar = c = 1$ ):

$$\sigma_{Mott} = \left( \frac{\alpha \cos(\theta_e/2)}{2\varepsilon \sin^2(\theta_e/2)} \right)^2 \quad (2.86)$$

and the recoil factor is given by

$$f_{rec} = \left| 1 + \frac{\omega p_x - E_x q \cos \theta_x}{m_i p_x} \right|. \quad (2.87)$$

The coefficients  $v_k$  are constructed from elements of the lepton tensor, and convey information about the polarization state of the virtual photon (for example, the  $v_{LT}$  term is generated by interference between longitudinal and transverse modes of the virtual photon). The  $R^k$  are the nuclear response functions and contain information on the nucleon electromagnetic current. In terms of the nucleon current 4-vector  $(\rho, \vec{J})$ , the  $R^k$  are:

$$\begin{aligned} R_{fi}^L &\equiv |\rho(\vec{q})_{fi}|^2 \\ R_{fi}^T &\equiv |J_+(\vec{q})_{fi}|^2 + |J_-(\vec{q})_{fi}|^2 \\ R_{fi}^{TT} &\equiv 2 \Re [J_+(\vec{q})_{fi} J_-(\vec{q})_{fi}] \\ R_{fi}^{TL} &\equiv -2 \Re [\rho^*(\vec{q})_{fi} (J_+(\vec{q})_{fi} - J_-(\vec{q})_{fi})] \\ R_{fi}^{T'} &\equiv |J_+(\vec{q})_{fi}|^2 - |J_-(\vec{q})_{fi}|^2 \\ R_{fi}^{TL'} &\equiv -2 \Re [\rho^*(\vec{q})_{fi} (J_+(\vec{q})_{fi} + J_-(\vec{q})_{fi})], \end{aligned} \quad (2.88)$$

The  $J_{\pm}$  are the spherical components of the current 3-vector [47].

In the non-relativistic case, the lab-frame cross-section in the Plane-Wave Impulse Approximation(PWIA) can be written:

$$\frac{d^5\sigma}{d\epsilon' d\Omega_e d\Omega_N} = \frac{m_N m_f p_N}{m_i} \sigma_{eN} f_{rec}^{-1} n(\vec{p}), \quad (2.89)$$

where  $n(\vec{p})$  is the nucleon momentum distribution (evaluated at the value of  $\vec{p}$  determined by the reaction kinematics), and the  $eN$  cross section is given by

$$\sigma_{eN} = \sigma_{Mott} \sum_k v_k R_k^{sn}. \quad (2.90)$$

The  $sn$  superscript indicates the single-nucleon response function. The single-nucleon response functions are related to the nuclear responses by

$$R_K^{nucleus} = (2\pi)^3 R_k^{single\ nucleon} n(\vec{p}) \quad (2.91)$$

Combining these, one has:

$$\frac{d^5\sigma}{d\epsilon' d\Omega_e d\Omega_N} = \frac{m_N m_f p_N}{m_i} f_{rec}^{-1} \sigma_{Mott} n(\vec{p}) \sum_k v_k R_k^{single\ nucleon} \quad (2.92)$$

The momentum distribution  $n(\vec{p})$  is obtained by Fourier transform of the nuclear wave function:

$$n(\vec{p}) = \frac{1}{2\pi^2} (u(p)^2 + w(p)^2) \quad (2.93)$$

where  $u(p), w(p)$  are the S-wave and D-wave components of the deuteron wave function in momentum space, and the normalization condition is

$$\int d^3\vec{p} n(\vec{p}) = 1 \quad (2.94)$$

The AV18 deuteron wave function [48] was used in the calculation.

The electromagnetic current operator for the nucleon is given by:

$$J^\mu(P\Lambda; P'\Lambda') = \bar{u}(P'\Lambda') \left[ F_1 \gamma^\mu + \frac{i}{2m_N} F_2 \sigma^{\mu\nu} Q_\nu \right] u(P\Lambda) \quad (2.95)$$

where  $P, P'$  indicate the four-momenta of the nucleon, and  $\Lambda, \Lambda'$  indicate the nucleon spin state. A non-relativistic reduction of the current operator is carried out in [43], after which the nuclear response functions can be written in terms of the Sachs form-

factors:

$$\begin{aligned}
R_L^{sn} &= f_o^2(\xi_o^2 + \kappa^2 \delta^2 \xi_o'^2) \\
&= \frac{\kappa^2}{\tau}(G_E^2 + \delta^2 W_2) \\
R_T^{sn} &= f_o^2(2\kappa^2 \xi_1'^2 + \kappa^4 \delta^2 \xi_2'^2 + \delta^2 \xi_1^2 + \kappa^2 \delta^4 \xi_3'^2 - 2\kappa^2 \delta^2 \xi_1' \xi_3') \\
&= 2W_1 + \delta^2 W_2 \\
R_{TT}^{sn} &= f_o^2(\kappa^4 \delta^2 \xi_2'^2 + 2\kappa^2 \delta^2 \xi_1' \xi_3' - \delta^2 \xi_1^2 - \kappa^2 \delta^4 \xi_3'^2) \cos(2\varphi) \\
&= -\delta^2 W_2 \cos(2\varphi) \\
R_{TL}^{sn} &= 2\sqrt{2} \cos(\varphi) f_o^2(\delta \xi_o \xi_1 + \kappa^2 \delta \xi_o'(\xi_1' - \delta^2 \xi_3')) \\
&= 2\sqrt{2} \cos(\varphi) \frac{\kappa}{\sqrt{\tau}} \sqrt{1 + \tau + \delta^2} \delta W_2
\end{aligned} \tag{2.96}$$

where the  $W_1 = \tau G_M^2$  and  $W_2 = \frac{1}{1+\tau}(G_E^2 + \tau G_M^2)$ . The other factors are kinematic terms:

$$\begin{aligned}
\kappa &= \frac{|\vec{q}|}{2m_N} \\
\delta &= \frac{p_\perp}{m_N} \\
\lambda &= \frac{\omega}{2m_N} \\
\tau &= \kappa^2 - \lambda^2 = \frac{Q^2}{(2M_N)^2}
\end{aligned} \tag{2.97}$$

The dipole parametrization was used for all form factors in the calculation, except  $G_E^n$  which was set to 0.

It is possible for the struck nucleon to interact strongly with other nucleons as it exits the nucleus, as shown in Fig 2.79. The inclusion of Final-State Interactions (FSI) changes the matrix element of interest from  $\mathcal{M}_{fi} = \langle f | J_{em} | i \rangle$  to  $\mathcal{M}_{fi} = \langle f | S J_{em} | i \rangle$ , where  $S$  is the FSI operator. The final-state interactions were calculated in the context of Glauber theory [44]. In this framework, the FSI operator for interaction with a single spectator nucleon takes the form:

$$S(\vec{r}) = 1 - \theta(z) \cdot \Gamma(\vec{b}), \tag{2.98}$$

where the distance  $\vec{r}$  between the two interacting nucleons is decomposed into longitudinal and transverse parts:  $\vec{r} = \vec{b} + z \cdot \hat{q}$ , where  $\hat{q}$  indicates the direction of the virtual photon's momentum. The  $\theta$  function restricts the interaction to nucleons in the struck nucleon's forward hemisphere.  $\Gamma(b)$  is called the profile function, and is related to the nucleon-nucleon scattering amplitude via a Fourier transform:

$$\Gamma(\vec{b}) = \frac{1}{2\pi i k} \int d^2 \vec{l} \exp(-i\vec{l} \cdot \vec{b}) f(\vec{l}). \tag{2.99}$$

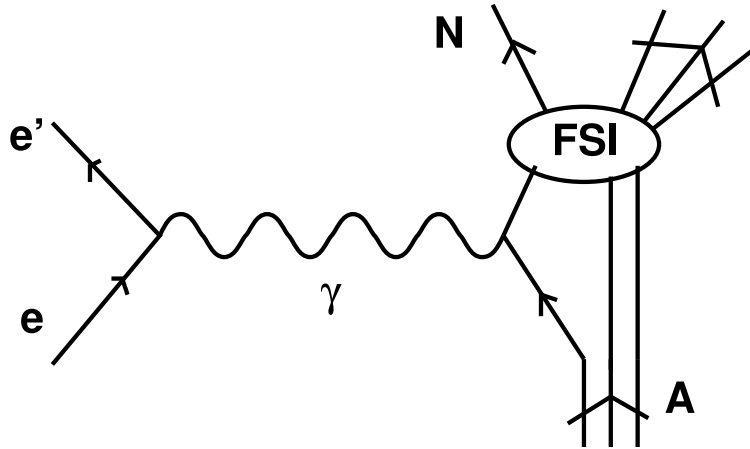


Figure 2.79: Diagrammatic representation of final-state interactions in the  $A(e,e'N)A-1$  single nucleon knockout reaction. The figure is from [44].

where  $\vec{k}$  is the incident nucleon momentum,  $\vec{k}'$  is the outgoing nucleon's momentum, and  $\vec{l} = \vec{k} - \vec{k}'$  is the momentum transferred in the nucleon-nucleon scattering. The most general form for the NN scattering amplitude (subject to the constraints of parity conservation, isospin invariance and the Pauli principle) is given by:

$$f(\vec{l}) = A(\vec{l}) + B(\vec{l}) (\vec{\sigma}_1 + \vec{\sigma}_2) \cdot \hat{n} + C(\vec{l}) (\vec{\sigma}_1 \cdot \hat{n}) (\vec{\sigma}_2 \cdot \hat{n}) + D(\vec{l}) (\vec{\sigma}_1 \cdot \hat{m}) (\vec{\sigma}_2 \cdot \hat{m}) + E(\vec{l}) (\vec{\sigma}_1 \cdot \hat{h}) (\vec{\sigma}_2 \cdot \hat{h}). \quad (2.100)$$

The nucleon spin operators are denoted by  $\vec{\sigma}_1$  and  $\vec{\sigma}_2$ , and  $\hat{n} \equiv \vec{k} \times \vec{k}' / |\vec{k} \times \vec{k}'|$ ,  $\hat{m} \equiv (\vec{k} - \vec{k}') / |\vec{k} - \vec{k}'|$ , and  $\hat{h} \equiv (\vec{k} + \vec{k}') / |\vec{k} + \vec{k}'|$ . In the approach used in [44], the amplitudes  $C, D, E$  are neglected (many implementations of Glauber theory also neglect  $B$ , keeping only the central amplitude  $A$ ), keeping only the central and spin-orbit terms  $A(l)$  and  $B(l)$ , which are parametrized in term of the results of phase shift analysis of NN scattering data:

$$A(l) = \frac{k \sigma_{tot}^{NN}}{4\pi} (\rho + i) \exp(-0.5 l^2 b_o^2) \quad (2.101)$$

$$(2.102)$$

where  $\sigma_{tot}^{NN}$  is the total NN cross-section,  $b_o$  is the diffractive slope and  $\rho$  is the ratio of the real to imaginary parts of the forward elastic amplitude.  $B(l)$  is parametrized in a similar fashion. The inclusion of the spin-orbit amplitude  $B(l)$  is significant for calculating FSI effects in the extraction of the  $R_{TT}$  and  $R_{LT}$  structure functions, but is not significant for the e-n/e-p ratio measurement since the TT and LT structure functions only contribute the total cross-section at the 1% level.

With a model chosen for the nuclear ground state and a prescription for the non-relativistic reduction of the electromagnetic current and a treatment of the final-state

Table 2.11: Nuclear corrections to e-n/e-p ratio from the Jeschonnek model.

$Q^2$	$f_{nuclear}$
1	0.999796
2	0.999714
3	0.999655
4	0.999624
5	0.999619

interactions, the correction to the ratio measurement was calculated by evaluating the ratio  $\sigma_{Full}/\sigma_{PWIA}$  for e-n and e-p scattering, where the “Full” calculations includes all FSI. The ratio of the e-n to e-p correction factors was taken, yielding the correction factor for the e-n/e-p ratio. The results for the 4.2 GeV beam energy are shown in Table 2.11.

The Jeschonnek model is not expected to be valid below  $Q^2 = 1$  (GeV/c)<sup>2</sup> at the lowest. The corrections at lower  $Q^2$  were supplied by the Arenhövel model [45]. The Arenhövel model is a non-relativistic deuteron electro-disintegration model. The Plane Wave Born Approximation (PWBA) is used. The PWBA is similar to the PWIA, but it also includes diagrams where the detected nucleon was *not* the struck nucleon. These diagrams are significant only at low- $Q^2$ . The model includes a treatment final-state interactions, and correction for relativistic effects. Some features not present in the Jeschonnek model are meson-exchange currents (MEC) to account for the possibility of the virtual photon coupling to mesons inside the deuteron, and isobar configurations (IC) to describe the virtual excitation of nucleon resonances, such as  $N\Delta$  or  $\Delta\Delta$ . The Bonn potential is used to model the nucleon-nucleon interaction. The correction factors were derived by comparing the full calculation to the PWBA(no FSI,MC,IC) in the quasi-elastic region. The calculated cross sections were integrated over a range of  $\theta_{pq}$  values used in the analysis, and the ratio of the full-to-PWBA integrated cross sections ratios for the neutron and proton was calculated. The results of the calculation are shown in Fig 2.80.

The Arenhövel model is not expected to be valid above  $Q^2 = 1$  (GeV/c)<sup>2</sup>. The predicted correction factors for the 2.6 GeV beam energy are shown in Table 2.12. Calculations for the 4.2 GeV beam energy were available only at one  $Q^2$  value,  $Q^2 = 0.811$ (GeV/c)<sup>2</sup>. The correction values for the two beam energies are shown in Fig 2.81. The figure shows a second order polynomial fit to the 2.6 GeV calculations, and the lone 4.2 GeV calculation. The nuclear correction at both beam energies will be performed using the fit shown in Fig 2.81.

It is seen that the two models disagree at  $Q^2 = 1$ (GeV/c)<sup>2</sup>, which is at the edge of the expected validity for both models. At  $Q^2 = 1$  (GeV/c)<sup>2</sup>, the average correction is 0.994, or a 0.6% correction. The average correction was used at this  $Q^2$  point, with a 100% uncertainty on the correction, so that a systematic uncertainty of 0.6% was assigned to the correction factor. This 0.6% systematic error was assigned to the

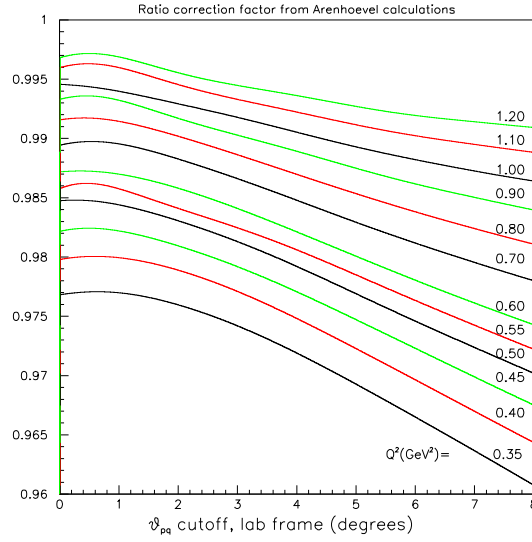


Figure 2.80: The e-n/e-p ratio correction factor, from the Arenhövel model, as a function of the  $\theta_{pq}$  cutoff, for several values of  $Q^2$ . The data shown is for the 2.6 GeV beam energy. The figure is from [49]

Table 2.12: Nuclear corrections to e-n/e-p ratio from the Arenhoevel model, for a 2.6 GeV beam energy.

$Q^2$	$f_{nuclear}$
0.5	0.977
0.75	0.983
1.0	0.989
1.2	0.993

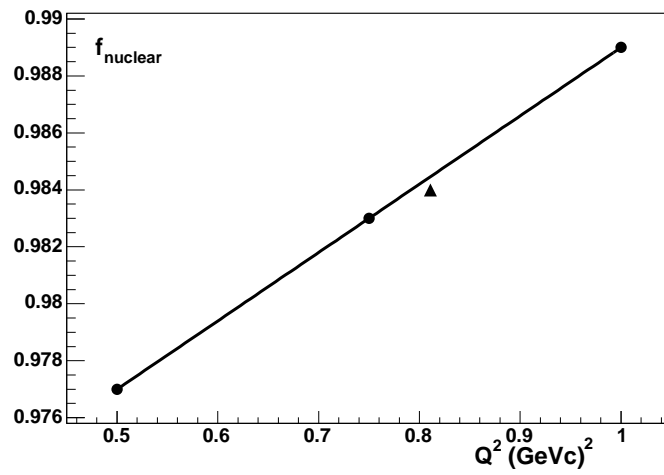


Figure 2.81: Nuclear correction factor for a 2.6 GeV energy beam (circles), and a 4.2 GeV beam (triangle). The curve is a second order polynomial fit to the 2.6 GeV points.

correction factor at all values of  $Q^2$ .

# Chapter 3

## Experiment Results

### 3.1 $G_M^n$ extraction from ratio

The corrected n/p ratio,

$$R_{corrected}(Q^2) = f_{nuclear}(Q^2)f_{radiative}(Q^2)f_{fermi}(Q^2)R_{observed}(Q^2) \quad (3.1)$$

is related to  $G_M^n$  through Eqn 1.12:

$$R_{corrected} = \frac{\sigma_{mott}^n \left( G_{E,n}^2 + \frac{\tau_n}{\epsilon_n} G_{M,n}^2 \right) \left( \frac{1}{1+\tau_n} \right)}{\sigma_{mott}^p \left( G_{E,p}^2 + \frac{\tau_p}{\epsilon_p} G_{M,p}^2 \right) \left( \frac{1}{1+\tau_p} \right)} \quad (3.2)$$

where super- or subscript  $n,p$  denote neutron or proton quantities. The kinematic variable  $\tau, \epsilon$  and the Mott cross section  $\sigma_{mott}$  are as previously defined.  $Q^2$  dependence of all quantities is assumed. Solving the equation above for  $G_M^n$  gives:

$$G_M^n = \sqrt{\left[ R_{corrected} \left( \frac{\sigma_{mott}^p}{\sigma_{mott}^n} \right) \left( \frac{1 + \tau_n}{1 + \tau_p} \right) \left( G_{E,p}^2 + \frac{\tau_p}{\epsilon_p} G_{M,p}^2 \right) - G_{E,n}^2 \right] \frac{\epsilon_n}{\tau_n}} \quad (3.3)$$

The Arrington parametrization [50] was used to evaluate the proton form factors and the Galster parametrization was used for  $G_E^n$ .

The  $G_M^n$  extraction was performed separately for each of the four measurements (2.6 and 4.2 GeV beam energy, SC and EC neutron detection). These four measurements are essentially independent. Two independent detector systems were used for detection of neutrons. Protons were detected in the DC/SC in all cases, however different regions of the drift chambers and SC panel were sampled at the two different beam energies. A comparison of the results from the four extractions is shown in Fig 3.1. The overlap of the four semi-independent measurements over a range of  $Q^2$  values suggests that systematic errors are under control. The necessity of applying the Fermi-momentum correction is shown by Fig 3.2, which shows a comparison of the four  $G_M^n$  measurements with *no* Fermi corrections applied.

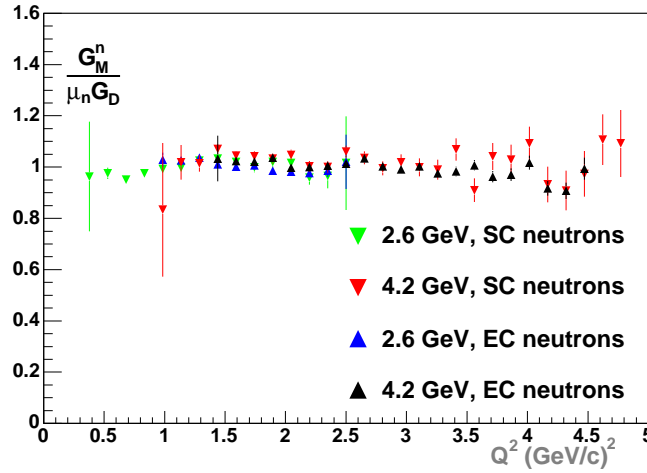


Figure 3.1: Comparison of  $G_M^n$  as a function of  $Q^2$  for four different measurements.  $G_M^n$  has been scaled to the dipole in this figure.

The  $G_M^n$  data from the four separate measurements were combined to form a weighted average. The weighting in each  $Q^2$  bin was chosen to minimize:

$$\chi^2 = \sum_j \frac{(x_j - \bar{x})^2}{\sigma_j^2} \quad (3.4)$$

where  $x_j$  and  $\sigma_j$  are the  $G_M^n$  value and statistical error associated with the  $j^{\text{th}}$  measurement contributing in that  $Q^2$  bin ( $j$  is an integer between 1 and 4). Setting  $\partial\chi^2/\partial\bar{x} = 0$  in Eqn 3.4 and solving for  $\bar{x}$  gives:

$$\bar{x} = \frac{\sum_j \frac{x_j}{\sigma_j^2}}{\sum_j \frac{1}{\sigma_j^2}} \quad (3.5)$$

The statistical error on each point in the weighted average was determined from:

$$\sigma_{\bar{x}}^2 = \sum_j \left( \frac{\partial\bar{x}}{\partial x_j} \right)^2 \sigma_j^2 \quad (3.6)$$

$$= \frac{1}{\sum_j \frac{1}{\sigma_j^2}} \quad (3.7)$$

The combined  $G_M^n$  histogram is shown in Fig 3.3. Tables giving numerical values for the four individual measurements, and the weighted average are shown in Appendix A.

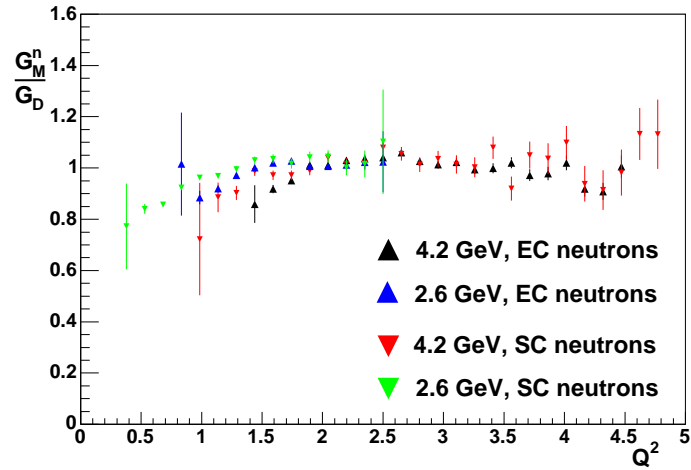


Figure 3.2: Comparison of  $G_M^n$  as a function of  $Q^2$  for four different measurements. The Fermi correction have *not* been applied.

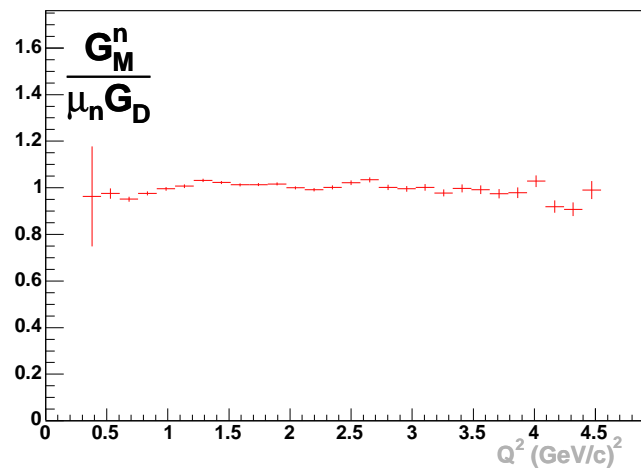


Figure 3.3: Weighted average  $G_M^n$ , binned in  $Q^2$  obtained by combining data from the four separate  $G_M^n$  measurements.  $G_M^n$  has been scaled to the dipole.

## 3.2 Systematic Errors

For the purpose of evaluating systematic errors, Eqn 3.3 can be simplified to:

$$G_M^n = \sqrt{(\sigma_p R_c - G_{E,n}^2) \frac{\epsilon}{\tau}} \quad (3.8)$$

by making the approximations

$$\frac{\sigma_{mott}^p}{\sigma_{mott}^n} \approx 1 \quad (3.9)$$

$$\frac{1 + \tau_n}{1 + \tau_p} \approx 1. \quad (3.10)$$

In Eqn 3.8,  $\sigma_p$  is the reduced proton cross section,  $\sigma_p = G_{E,p}^2 + \frac{\tau}{\epsilon} G_{M,p}^2$  and  $R_c$  is the corrected ratio. The corrected ratio is a function of a variety of parameters (location of cuts on missing mass in the calibration reaction, choice of cuts on  $\theta_{pq}$ ,  $W^2$ , acceptance matching, radiative correction, etc). This dependence on multiple parameters is summarized by writing:

$$R_c = R_c(\vec{f}). \quad (3.11)$$

All of the terms in Eqn 3.8 are understood to have a  $Q^2$  dependence.

The standard propagation of errors formula is applied:

$$(\delta G_M^n)^2 = \left(\frac{\partial G_M^n}{\partial \sigma_p}\right)^2 (\delta \sigma_p)^2 + \left(\frac{\partial G_M^n}{\partial G_E^n}\right)^2 (\delta G_E^n)^2 + \sum_i \left(\frac{\partial G_M^n}{\partial f_i}\right)^2 (\delta f_i)^2. \quad (3.12)$$

The errors are taken to be uncorrelated, so terms of the form  $\frac{\partial^2 G_M^n}{\partial a \partial b}$  are not considered.

### 3.2.1 Systematic error due to uncertainty in Proton cross-section

Consider the  $\sigma_p$  term in Eqn 3.12:

$$(\delta G_M^n)_p = \frac{\partial G_M^n}{\partial \sigma_p} \delta \sigma_p. \quad (3.13)$$

We have:

$$\frac{\partial G_M^n}{\partial \sigma_p} = \frac{1}{2} \frac{1}{G_M^n} R_c \frac{\epsilon}{\tau} \quad (3.14)$$

and the fractional error on  $G_M^n$  due to uncertainty in the proton reduced cross-section is:

$$\frac{(\delta G_M^n)_p}{G_M^n} = \frac{1}{2} \frac{1}{G_{M,n}^2} R_c \frac{\epsilon}{\tau} \delta \sigma_p \quad (3.15)$$

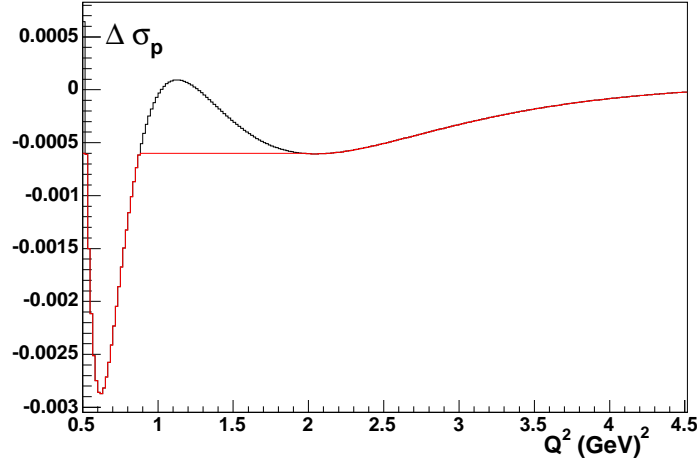


Figure 3.4: The difference in the proton reduced cross section  $\sigma_p$ , as determined from the Bosted and Arrington parameterizations. The black curve shows  $\sigma_p^{arrington} - \sigma_p^{bosted}$ . The red curve shows the value of  $\delta$  used to estimate the systematic error.

To estimate this contribution, we assume:  $G_M^n \approx \mu_n G_D$ , take  $R_c$  from the measurement, and take  $\delta\sigma_p$  to be the difference in  $\sigma_p$  as determined by the Arrington [50] and Bosted [51] parameterizations:

$$\delta\sigma_p = \sigma_p^{arrington} - \sigma_p^{bosted} \quad (3.16)$$

The difference in these two parameterizations is shown by the black curve in Fig 3.4. The parameterizations cross at  $Q^2 \approx 1.1$  GeV/c, giving a value of  $\delta = 0$ . To avoid this unrealistic estimate of  $\delta$ , a value of  $\delta = -0.0006$  is used in the region of the crossing. This substitution is shown by the red curve in Fig 3.4.

Using the  $\delta\sigma_p$  values shown in Fig 3.4 in Eqn 3.15, the estimated systematic uncertainty on  $G_M^n$  caused by the uncertainty in the proton reduced cross-section can be determined. The relative size of the difference in the two parameterizations is shown in Fig 3.5. The fractional uncertainty on  $G_M^n$ , expressed as a percentage, is shown in Fig 3.6 for the 4.2 GeV data, and in Fig 3.7 for the 2.6 GeV data.

### 3.2.2 Systematic error due to uncertainty in $G_E^n$

Consider the  $G_E^n$  term in Eqn 3.12:

$$(\delta G_M^n)_E = \frac{\partial G_M^n}{\partial G_E^n} \delta G_E^n \quad (3.17)$$

We have:

$$\frac{\partial G_M^n}{\partial G_E^n} = \frac{G_E^n}{G_M^n} \frac{\epsilon}{\tau} \quad (3.18)$$

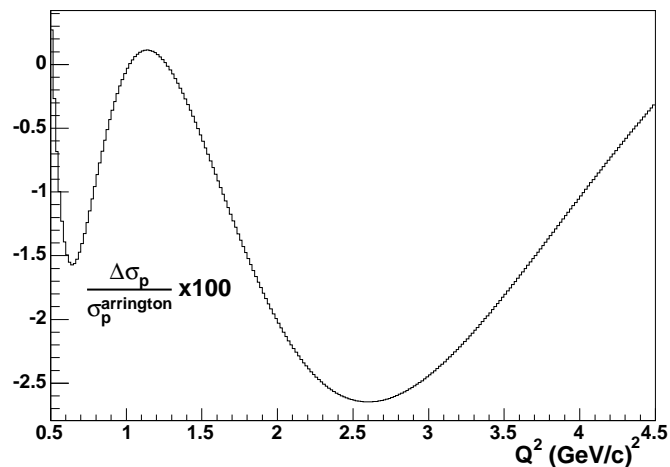


Figure 3.5: The relative difference in the proton reduced cross section  $\sigma_p$ , as determined from the Bosted and Arrington parameterizations, scaled to the Arrington result.

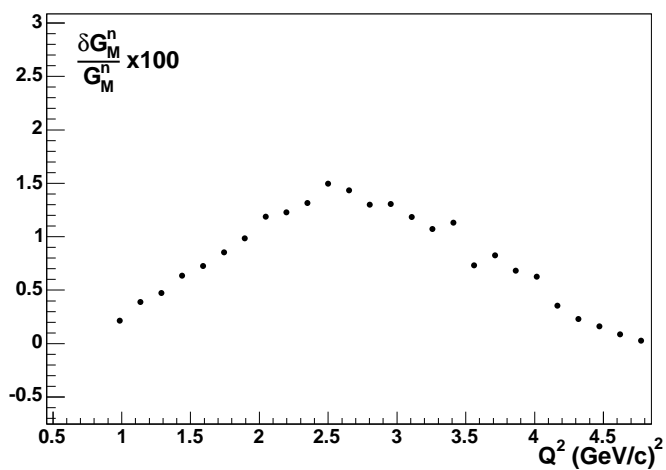


Figure 3.6: The systematic error on  $G_M^n$  due to uncertainties in the reduced proton cross-section, expressed as a percent error, for the 4.2 GeV beam energy.

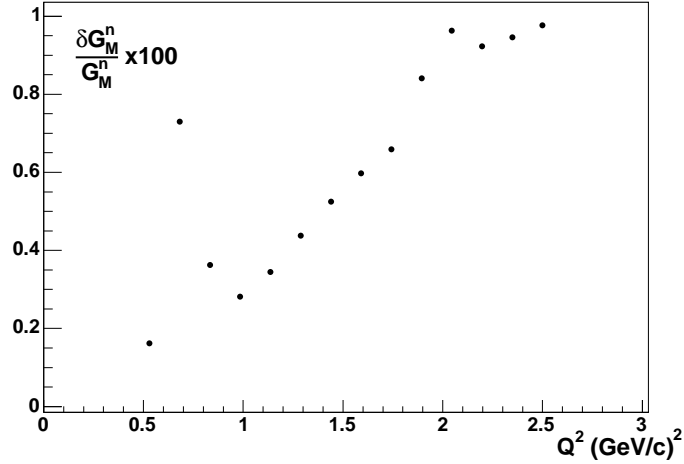


Figure 3.7: The systematic error on  $G_M^n$  due to uncertainties in the reduced proton cross-section, expressed as a percent error, for the 2.6 GeV beam energy.

and the fractional error on  $G_M^n$  due to uncertainty in the neutron electric form factor is:

$$\frac{(\delta G_M^n)_E}{G_M^n} = \frac{G_E^n}{G_{M,n}^2} \frac{\epsilon}{\tau} \delta G_E^n \quad (3.19)$$

To estimate this contribution, we assume  $G_M^n \approx \mu_N G_D$ , and use the Galster parametrization for  $G_E^n$ :

$$G_E^n \approx \frac{\mu_n \tau G_D}{1 + \eta \tau} \quad (3.20)$$

where  $\eta = 5.6$ . With this, we have:

$$\frac{\delta G_M^n}{G_M^n} = \frac{\epsilon}{\mu_n (1 + \eta \tau) G_D} \delta G_E^n \quad (3.21)$$

We take  $\delta G_E^n$  to be the difference between the Galster parametrization and the Lomon [9] model prediction:

$$\delta G_E^n = G_{E,\text{galster}}^n - G_{E,\text{lomon}}^n \quad (3.22)$$

The Galster and Lomon results are shown in Fig 3.8, along with the high- $Q^2$   $G_E^n$  data of Lung [24] and Schiavilla and Sick [52]. The two parameterizations cross at  $Q^2 \approx 0.7$  GeV/c. This would give the unrealistic result of  $\delta G_M^n = 0$  at the crossing point, and predict unreasonably small errors in the neighborhood of the crossing. To avoid this,  $\delta G_E^n$  in the region  $0.6 \leq Q^2 \leq 1.2$  GeV/c was assigned a value of 0.0036, equal to the value of  $\delta G_E^n$  at  $Q^2 = 1.2$  GeV/c.

The estimated systematic uncertainty on  $G_M^n$  caused by uncertainty in  $G_E^n$  is shown in Fig 3.9 for the 4.2 GeV data, and in Fig 3.10 for the 2.6 GeV data.

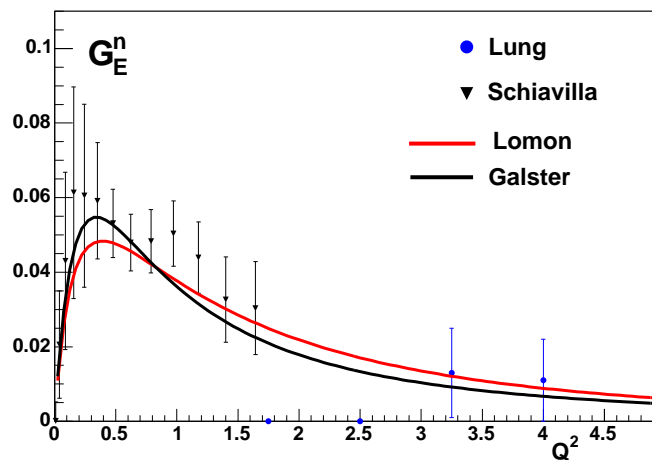


Figure 3.8: The Galster parametrization of  $G_E^n$ , along with the Lomon [9] model prediction and data from Lung [24] and Schiavilla [52].

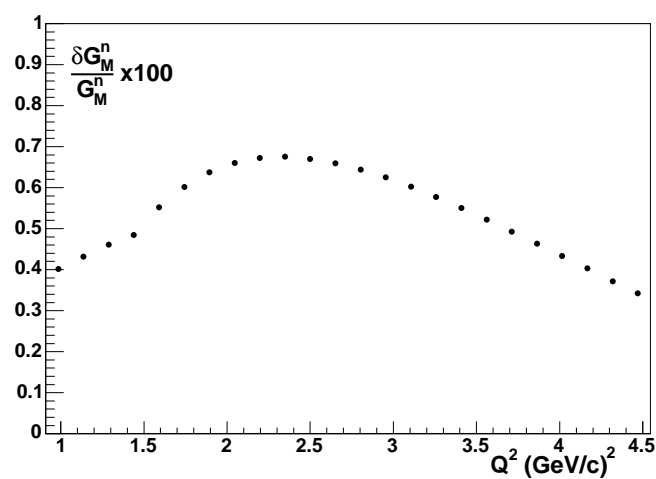


Figure 3.9: The estimated systematic error on  $G_M^n$  due to uncertainties in  $G_E^n$ , expressed as a percent error, for the 4.2 GeV data.

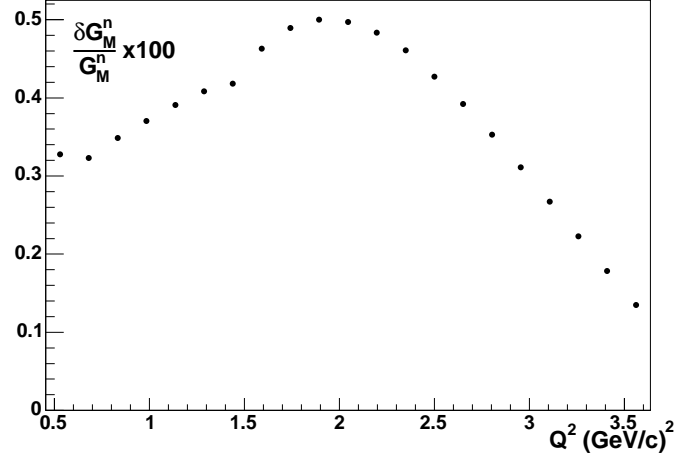


Figure 3.10: The estimated systematic error on  $G_M^n$  due to uncertainties in  $G_E^n$ , expressed as a percent error, for the 2.6 GeV data.

### 3.2.3 Other sources of systematic error

Consider the  $R_c(\vec{f})$  term in Eqn 3.12. The uncertainty in  $G_M^n$  due to the set of parameters  $\vec{f}$  is:

$$(\delta G_M^n)_R^2 = \sum_i \left( \frac{\partial G_M^n}{\partial f_i} \right)^2 (\delta f_i)^2 \quad (3.23)$$

$$= \sum_i \left( \frac{\partial G_M^n}{\partial R_c} \frac{\partial R_c}{\partial f_i} \right)^2 (\delta f_i)^2 \quad (3.24)$$

$$= \sum_i \left( \frac{\sigma_p \epsilon}{2G_M^n \tau} \frac{\partial R_c}{\partial f_i} \right)^2 (\delta f_i)^2 \quad (3.25)$$

The functional dependence of  $R_c$  on some of the  $f_i$  is not always clear, so we approximate:

$$\frac{\partial R_c}{\partial f_i} \approx \frac{\delta R_c}{\delta f_i} \quad (3.26)$$

and obtain

$$\left( \frac{\delta G_M^n}{G_M^n} \right)^2 = \sum_i \left( \frac{\sigma_p \epsilon}{2\mu_n^2 G_D^2 \tau} \right)^2 (\delta R_c)_i^2 \quad (3.27)$$

where we have used the approximation  $G_M^n \approx \mu_n G_D$  in the denominator on the right hand side, and  $(\delta R_c)_i$  is the variation in  $R_c$  induced by varying parameter  $f_i$ .

#### 3.2.3.1 Accidental background in neutron detection

The presence of accidental background in the  $ep \rightarrow e\pi^+(n)$  reaction was investigated by re-analyzing the calibration data. The assumption was made that the accidental

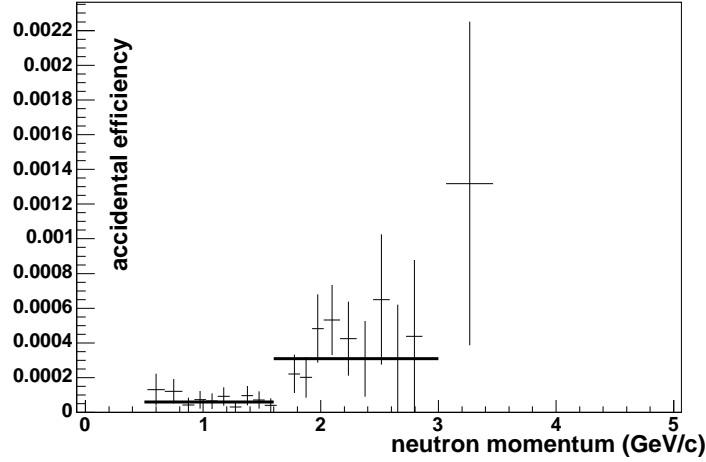


Figure 3.11: Accidental contribution to the neutron detection efficiency in the SC, for the 4.2 GeV data. The horizontal lines are fits of a constant to the data

background was the same in each of the six sectors. On an event-by-event basis, the reconstructed neutron 3-momentum was rotated around the beam-axis by a random multiple of  $60^\circ$  into some sector other than the original sector. The rest of the neutron detection efficiency analysis was carried out as usual. Any non-zero efficiency measured by this procedure must be due to accidental background. It was found that for the EC, no accidental efficiency was observed. For the SC, the accidental efficiencies are shown in Fig 3.11 and Fig 3.12 for the 4.2 GeV and 2.6 GeV data respectively.

The accidental efficiency was fitted with a constant

$$\eta_{\text{accidental}} = 7.5 \times 10^{-5} \quad (3.28)$$

for the 2.6 GeV case, and

$$\eta_{\text{accidental}} = \begin{cases} 6.05 \times 10^{-5} & p < 1.6 \text{ GeV}/c \\ 3.1 \times 10^{-4} & p > 1.6 \text{ GeV}/c \end{cases} \quad (3.29)$$

for the 4.2 GeV case. The accidental contribution to the efficiency is treated as a systematic error, using

$$\delta R_c = R_0 \left( \frac{1}{\eta} - \frac{1}{\eta - \eta'} \right) \quad (3.30)$$

where  $R_0$  is the measured ratio with no neutron detection efficiency applied,  $\eta$  is the normal neutron detection efficiency, and  $\eta'$  is the estimated accidental efficiency given above. All of these quantities have an understood  $Q^2$  dependence. This expression for  $\delta R_c$  is inserted into Eqn 3.27. The resulting systematic error is shown in Fig 3.13 for the 4.2 GeV data and Fig 3.14 for the 2.6 GeV data.

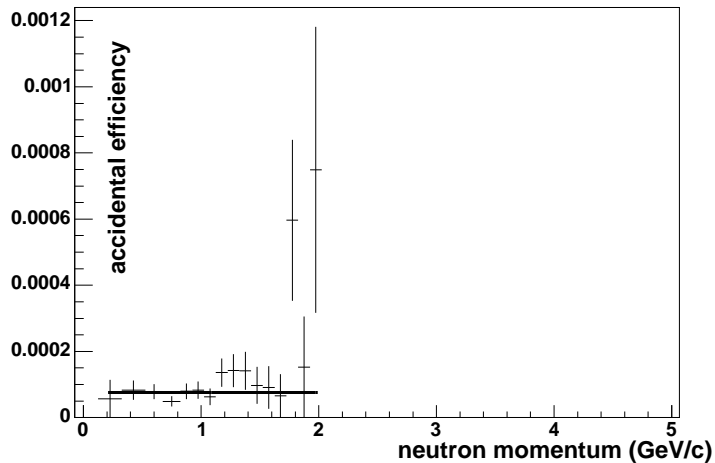


Figure 3.12: Accidental contribution to the neutron detection efficiency in the SC, for the 2.6 GeV data. The horizontal line is a fit of a constant to the data.

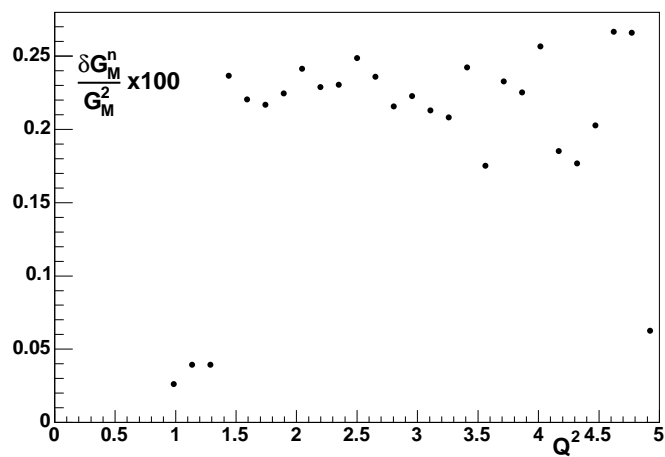


Figure 3.13: Fractional systematic error on  $G_M^n$  due to accidental background in the SC neutron detection efficiency, for the 4.2 GeV data.

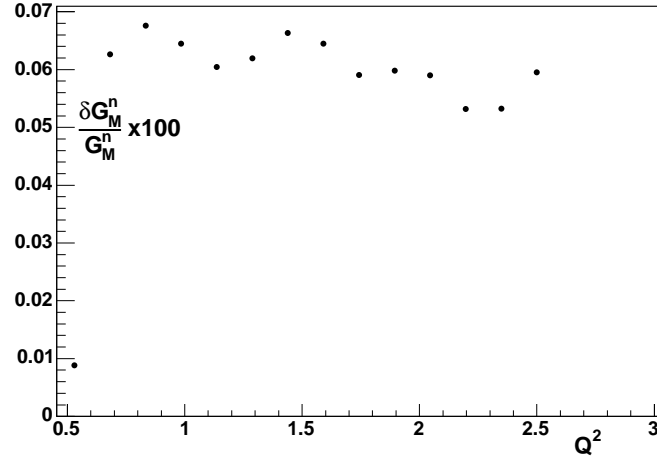


Figure 3.14: Fractional systematic error on  $G_M^n$  due to accidental background in the SC neutron detection efficiency, for the 2.6 GeV data.

### 3.2.3.2 Missing mass cut in neutron detection efficiency measurement

The neutron missing mass peak observed in the  $ep \rightarrow e\pi^+(n)$  reaction does not show a Gaussian shape, but has a tail toward higher missing mass. The upper end of the missing mass cut was set to avoid this region. The tail may be caused by detector resolution effects (mismeasurement of the electron or  $\pi^+$  momentum will generate an incorrect value for the missing mass), radiative effects, or the presence of misidentified non- $e\pi^+n$  states contaminating the signal. The GSIM Monte Carlo package was used to investigate the presence of background channels contributing to the neutron missing mass peak. The CELEG event generator was used, with all resonance channels active. The gpp package was used for resolution smearing according to two prescriptions: the default setting, and smearing the Distance Of Closest Approach (DOCA) in drift chambers regions (R1,R2,R3) by a factor of (2.0,2.5,3.0) relative to the default values, respectively. Previous analyses [53] have indicated that the default DOCA smearing performed by gpp is inadequate and the values listed give a better agreement between real data and simulation. The smeared GSIM events are then cooked and analyzed using the same procedure as described for the real data. The results of the default DOCA-smearing setting are shown in Fig 3.16 and the extra-smearing results are shown in Fig 3.17.

Neither of the two DOCA settings seems to get the missing mass distribution quite right. A detailed study of which GSIM/GPP settings optimize the simulation performance for this reaction channel was not made. From the simulation results presented, it appears that non- $e\pi^+n$  channels do not contribute a significant background in the  $0.9\text{GeV} \leq MM \leq 1.0\text{GeV}$  region. The skewing of the observed missing mass spectrum appears to be due to detector resolution effects. An investigation was

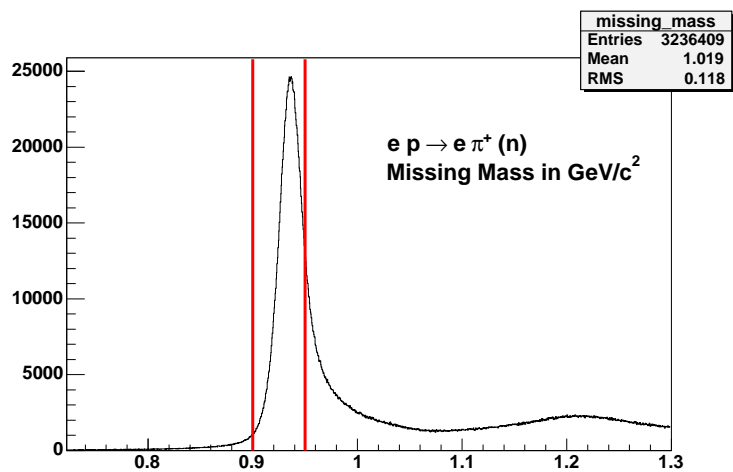


Figure 3.15: The observed missing mass distribution in the  $ep \rightarrow e\pi^+(n)$  reaction. The red lines show the cut used in the neutron detection efficiency analysis.

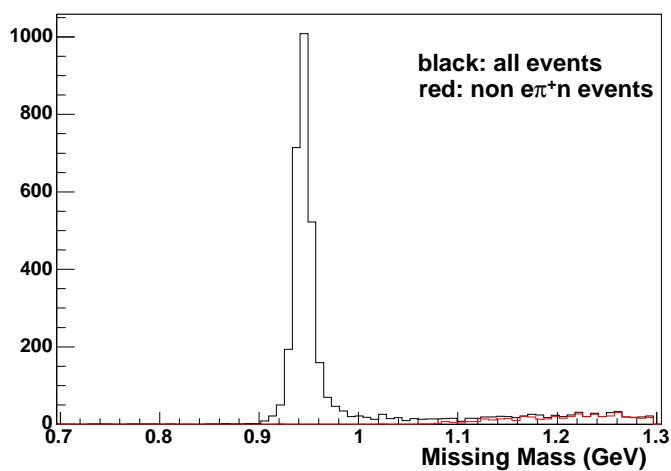


Figure 3.16: Missing mass spectrum in the  $ep \rightarrow e\pi^+(n)$  reaction, generated from CELEG/GSIM, with default DOCA smearing.

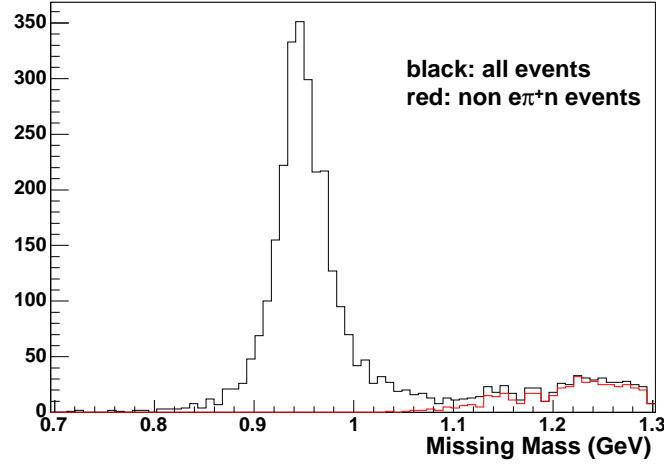


Figure 3.17: Missing mass spectrum in the  $ep \rightarrow e\pi^+(n)$  reaction, generated from CELEG/GSIM, with extra DOCA smearing factor (2.0,2.5,3.0) in (R1,R2,R3).

made of how far the upper limit of the missing mass cut can be pushed before the measured efficiency begins to degrade due to the angle between the reconstructed and real neutron 3-momentum becoming too large. The missing mass peak was sliced into several sections, and the EC neutron detection efficiency was measured for each section, using the 4.2 GeV data. The results are shown in Figs 3.18, 3.19, 3.20.

Consistent results were obtained for missing mass slices in the 0.9 to 0.96 range, but beyond that, the performance began to degrade. To assess the effect of changes in the location of the upper bound of the missing mass cut on  $G_M^n$ , Eqn 3.27 was used with:

$$\delta R_c = R_0 \frac{1}{2} \left( \frac{1}{\eta_{94}} - \frac{1}{\eta_{96}} \right) \quad (3.31)$$

where  $\eta_{94}$  is the efficiency evaluated using the missing mass region  $0.9 < MM < 0.94$ , and  $\eta_{96}$  is the efficiency evaluated using the missing mass region  $0.9 < MM < 0.96$ . The cuts were chosen to bracket the cut value of 0.95 used in the analysis. The upper value of 0.96 was chosen as the largest value of the cut at which sensible efficiency results are obtained. Since the shape of the efficiency curve doesn't vary much for cut values below 0.95, a value of 0.94 was chosen for symmetry. The resulting error estimates are shown in Fig 3.21 for the 4.2 GeV data and Fig 3.22 for the 2.6 GeV data.

### 3.2.3.3 Distance cut in EC calibration neutron selection

In the neutron detection efficiency calibration, a cut was applied requiring that any neutron from the  $ep \rightarrow e\pi^+(n)$  reaction found in the EC satisfy the cut  $\Delta R < 60$  cm where  $\Delta R$  is the distance between the observed hit location and the hit location

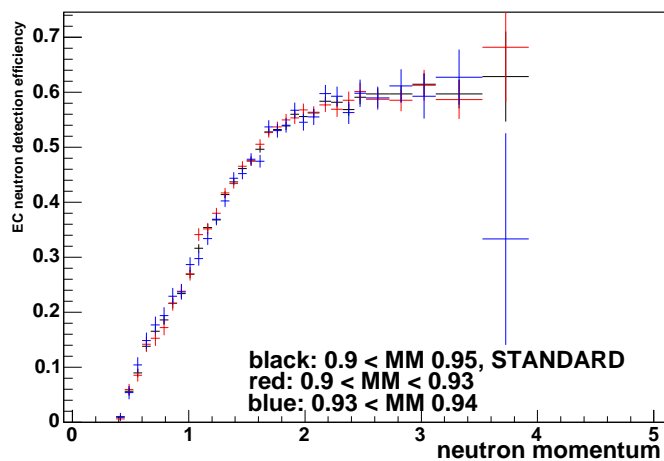


Figure 3.18: The EC neutron detection efficiency in the 4.2 GeV data, for various slices of the neutron missing mass peak. The black points show the standard cut,  $0.9 < MM < 0.95$ .

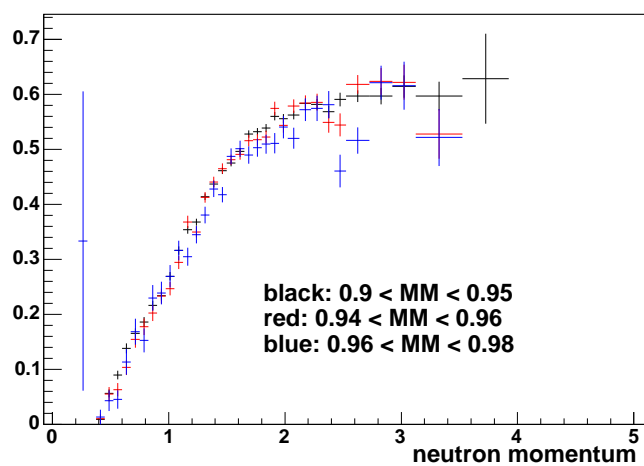


Figure 3.19: The EC neutron detection efficiency in the 4.2 GeV data, for various slices of the neutron missing mass peak. The black points show the standard cut,  $0.9 < MM < 0.95$ .

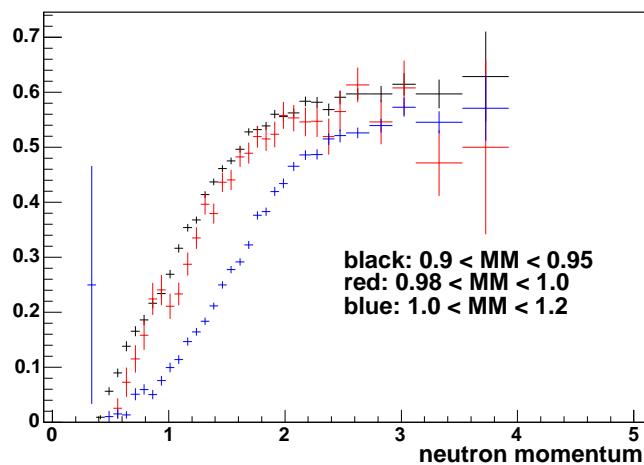


Figure 3.20: The EC neutron detection efficiency in the 4.2 GeV data, for various slices of the neutron missing mass peak. The black points show the standard cut,  $0.9 < MM < 0.95$ .

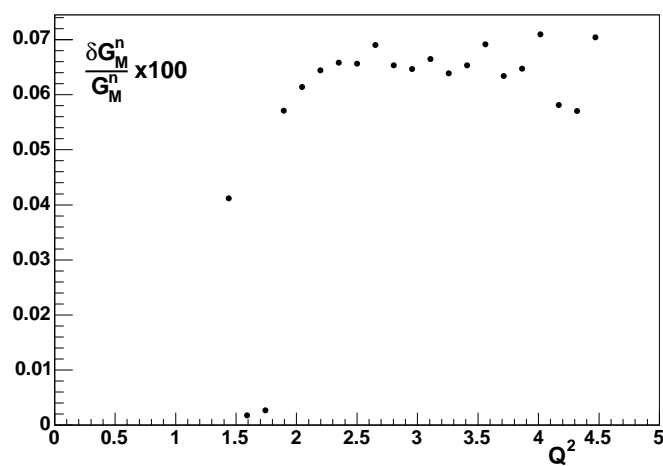


Figure 3.21: Estimated fractional systematic error on  $G_M^n$  due to the selection of the upper edge of the missing mass cut in the  $ep \rightarrow e\pi^+(n)$  reaction, for the 4.2 GeV EC data.

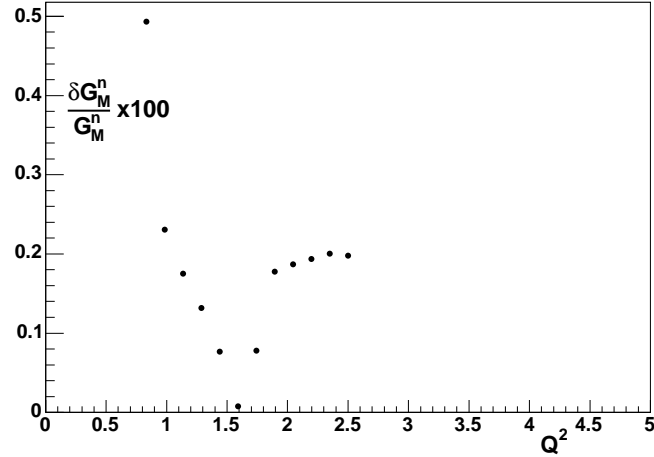


Figure 3.22: Estimated fractional systematic error on  $G_M^n$  due to the selection of the upper edge of the missing mass cut in the  $ep \rightarrow e\pi^+(n)$  reaction, for the 2.6 GeV EC data.

expected from the neutron missing momentum. The accuracy of the position reconstruction in the EC is estimated to be  $\approx 0.5$  degrees [54]. A value of 525 cm was taken as a typical target to calorimeter distance, giving a position resolution of  $\approx 4.5$  cm. The fractional uncertainty in  $G_M^n$  due to this cut is estimated from Eqn 3.27 with:

$$\delta R = \frac{1}{2} R_0 \left( \frac{1}{\eta_1} - \frac{1}{\eta_2} \right) \quad (3.32)$$

where  $\eta_1$  is the global EC efficiency evaluated with a  $\Delta R < 55.5$  cm cut, and  $\eta_2$  is the global EC efficiency evaluated with a  $\Delta R < 64.5$  cm cut. The global efficiencies for the two  $\Delta R$  selections are shown in Fig 3.23 and 3.24 for the 4.2 GeV and 2.6 GeV data respectively. The estimated systematic errors for the 4.2 and 2.6 GeV data are shown in Fig 3.25 and 3.26.

### 3.2.3.4 EC neutron detection efficiency parametrization

The neutron detection efficiency in the EC is parametrized by a third order polynomial at low neutron momentum, and a flat line at high momentum, as described in Section 2.3.4.2. To investigate the sensitivity to the details of this fit, the fitting procedure was modified by switching off the  $p^3$  term in the fitting function. The standard fit applied to the global efficiency data is shown in Fig 3.27, along with the modified fit. The systematic error is estimated by using Eqn 3.27 with:

$$\delta R = |R_{standard} - R_{modified}| \quad (3.33)$$

The estimated systematic error due to the parametrization of the EC neutron detection efficiency is shown in Fig 3.28 for the 4.2 GeV data. Based on the results

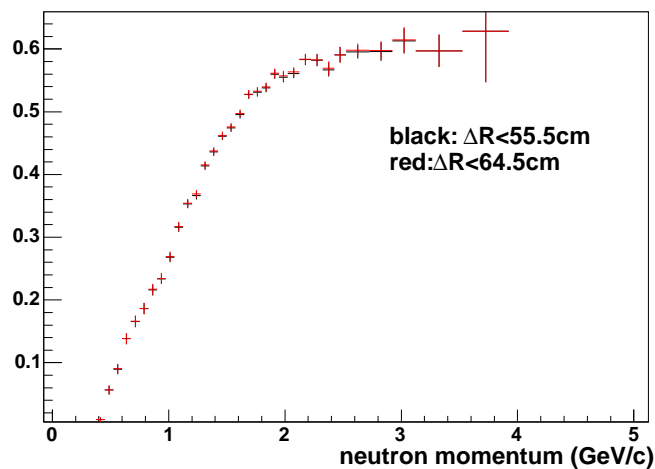


Figure 3.23: Comparison of EC neutron detection efficiency, integrated over all sectors, for two choices of the  $\Delta R$  cut, from the 4.2 GeV data.

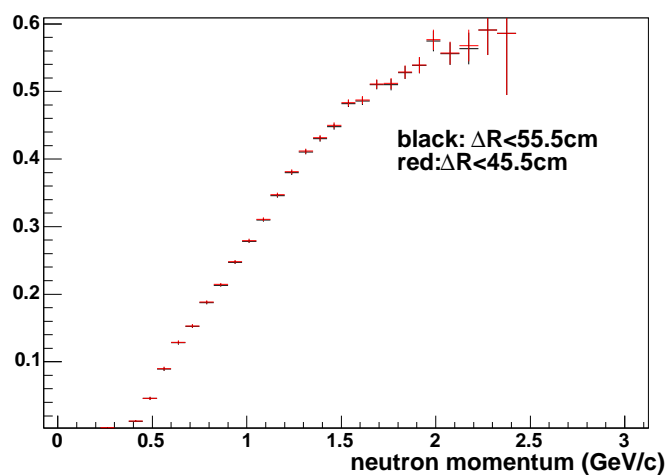


Figure 3.24: Comparison of EC neutron detection efficiency, integrated over all sectors, for two choices of the  $\Delta R$  cut, from the 2.6 GeV data.

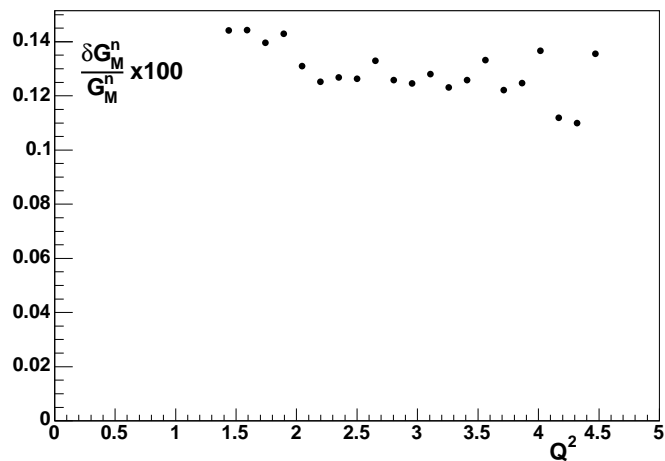


Figure 3.25: Estimated fractional systematic error on  $G_M^n$  due to the choice of  $\Delta R$  cuts in EC neutron selection in the calibration reaction in the 4.2 GeV data.

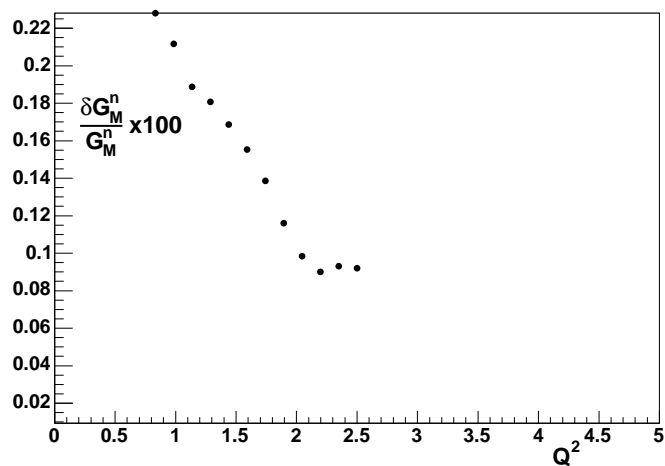


Figure 3.26: Estimated fractional systematic error on  $G_M^n$  due to the choice of  $\Delta R$  cuts in EC neutron selection in the calibration reaction in the 2.6 GeV data.

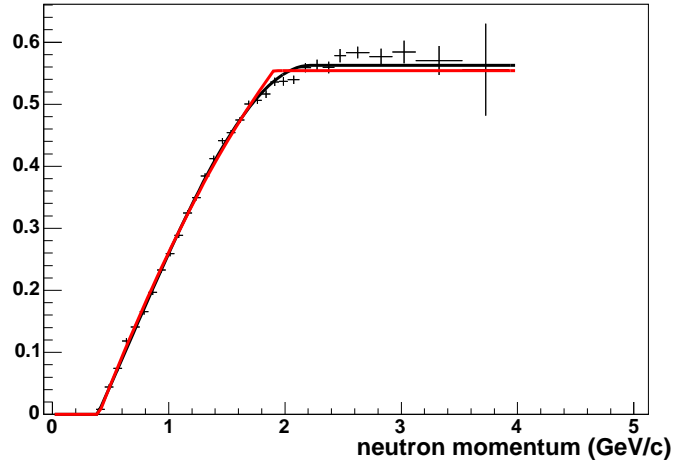


Figure 3.27: The black curve shows the global EC neutron detection efficiency data, fitted by the third order standard fit. The red curve shows the modified fit, obtained by switching off the  $p^3$  term.

shown in the figure, a flat systematic uncertainty of 1.0% is assigned at all  $Q^2$  values for the 4.2 GeV data. A similar procedure was carried out for the 2.6 GeV data. The comparison of the standard and modified fits is shown in Fig 3.29. The systematic error induced by varying the fit is shown in Fig 3.30. Based on this figure, a flat systematic uncertainty of 1.5% was assigned at all values of  $Q^2$  for the 2.6 GeV data.

In the standard fitting procedure, the point at which the efficiency function switches from a third-order polynomial to a constant is left as a parameter of the fit. To test the sensitivity to the selection of the location of the switching point, a series of fits was performed where the location of the switching point was fixed. For reasonable values of the switching point (between 1.9 and 2.4 GeV/c in neutron momentum), it was found that the value of the fit for momenta *below* the switching point was essentially unchanged. For momenta above the switching point, variations in efficiency of up to 2% of the standard value could be produced. As  $G_M^n$  varies with the square root of the efficiency, a systematic error of 1% was assigned for  $Q^2$  values greater than 2 (GeV/c)<sup>2</sup>. This error was treated as an independent error.

### 3.2.3.5 SC neutron detection efficiency parametrization

The neutron detection efficiency in the SC is parametrized by a third order polynomial at low neutron momentum, and a flat line at higher momentum, as described in Sec 2.3.5.1. To investigate the sensitivity to the details of this fit, the fitting procedure was modified by switching off the  $p^3$  and  $p^2$  terms in the fit. The standard fit applied to the global SC data is shown in Fig 3.31, and the modified fit is shown in Fig 3.32.

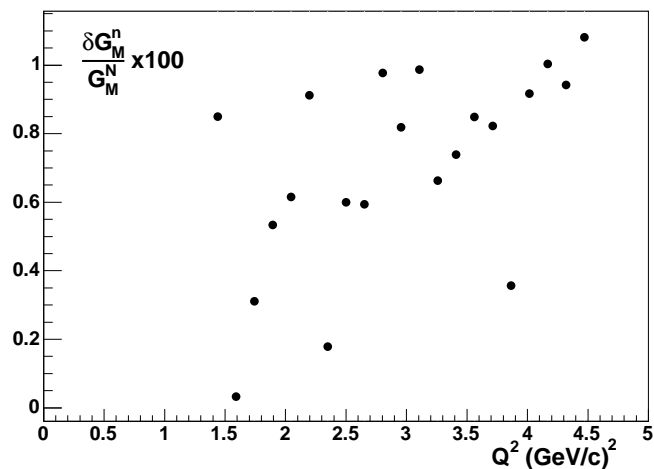


Figure 3.28: The estimated fractional systematic error on  $G_M^n$ , due to the parametrization of the EC neutron detection efficiency.

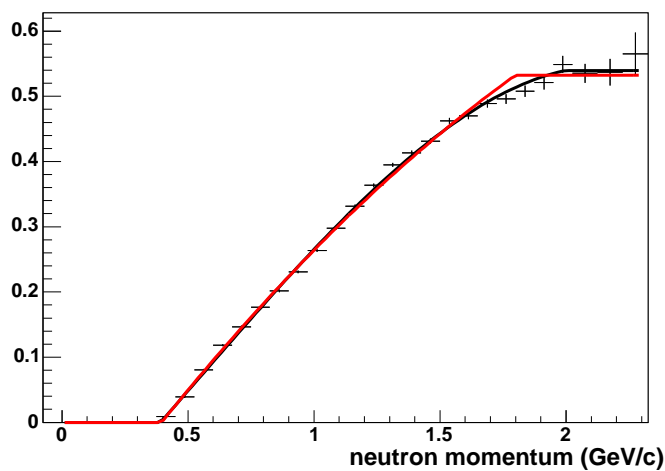


Figure 3.29: The black curve shows the 2.6 GeV global EC neutron detection efficiency data, fitted by the third order standard fit. The red curve shows the modified fit, obtained by switching off the  $p^3$  term.

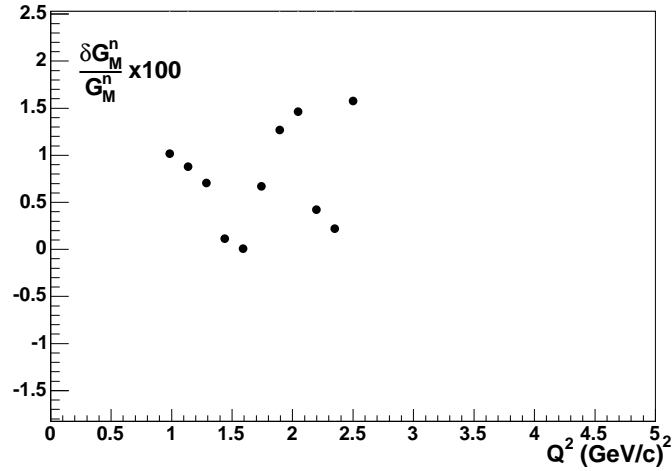


Figure 3.30: The estimated fractional systematic error on  $G_M^n$ , due to the parametrization of the EC neutron detection efficiency.

The systematic error is estimated by using Eqn 3.27 using:

$$\delta R = |R_{standard} - R_{modified}| \quad (3.34)$$

The estimated systematic error due to the parametrization of the SC neutron detection efficiency is shown in Fig 3.33. Based on this plot, a flat systematic error of 2% was assigned at all values of  $Q^2$  for the both the 4.2 GeV data and the 2.6 GeV data (results similar to Fig 3.33 were obtained for the 2.6 GeV data).

In the standard fitting procedure, the point at which the efficiency function switches from a third-order polynomial to a constant is left as a parameter of the fit. To test the sensitivity to the selection of the location of the switching point, a series of fits was performed where the location of the switching point was fixed. For reasonable values of the switching point (between 1.4 and 1.7 GeV/c in neutron momentum), it was found that the value of the fit for momenta *below* the switching point was essentially unchanged. For momenta above the switching point, variations in efficiency of up to 3.5% of the standard value could be produced. As  $G_M^n$  varies with the square root of the efficiency, a systematic error of 1.74% was assigned for  $Q^2$  values greater than 1 (GeV/c)<sup>2</sup>. This error was treated as an independent error.

### 3.2.3.6 Proton detection efficiency

A comparison was made of the momentum-averaged proton detection efficiency on SC paddles which were used in both the 4.2 GeV and 2.6 GeV analyses. The relative difference in efficiency on each paddle is shown in Fig 3.34. From the scattered points in Fig 3.34, a systematic uncertainty of 0.75% was assigned to the proton detection

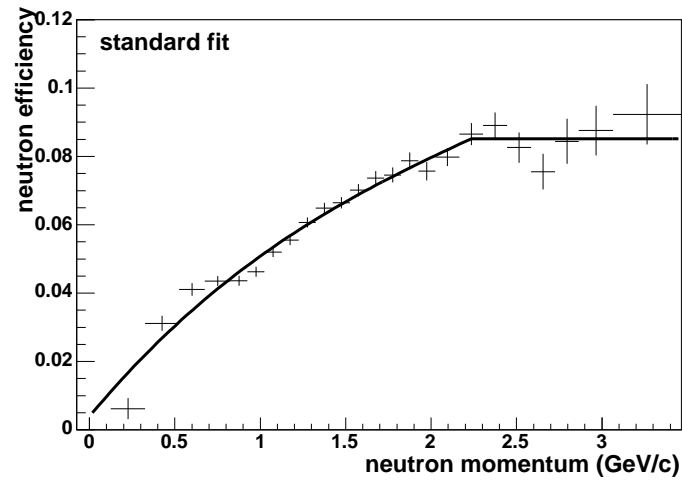


Figure 3.31: The global SC neutron detection efficiency data, fitted by the third order standard fit.

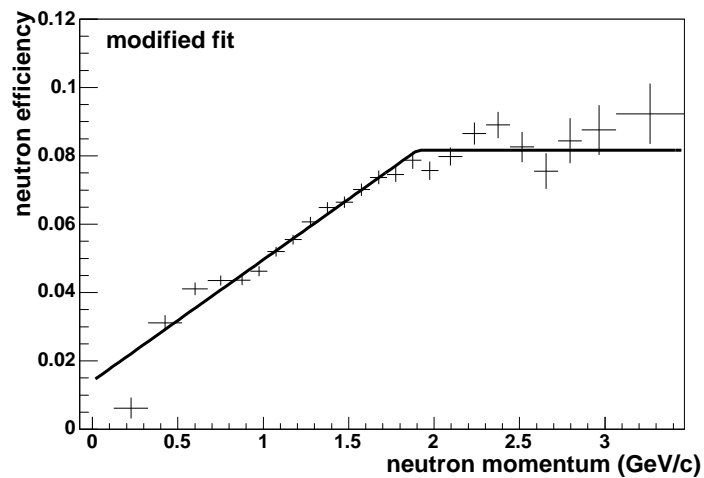


Figure 3.32: The global SC neutron detection efficiency data, fitted by the first order modified fit.

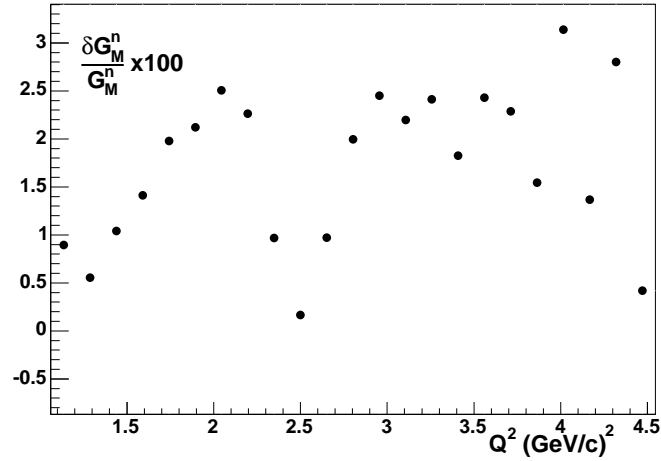


Figure 3.33: The estimated fractional systematic error on  $G_M^n$ , due to the parametrization of the SC neutron detection efficiency.

efficiency. The systematic error on  $G_M^n$  was determined from Eqn 3.27 using:

$$\delta R_c = \delta \eta_p R_0 \quad (3.35)$$

where  $\delta \eta_p = 0.0075$  and  $R_0$  is the measured ratio with no proton detection efficiency applied. The systematic error is shown in Fig 3.35 for the 4.2 GeV data, and in Fig 3.36 for the 2.6 GeV data.

### 3.2.3.7 Accidental background in quasi-elastic events

The presence of accidental background in the quasi-elastic channel was investigated using the same technique applied in the neutron detection efficiency case. The expected neutron 3-momentum vector was rotated about the beam-axis by a multiple of  $60^\circ$ , placing the expected hit location in a sector where the neutron ought not to have been seen. Any neutral hits found after this rotation were attributed to accidental background. The accidental rate was assumed to be the same in all sectors.

The result of the procedure was that no significant background was found. Any neutrals found after the rotation were rejected by some combination of the cuts on energy deposited,  $W^2$  or  $\theta_{pq}$ . Fig 3.37 shows the  $\theta_{pq}$  spectrum for rotated quasi-elastic events in the SC. Similar results were obtained for both beam energies, in the EC and the SC.

### 3.2.3.8 Acceptance/Fermi loss correction

To test the sensitivity of the ratio measurement to the details of the Fermi loss correction procedure, the shape of the nucleon momentum distribution was altered.

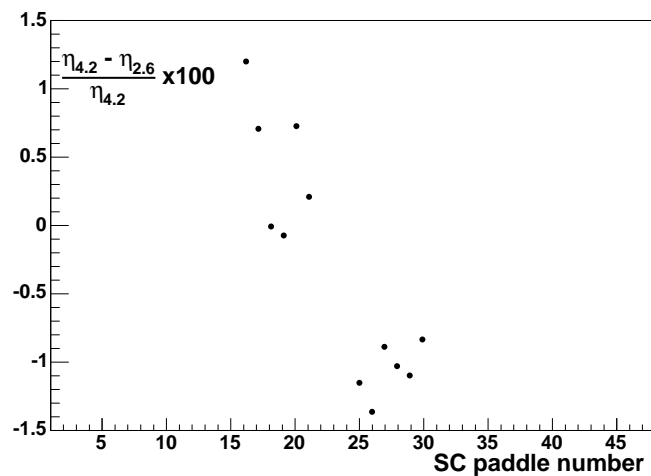


Figure 3.34: The relative difference in the average proton detection efficiency in the 4.2 GeV and 2.6 GeV data sets.

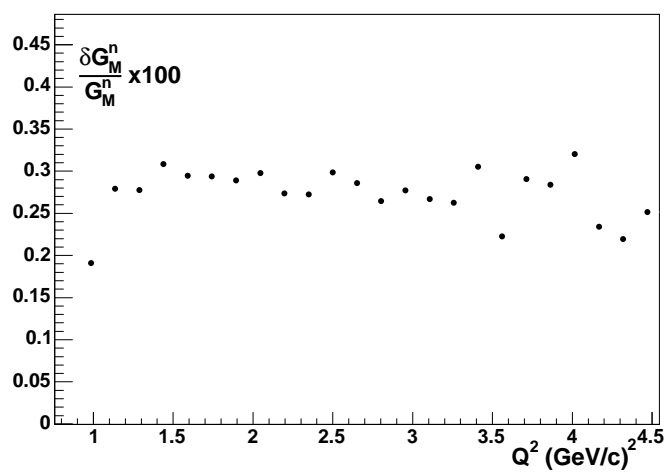


Figure 3.35: Estimated fractional systematic error on  $G_M^n$  due to uncertainties in the proton efficiency correction in the 4.2 GeV data set.

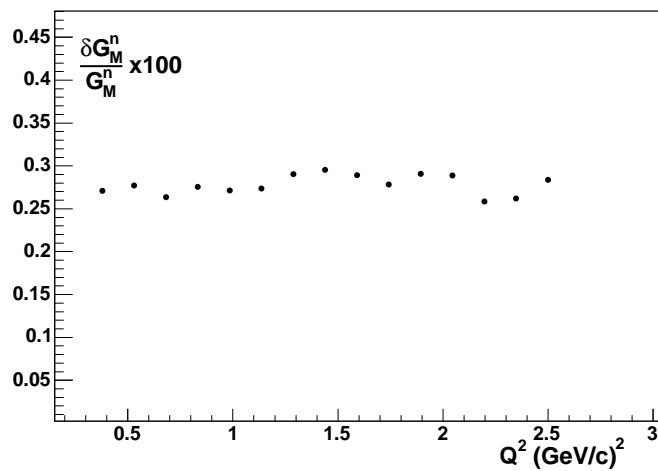


Figure 3.36: Estimated fractional systematic error on  $G_M^n$  due to uncertainties in the proton efficiency correction in the 2.6 GeV data set.

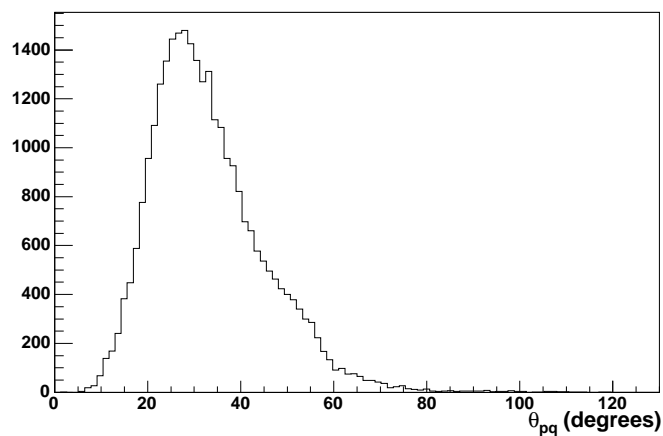


Figure 3.37:  $\theta_{pq}$  spectrum for quasi-elastic e-n candidate events in the SC, *after* the expected neutron momentum vector was rotated about the beam axis into an adjacent sector.

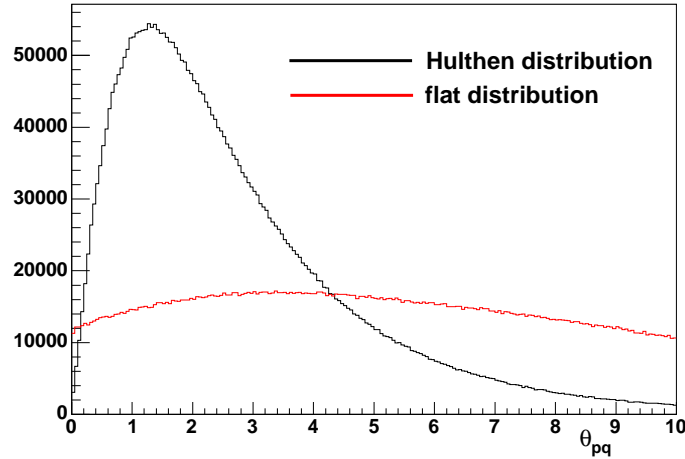


Figure 3.38: A comparison of the  $\theta_{pq}$  distributions obtained from the deuteron model, for the Hulthen (black line) and flat (red line) nucleon momentum distributions.

The most severe alteration that was tested replaced the Hulthen distribution shown in Fig 2.46 with a flat distribution that assigned the nucleon an equal probability of being found with any momentum between 0 and  $600MeV/c$ . The  $\theta_{pq}$  distributions obtained from the Hulthen and flat nucleon momentum distributions are shown in Fig 3.38. The shape of the  $\theta_{pq}$  distribution observed for e-p quasi-elastics was seen to be consistent with the event-generator prediction, so the comparison to the flat distribution should be seen as an extreme case.

The shape of the loss fraction curves for neutrons and protons (the standard loss fraction curves were shown in Fig 2.55 and 2.56) were found to have a significant dependence on the shape of the nucleon momentum distribution used. A comparison of the Hulthen and flat distribution results is shown in Fig 3.39 for SC neutrons in the 4.2 GeV data, and in Fig 3.40 for protons in the 4.2 GeV data. The correction to the ratio was found to have only a weak dependence on the shape of the nucleon momentum distribution, as shown in Fig 3.41 for the 4.2 GeV SC neutron data. The fractional difference in the correction factor obtained from the two different momentum distributions is shown in Fig 3.42

Other variations, less pathological than the flat distribution, on the shape of the nucleon momentum distribution were considered, generally giving variations in the correction factor less extreme than those obtained from the flat distribution. Based on these results, a systematic uncertainty of 0.25% is assigned to the correction factor in those  $Q^2$  regions where the correction is less than 5%, and an uncertainty of 1.5% is assigned when the correction is larger than 5%. Using

$$\delta R = \delta f R \quad (3.36)$$

where  $\delta f = 0.005$  or  $0.015$  depending on  $Q^2$ , in Eqn 3.27 gives the systematic error

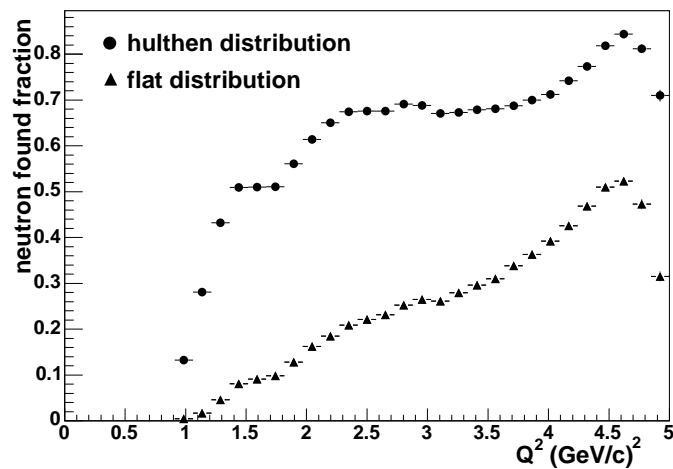


Figure 3.39: A comparison of the neutron loss fraction obtained from the Hulthen and flat distributions for SC neutrons in the 4.2 GeV data set.

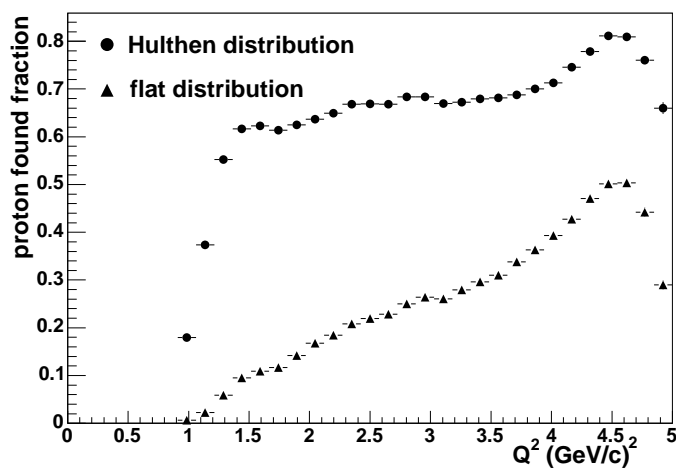


Figure 3.40: A comparison of the proton loss fraction obtained from the Hulthen and flat distributions in the 4.2 GeV data set.

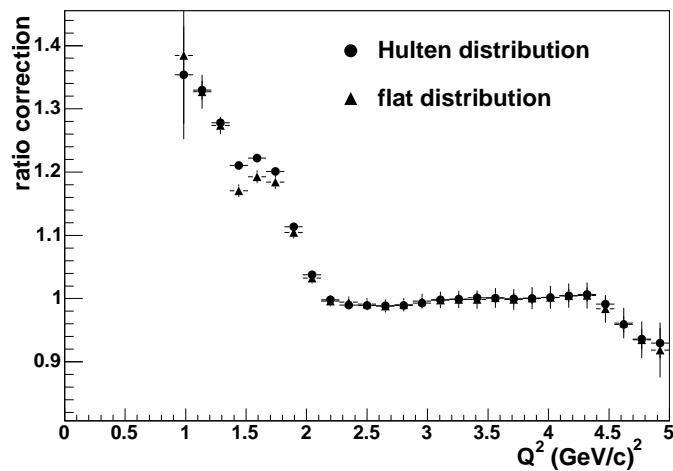


Figure 3.41: A comparison of the ratio correction factor obtained from the Hulthen and flat nucleon momentum distributions in the 4.2 GeV data.

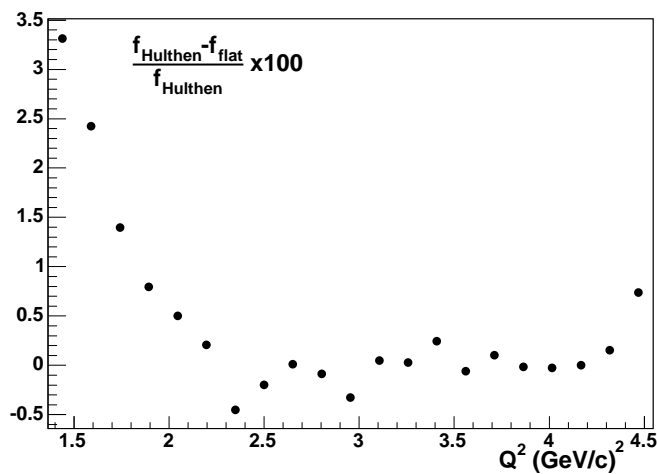


Figure 3.42: The fractional difference in the ratio correction factor obtained from the Hulthen and flat nucleon momentum distributions.

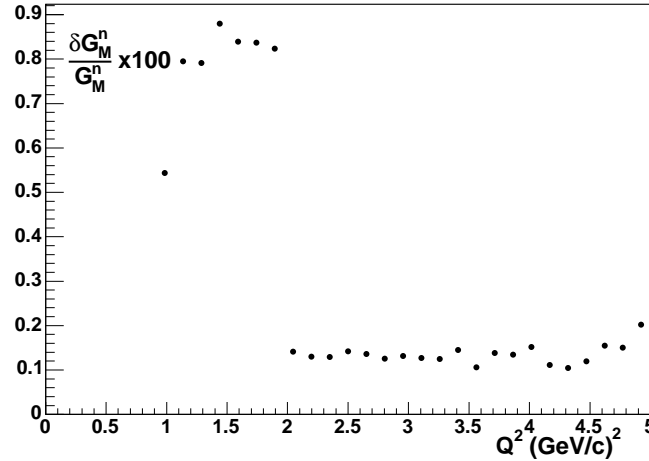


Figure 3.43: The estimated fractional systematic error on  $G_M^n$  due to uncertainties in the acceptance/Fermi-motion correction, for the 4.2 GeV data.

estimates shown in Fig 3.43 and Fig 3.44.

### 3.2.3.9 $\theta_{pq}$ cut

The value of the  $\theta_{pq}$  cut used in the quasi-elastic event selection was varied by 10% in each direction. The systematic error was calculated using Eqn 3.27 with:

$$\delta R = \frac{1}{2}(R_{110} - R_{90}) \quad (3.37)$$

where  $R_{110}$  is the ratio evaluated with the  $\theta_{pq}$  cut 10% larger, and  $R_{90}$  is the ratio evaluated with the  $\theta_{pq}$  cut 10% smaller. The systematic error estimates obtained from this procedure are shown in Fig 3.45 and Fig 3.46 for the 4.2 GeV data, and Fig 3.47 and Fig 3.48 for the 2.6 GeV data.

### 3.2.3.10 Nuclear Corrections

As mentioned in section 2.7.6, a systematic error of 0.6% was assigned to the nuclear correction factor at all values of  $Q^2$ . The systematic error on  $G_M^n$  was calculated using Eqn 3.27 with:

$$\delta R = 0.006R \quad (3.38)$$

The fractional systematic error on  $G_M^n$  due to systematic uncertainties in the nuclear correction is shown in Fig 3.49 for the 4.2 GeV data, and in Fig 3.50 for the 2.6 GeV data.

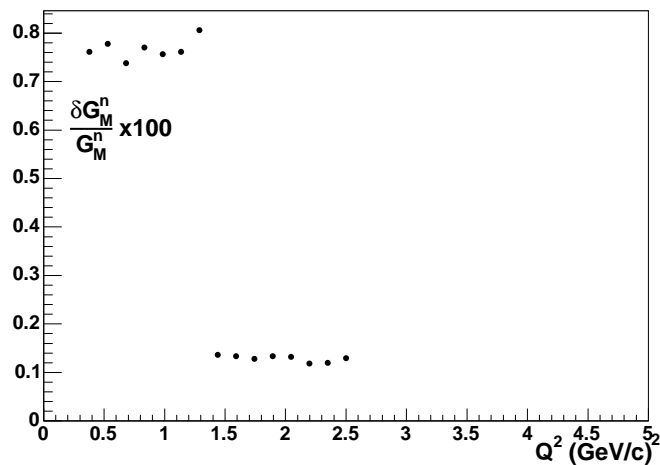


Figure 3.44: The estimated fractional systematic error on  $G_M^n$  due to uncertainties in the acceptance/Fermi-motion correction, for the 2.6 GeV data.

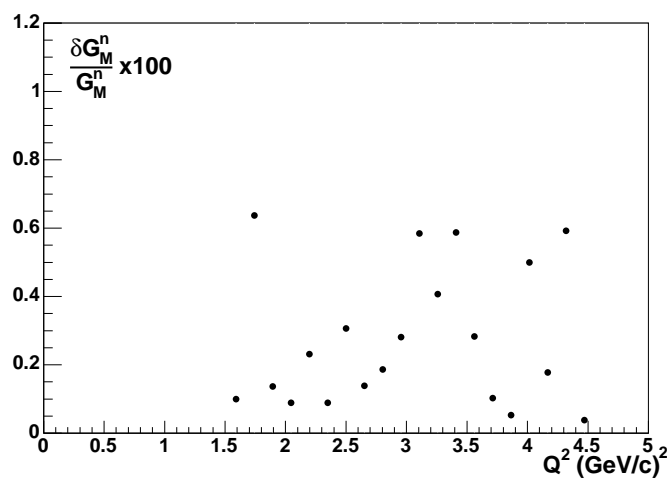


Figure 3.45: Estimated systematic error induced by variation in the  $\theta_{pq}$  cut, for EC neutrons in the 4.2 GeV data set.

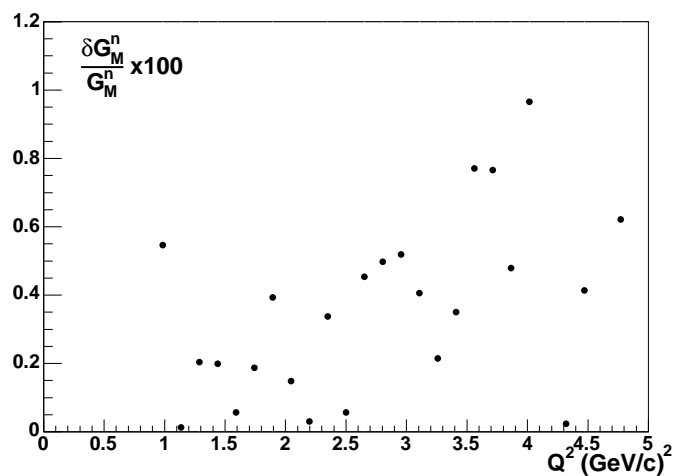


Figure 3.46: Estimated systematic error induced by variation in the  $\theta_{pq}$  cut, for SC neutrons in the 4.2 GeV data set.

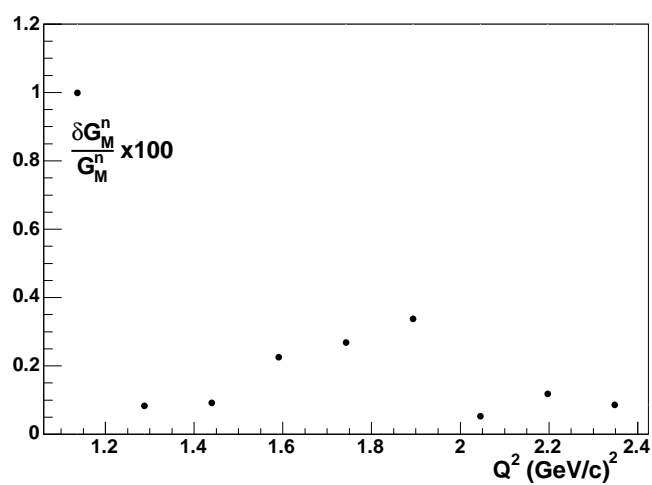


Figure 3.47: Estimated systematic error induced by variation in the  $\theta_{pq}$  cut, for EC neutrons in the 2.6 GeV data set.

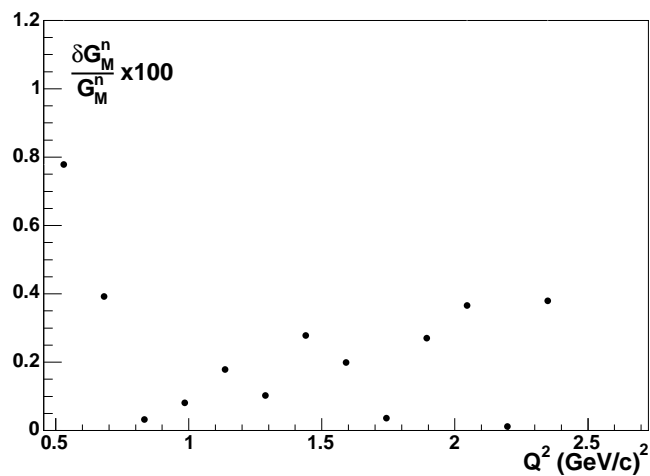


Figure 3.48: Estimated systematic error induced by variation in the  $\theta_{pq}$  cut, for SC neutrons in the 2.6 GeV data set.

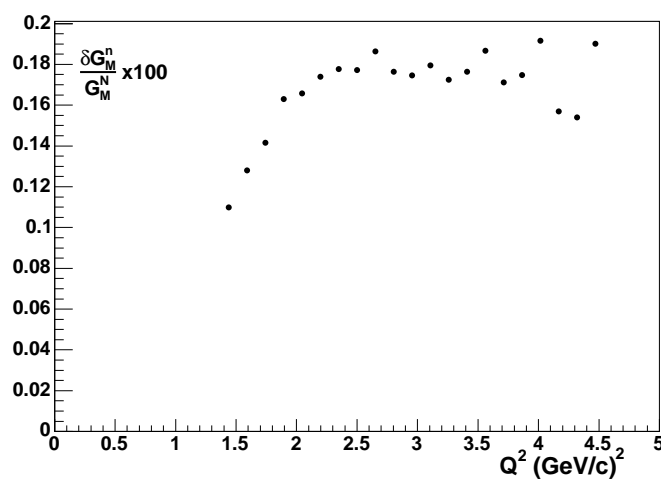


Figure 3.49: Estimated fractional systematic error induced in  $G_M^n$  by systematic error on the nuclear correction, for the 4.2 GeV data set.

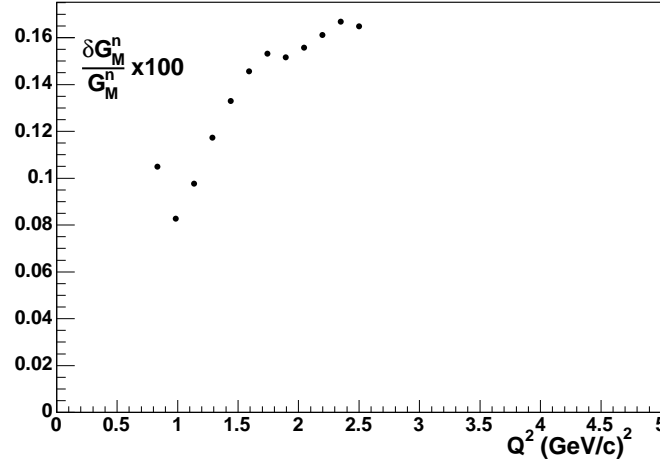


Figure 3.50: Estimated fractional systematic error on  $G_M^n$  induced by systematic error on the nuclear correction, for the 2.6 GeV data set.

### 3.2.3.11 Radiative Corrections

As mentioned in section 2.7.5, a systematic error of 0.17% was assigned to the radiative correction factor at all values of  $Q^2$ . The systematic error on  $G_M^n$  was calculated using Eqn 3.27 with:

$$\delta R = 0.0017R \quad (3.39)$$

The fractional systematic error on  $G_M^n$  due to systematic uncertainties in the radiative correction is shown in Fig 3.51 for the 4.2 GeV data, and in Fig 3.52 for the 2.6 GeV data.

### 3.2.3.12 Electron Resolution Effects on the Fermi Correction

We have studied the effect of the electron angular resolution as described in Section 2.7.4.3. Using the maximum value of the drift chamber electron angular resolution (4 mrad), we randomly smeared the electron polar angle in the GSIM simulation and then extracted the difference in the Fermi correction with this smearing turned on and with the effect turned off. The results are shown in Figures 2.71-2.74. The right-hand panel in each figure shows the fractional difference between the smeared and standard Fermi corrections. The effect is small and consistent with zero within the statistical uncertainties of the Monte Carlo simulation. We assign a systematic uncertainty of 0.6% on the Fermi correction factor so

$$\delta R = 0.0060R \quad (3.40)$$

which will be added in quadrature with the other uncertainties described in Section 3.2.3. The fractional systematic error on  $G_M^n$  due to systematic uncertainties in the

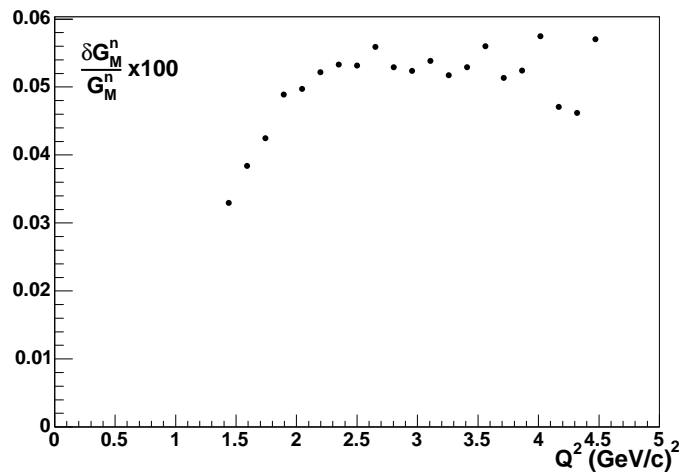


Figure 3.51: Estimated systematic error induced by uncertainties in the radiative correction, for the 4.2 GeV data set.

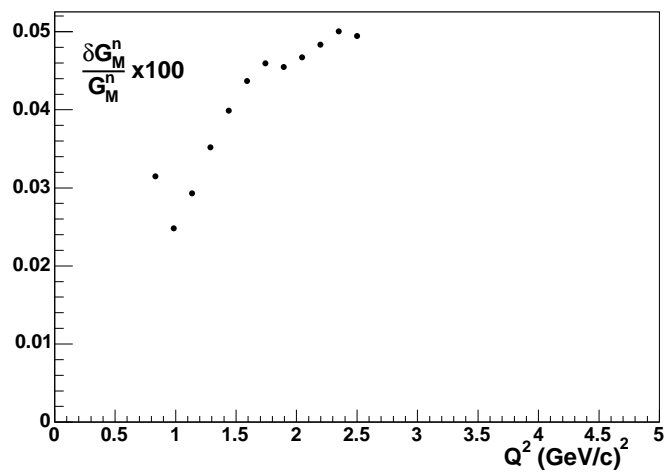


Figure 3.52: Estimated systematic error induced by uncertainties in the radiative correction, for the 2.6 GeV data set.

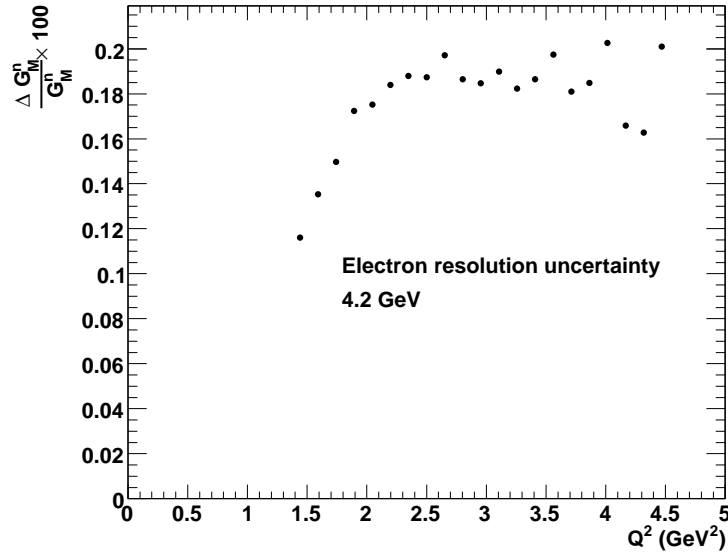


Figure 3.53: Estimated systematic error induced by the electron resolution for the 4.2 GeV data set.

electron resolution is shown in Fig 3.53 for the 4.2 GeV data, and in Fig 3.54 for the 2.6 GeV data.

### 3.2.4 Combined systematic error

The combined systematic error for each of the 4 measurements (EC and SC neutrons at two different beam energies) was obtained by adding the applicable errors in quadrature. The results are shown in Fig 3.55, 3.56, 3.57, and 3.58. The systematic errors from the four individual measurements were combined into an averaged systematic error for comparison with the weighted average  $G_M^n$  plot. To determine a value of the average systematic error, the following quantity was calculated:

$$\tilde{x} = \frac{\sum_j \frac{x_j + \sigma_j^s}{\sigma_j^2}}{\sum_j \frac{1}{\sigma_j^2}} \quad (3.41)$$

where  $\sigma_j^s$  is the systematic error on the  $j^{\text{th}}$  histogram contributing in a given  $Q^2$  bin, and the other terms are as defined in Sec 3.1. The average systematic error in each  $Q^2$  bin was then taken to be:

$$\overline{\sigma_j^s} = |\tilde{x} - \bar{x}| \quad (3.42)$$

The weighted average systematic error, binned in  $Q^2$  is shown in Fig 3.59.

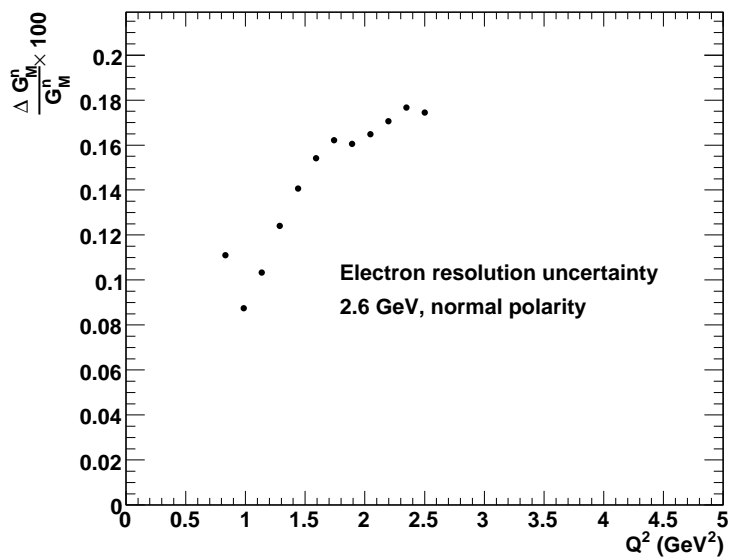


Figure 3.54: Estimated systematic error induced by the electron resolution for the 2.6 GeV data set.

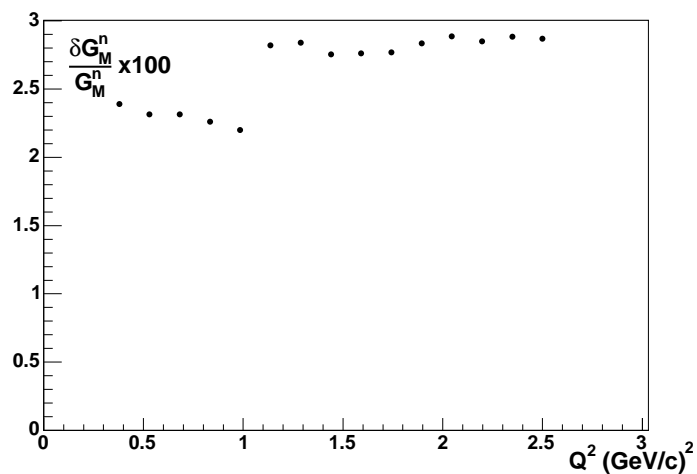


Figure 3.55: Combined fractional systematic error for the 2.6 GeV beam energy, with SC neutron detection.

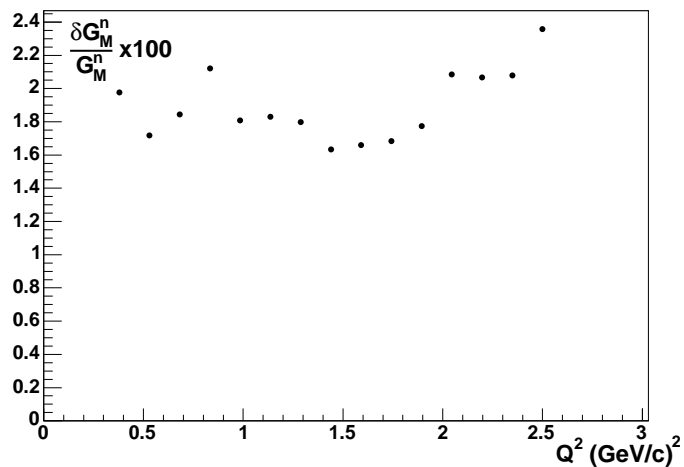


Figure 3.56: Combined fractional systematic error for the 2.6 GeV beam energy, with EC neutron detection.

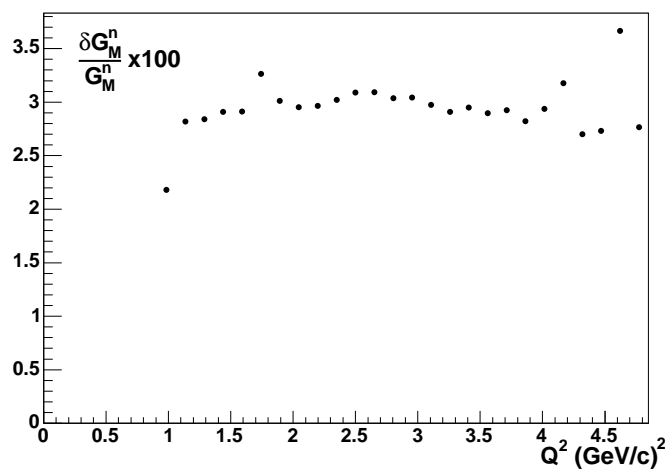


Figure 3.57: Combined fractional systematic error for the 4.2 GeV beam energy, with SC neutron detection.

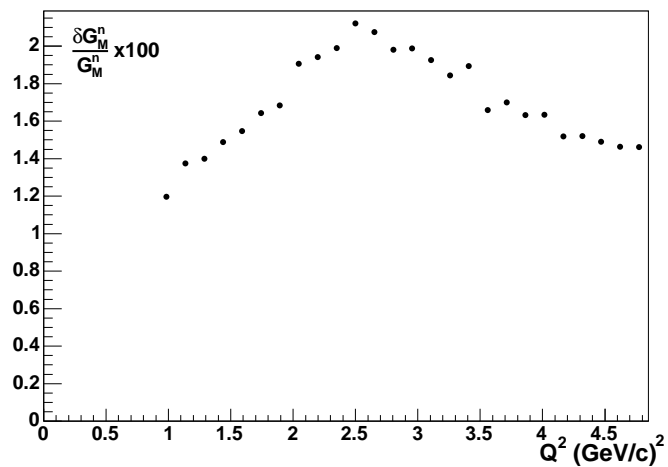


Figure 3.58: Combined fractional systematic error for the 4.2 GeV beam energy, with EC neutron detection.

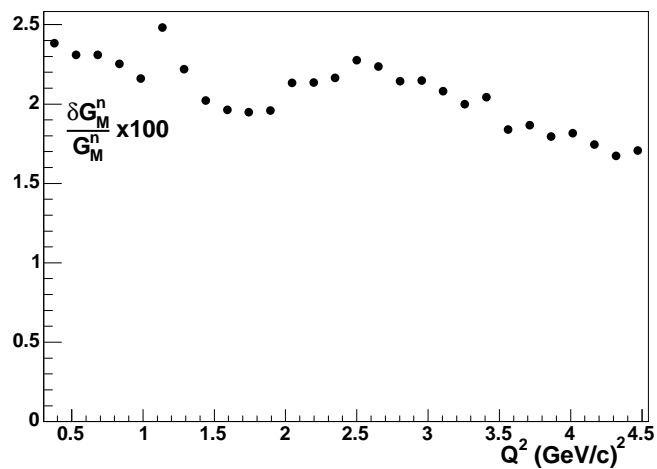


Figure 3.59: Weighted average fractional systematic error.

# Chapter 4

## Conclusions

The magnetic form factor of the neutron  $G_M^n$  has been extracted from the ratio of quasi-elastic e-n to e-p scattering from a deuterium target over a wide range of  $Q^2$  values. The use of the ratio technique resulted in the cancellation of many uncertainties. Neutrons were detected in two different detector systems (the time-of-flight detector and the forward calorimeter) at two different beam energies. This combination of multiple beam energies and multiple neutron detectors allowed four semi-independent measurements of  $G_M^n$  to be performed. The two neutron detectors are subject to completely different systematic errors, and the protons sample different regions of the drift chambers and time-of-flight detector at the two beam energies. The  $Q^2$  region covered by any of the four measurements overlaps a portion of the  $Q^2$  region covered by any of the other three measurements. The consistency of the measurements in the overlap regions gives confidence that systematic errors are under control.

### 4.1 Comparison to previous measurements

A comparison of the weighted average determination of  $G_M^n$  (scaled to the dipole parametrization) to previous measurements is shown in Figure 4.1. The weighted average systematic error is shown as an error band, and a line showing  $G_M^n = \mu_n G_D$  is drawn. A similar plot is shown in Fig 4.2. Fig 4.3 shows the statistical and systematic errors added in quadrature. The data is seen to be in agreement with previous measurements in the  $Q^2 > 1$  (GeV/c)<sup>2</sup> region. In the  $Q^2 < 1$  (GeV/c)<sup>2</sup> region, significant disagreement is seen with the Jourdan [55] measurement. The region of disagreement is the only  $Q^2$  region covered by a single measurement (SC neutrons at 2.6 GeV). The disagreement in this region provides a strong motivation to make further efforts to complete the analysis of the reversed-field portion of the e5 data, which was not performed as a part of this thesis. If successfully analyzed, the reversed field data will provide a second SC-based measurement, an EC-based measurement and possibly a Large-Angle Calorimeter based measurement of  $G_M^n$  in the low- $Q^2$  region.

The range of  $Q^2$  covered by this experiment, the number of points at which  $G_M^n$

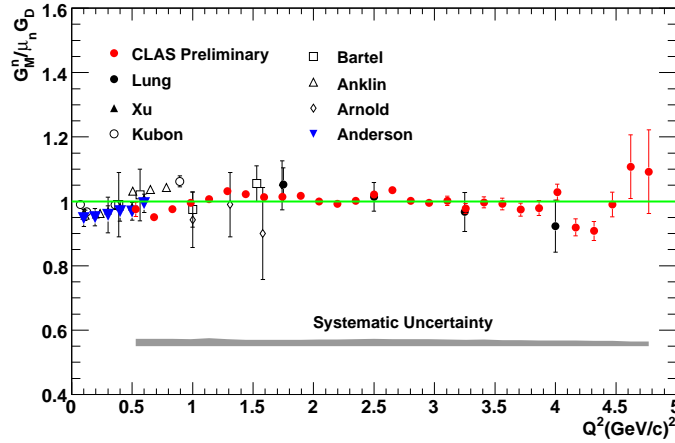


Figure 4.1: The weighted average value of  $G_M^n$ , scaled to the dipole parametrization. A selection of previous measurements is shown. The red points indicate the results of this analysis. The weighted average systematic error is shown as a grey band. The green line indicates  $G_M^n = \mu_n G_D$

was measured, and the precision with which it was measured represent a substantial improvement to the world data set. The standard dipole parametrization is seen to give a good representation of the data for  $Q^2 > 1$  (GeV/c)<sup>2</sup>, although the data may show  $G_M^n$  falling off faster than the dipole for  $Q^2 > 3.5$  (GeV/c)<sup>2</sup>. In the time elapsed since the e5 data set was taken, the maximum beam energy at Jefferson Lab has increased to 6 GeV. The e5 experiment used a proven technique, and the experiment could be repeated at the higher beam energy to extend the  $Q^2$  coverage up to  $Q^2 \approx 7$  (GeV/c)<sup>2</sup>. This would allow investigation of the possibility of deviations from the dipole at higher  $Q^2$ , and would extend our knowledge of  $G_M^n$  into a  $Q^2$  region where no reliable measurement currently exists.

#### 4.1.1 Comparison to theoretical predictions and fits

A comparison between the weighted average value of  $G_M^n$  and the various theoretical predictions and fits discussed in Section 1.1.3 is shown in Fig 4.4. A close-up view is shown in Fig 4.5. The models that do the best, Lomon and Kelley, are the ones that are most tightly linked to previous data (the Kelley curve is really nothing more than a fit with a ratio of polynomials). This is not unexpected, as (at least in the  $Q^2 > 1$  (GeV/c)<sup>2</sup> region), the e5 data is consistent with previous world data. The Lomon results are seen to be superior to the Kelley fit. The IJL model appears to be ruled out, as its prediction of rapid growth with  $Q^2$  is entirely inconsistent with the data. This is surprising, given its success in the proton sector. The lattice prediction fails completely, never predicting a value less than  $\approx 35\%$  different from the data.

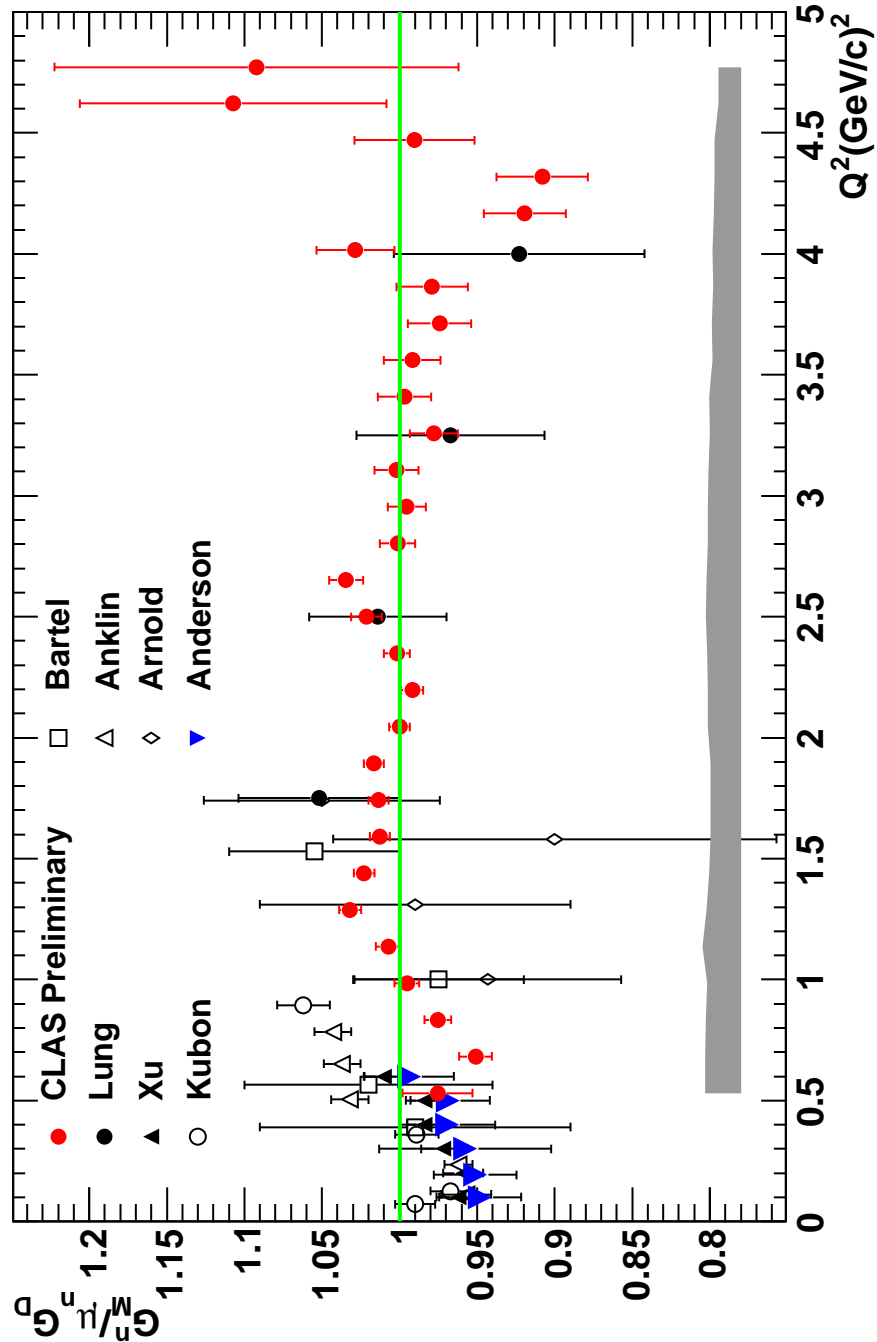


Figure 4.2: The weighted average value of  $G_M^n$ , scaled to the dipole parametrization. A selection of previous measurements is shown. The red points indicate the results of this analysis. The weighted average systematic error is shown as a grey band. The green line indicates  $G_M^n = \mu_n G_D$

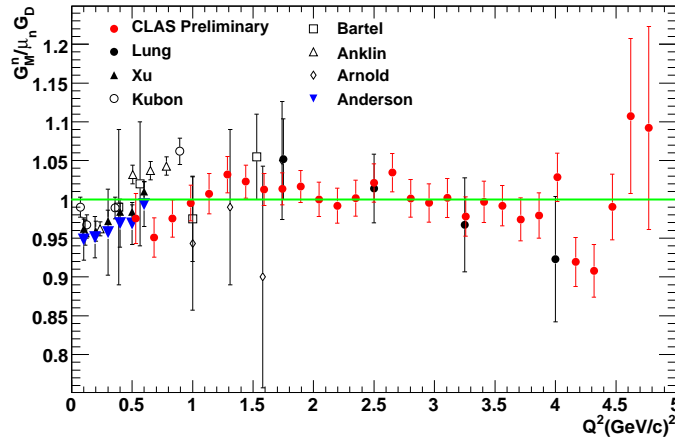


Figure 4.3: The weighted average value of  $G_M^n$ , scaled to the dipole parametrization. A selection of previous measurements is shown. The error bars on the data points are the quadrature sum of the statistical and systematic errors. The green line shows  $G_M^n = \mu_n G_D$

Hopefully, the lattice results will improve in the future as computer power increases. The other two models do an adequate job in one  $Q^2$  region (low  $Q^2$  for Wagenbrunn, high  $Q^2$  for Miller), but are unable to reproduce the data over the full  $Q^2$  range. The Miller model is a hybrid which uses a pion cloud, implemented with a cloudy bag model and a relativistic constituent quark model. The pion cloud is important at low momentum transfer, while in the large momentum transfer region the prediction is dominated by a relativistic constituent quark model. The comparison with the data suggest the pion cloud portion of the model is not adequate, while the relativistic constituent quark portion performs well as  $Q^2$  becomes large.

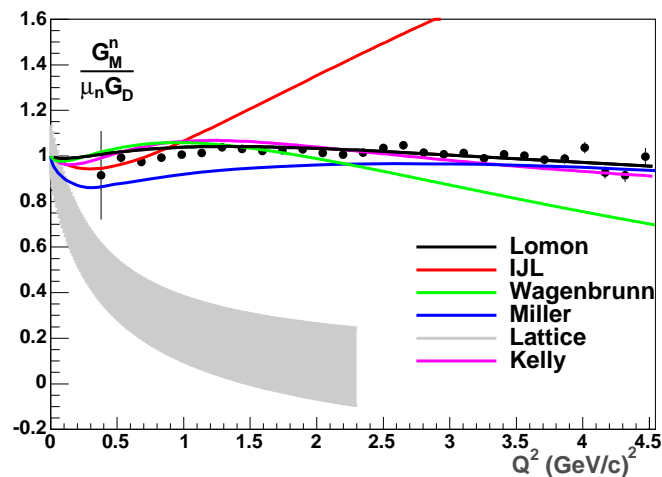


Figure 4.4: A comparison of the e5 data and the theoretical predictions discussed in Section 1.1.3. Only the statistical errors are shown.

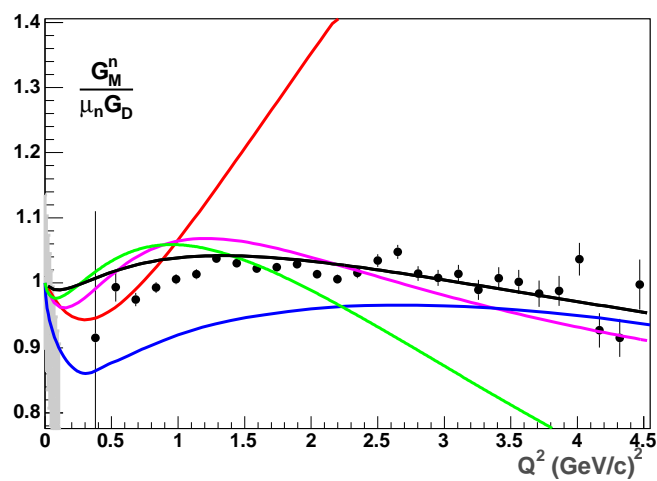


Figure 4.5: A comparison of the e5 data and the theoretical predictions discussed in Section 1.1.3. Only the statistical errors are shown. The colors have the meaning indicated in Fig 4.4.

# Bibliography

- [1] F.Halzen and A.Martin. *Quarks and Leptons*. J.Wiley, 1984.
- [2] F.Iachello, A.D.Jackson, and A.Lande. *Phys.Lett B*, 43B:191, 1973.
- [3] J.Bjorken and S.Drell. *Relativistic Quantum Mechanics*. McGraw Hill, 1965.
- [4] M.K.Jones et al. *Phys.Rev.Lett*, 84:1398, 2000.
- [5] O.Gayou et al. *Phys.Rev.Lett*, 88:092301, 2002.
- [6] M.Gari and W.Krumpelmann. *Z.Phys.A*, 322:689, 1985.
- [7] U. Kaulfuss and M. Gari. *Nucl.Phys.A*, 408, 1983.
- [8] S.Brodsky and S.Farrar. *Phys.Rev.D*, 11, 1975.
- [9] E.Lomon. *Phys.Rev.C*, 64, 2001.
- [10] E.Lomon. *nucl-th/0203081*.
- [11] P.Mergell, U.Meissner, and D.Dreschel. *Nucl.Phys.A*, 596, 1996.
- [12] G.Miller. *Phys. Rev. C*, 66, 2002.
- [13] V.B.Berestetskii and M.V.Terentev. *Sov.J.Nucl.Phys.*, 1977.
- [14] P. L. Chung and F. Coester. *Phys. Rev.*, D44:229–241, 1991.
- [15] R.F. Wagenbrunn *et al.*. *Eur. Phys. J. A.*, 18, 2002.
- [16] L. Ya. Glozman, W. Plessas, K. Varga, and R. F. Wagenbrunn. *Phys. Rev.*, D58:094030, 1998.
- [17] M.Gockeler et al. *hep-lat/0303019*.
- [18] J.D. Ashley et al. *Eur. Phys. J A*, 19, s01:9–14, 2004.
- [19] J.J.Kelly. *Phys. Rev. C*, 70:068202, 2004.
- [20] E.B.Hughes et al. *Phys. Rev.*, 146:973, 1965.

- [21] B.Grossetete et al. *Phys. Rev.*, 141:1435, 1966.
- [22] A.S. Esaulov et al. *Sov. J. Nucl. Phys.*, 45:258, 1987.
- [23] R. G. Arnold et al. *Phys. Rev. Lett.*, 61:806, 1988.
- [24] A.Lung et al. *Phys. Rev. Lett.*, 70:718, 1993.
- [25] P.Stein et al. *Phys. Rev. Lett.*, 16:592, 1966.
- [26] W.Bartel et al. *Nuc. Phys. B*, 58:429–475, 1973.
- [27] P. Markowitz et al. *Phys. Rev. C*, 48:R5, 1993.
- [28] K.M. Hanso et al. *Phys. Rev. D*, 8:753, 1973.
- [29] H. Anklin et al. *Phys. Lett.*, B336:313, 1994.
- [30] E.E.W. Bruins et al. *Phys. Rev. Lett.*, 75:21, 1995.
- [31] G. Kubon et al. *Phys. Lett.*, B524:26–32, 2002.
- [32] H. Gao. *nucl-ex/0301002v1*.
- [33] J.W.C. McNabb. Ph.d. thesis. 2002.
- [34] M.Amarian et al. *NIM A*, 460:239, 2001.
- [35] E. J. Brash, A. Kozlov, S. Li, and G. M. Huber. *Phys. Rev.*, C65:051001, 2002.
- [36] M.D. Mestayer et al. *NIM A*, 449:81, 2000.
- [37] Luke W. Mo and Yung-Su Tsai. *Rev. Mod. Phys.*, 41:205–235, 1969.
- [38] A. Afanasev, I. Akushevich, V. Burkert, and K. Joo. *Phys. Rev.*, D66:074004, 2002.
- [39] Jr. Adam, J., Franz Gross, Sabine Jeschonnek, Paul Ulmer, and J. W. Van Orden. *Phys. Rev.*, C66:044003, 2002.
- [40] J.Schwinger. *Phys.Rev.*, 76, 1949.
- [41] S.Jeschonnek. private communication.
- [42] S.Jeschonnek and T.Donnely. *Phys. Rev. C*, 57:2438–2452, 1998.
- [43] S.Jeschonnek and J.W. Van Orden. *Phys. Rev. C*, 62:044613, 2000.
- [44] S.Jeschonnek and T.Donnely. *Phys. Rev. C*, 59:2676–2668, 1998.

- [45] H.Arenhovel. private communication.
- [46] A.S.Raskin and T.W.Donnely. *Ann.Phys.*, 191:78, 1989.
- [47] T.W.Donnely and A.S.Raskin. *Ann. Phys.*, 169:247–351, 1986.
- [48] V.G.J.Stoks R.B.Wiringa and R.Sciavilla. *Phys. Rev. C*, 51:38, 1995.
- [49] W.Brooks. private communication.
- [50] J.Arrington. private communication.
- [51] P.Bosted. *Phys. Rev. C*, 51:409–411, 1995.
- [52] R.Schiavilla and I.Sick. *Phys. Rev. C*, 64:041002–1, 2001.
- [53] R.Bradford. private communication.
- [54] W.Brooks et al. E5 experiment proosal. 1994.
- [55] J. Jourdan. *Nucl. Phys.*, A721:395–400, 2003.

# Appendix A

## Measured $G_M^n$ values and errors

Table A.1: Measured values of  $\frac{G_M^n}{\mu_n G_D}$ , statistical and systematic errors for the 4.2 GeV beam energy with EC neutron detection. The  $Q^2$  values given are the central value of each  $Q^2$  bin.

$Q^2$	$\frac{G_M^n}{\mu_n G_D}$	Statistical	Systematic
1.4393	1.0330	0.08922	0.01480
1.5909	1.0232	0.01747	0.01536
1.7424	1.0207	0.01236	0.01632
1.8939	1.0369	0.00955	0.01672
2.0454	0.9977	0.00892	0.01890
2.1969	0.9997	0.00936	0.01919
2.3484	1.0058	0.00992	0.01972
2.5	1.0130	0.01090	0.02103
2.6515	1.0340	0.01184	0.02057
2.8030	1.0024	0.01244	0.01965
2.9545	0.9906	0.01346	0.01972
3.1060	1.0023	0.01557	0.01910
3.2575	0.9756	0.01682	0.01830
3.4090	0.9832	0.01871	0.01878
3.5606	1.0073	0.02009	0.01647
3.7121	0.9623	0.02196	0.01687
3.8636	0.9703	0.02497	0.01620
4.0151	1.0169	0.02741	0.01622
4.1666	0.9170	0.02867	0.01509
4.3181	0.9078	0.03173	0.01510
4.4697	0.9941	0.04281	0.01481

Table A.2: Measured values of  $\frac{G_M^n}{\mu_n G_D}$ , statistical and systematic errors for the 4.2 GeV beam energy with SC neutron detection. The  $Q^2$  values given are the central value of each  $Q^2$  bin.

$Q^2$	$\frac{G_M^n}{\mu_n G_D}$	Statistical	Systematic
0.9848	0.8333	0.26057	0.02175
1.1363	1.0184	0.06736	0.02811
1.2878	1.0142	0.03161	0.02830
1.4393	1.0701	0.01953	0.02899
1.5909	1.0439	0.01900	0.02901
1.7424	1.0416	0.01964	0.02941
1.8939	1.0323	0.01954	0.03000
2.0454	1.0477	0.02005	0.02943
2.1969	1.003	0.02073	0.02955
2.3484	1.0006	0.02177	0.03011
2.5	1.0602	0.02380	0.03078
2.6515	1.0360	0.02579	0.03082
2.8030	0.9954	0.02753	0.03026
2.9545	1.0190	0.03008	0.03033
3.1060	0.9992	0.03519	0.02963
3.2575	0.9900	0.03869	0.02900
3.4090	1.0687	0.04336	0.02938
3.5606	0.9096	0.04627	0.02886
3.7121	1.0413	0.05226	0.02914
3.8636	1.0287	0.05935	0.02814
4.0151	1.0928	0.06469	0.02928
4.1666	0.9321	0.06916	0.03164
4.3181	0.9085	0.07746	0.02691
4.4697	0.9731	0.08910	0.02723

Table A.3: Measured values of  $\frac{G_M^n}{\mu_n G_D}$ , statistical and systematic errors for the 2.6 GeV beam energy with EC neutron detection. The  $Q^2$  values given are the central value of each  $Q^2$  bin.

$Q^2$	$\frac{G_M^n}{\mu_n G_D}$	Statistical	Systematic
0.9848	1.0290	0.02749	0.01812
1.1363	1.0259	0.01348	0.01834
1.2878	1.0371	0.00934	0.01802
1.4393	1.0110	0.00820	0.01640
1.5909	1.0017	0.00855	0.01665
1.7424	1.0065	0.00966	0.01690
1.8939	0.9859	0.01064	0.01778
2.0454	0.9824	0.01211	0.02087
2.1969	0.9763	0.01455	0.02069
2.3484	0.9857	0.02496	0.02080
2.5	1.0205	0.10604	0.02357

Table A.4: Measured values of  $\frac{G_M^n}{\mu_n G_D}$ , statistical and systematic errors for the 2.6 GeV beam energy with SC neutron detection. The  $Q^2$  values given are the central value of each  $Q^2$  bin.

$Q^2$	$\frac{G_M^n}{\mu_n G_D}$	Statistical	Systematic
0.5303	0.9754	0.02251	0.02307
0.6818	0.9509	0.01049	0.02307
0.8333	0.9753	0.00855	0.02252
0.9848	0.9921	0.00836	0.02193
1.1363	0.9972	0.00976	0.02809
1.2878	1.0256	0.01210	0.02829
1.4393	1.0330	0.01432	0.02742
1.5909	1.0199	0.01635	0.02749
1.7424	0.9986	0.01854	0.02757
1.8939	1.0199	0.02039	0.02824
2.0454	1.0158	0.02326	0.02874
2.1969	0.9589	0.02801	0.02837
2.3484	0.9648	0.04780	0.02871
2.5	1.0154	0.18269	0.02856

Table A.5: Measured values of  $\frac{G_M^n}{\mu_n G_D}$ , statistical and systematic errors from the weighted average.

$Q^2$	$\frac{G_M^n}{\mu_n G_D}$	Statistical	Systematic
0.5303	0.9754	0.02251	0.02307
0.6818	0.9509	0.01049	0.02307
0.8333	0.9753	0.00855	0.02252
0.9848	0.9953	0.00800	0.02161
1.1363	1.0072	0.00785	0.02478
1.2878	1.0318	0.00720	0.02218
1.4393	1.0228	0.00667	0.02023
1.5909	1.0126	0.00653	0.01964
1.7424	1.0136	0.00662	0.01951
1.8939	1.0166	0.00635	0.01961
2.0454	1.0000	0.00649	0.02133
2.1969	0.9918	0.00712	0.02136
2.3484	1.0016	0.00836	0.02165
2.5	1.0211	0.00985	0.02274
2.6515	1.0344	0.01076	0.02235
2.8030	1.0012	0.01133	0.02144
2.9545	0.9954	0.01229	0.02148
3.1060	1.0018	0.01424	0.02082
3.2575	0.9779	0.01542	0.01999
3.4090	0.9966	0.01718	0.02044
3.5606	0.9918	0.01842	0.01843
3.7121	0.9742	0.02025	0.01870
3.8636	0.9791	0.02301	0.01799
4.0151	1.0284	0.02524	0.01819
4.1666	0.9192	0.02648	0.01750
4.3181	0.9079	0.02936	0.01679
4.4697	0.9902	0.03858	0.01712

# Appendix B

## EC neutron detection efficiency fits

### B.1 2.6 GeV beam energy

This section contains plots of the neutron detection efficiency measured on each of nine superpixels in each of six EC modules, as a function of neutron momentum for the 2.6 GeV dataset. Each plot is labelled by a pair of numbers  $a, b$  where  $a$  is the sector number of the EC modules and  $b$  is the superpixel number, as shown in Fig 2.13. Two curves are superimposed on each figure. The red curve shows the result of the maximum-likelihood fit performed on the whole-sector efficiency. The black curve shows the results of scaling the whole-sector efficiency to the superpixel measurements (see Eqn 2.31). Two numbers are indicated in black in each plot. The upper number is the value of  $\chi^2/ndf$  obtained from comparing the measured efficiency of each pixel to the sector fit. The lower black number is the value of  $\chi^2/ndf$  obtained from comparing the measured efficiency to the scaled fit. The blue number is the value of the scale factor, and the magenta number is the error on the scale factor.

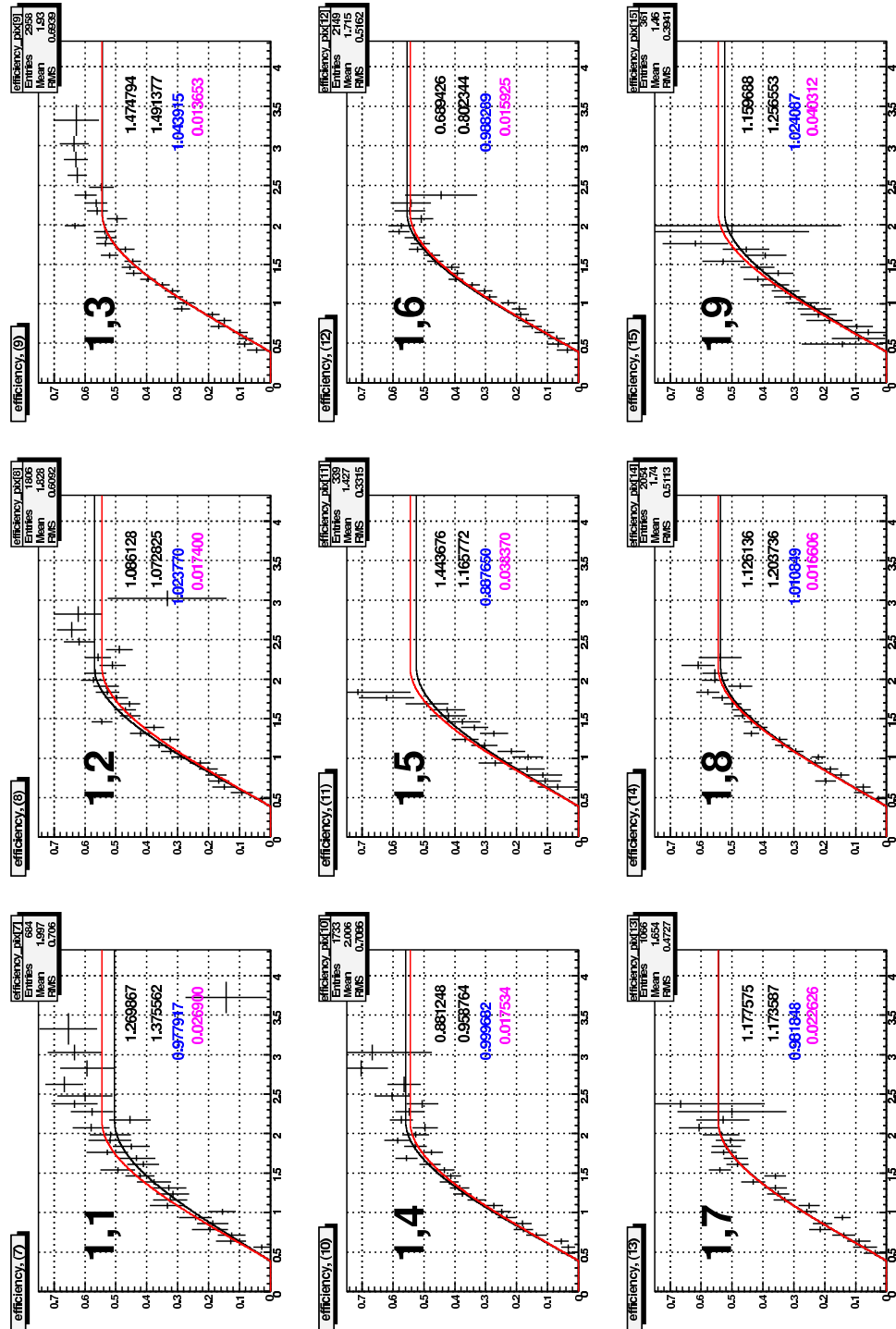


Figure B.1: Neutron detection efficiency by superpixel in sector 1, from the 2.6 GeV data. The red line shows the results of the fit to the entire sector. The black line shows the scaled sector fit.

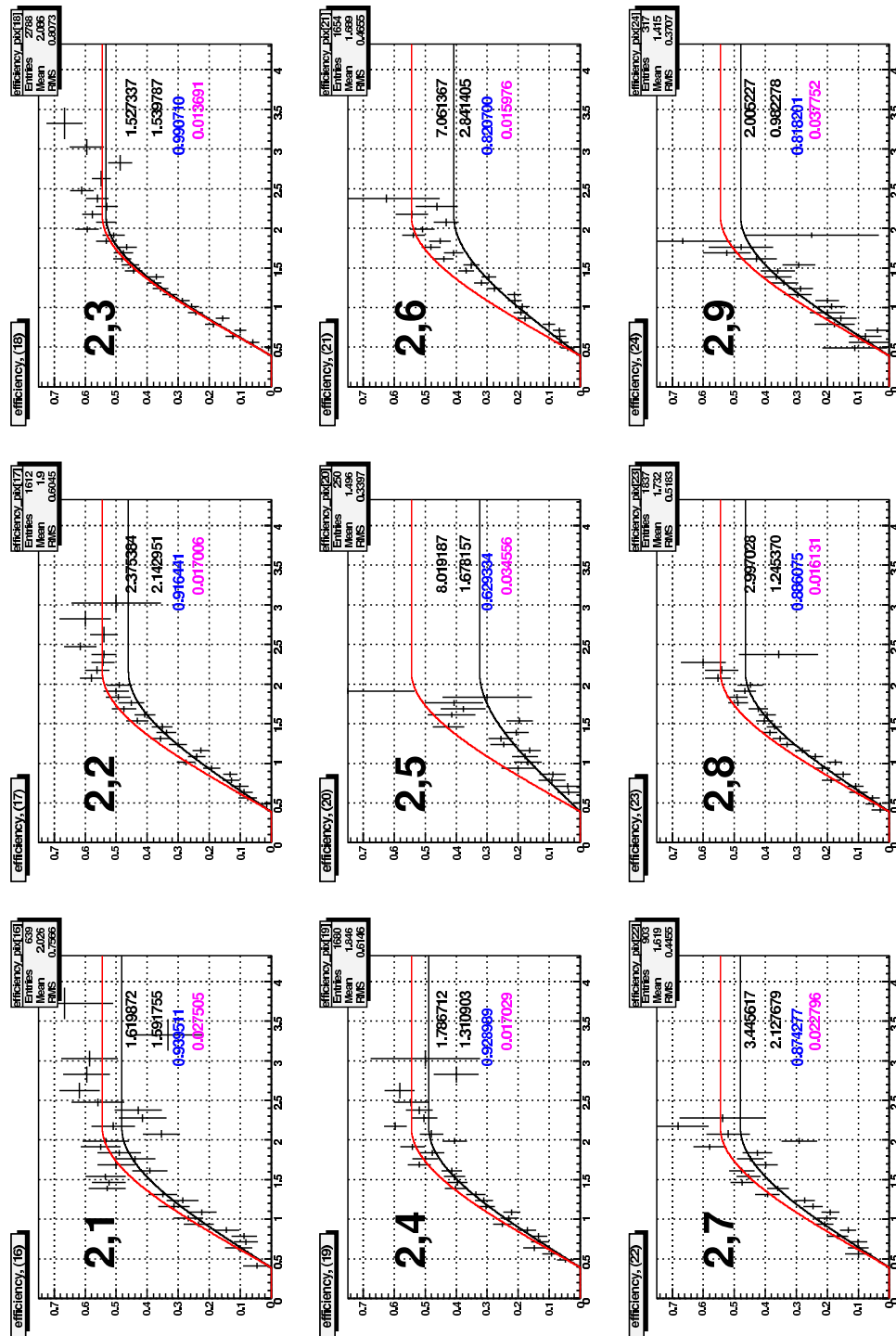


Figure B.2: Neutron detection efficiency by superpixel in sector 2, from the 2.6 GeV data. The red line shows the results of the fit to the entire sector. The black line shows the scaled sector fit.

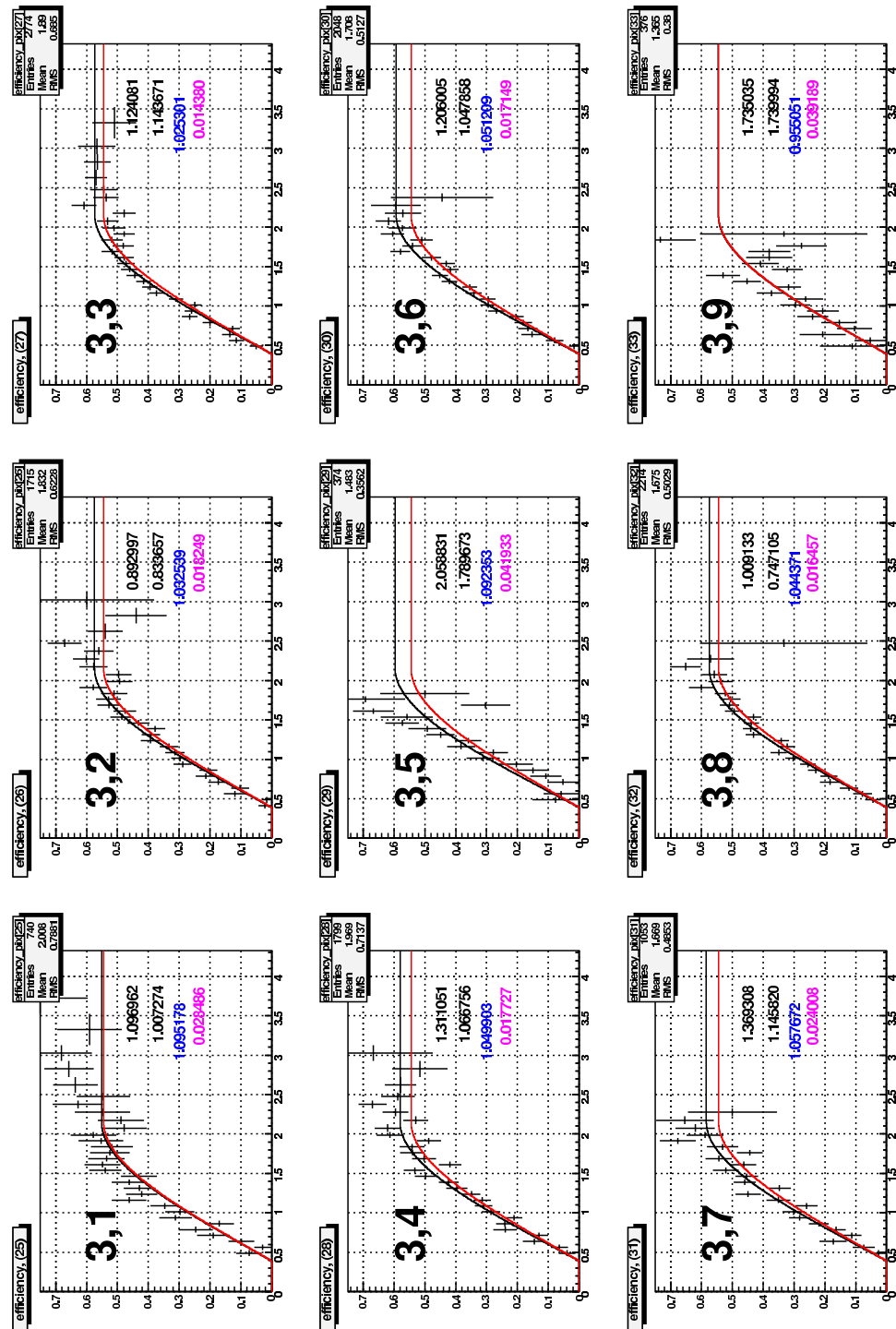


Figure B.3: Neutron detection efficiency by superpixel in sector 3, from the 2.6 GeV data. The red line shows the results of the fit to the entire sector. The black line shows the scaled sector fit.

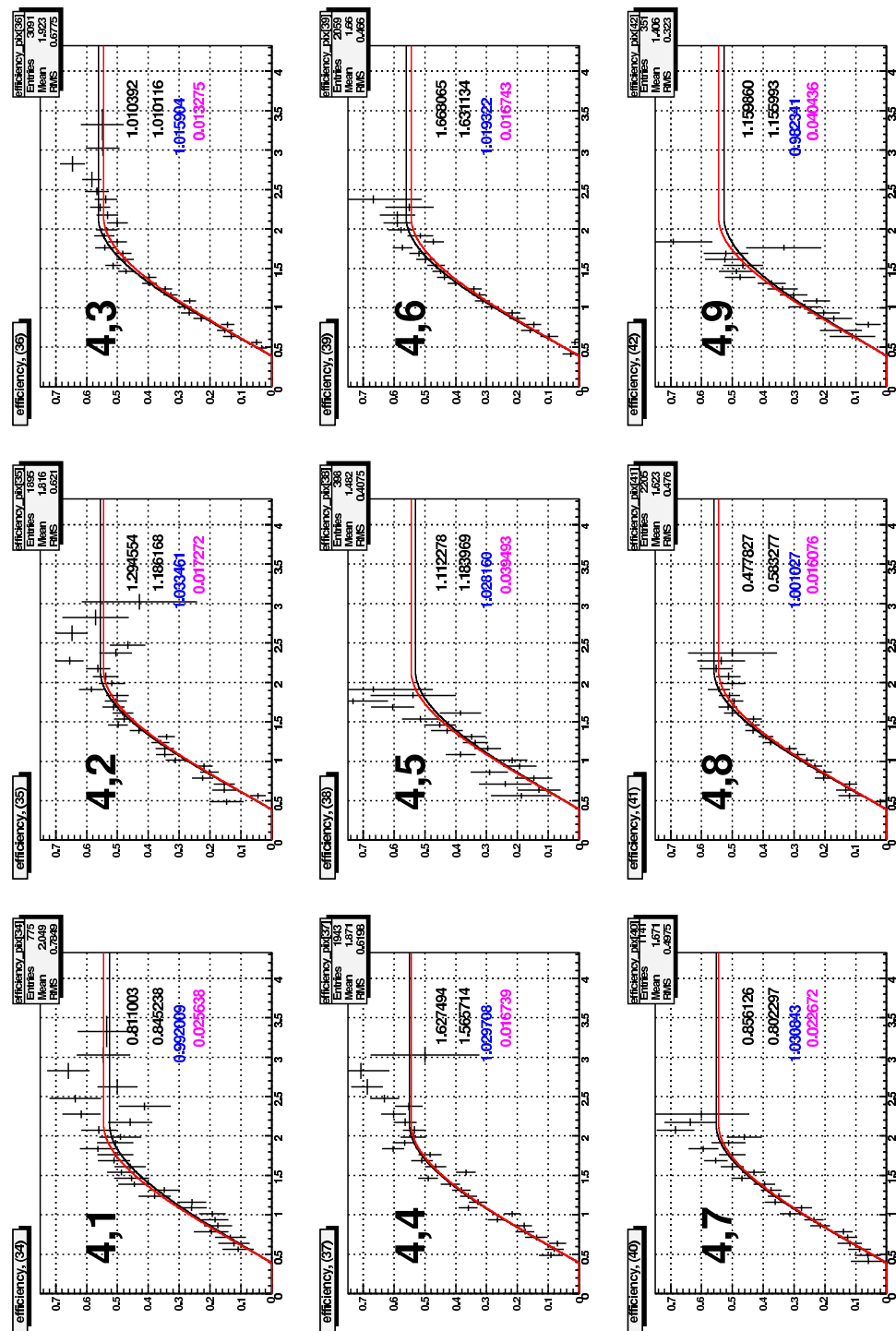


Figure B.4: Neutron detection efficiency by superpixel in sector 4, from the 2.6 GeV data. The red line shows the results of the fit to the entire sector. The black line shows the scaled sector fit.

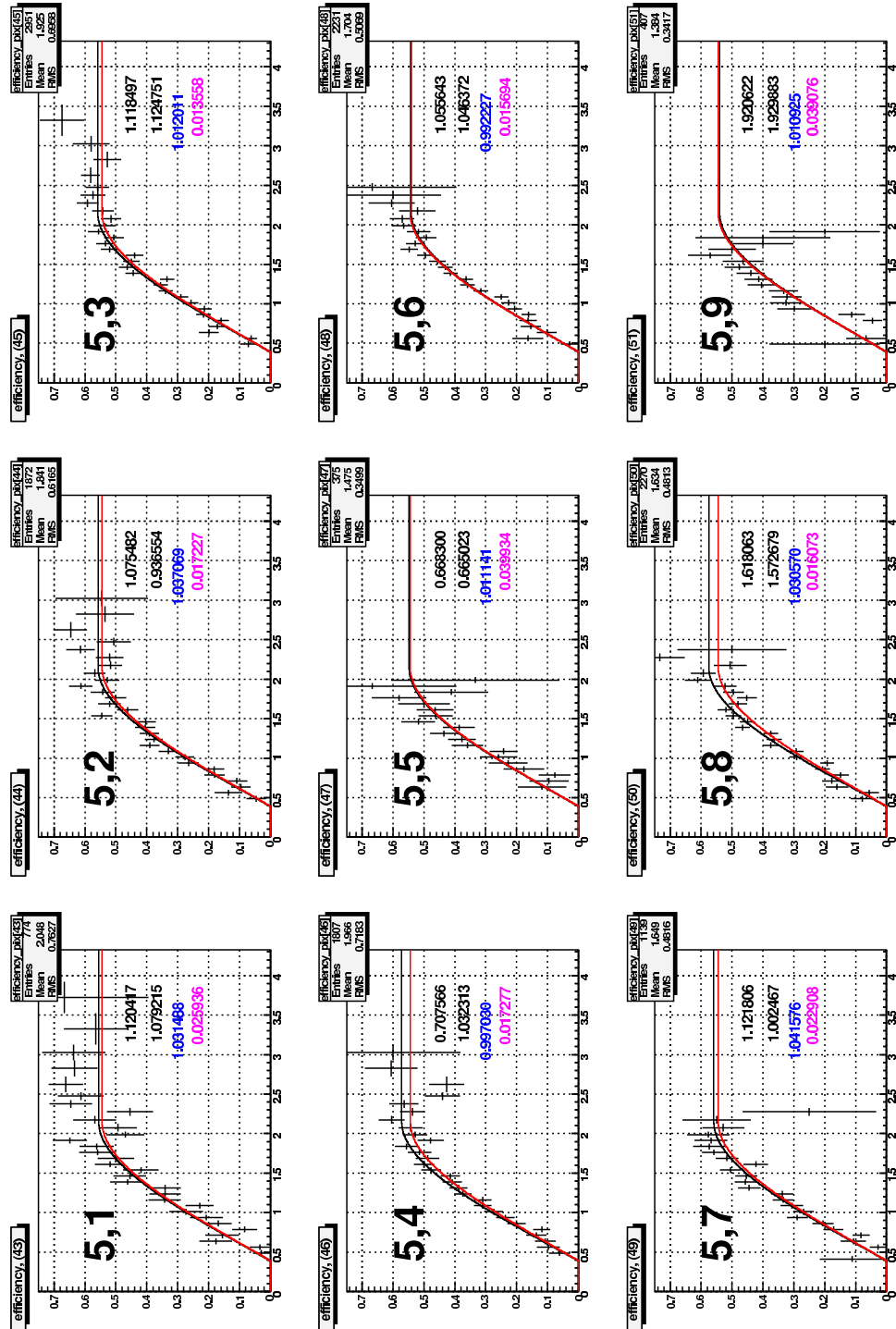


Figure B.5: Neutron detection efficiency by superpixel in sector 5, from the 2.6 GeV data. The red line shows the results of the fit to the entire sector. The black line shows the scaled sector fit.

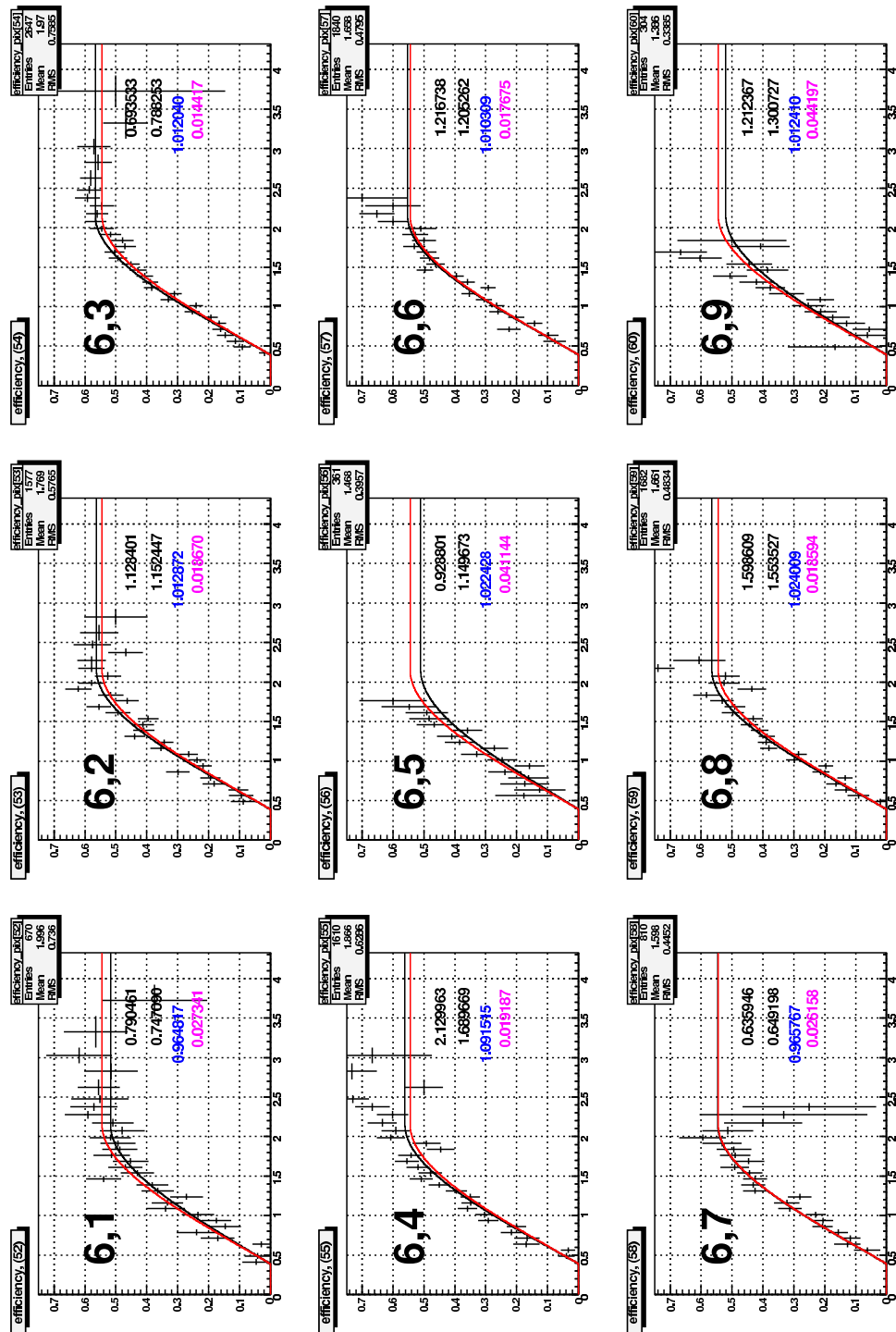


Figure B.6: Neutron detection efficiency by superpixel in sector 6, from the 2.6 GeV data. The red line shows the results of the fit to the entire sector. The black line shows the scaled sector fit.

## B.2 4.2 GeV beam energy

This section contains plots of the neutron detection efficiency measured on each of nine superpixels in each of six EC modules, as a function of neutron momentum for the 4.2 GeV dataset. Each plot is labelled by a pair of numbers  $a, b$  where  $a$  is the sector number of the EC modules and  $b$  is the superpixel number, as shown in Fig 2.13. Two curves are superimposed on each figure. The red curve shows the result of the maximum-likelihood fit performed on the whole-sector efficiency. The black curve shows the results of scaling the whole-sector efficiency to the superpixel measurements (see Eqn 2.31). Two numbers are indicated in black in each plot. The upper number is the value of  $\chi^2/ndf$  obtained from comparing the measured efficiency of each pixel to the sector fit. The lower black number is the value of  $\chi^2/ndf$  obtained from comparing the measured efficiency to the scaled fit. The blue number is the value of the scale factor, and the magenta number is the error on the scale factor.

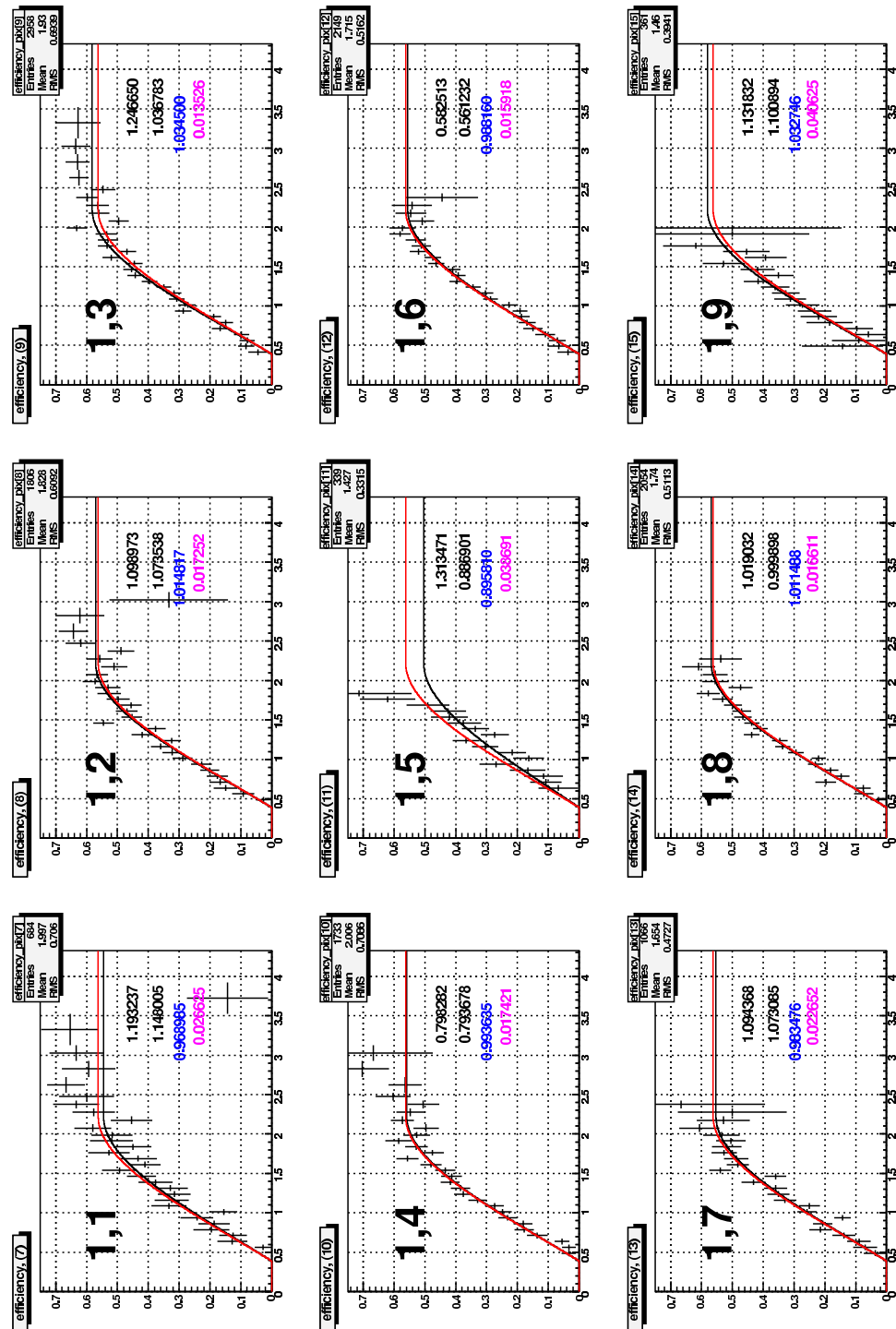


Figure B.7: Neutron detection efficiency by superpixel in sector 1, from the 4.2 GeV data. The red line shows the results of the fit to the entire sector. The black line shows the scaled sector fit.

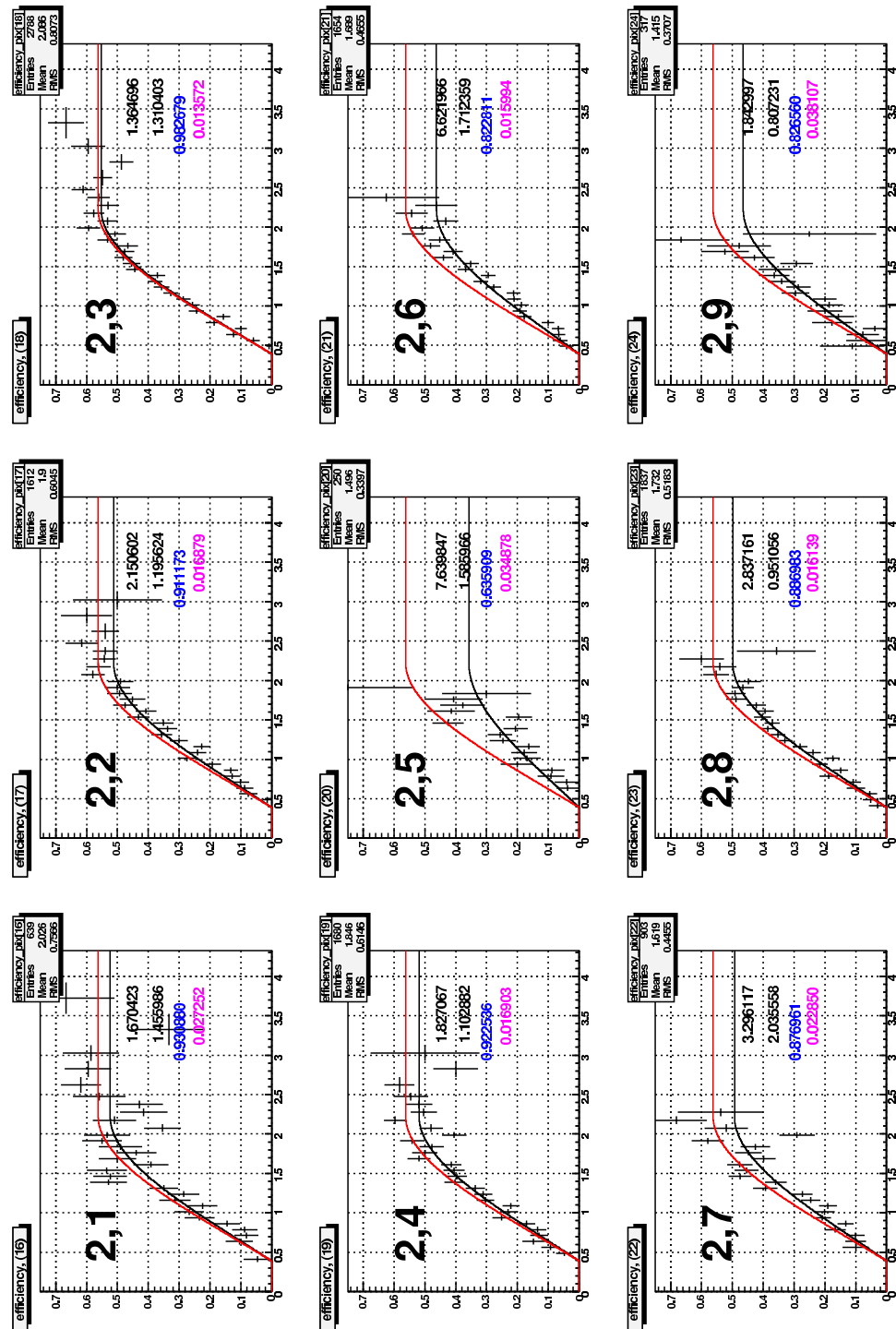


Figure B.8: Neutron detection efficiency by superpixel in sector 2, from the 4.2 GeV data. The red line shows the results of the fit to the entire sector. The black line shows the scaled sector fit.

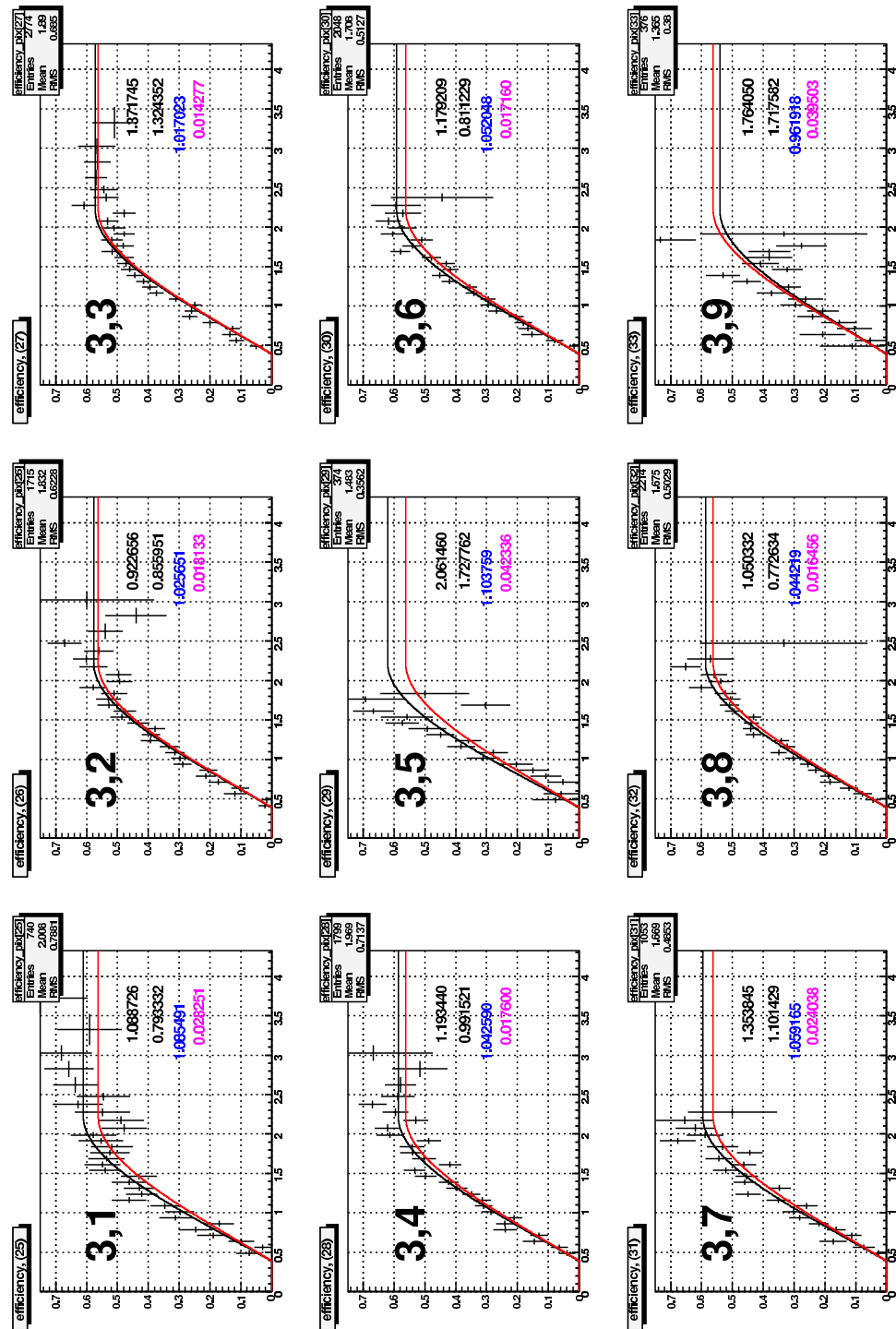


Figure B.9: Neutron detection efficiency by superpixel in sector 3, from the 4.2 GeV data. The red line shows the results of the fit to the entire sector. The black line shows the scaled sector fit.

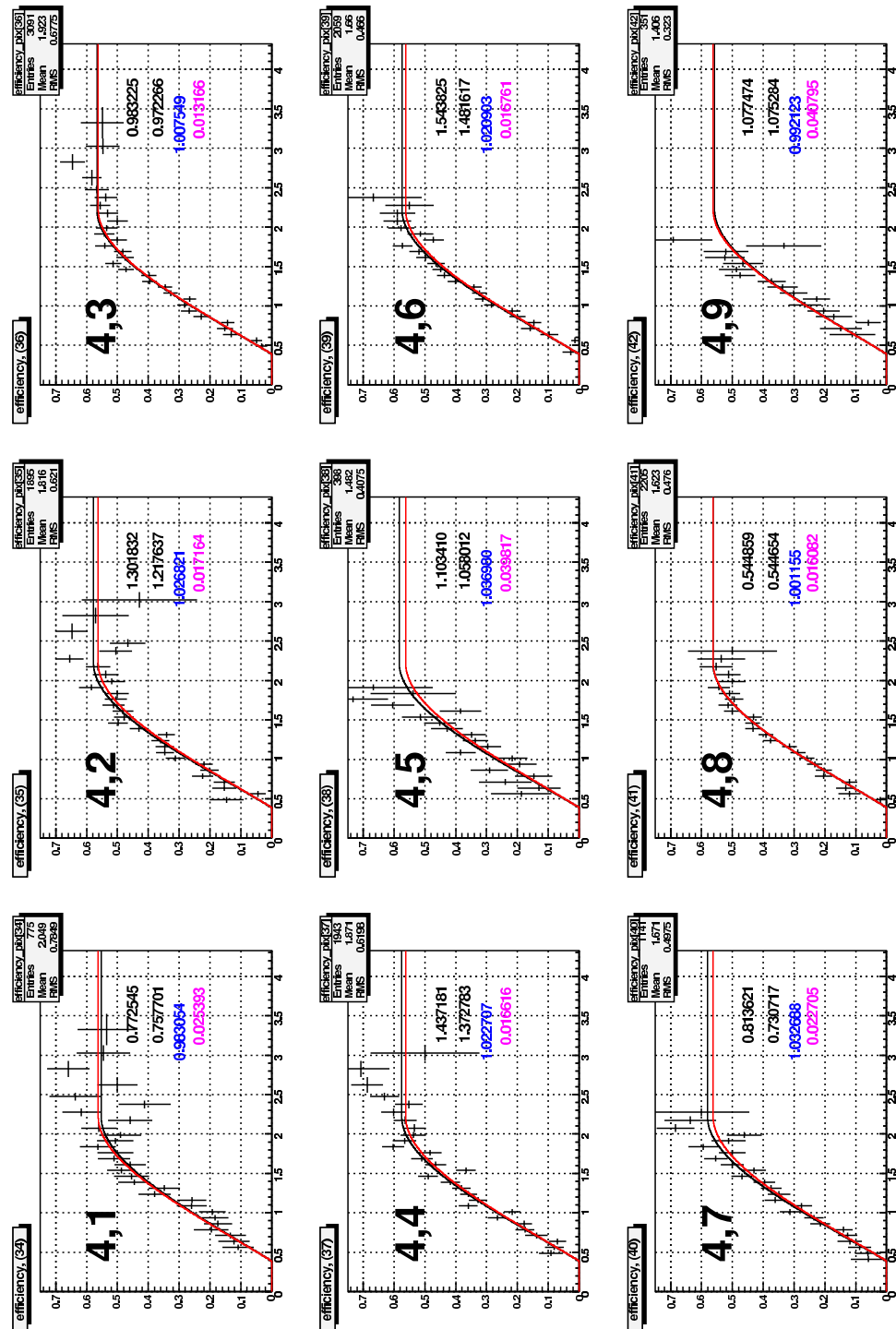


Figure B.10: Neutron detection efficiency by superpixel in sector 4, from the 4.2 GeV data. The red line shows the results of the fit to the entire sector. The black line shows the scaled sector fit.

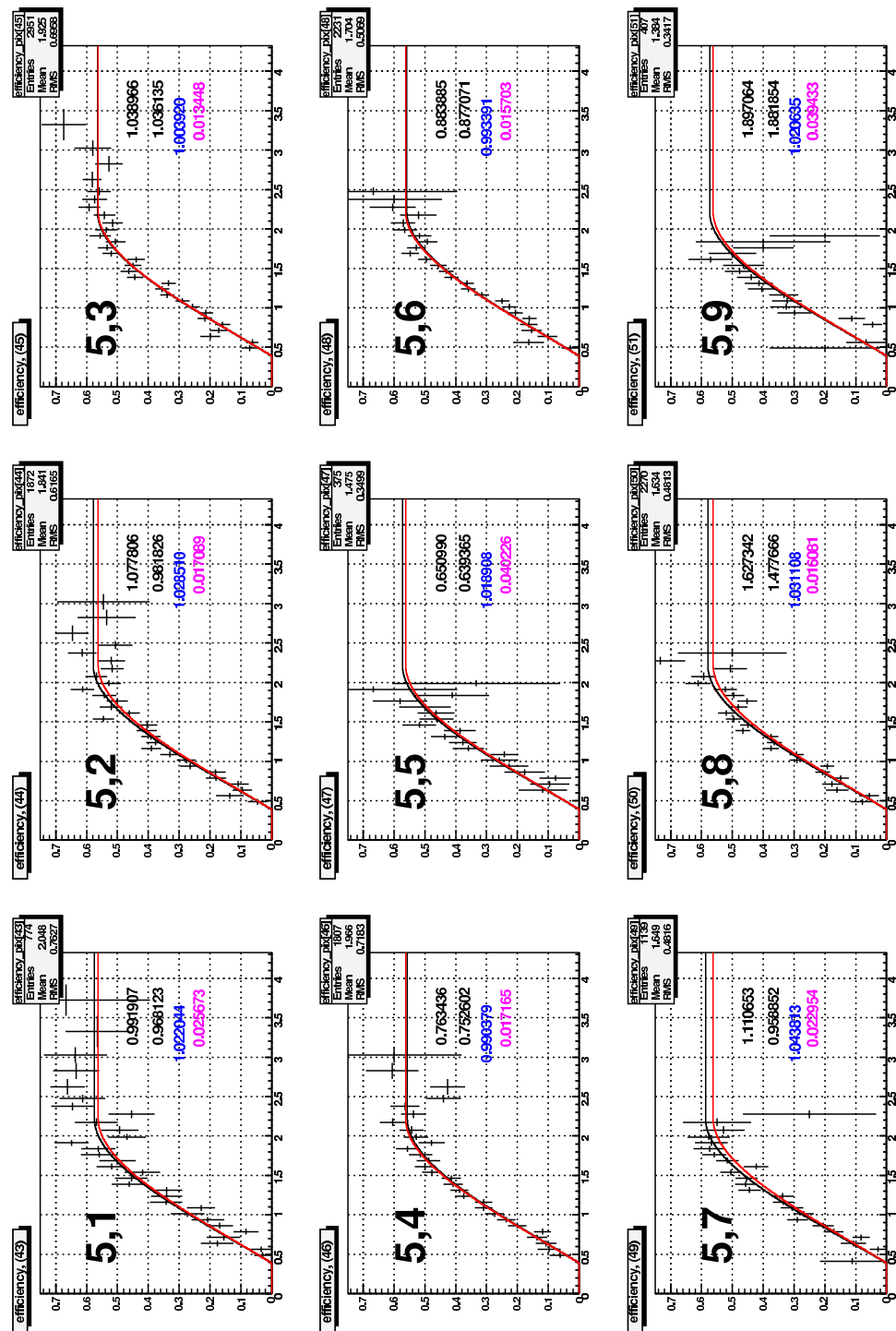


Figure B.11: Neutron detection efficiency by superpixel in sector 5, from the 4.2 GeV data. The red line shows the results of the fit to the entire sector. The black line shows the scaled sector fit.

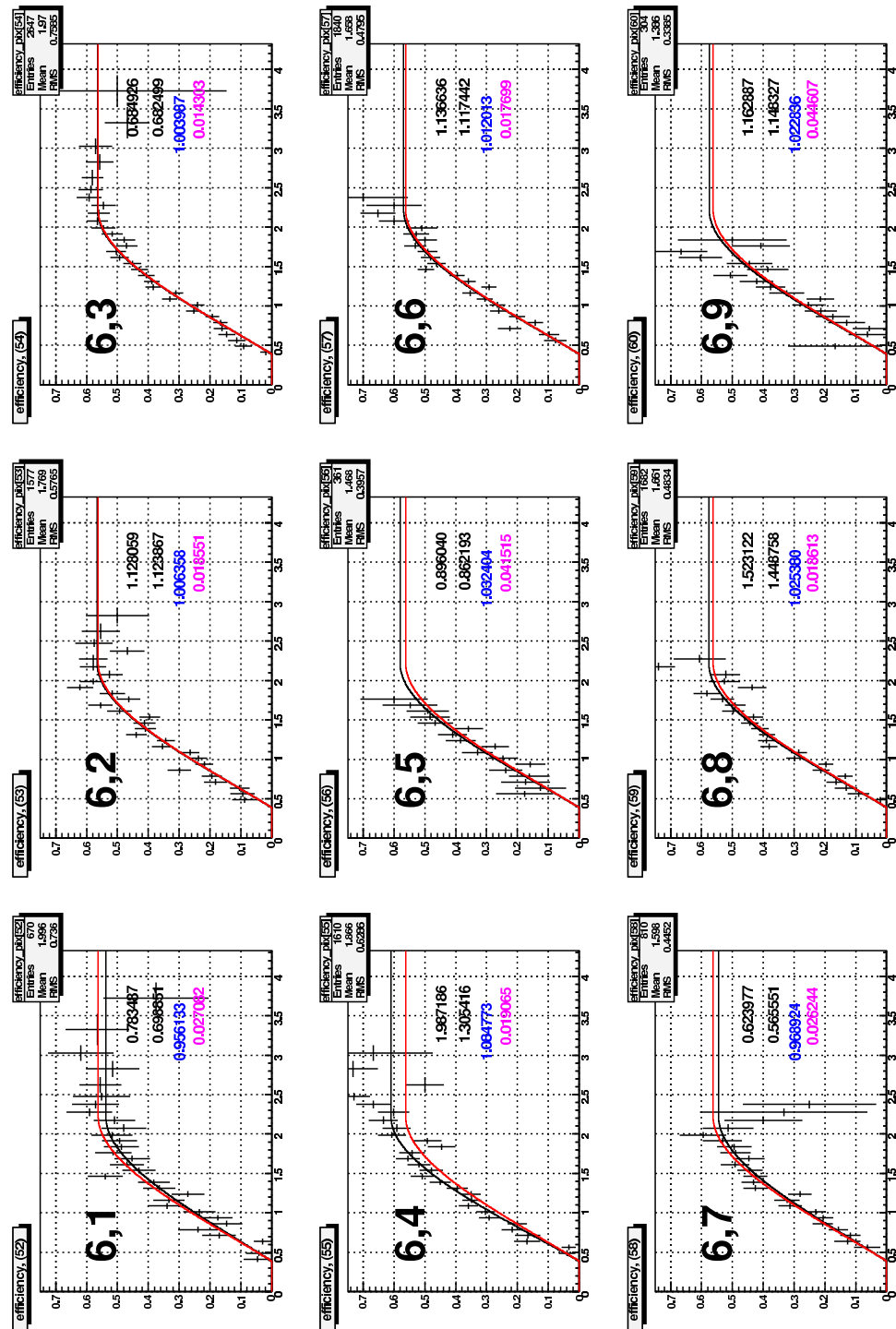


Figure B.12: Neutron detection efficiency by superpixel in sector 6, from the 4.2 GeV data. The red line shows the results of the fit to the entire sector. The black line shows the scaled sector fit.

# Appendix C

## SC neutron detection efficiency fits

### C.1 2.6 GeV beam energy

This section contains plots of the neutron detection efficiency measured on each of the paddles in each of the six sectors of the SC system, as a function of neutron momentum for the 2.6 GeV data set. Each plot is labelled by a pair of numbers  $a, b$ , where  $a$  is the sector number and  $b$  is the SC paddle number. Each plot shows a second pair of numbers. The upper number is the value of  $\chi^2/ndf$  for the comparison of the sector-based fit to the efficiency measured on the paddle. The lower number is the value of  $\chi^2/ndf$  for the comparison of the scaled, paddle-specific fit to the efficiency measured on the paddle. Two curves are superimposed on each figure. The blue number is the value of the scale factor, and the magenta number is the error on the scale factor. The red curve shows the result of the fit to the whole-sector efficiency. The black curve shows the results of scaling the whole-sector efficiency to the paddle measurements.

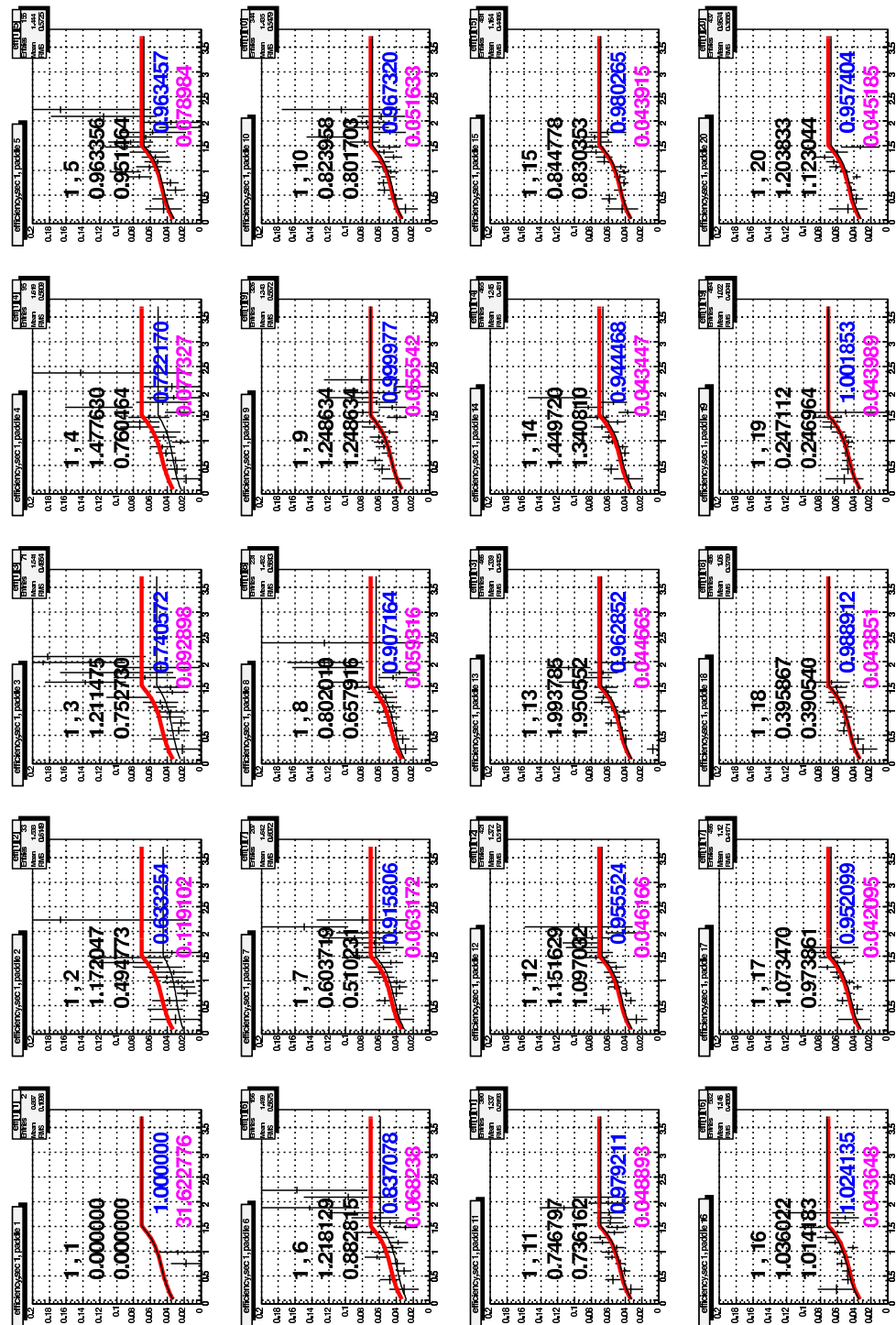


Figure C.1: Neutron detection efficiency by paddle in the SC, from the 2.6 GeV data. The red line shows the results of the fit to the entire sector. The black line shows the results of the scaled sector fits.



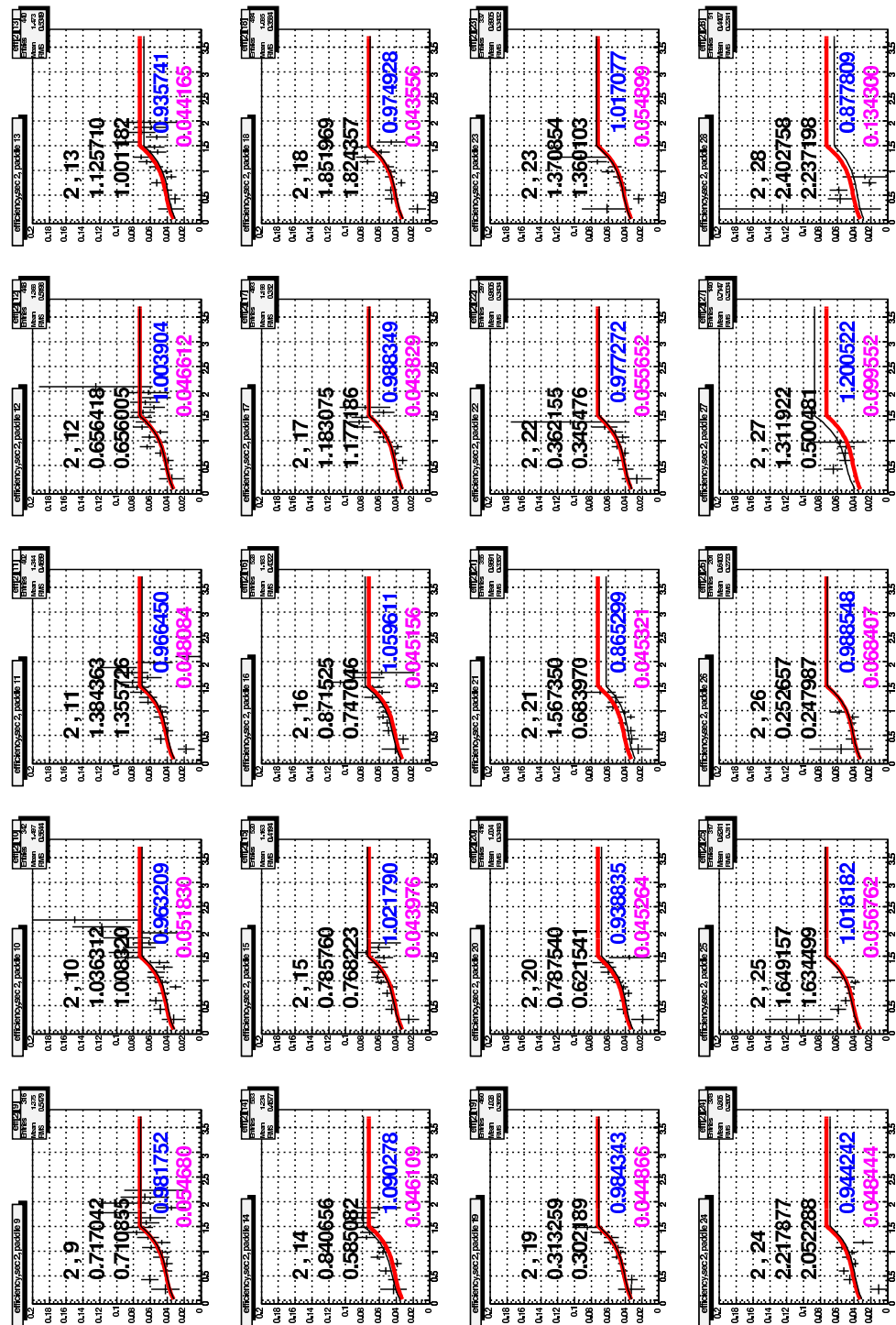


Figure C.3: Neutron detection efficiency by paddle in the SC, from the 2.6 GeV data. The red line shows the results of the fit to the entire sector. The black line shows the results of the scaled sector fits.

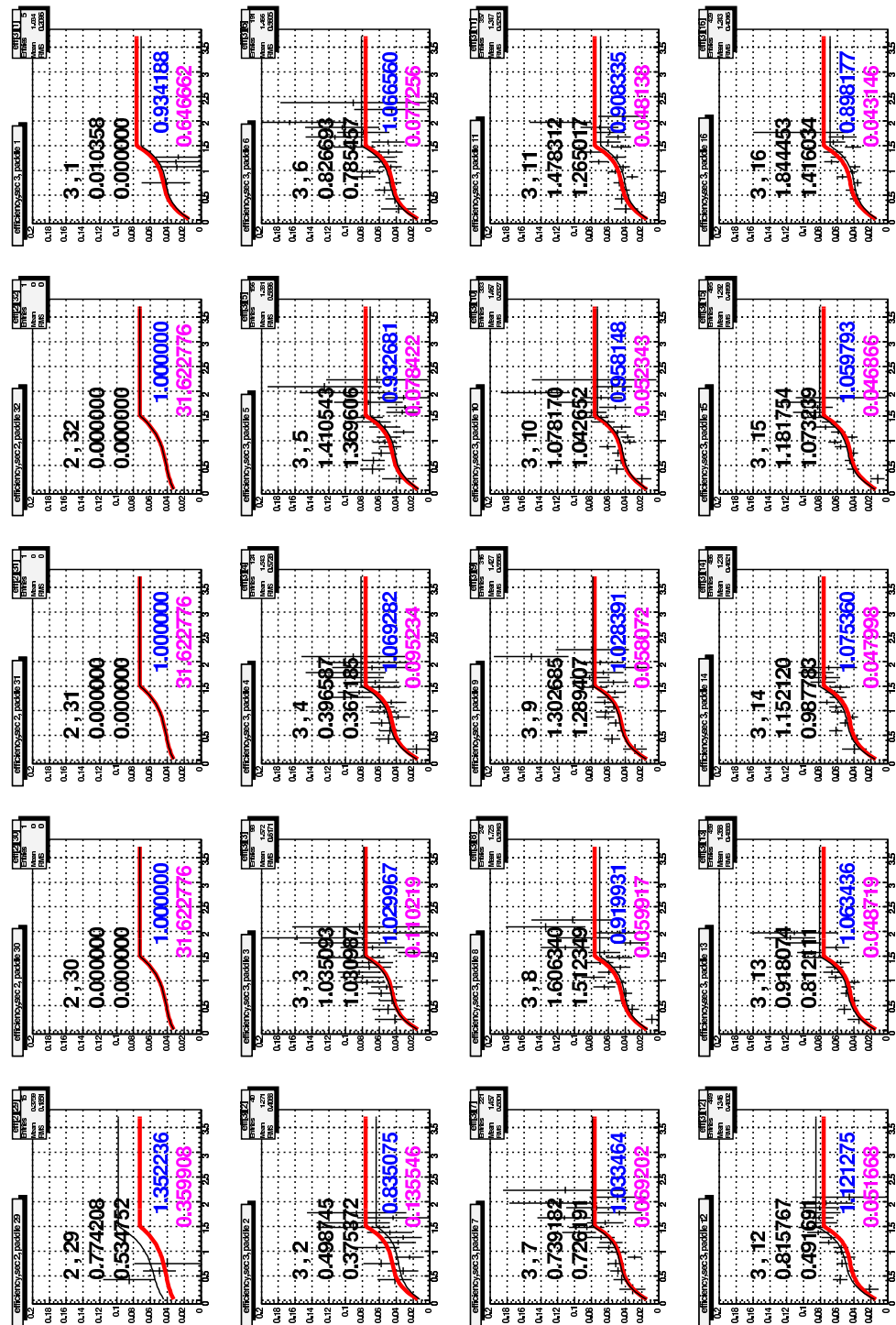


Figure C.4: Neutron detection efficiency by paddle in the SC, from the 2.6 GeV data. The red line shows the results of the fit to the entire sector. The black line shows the results of the scaled sector fits.

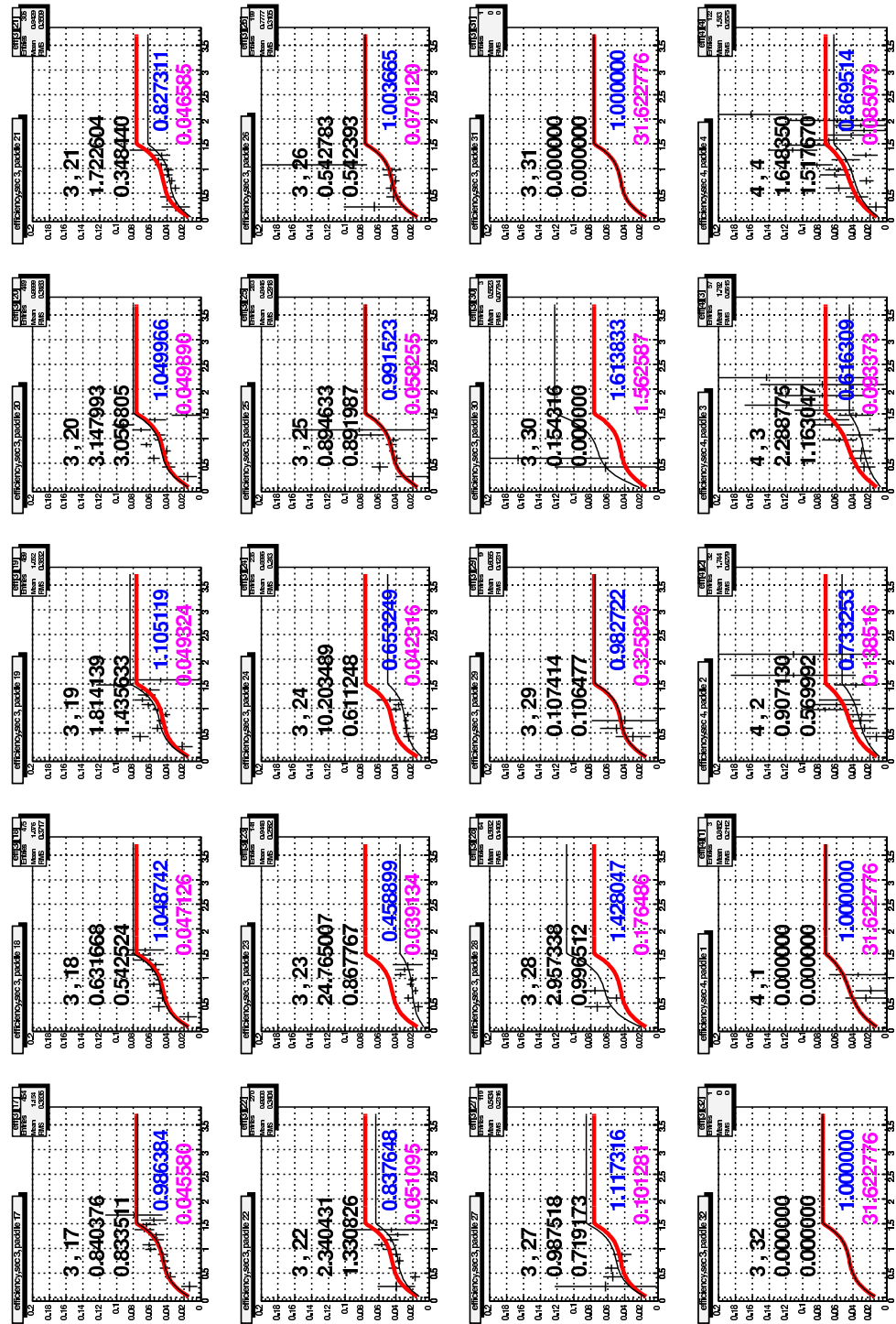


Figure C.5: Neutron detection efficiency by paddle in the SC, from the 2.6 GeV data. The red line shows the results of the fit to the entire sector. The black line shows the results of the scaled sector fits.

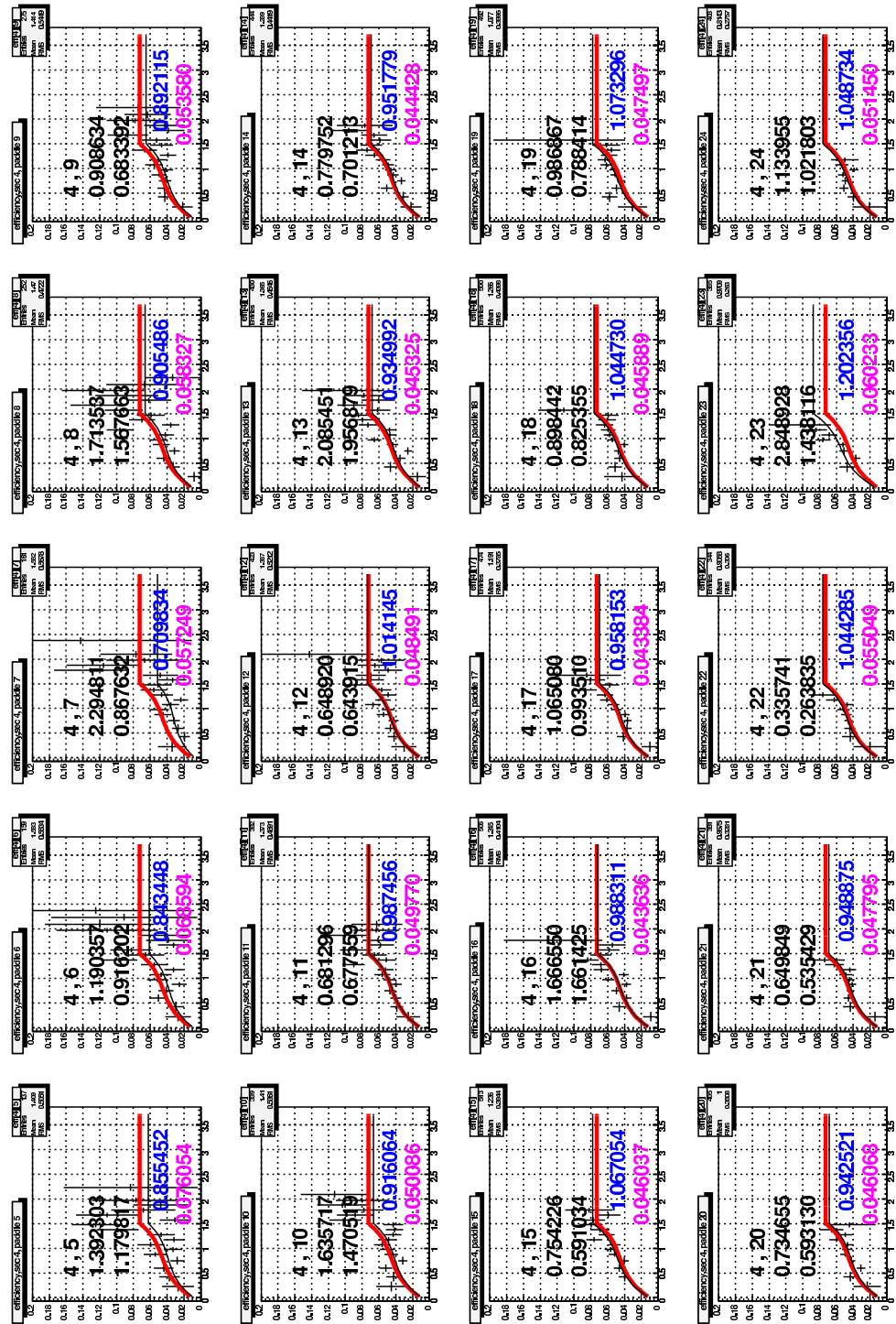


Figure C.6: Neutron detection efficiency by paddle in the SC, from the 2.6 GeV data. The red line shows the results of the fit to the entire sector. The black line shows the results of the scaled sector fits.

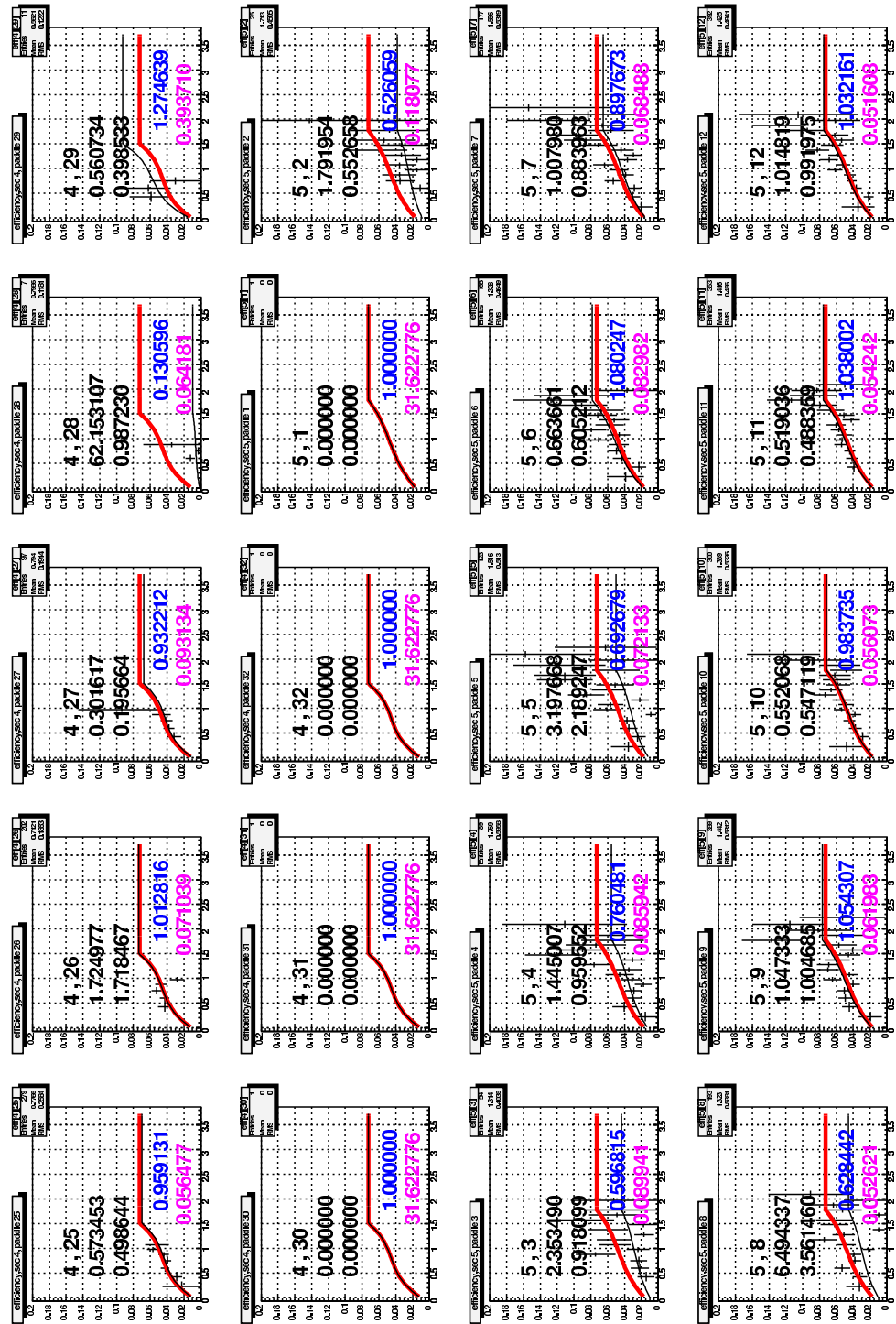


Figure C.7: Neutron detection efficiency by paddle in the SC, from the 2.6 GeV data. The red line shows the results of the fit to the entire sector. The black line shows the results of the scaled sector fits.

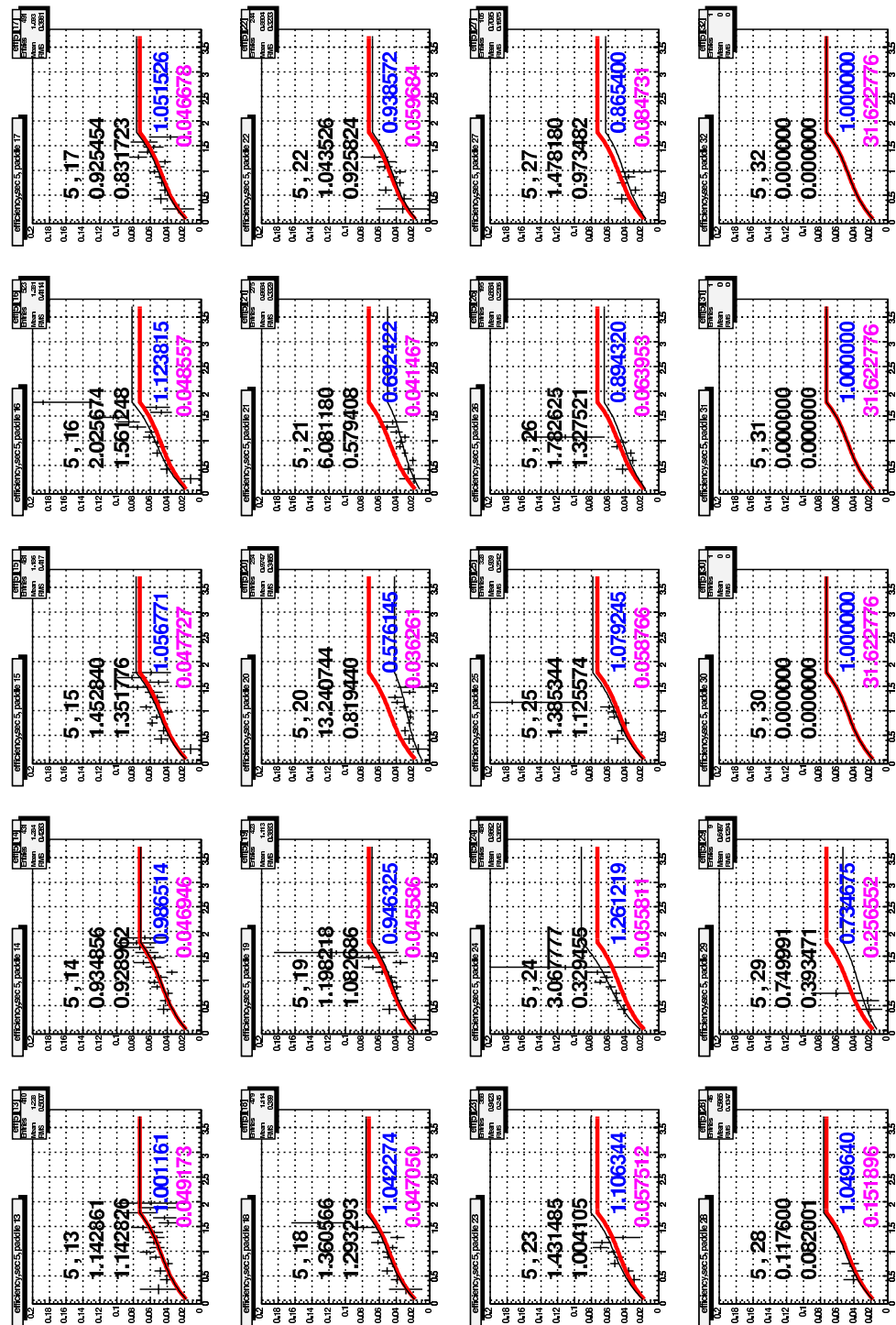


Figure C.8: Neutron detection efficiency by paddle in the SC, from the 2.6 GeV data. The red line shows the results of the fit to the entire sector. The black line shows the results of the scaled sector fits.

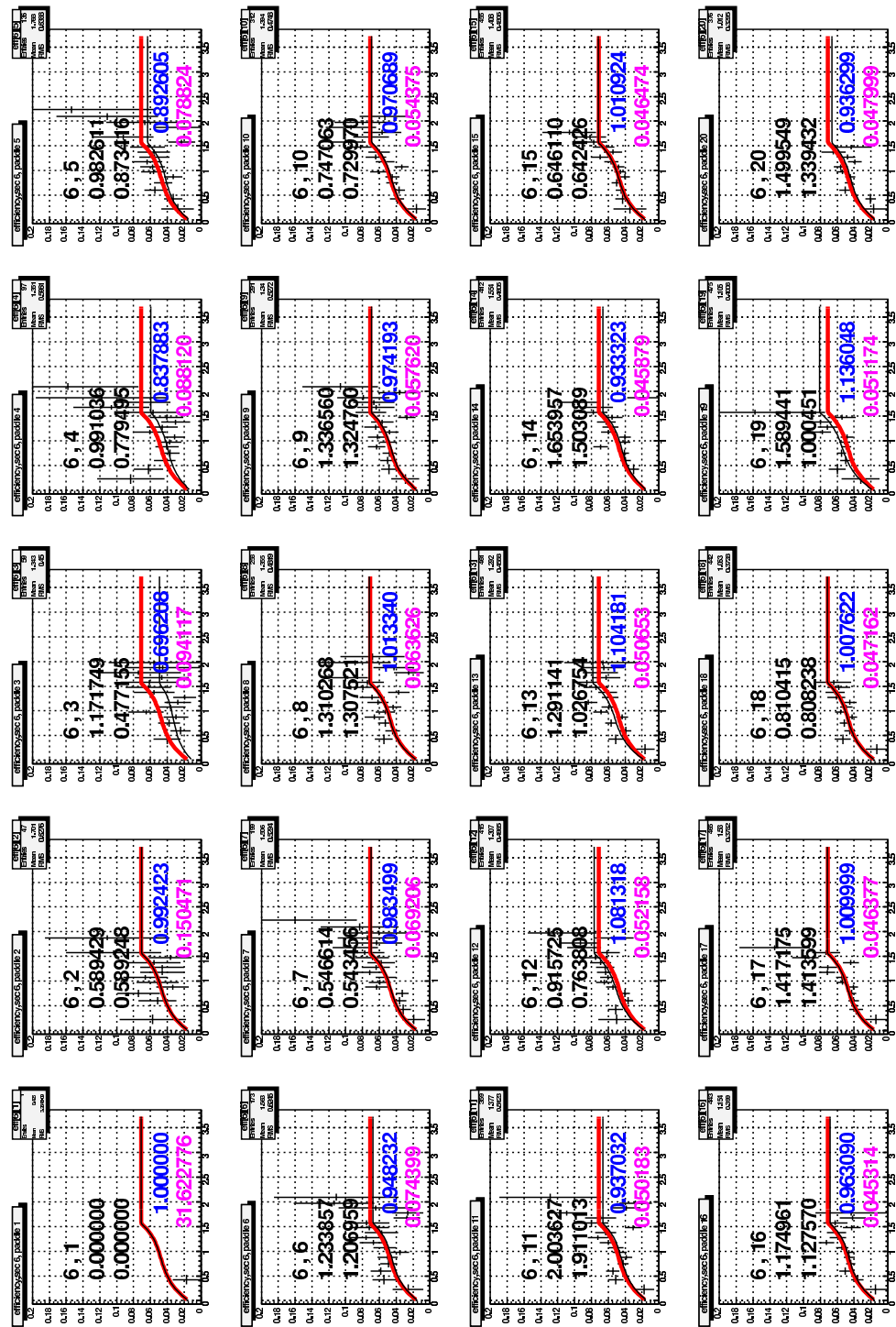


Figure C.9: Neutron detection efficiency by paddle in the SC, from the 2.6 GeV data. The red line shows the results of the fit to the entire sector. The black line shows the results of the scaled sector fits.

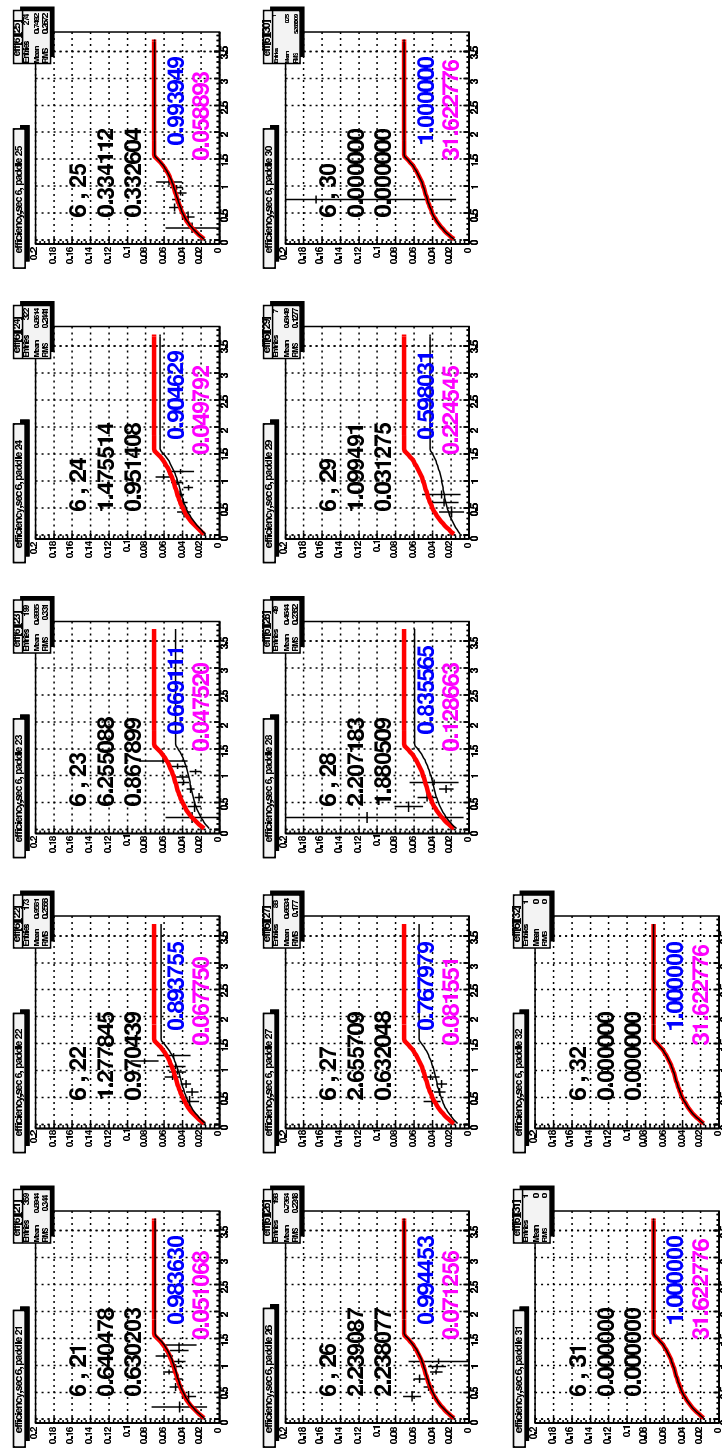


Figure C.10: Neutron detection efficiency by paddle in the SC, from the 2.6 GeV data. The red line shows the results of the fit to the entire sector. The black line shows the results of the scaled sector fits.

## C.2 4.2 GeV beam energy

This section contains plots of the neutron detection efficiency measured on each of the paddles in each of the six sectors of the SC system, as a function of neutron momentum for the 4.2 GeV data set. Each plot is labelled by a pair of numbers  $a, b$ , where  $a$  is the sector number and  $b$  is the SC paddle number. Each plot shows a second pair of numbers. The upper number is the value of  $\chi^2/ndf$  for the comparison of the sector-based fit to the efficiency measured on the paddle. The lower number is the value of  $\chi^2/ndf$  for the comparison of the scaled, paddle-specific fit to the efficiency measured on the paddle. The blue number is the value of the scale factor, and the magenta number is the error on the scale factor. Two curves are superimposed on each figure. The red curve shows the result of the fit to the whole-sector efficiency. The black curve shows the results of scaling the whole-sector efficiency to the paddle measurements.

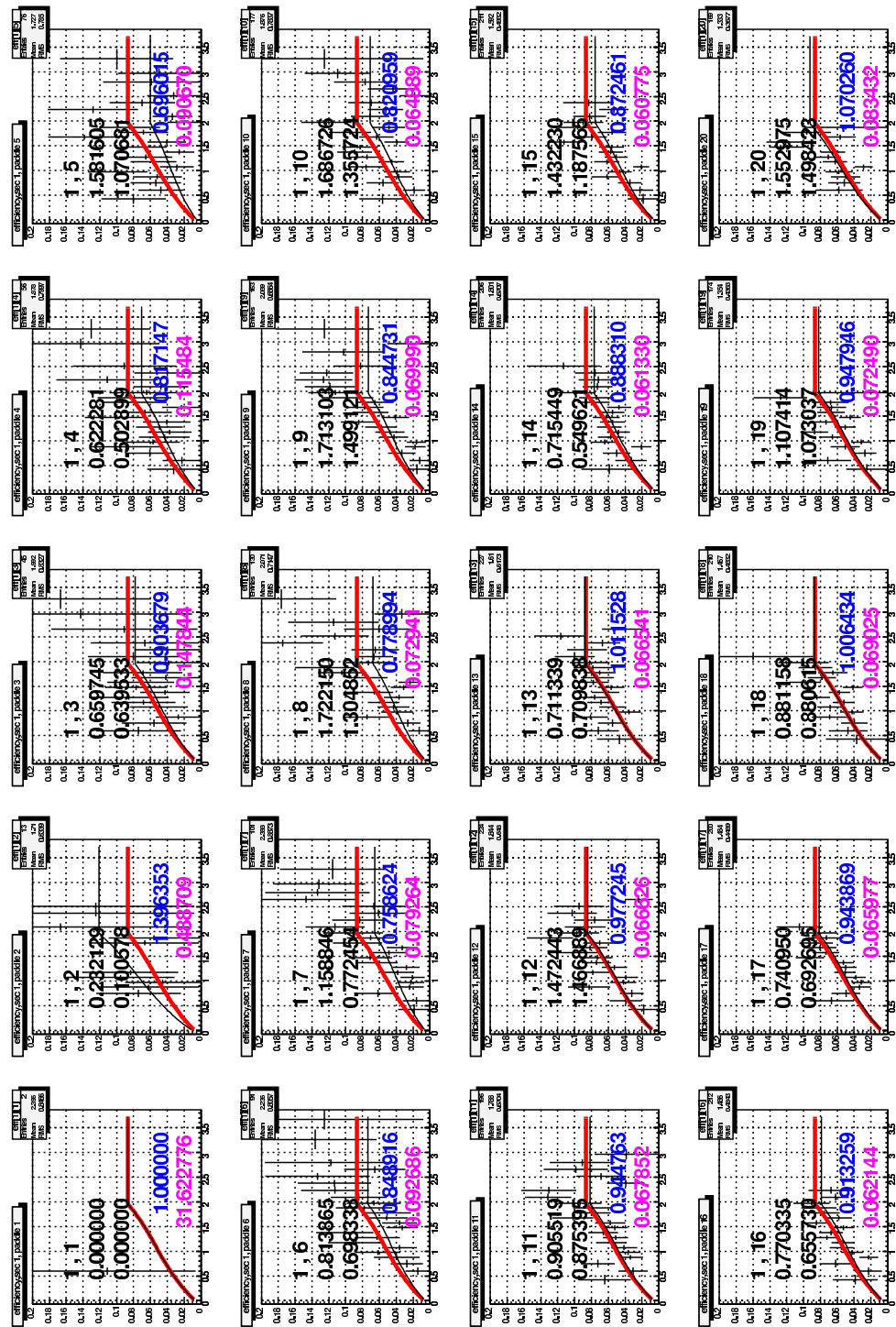


Figure C.11: Neutron detection efficiency by paddle in the SC, from the 4.2 GeV data. The red line shows the results of the fit to the entire sector. The black line shows the results of the scaled sector fits.

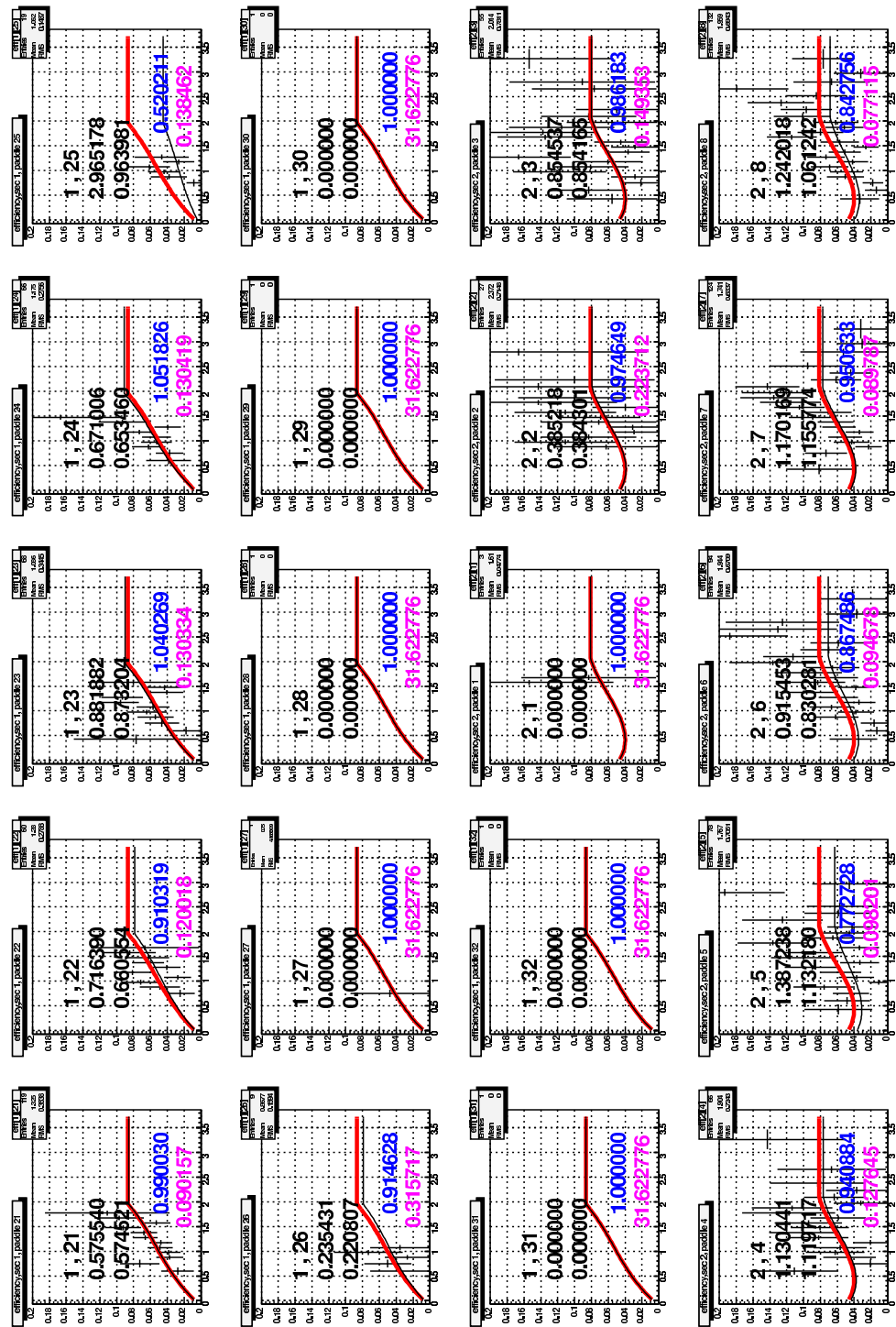


Figure C.12: Neutron detection efficiency by paddle in the SC, from the 4.2 GeV data. The red line shows the results of the fit to the entire sector. The black line shows the results of the scaled sector fits.

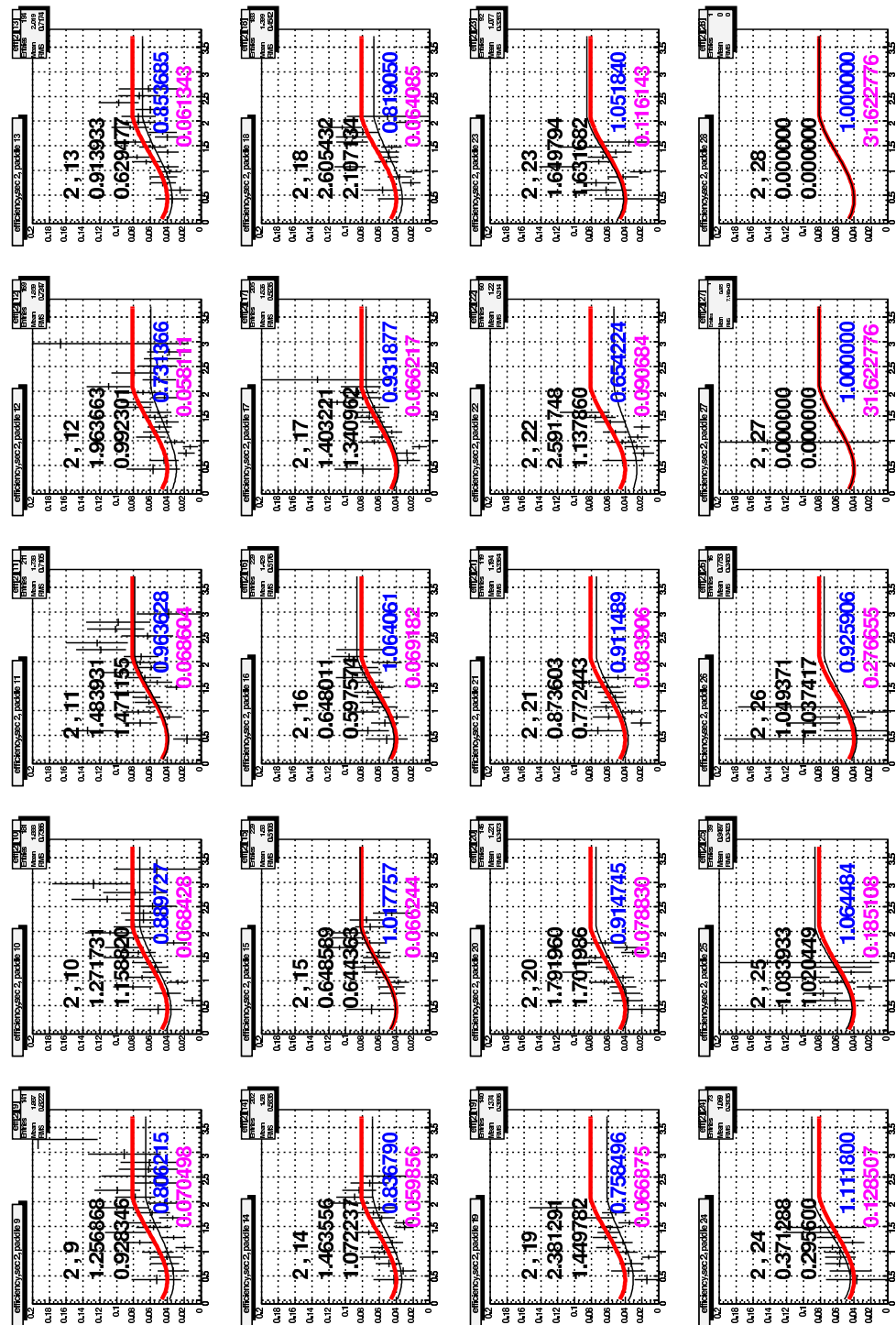


Figure C.13: Neutron detection efficiency by paddle in the SC, from the 4.2 GeV data. The red line shows the results of the fit to the entire sector. The black line shows the results of the scaled sector fits.

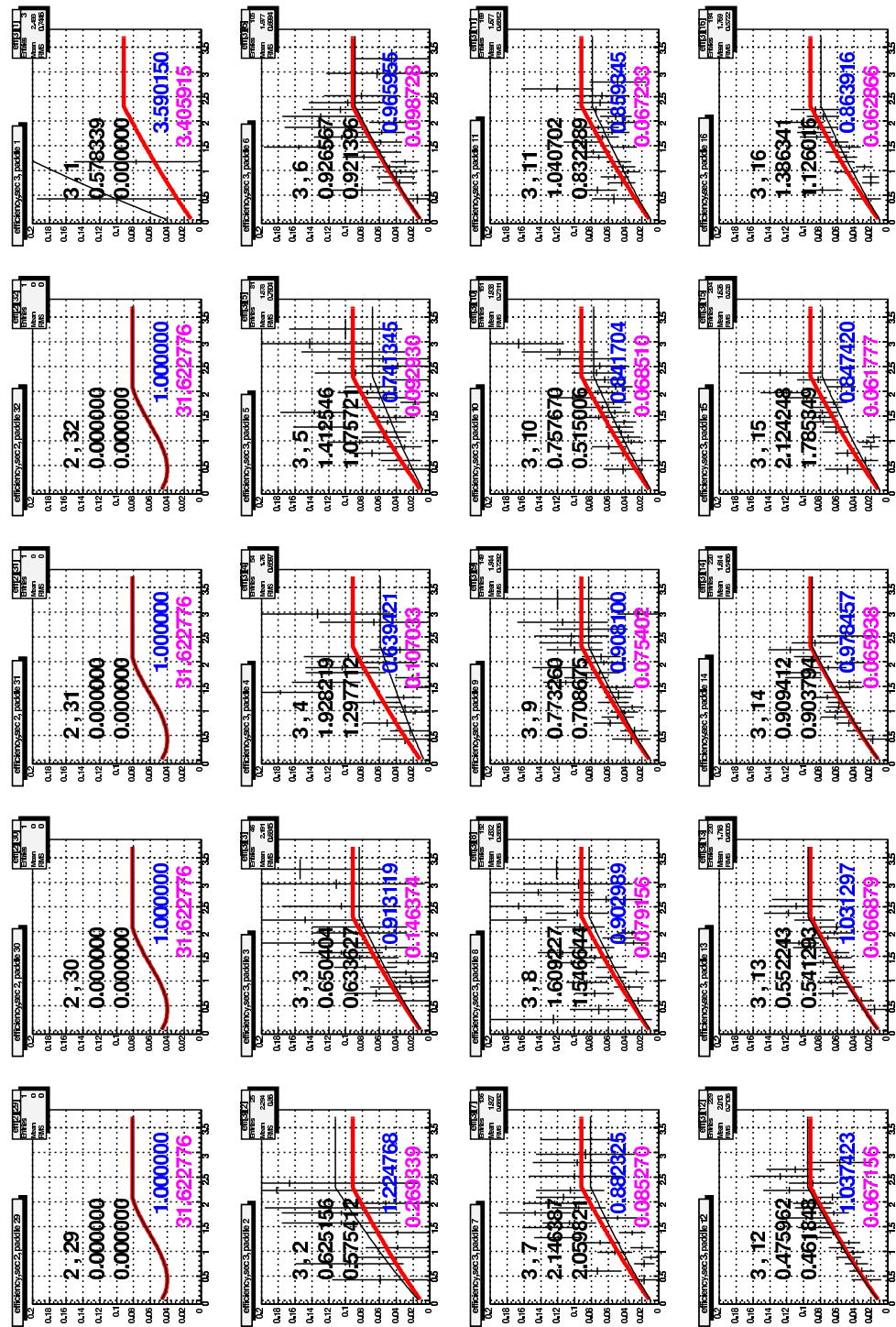


Figure C.14: Neutron detection efficiency by paddle in the SC, from the 4.2 GeV data. The red line shows the results of the fit to the entire sector. The black line shows the results of the scaled sector fits.

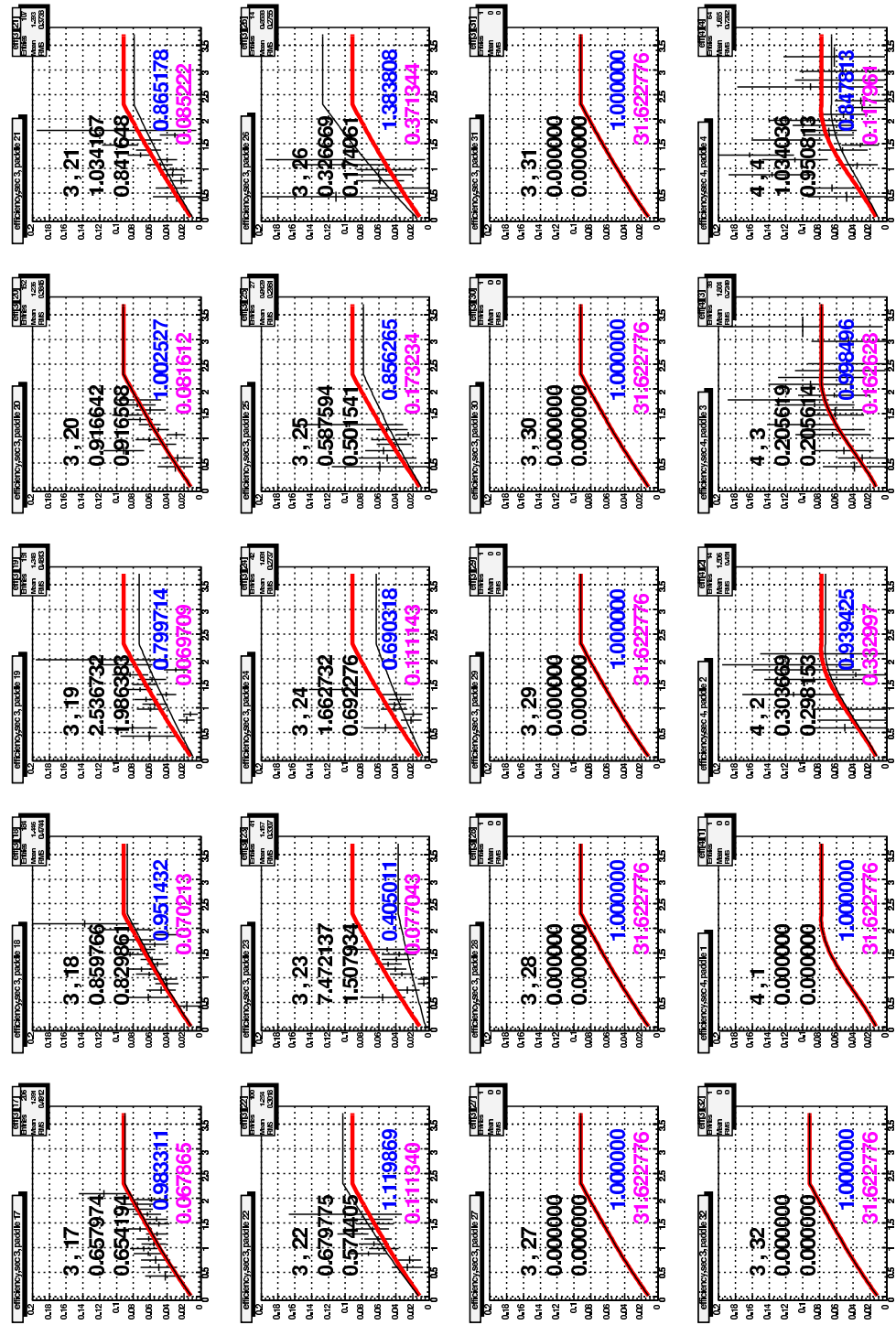


Figure C.15: Neutron detection efficiency by paddle in the SC, from the 4.2 GeV data. The red line shows the results of the fit to the entire sector. The black line shows the results of the scaled sector fits.

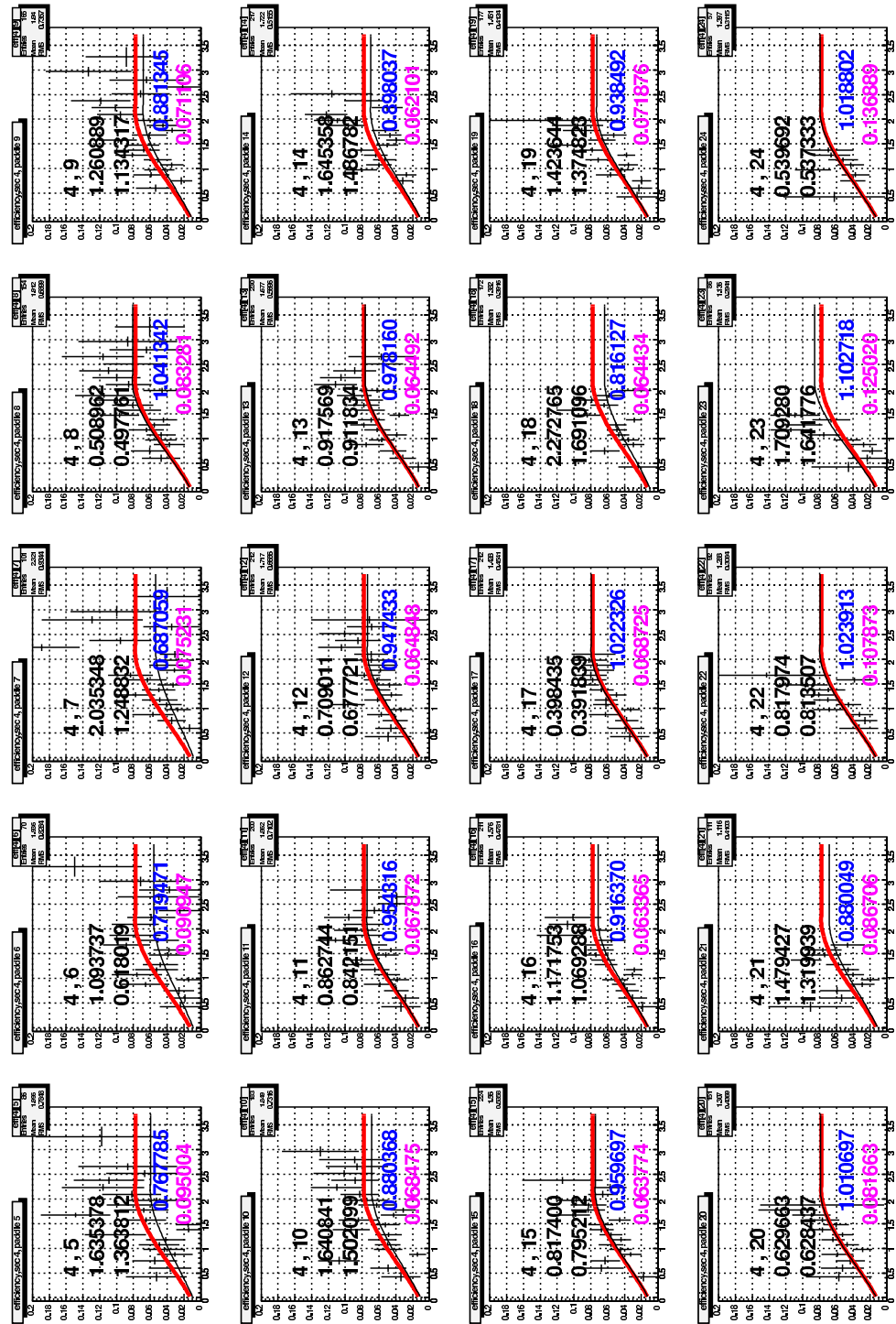


Figure C.16: Neutron detection efficiency by paddle in the SC, from the 4.2 GeV data. The red line shows the results of the fit to the entire sector. The black line shows the results of the scaled sector fits.

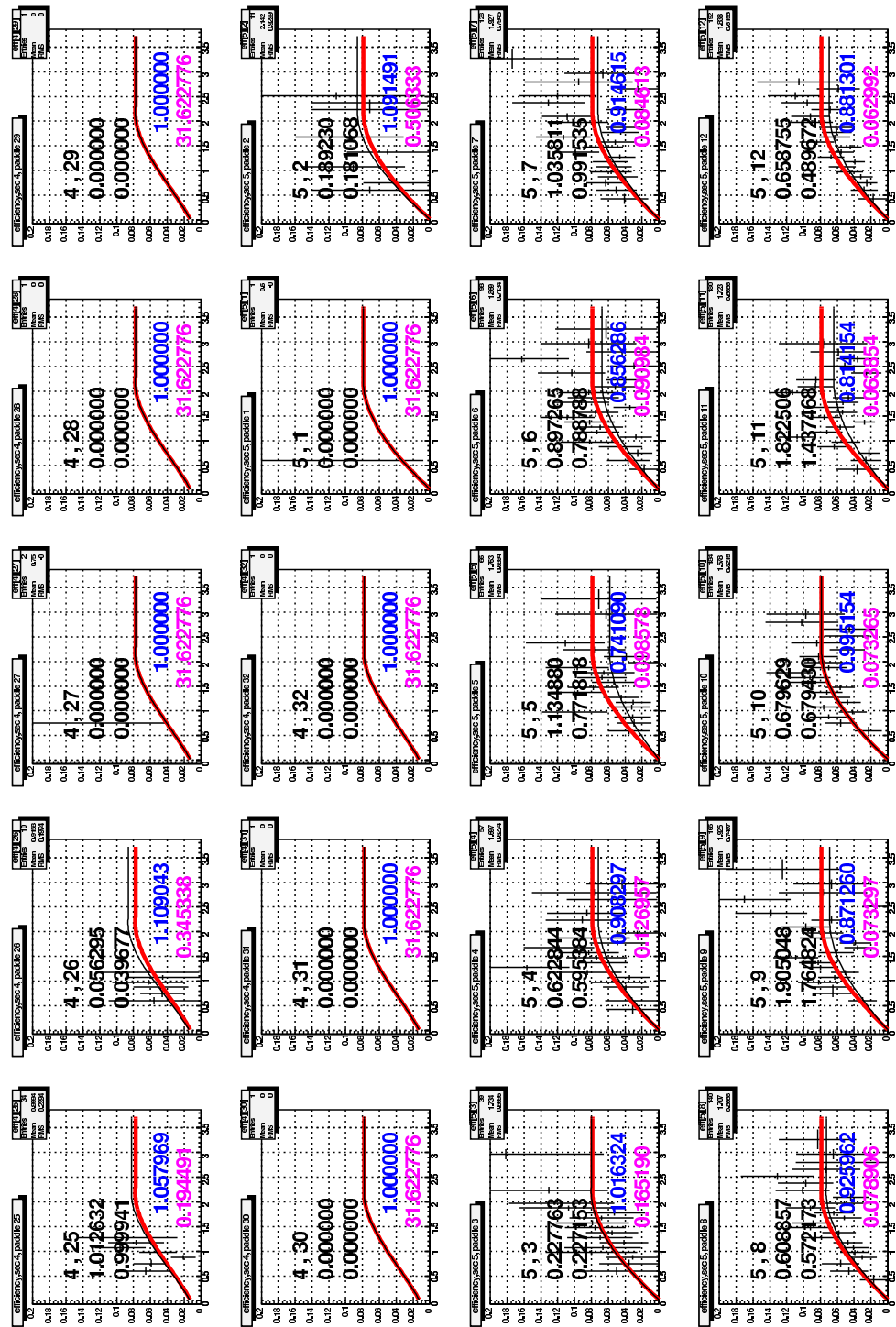


Figure C.17: Neutron detection efficiency by paddle in the SC, from the 4.2 GeV data. The red line shows the results of the fit to the entire sector. The black line shows the results of the scaled sector fits.

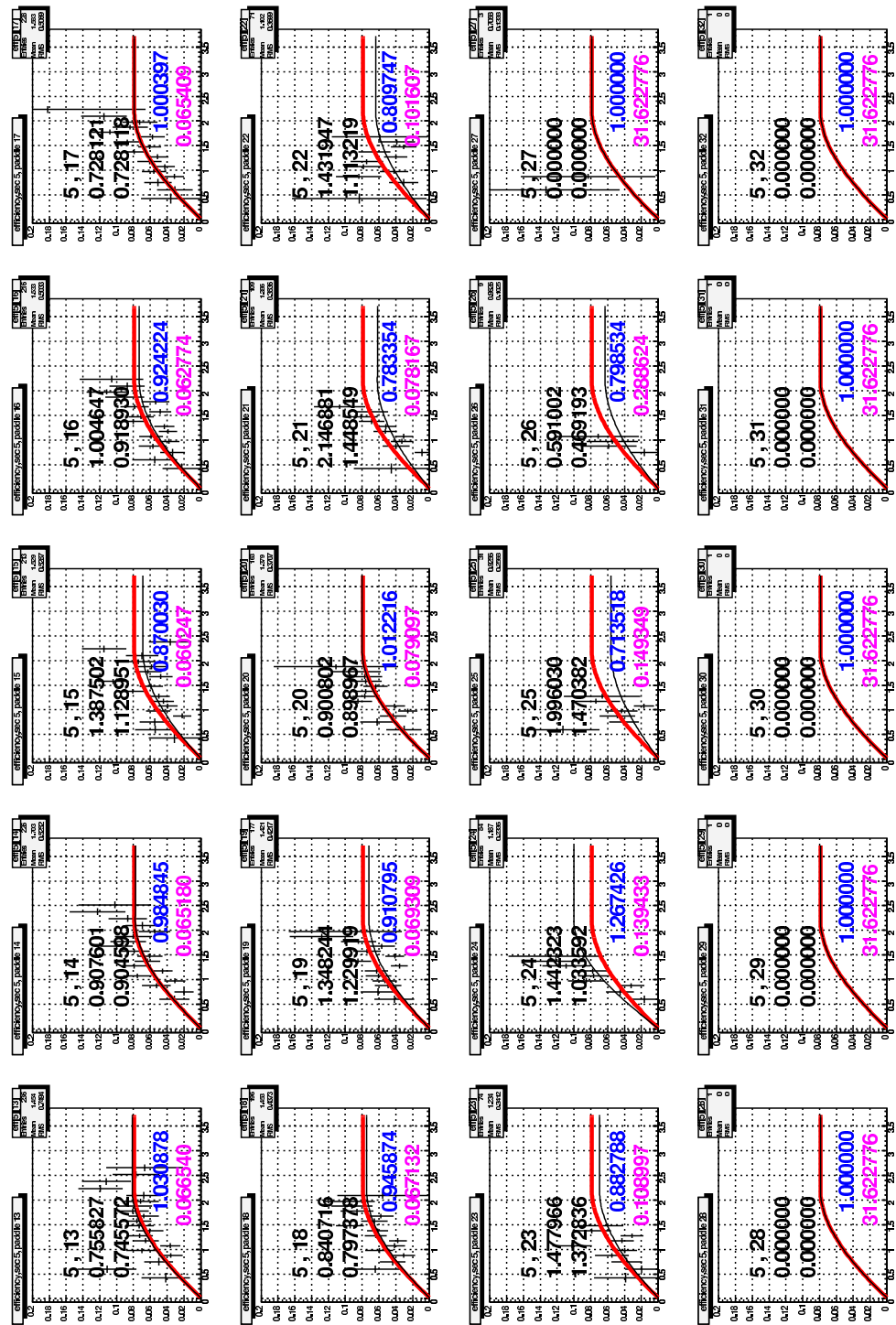


Figure C.18: Neutron detection efficiency by paddle in the SC, from the 4.2 GeV data. The red line shows the results of the fit to the entire sector. The black line shows the results of the scaled sector fits.

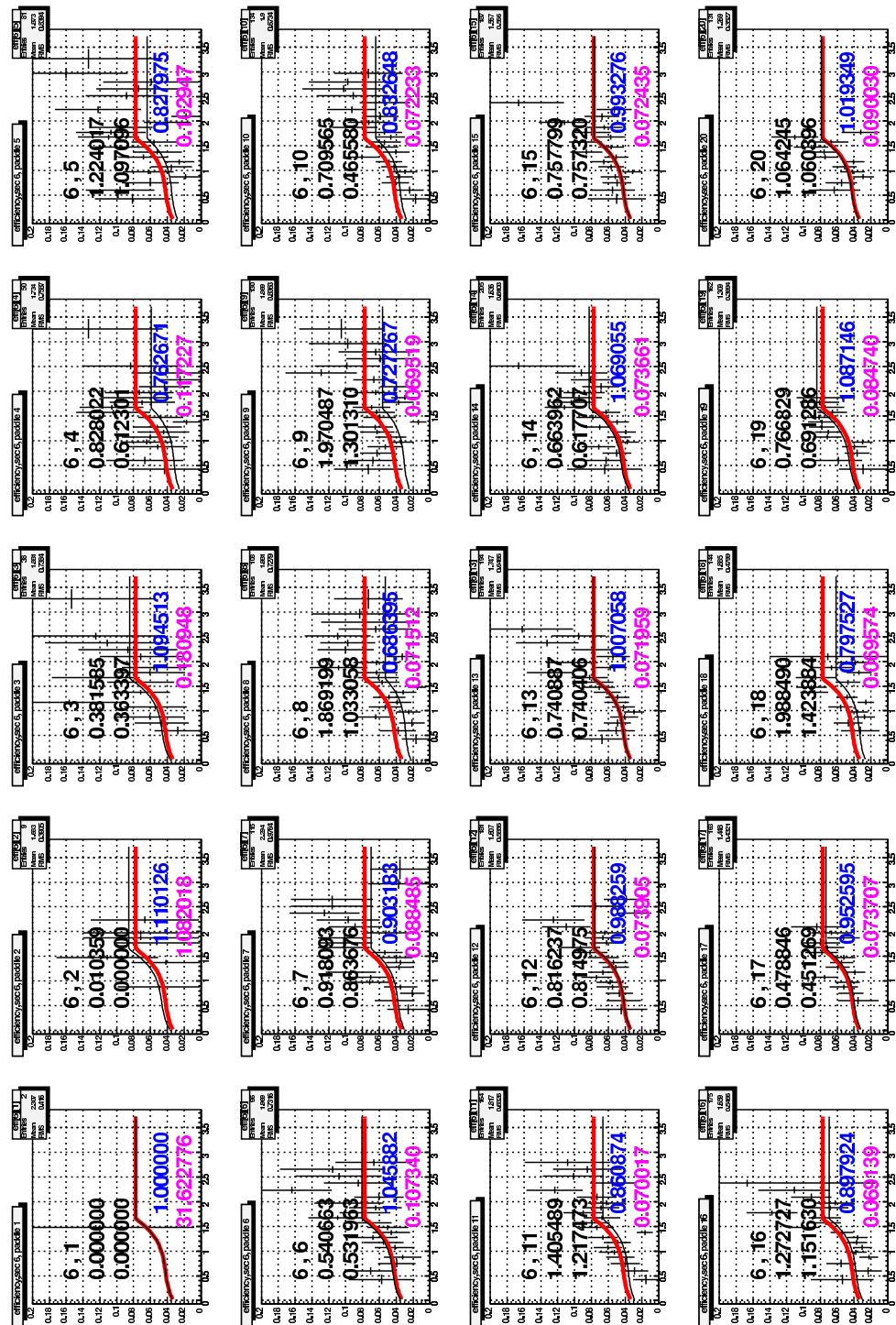


Figure C.19: Neutron detection efficiency by paddle in the SC, from the 4.2 GeV data. The red line shows the results of the fit to the entire sector. The black line shows the results of the scaled sector fits.

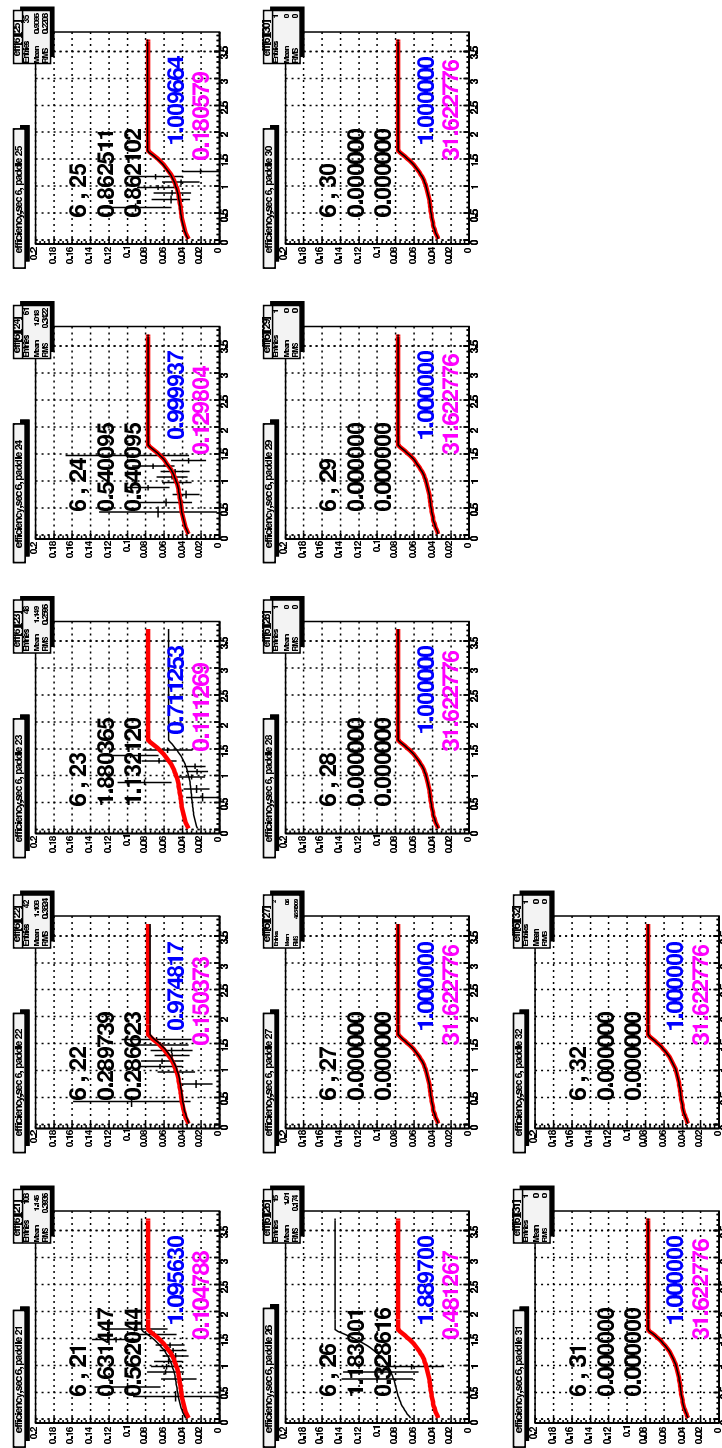


Figure C.20: Neutron detection efficiency by paddle in the SC, from the 4.2 GeV data. The red line shows the results of the fit to the entire sector. The black line shows the results of the scaled sector fits.

# Appendix D

## Kinematics of quasi-elastic scattering

There are two frames of interest for the analysis of quasi-elastic scattering: the lab frame, in which both the electron and the nucleon are moving, and the rest frame, in which the nucleon is stationary. Scattering in the rest frame is illustrated in Fig D.1.

In the rest frame, the particles have 4-momenta:

$$P_1 = E(1, \hat{P}_1) \quad (\text{D.1})$$

$$P_2 = (M_N, 0) \quad (\text{D.2})$$

$$P_3 = E'(1, \hat{P}_3) \quad (\text{D.3})$$

$$P_4 = (E'_N, \vec{P}_4) \quad (\text{D.4})$$

where  $P_1, P_3$  are the initial and final electron 4-momenta and  $P_2, P_4$  are the initial and final nucleon 4-momenta.

Scattering in the lab frame is illustrated in Fig D.2.

In the lab frame, the particles have 4-momenta:

$$P_1^* = E^*(1, \hat{P}_1^*) \quad (\text{D.5})$$

$$P_2^* = (E_N^*, \vec{p}_f) \quad (\text{D.6})$$

$$P_3^* = E^{*'}(1, \hat{P}_3^*) \quad (\text{D.7})$$

$$P_4^* = (E_N^{*'}, \vec{P}_4^*) \quad (\text{D.8})$$

where the \* denotes a lab frame quantity,  $p_f$  is the magnitude of the nucleon Fermi momentum,  $\theta_f$  is the angle between the direction of the Fermi momentum and the incident electron,  $E^*$  is the incident electron beam energy and  $E_N^* = \sqrt{M_N^2 + p_f^2}$ .

The relationship between the starred and unstarred quantities can be determined by considering invariant scalar products of 4-vectors. First,  $P_1 \cdot P_2$ :

$$\begin{aligned} P_1 \cdot P_2 &= P_1^* \cdot P_2^* \\ EM_N &= E^* E_N^* - E^* p_f \cos \theta_f \end{aligned}$$

which yields the relation between the incident electron energy in the rest frame and the incident electron energy in the lab frame:

$$E = \frac{E^*}{M_N} (E_N^* - p_f \cos \theta_f) \quad (\text{D.9})$$

Next, consider  $P_1 \cdot P_3$ :

$$\begin{aligned} P_1 \cdot P_3 &= P_1^* \cdot P_3^* \\ EE' - EE' \cos \theta_3 &= E^* E^{*'} - E^* E^{*'} \cos \theta_3^* \end{aligned}$$

which after rearrangement gives a relationship between the electron scattering angles in the two frames:

$$\frac{1 - \cos \theta_3}{1 - \cos \theta_3^*} = \frac{E^* E^{*'}}{EE'} \quad (\text{D.10})$$

Lastly, consider  $P_2 \cdot P_3$ :

$$\begin{aligned} P_2 \cdot P_3 &= P_2^* \cdot P_3^* \\ E' M_n &= E_N^* E^{*'} - E^{*'} p_f \cos(\theta_3^* - \theta_f) \end{aligned}$$

This yields a relationship between the scattered electron energies in the two frames:

$$E^{*'} = \frac{E' M_N}{E_N^* - p_f \cos(\theta_3^* - \theta_f)} \quad (\text{D.11})$$

Combining Eqns D.10 and D.11 gives:

$$\frac{1 - \cos \theta_3}{1 - \cos \theta_3^*} = \left( \frac{E^*}{EE'} \right) \left( \frac{E' M_N}{E_N^* - p_f \cos(\theta_3^* - \theta_f)} \right) \quad (\text{D.12})$$

which can be solved for  $\theta_3$ :

$$\theta_3 = \cos^{-1} \left\{ 1 - \left( \frac{M_N E^*}{E} \right) \left( \frac{1 - \cos \theta_3^*}{E_N^* - p_f \cos(\theta_3^* - \theta_f)} \right) \right\} \quad (\text{D.13})$$

This equation can be solved numerically to extract  $\theta_3^*$  given  $\theta_3$ .

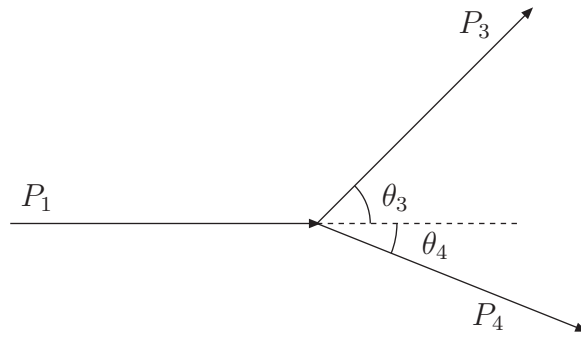


Figure D.1: Elastic scattering in the nucleon rest frame.

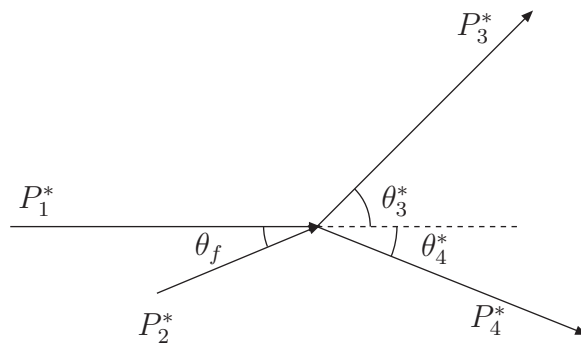


Figure D.2: Elastic scattering in the lab frame.

# Appendix E

## Response to Analysis Review Committee 1

### A High Precision Measurement of the Neutron Magnetic Form Factor Using the CLAS Detector

#### Analysis Review Committee Response I

April 6, 2007

*Jeff Lachniet, Will Brooks, Jerry Gilfoyle, Brian Quinn, and Mike Vineyard*

In order to better understand where we are in addressing the questions and comments of the review committee, the following key is being used:

- ✓ - Question/comment has been adequately addressed. (24)
- ✗ - More work is needed to address the question/comment. (0)

---

Analysis review committee members: Michail Osipenko (chair), Michel Guidal, and Henry Juengst.

We have read with great interest your note and we acknowledge thorough job done by the authors and shape of the written document. Also the presented results seem to us pretty robust and unlikely will need many changes. However, committee needs more technical details of the analysis to make it's judgement and has some (so far minor) concerns. Our requests and concerns are listed below.

With best regards,  
Mikhail, Michel and Henry.

✓ 1) Your analysis is based on "measured efficiency" while most of CLAS data are obtained with GSIM simulations. Neutron detection efficiency was studied also with GSIM (see CLAS-Note-2001-006). And off course the proton detection efficiency can be extracted with GSIM. Why don't you compare your extracted neutron/proton efficiency with GSIM? Possibly you can increase your statistics considering different acceptance area for the proton and neutron detection?

Because simulations are always an approximation to reality, it is always better to have an accurate direct measurement of efficiency than it is to simulate the efficiency. In the best case, a simulation can be used as a cross-check on the method of measuring the efficiency. CLAS efficiencies for charged particle reconstruction are usually simulated because there is often no direct way to measure the efficiency over the same phase space as in the reaction of interest. In the case of our measurement, the reaction is elastic scattering for the efficiency measurement and quasielastic scattering for the reaction of interest; these have a very similar phase space. Even if the proton momentum is Fermi-smeared, its trajectory and momentum are similar to that of the unmeasured proton. Since the efficiency is tabulated in terms of which TOF paddle is struck, the average efficiency for the Fermi-smeared protons is automatically calculated correctly.

In the case of neutrons, the accurate simulation of efficiencies is a notoriously difficult technical problem. As an example, the Kent State University neutron detection efficiency code required many years to develop and it was tested against many measurements with different scintillator types and geometries. The conclusion of these efforts is a code that has a systematic accuracy that is at best at the 5% level when used with simple geometries and well-characterized scintillators. The ingredients that make this technically difficult include: (1) There are dozens of relevant neutron cross-sections that contribute, all known with varying uncertainties, and some very difficult to measure, such as the breakup of carbon into three alpha particles, which is a non-trivial part of the neutron cross section. Thus accurate simulations require some parameterization and 'tuning' of these cross sections, always comparing to accurate measurements of the neutron detection efficiency. (2) The light 'quenching' of the particular scintillator to heavily ionizing particles such as alpha particles must be taken into account. Heavily ionizing particles do not induce as much light in scintillators as less ionizing particles which have the same energy deposit. (3) The geometries and material compositions of the detectors must be known accurately. (4) The attenuation of light in the scintillator must be known accurately, as must the electron-equivalent energy deposit threshold. In the ideal case this threshold would be calibrated for each individual scintillator element.

While it is true that GSIM simulations have been performed for neutrons (in addition to the CLAS Note referenced, one can look at Fig. 10 of the proposal for 94-017 at [http://www.jlab.org/exp\\_prog/proposals/94/PR94-017.pdf](http://www.jlab.org/exp_prog/proposals/94/PR94-017.pdf)), it cannot be expected that a simulation can produce as accurate of a result as a clean direct measurement. Following the numbered points in the paragraph above, (1) the hadronic package used by GSIM is known to be less accurate at few GeV energies and below, and there is no fine-tuning of these cross sections to reproduce neutron detection efficiency, (2) while the quenching parameterizations for known scintillators are published in the literature with reasonable accuracy, they have never been implemented in GSIM, (3) the lead thickness and scintillator thickness for individual pieces vary by +/- 5% in the forward calorimeters, but these variations are not included in GSIM, and there

is a significant amount of material (Teflon and paper filling) which is not present in the simulation, and (4) while the attenuation of light is accounted for on a strip-by-strip basis in GSIM, since the scintillators are read out in groups of 5 or 8 into one phototube, it is not possible to calibrate the energy deposit threshold on individual strips; averages can be calibrated using MIP, but these averages are not accurate for neutrons which do not sample the strips with the same relative probabilities; for a given stack of scintillators read out by one phototube, the neutrons may interact anywhere within the stack, which will usually sample a subset of the scintillator strips. One can try to work with averages, but the uncertainties on such an approach would be difficult to estimate. Even a comparison of MIP response to GSIM calculations, which can be seen in the EC paper ([http://www.jlab.org/Hall-B/pubs/ec\\_nim.ps](http://www.jlab.org/Hall-B/pubs/ec_nim.ps) or NIM A **460**, 239 (2001)) shows significant discrepancies, which is an indication of the level of understanding of the absolute energy response of the scintillator stacks.

Concerning the geometric acceptance of the proton vs. the neutron, the philosophy is to make the neutron and proton acceptance \*identical\*. The only practical way to do this is to define the geometrical acceptance of both particles by the \*electron\* kinematics. In practice this is not possible to do perfectly because of experimental resolution. Therefore, what is done in practice is to calculate the angle of the proton or neutron with respect to the angle between the nucleon and the virtual photon, and to make a loose cut on this angular distribution. While the proton and neutron resolutions are different in the region of the cut, in this region the distribution is approximately linear, so that no residual bias is introduced by making the cut.

✓ 2) The analysis is based on comparison of data from two target cells, however a description of such complex target is missing making difficult to understand if efficiency/acceptance/corrections apply to both cells exactly in the same manner.

This is a valid point. We will update the analysis document with a schematic drawing of the target as seen in Fig. E.1 and a brief description. The cells for the hydrogen and deuterium were essentially identical geometrically. The two cells were maintained at slightly different temperatures as appropriate to staying in the saturated phase of  $H_2$  and  $D_2$  separately, without risking the freezing of either cell. This was accomplished by constructing a new heat exchanger that had independent chambers and heaters for both liquids. The practical difference between the two cells was that the upstream cell, which contained deuterium, was surrounded by a thin vacuum space and this region was surrounded by aluminum with a thickness of 0.0015 in, a thin layer of liquid hydrogen, and a final layer of aluminum with thickness 0.0015 in. The details of the target can be seen in Fig. E.1. Outside of this were 3 layers of superinsulation that was common to both cells.

✓ 3) In sec. 2.3.3 there is no mention of momentum corrections (which appear later however). The question is whether those were used to select expected neutrons? Can you give the centroid of the missing neutron peak in Fig. 2.8?

The momentum corrections were derived from elastic scattering data and were only applied to the elastic and quasi-elastic data. The method used is not easily

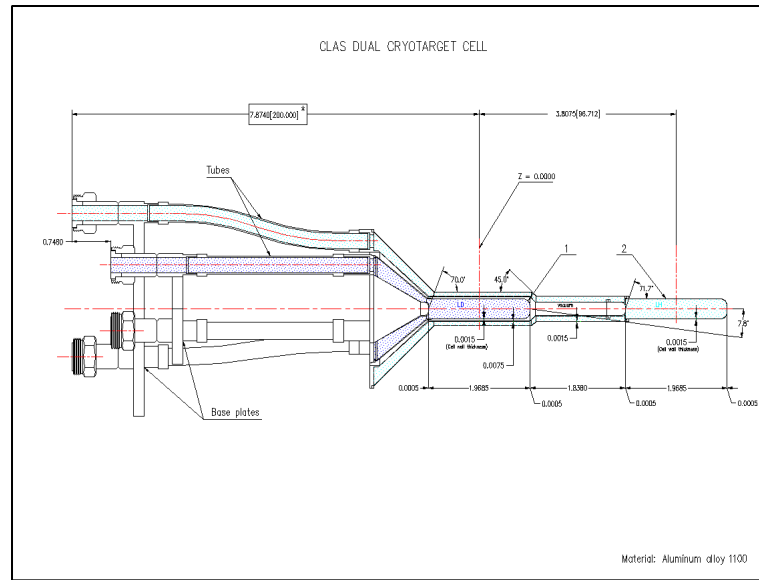


Figure E.1: A drawing of the E5 dual-cell cryotarget.

extended to inelastic reactions, and was not used in the  $ep \rightarrow e'\pi^+(n)$  reaction. A plot of the missing mass distribution fitted with a gaussian is shown in Fig. E.2. The gaussian fit has a centroid of  $0.937 \text{ GeV}/c^2$ .

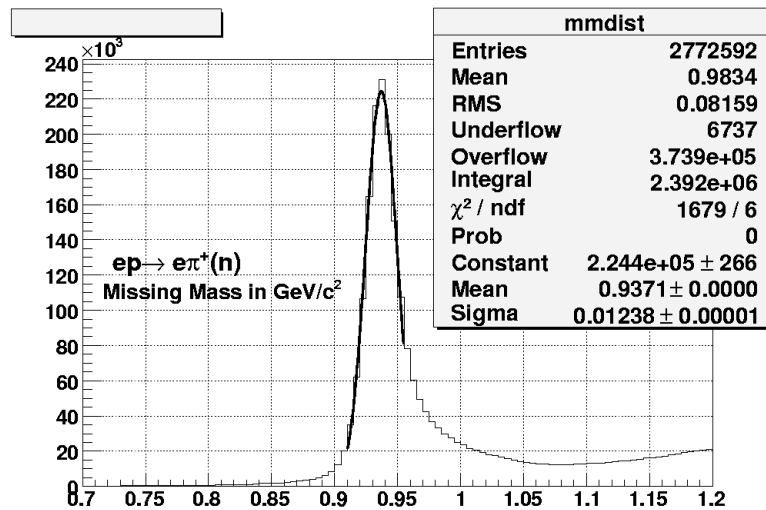


Figure E.2: Missing mass spectrum for the  $ep \rightarrow e'\pi^+(n)$  reaction. The neutron peak is fitted with a gaussian.

✓ 4) If momentum correction are used in the efficiency study then how these corrections defined for elastic scattering can be applied to a broader kinematics ( $\pi^+n$  reaction)?

Momentum corrections were not applied for the calibration reaction studies. They were not found to be necessary for the purpose of cleanly tagging events in which a neutron was produced. As shown in figure 3.15 of the analysis note, a conservative cut on missing mass was used to select only events with missing mass between 0.900 and 0.950  $\text{GeV}/c^2$ . The increase in calibration-event statistics which might be gained by relaxing this cut would be modest and did not justify the effort of attempting to improve the momentum resolution. Furthermore it is not at all clear that momentum aberrations were a dominant contribution to the asymmetric tail which was cut by this choice of missing mass range.

A slight shift in the position of the missing-mass peak resulted from the fact that no momentum corrections were applied. This, in itself, was of no consequence since the neutron peak could be clearly identified. The chief concern was that the selected events be free of contamination from two-pion production events which might cause the neutron efficiency to be underestimated. Figure 3.17 of the analysis note shows the result of a simulation with CELEG events being fed into GSIM with the gpp package used to simulate effects of finite resolution. As described in the note, the smearing of closest-approach positions in the drift chambers was increased by factors which have been found empirically to improve the match to observed data. While the simulation seems to overestimate the width of the missing mass distribution, it gives no indication of leakage of undesired events into the range of the missing-mass cut.

Further tests of purity of the selection of calibration events are shown in figures 3.18, 3.19 and 3.20 of the analysis note where estimated neutron efficiencies are shown as they would be calculated by using various strips in missing mass and treating the selected events as if they were single-pion production events. Clear evidence of contamination (resulting in underestimation of neutron efficiency) is seen only when events are chosen with a missing mass over 0.980  $\text{GeV}/c^2$ , with a possible indication of a small degree of contamination for the strip chosen with missing mass in the range of 0.960 to 0.980  $\text{GeV}/c^2$ . This provides independent support that the upper limit of 0.950  $\text{GeV}/c^2$ , which was used, safely eliminates the undesired events.

There is little concern that the small aberration due to lack of momentum corrections would cause the loss of real neutrons due to a distortion of their predicted momenta. The tolerance of 60 cm about the expected position for the EC or a full paddle width for the SC should be large enough to allow the neutron to be correctly associated with the slightly distorted momentum vector.

✓ 5) In Fig. 2.9 the  $\Delta R$  peak is shifted from zero: could you explain for how much and why?

This is simply a geometric effect.  $\Delta R$  is the radial distance from the predicted hit position to the observed hit position in the calorimeter. The area available for hits to fall within a distance  $\Delta R$  vanishes quadratically as  $\Delta R$  goes to zero and so the

probability of finding a hit within distance  $\Delta R$  must vanish as  $\Delta R$  goes to zero.

If  $\Delta x$  and  $\Delta y$  are two orthogonal transverse displacements of the observed hit from the predicted position then  $\Delta R$  is simply the quadrature sum,

$$\Delta R = \sqrt{(\Delta x^2 + \Delta y^2)}.$$

If, for example,  $\Delta x$  and  $\Delta y$  were each Gaussianly distributed with width  $\sigma$  it is easy to show that the expected distribution of  $\Delta R$  would be:

$$P(\Delta R) = \frac{\Delta R}{\sigma^2} e^{-(\Delta R)^2/2\sigma^2}$$

This agrees with the observed linear rise from zero probability at  $\Delta R = 0$ . In this simple case, the peak of the distribution is at  $\Delta R = \sigma$ . The observed shape has not been fitted, but is in qualitative agreement with this simple prediction.

✓ 6) Would it help to exploit the hit timing information in EC in the neutron reconstruction and neutron/photon separation? Can we see beta vs. p plot of the neutrons in EC?

A plot of  $\beta$  vs. p for identified neutrons can be seen in the EC paper referenced in the answer to question 1 above. It is important not to introduce a momentum bias into the neutron detection efficiency. The calculation of  $\beta$  and its resolution are strongly momentum-dependent. Making a cut on this quantity in both the calibration reaction and the quasielastic reaction is possible in principle, but we feel that it would not be worth the effort and risk. The primary photon rejection technique that we use is to make a loose cut on the direction of the neutral hit relative to its direction as predicted from quasi-elastic kinematics. The residual background, which includes photons, can be estimated by the background under the missing mass, and it is seen in Fig. E.2 to be small.

✓ 7) Fig. 2.33 (2.37) does not give an impression that neutrons can be clearly separated (from photons?) by  $E_{dep} > 5$  MeV cut. How the remaining background (if any?) is removed? By angular cuts? Can you add plots of angular reconstruction quality ( $\theta_{\text{expected}} - \theta_{\text{measured}}$  and  $\phi_{\text{expected}} - \phi_{\text{measured}}$ ) and their correlations with  $E_{dep}$ ?

Certainly not all photons can be separated from neutrons by a cut on energy deposited. The cut which distinguishes the two is the time-of-flight cut, given by equation 2.36 and shown in figure 2.16. The cut on  $E_{dep} > 5$  MeV is used to eliminate a large flux of very low energy photons and to select events for which time resolution is adequate to allow a meaningful cut on time-of-flight to be applied.

Many of the low energy-deposited events are expected to result from photons (appearing as a broadly spread background in Figure 2.16). Some of the events are expected to result from neutrons which happen to deposit relatively little energy in the scintillator. These may result in some enhancement of the black curve over the green one near  $\Delta t = 0$  in that figure. The time resolution is degraded for such low

energy-deposited and the background is seen to be large. It is therefore not possible to distinguish those low energy-deposited neutrons from the photons.

✔ 8) In section 2.3.4.1 you mention the cut on EC deposited energy for neutrons: 30 MeV, but there is not any plot showing this distribution. Justify the cut and show correlation plot with  $\Delta R$ .

Actually the cut is not at 30 MeV, but at 15 MeVee. (A typo in the note gives the incorrect units of 15 MeV instead of 15 MeVee).

This is not a very significant cut, removing only a very small fraction of neutral candidate events which have anomalously low energy-deposited. Fig. E.3 shows the distribution of energy-deposited (in MeVee) by neutral hits (in the sector where a neutron is expected). The second plot is the same thing, but expanding only the region from 0 to 100 MeVee. It can be seen that the 15 MeVee cut eliminates a very small fraction of the events. (Since such hits are eliminated in the calibration as well, they are not expected to directly contribute any systematic error.)

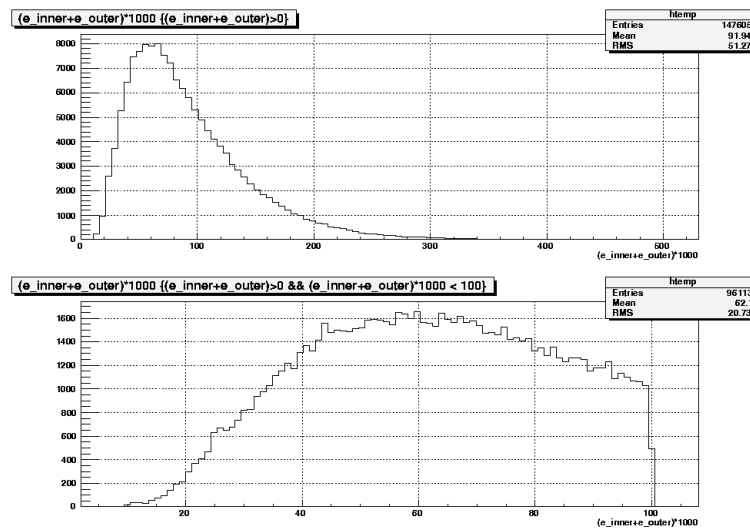


Figure E.3: Distributions of energy-deposited (in MeVee) by neutral hits in the sector where a neutron is expected.

The concern that the cut might be too low, allowing contamination by accidental background is addressed by a separate study. A search was made for neutral hits in the wrong sector, different from that in which the neutron was actually expected. Once all neutron-selection cuts were applied, no background events survived in the EC.

Section 2.6.3 fails to mention that this cut was also applied in selecting quasi-elastic neutrons from the deuterium target, as was the time-of-flight cut for neutrons

detected in the SC. Text will be added to indicate that these cuts are applied to the measured neutrons as they are applied to calibration events.

✔ 9) EC neutron efficiency is obtained separately for each "superpixel" (12 scintillator strips) while in SC for each separate scintillator paddle. Can the averaging over 12 strips in EC wash out single paddle problems? How did you check this?

We formed EC superpixels to compensate for limited statistics in the smaller and much more numerous EC pixels (there are about 1296 triangular pixels on the face of each calorimeter). If there is a problem with a single paddle in a superpixel, it will effect the scale factor for that superpixel (see Section 2.3.4.2 of the analysis note) and be incorporated into the neutron detection efficiency for that part of the EC. To test this idea we developed a method for identifying single-paddle problems in the EC and then studying their effect on the  $G_M^n$  measurement.

To identify problems with individual paddles in the EC, we examined the distribution of 'single-pixel'  $\pi^+$ 's in the EC. Positive pions tend to be minimum ionizing and are used to tag the neutrons in the neutron detection efficiency measurement. If this pion efficiency is uniform across the EC, then we expect the efficiency of the neutrons will also be uniform. The large number of pions will give us abundant statistics. We focused on single-pixel events simply to make it easier to detect paddles that may be malfunctioning.

Figures E.4-E.6 show the U, V, and W distributions for positive pions at 2.6 GeV with reversed torus polarity. The reversed polarity data are better for this comparison because the  $\pi^+$ 's strike the entire face of the EC. For normal torus polarity settings portions of the EC see very few  $\pi^+$ 's. We required that all events have no more than one strip firing for each EC view (U, V, or W) to select single-pixel events and minimum ionizing particles. As a result all of the events in Figs. E.4-E.6 are single-pixel EC events which we bin in EC strip number for each view.

Figures E.4-E.6 show the count rates for each EC strip in each view and broken down by sector. Some significant variations from sector to sector and strip to strip can be seen. For example, sector 2 in Figure E.6 (W view) shows 'holes' (low-efficiency components) among strips in the range 25-30. To test the effect of these inefficiencies on our results, we repeated the extraction of  $G_M^n$  from the 4.2-GeV data excluding sector 2 from the analysis. The results are shown in Figure E.7. Leaving sector 2 out has little effect on  $G_M^n$ .

For completeness, we did the same test on all of the sectors. Figure E.8 shows  $G_M^n$  extracted with a different sector excluded in each panel. Sector 1 is excluded in the upper-left panel, sector 2 in the upper right, sector 3 in the middle left, sector 4 in the middle right, sector 5 in the lower left, and sector 6 in the lower right. Again, there is no significant effect on the measurement.

To make a more global test of the effect of inefficiencies on  $G_M^n$  we excluded all super-pixels whose scale factor varied by more than 10% from the average for the sector as a whole (i.e.  $0.9 < \alpha < 1.1$ ). The results are shown in Figure E.9. Again there is little effect on  $G_M^n$ . We saw similar results when we increased and decreased the

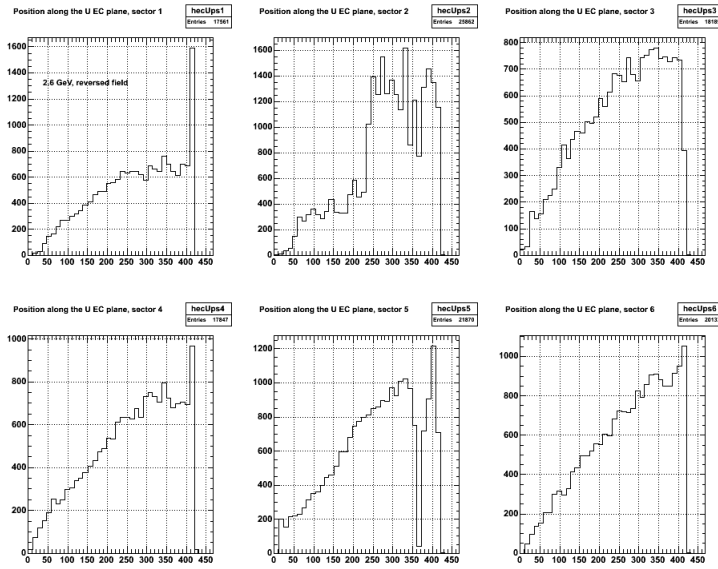


Figure E.4: Distribution of counts in the U-view of the EC for single-pixel  $\pi^+$  events for the 2.6-GeV, reversed torus polarity data.

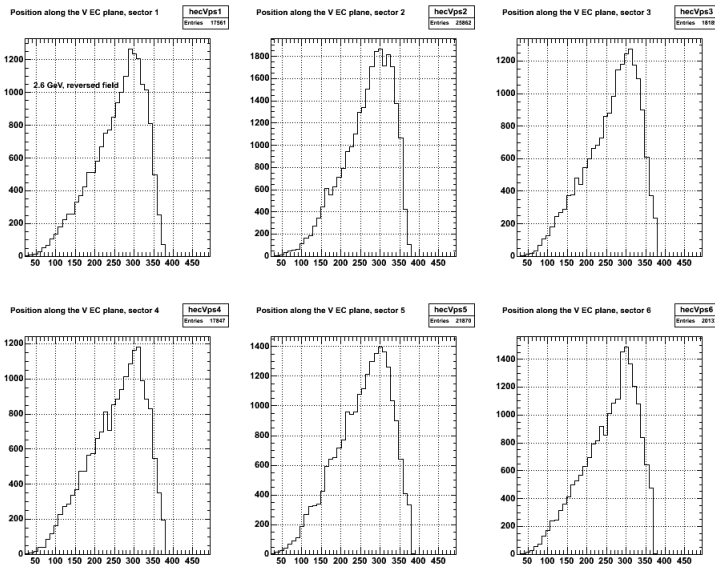


Figure E.5: Distribution of counts in the V-view of the EC for single-pixel  $\pi^+$  events for the 2.6-GeV, reversed torus polarity data.

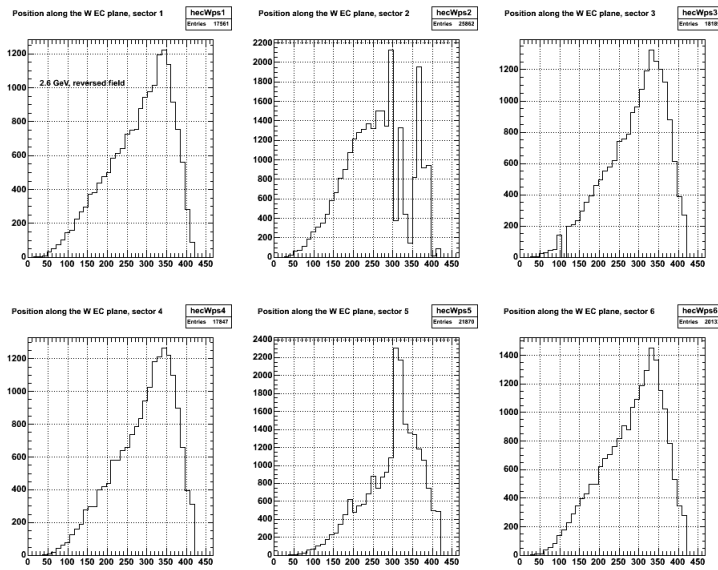


Figure E.6: Distribution of counts in the W-view of the EC for single-pixel  $\pi^+$  events for the 2.6-GeV, reversed torus polarity data.

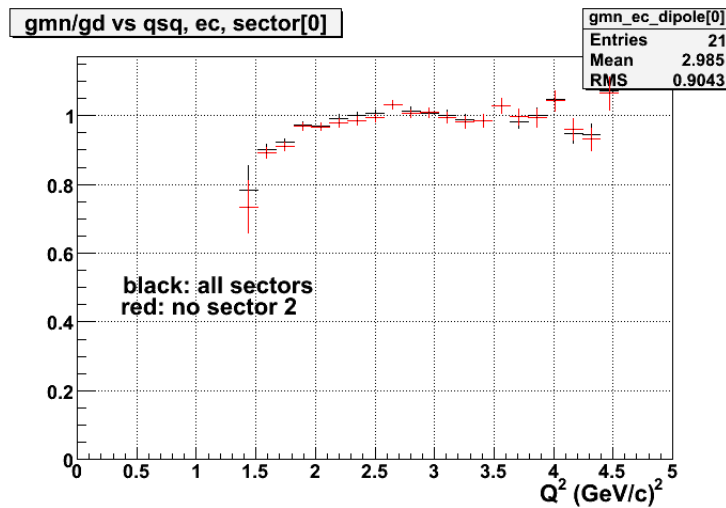


Figure E.7: Neutron magnetic form factor extracted with sector 2 excluded (red points) compared with  $G_M^n$  extracted using all sectors (black points).

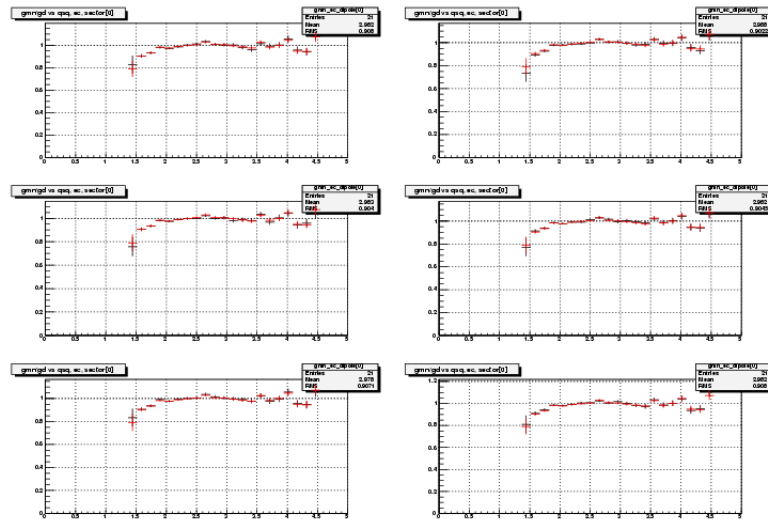


Figure E.8: Neutron magnetic form factor as a function of  $Q^2$  with different sectors excluded from the measurements.

allowed range of the scale factor.

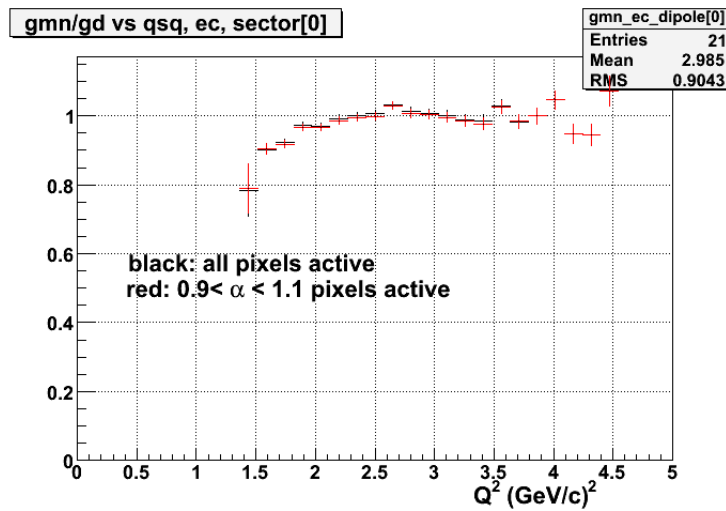


Figure E.9: Neutron magnetic form factor extracted without super-pixels whose efficiency varied by more than 10% from the value for the entire sector (red points) compared with the measurement using all pixels (black points).

We have developed a method to check for inefficiencies and noise in single paddles in the EC. We have examined the effect of excluding 'problem' paddles and even whole

sectors from the analysis and found that it has no effect on the  $G_M^n$  measurement. We also note that inefficiencies in single paddles are folded into the scale factor for each superpixel in the neutron efficiency measurement.

✓ 10) Neutron detection efficiency evaluation is based on the  $\pi^+$  measurement, possible  $\pi^+$  decay inside of CLAS DC can result in an uncertainty in the momentum reconstruction and therefore impact neutron efficiency calculation. Can you give an estimate of possible effect e.g. with GSIM simulations?

We have performed GSIM simulations to investigate the effect of  $\pi^+$  decay on the measurement of the neutron detection efficiency. Approximately 3 million events were generated with CELEG and run through GSIM with and without  $\pi^+$  decay turned on. The simulated data were then processed with GPP and analyzed in the same way as the real data to determine the neutron detection efficiency. The neutron detection efficiencies in the EC determined with (red up-side-down triangles) and without (blue triangles)  $\pi^+$  decay turned on are compared in Fig. E.10. It is clear from this figure that the possible decay of  $\pi^+$ s in the CLAS detector has little effect on the determination of the neutron detection efficiency.

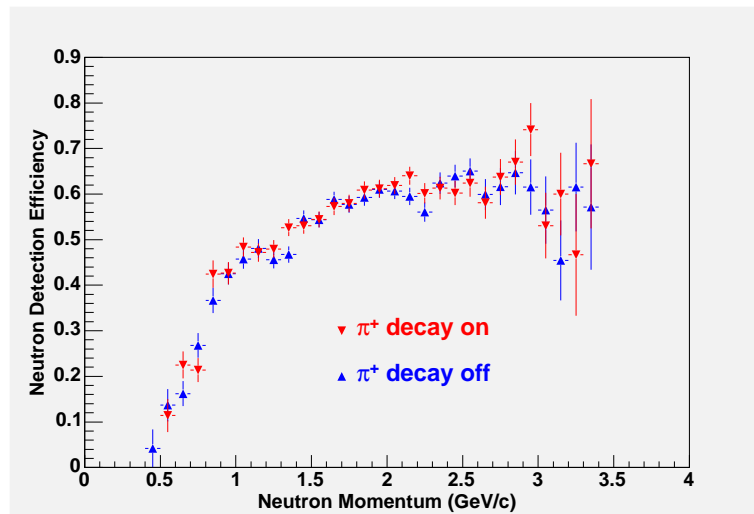


Figure E.10: A comparison of the neutron detection efficiency in the EC determined from GSIM simulations with (red up-side-down triangles) and without (blue triangles)  $\pi^+$  decay turned on.

✓ 11) Reconstructing neutron hits in EC and SC you apply some "fiducial cuts" (e.g. cut borders). While it is clear why you need these cuts we don't find appropriate justification of them in the note. Could you show that these cut are sufficient to avoid released energy losses?

The cut used in the EC efficiency analysis was 30 cm. This is the width of 3 strips. The sensitivity to this cut was investigated by changing the cut to 2 strip widths, and four strip widths. The change in the neutron detection efficiency is shown in Fig. E.11.

The effect of this choice on  $G_M^n$  was investigated by redoing the 4 GeV EC  $G_M^n$  extraction, using the 3 different efficiency curves shown in Fig. E.11. Fig. E.12 shows the difference between  $G_M^n(\text{EC\_FID}=20\text{cm})$  and  $G_M^n(\text{EC\_FID}=40\text{cm})$ , divided by  $G_M^n(\text{EC\_FID}=30\text{cm})$ , and multiplied by 100.

These figures will be added to the analysis note and the text will be modified to describe more clearly the cuts that were applied.

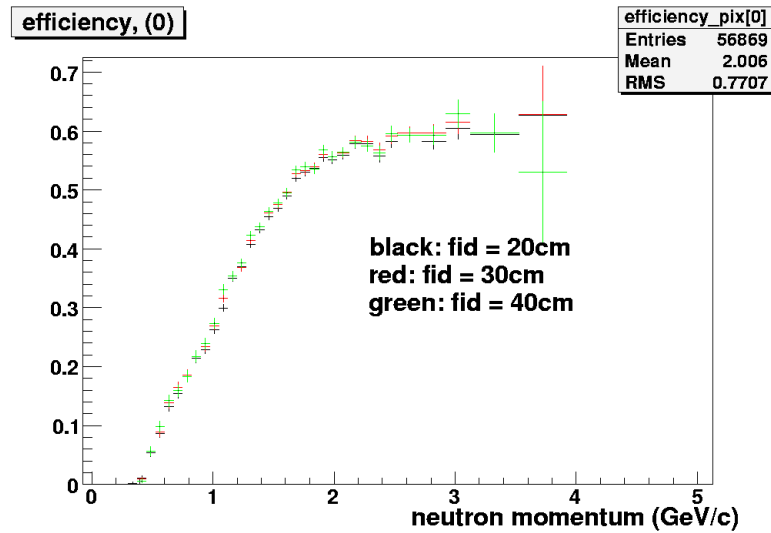


Figure E.11: EC neutron detection efficiency for different fiducial cuts.

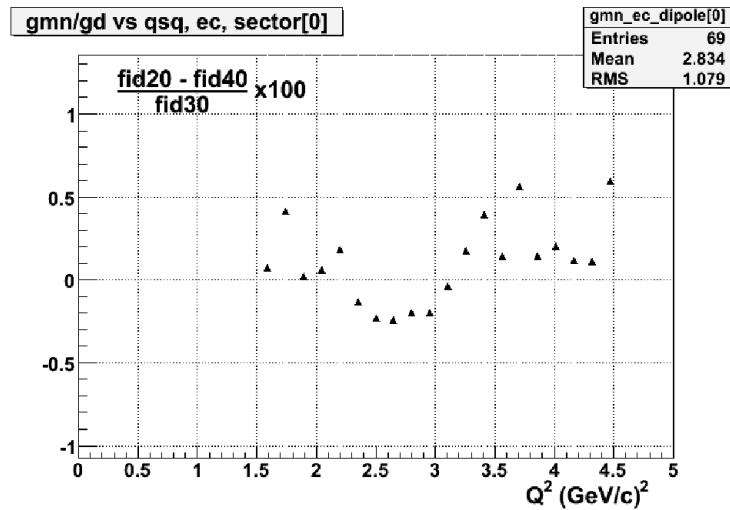


Figure E.12: Percentage change in  $G_M^n$  for different EC fiducial cut choices.

✓ 12) You are measuring the ratio of e'n and e'p events: why do you select runs on the basis of  $N_p/N_e$  and  $N_{ibt}/N_{hbt}$  rate stability shown in Figs. 2.1-2.4? Should it be  $N_n/N_p$  instead? Are these related?

These overall-quality cuts are intended to reject runs for which running conditions were not reasonable due to beam steering, beam scraping, detector HV trips, trigger problems, CODA problems, etc. They are based upon statistics which are available in the cooking data base and so can be used to reject a run before it has been analyzed for neutrons and quasi-free protons.

A cut on  $N_n/N_p$  could also have been applied to reject more subtle problems, such as gain variations which particularly affect neutron measurements. Such a cut was not necessary, however, since the calibration technique automatically allows for any time-variation of the efficiency and properly includes it in the measured efficiency, with the correct luminosity-weighting.

✓ 13) EC electron cuts: do you have electrons with  $EC_{inner} = 0$  (e.g. negative particles with large number of photoelectrons in CC)? Can you justify your EC sampling fraction parameterization separately for each sector (e.g. show distribution and the fit on top of it)? Why do you need the lower limit in EC s.f. cut?

As stated on page 19 of the analysis note, it was required that the energy deposited by electrons in the inner layer of the EC be greater than 50 MeV. The difference between the electron energy determined from DC tracking and sampling-fraction corrected energy deposited in the EC shown in Fig. 2.5 on page 20 of the analysis note shows that the sampling-fraction parametrization is quite reasonable. The lower limit of the cut on the difference between the energies determined in the DC and EC shown in Fig. 2.5 may not be necessary, but it's not hurting anything either.

✓ 14) Many plots in the note have inappropriately large scale making hard to understand their meaning: e.g. Fig.2.5, 2.9 2.15, 2.33, 2.37. Can you focus on significant range only?

The ranges were chosen to show the part of the range which we considered significant.

In Fig. 2.5, for example, the fact that there is NOT a broad background is an important point of the plot. We could re-plot this with a narrower range, such as -0.5 through 1.0 GeV, without making the reader wonder whether something is hidden just beyond the edges of the plot.

In Fig. 2.9, the breadth and height of the large- $\Delta R$  tail is an important point of the plot. We would be reluctant to significantly tighten the range.

In Fig. 2.15 the range was chosen to show most of the accepted data, above 5 MeVee as well as the large peak of rejected events below 5 MeVee. It is not clear whether the suggestion is that we focus on the narrow peak of rejected events or on the broad distribution of accepted events. We find the present range reasonable and would be reluctant to change it significantly.

In Figs. 2.33 and 2.37 it is important to allow the reader to estimate the shape of the background lying under the Min-I peak and we would be reluctant to significantly

decrease the range of the data.

We can certainly provide additional (as opposed to replacement) versions of any plot which the committee would like to see on a different scale. It would be necessary for the committee to specify the desired scale, however, since we have already chosen scales which we consider reasonable.

✔ 15) CC electron cut: you cut on 1 photoelectron, why? Add in the note few words why you are doing these cuts and explain why 1 photoelectron is sufficient.

The distribution of the number of photoelectrons (x10) produced in the CC for candidate quasi-elastic events is shown in Fig. E.13. This distribution includes all events in which a negative track was seen in one sector and 0 or 1 positive track was seen in the opposite sector. The additional kinematic constraints that the q-vector determined from the negative track is traced/swam out to the SC or EC and that a neutral or positive hit must be seen near the expected location are applied later in the analysis. These constraints eliminate much of the  $\pi^-$  contamination. The cut at 10 (1 photoelectron) that was used in the analysis is indicated by the red line in Fig. E.13. This cut was chosen to eliminate the large spike at zero.

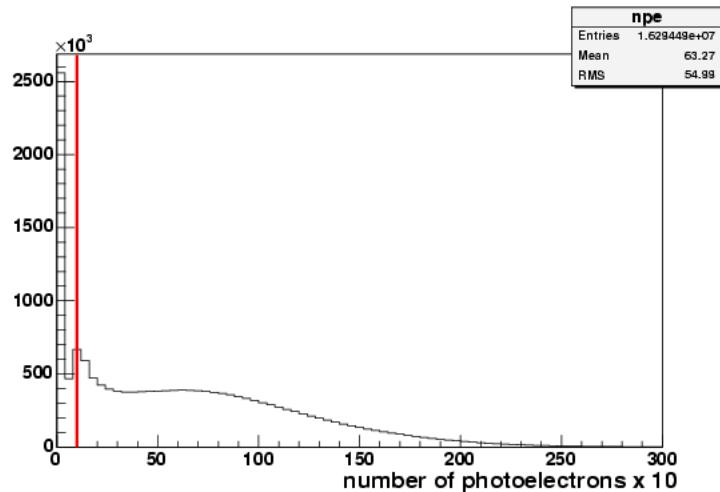


Figure E.13: The distribution of the number of photoelectrons produced in the CC for candidate quasi-elastic events.

To investigate the effect of this cut on the results for  $G_M^n$ , we have reanalyzed the 4-GeV EC data using two other values for the cut. Shown in Fig. E.14 is a comparison of  $G_M^n$  for neutrons detected in the EC for three different choices for the cut on the number of photoelectrons in the CC. Except at the lowest  $Q^2$  point, the difference is not very noticeable at this scale. Shown in Fig. E.15 is a comparison of  $G_M^n$  for neutrons detected in the EC for the two extreme cuts of 0 and 20, with an expanded vertical scale. At this scale, some small differences can be seen. The percent variation in  $G_M^n$  for the different cuts is shown in Fig. E.16. Even with the cut varied all the way down to 0, there are only a few points where the variation is

greater than 0.5 %.

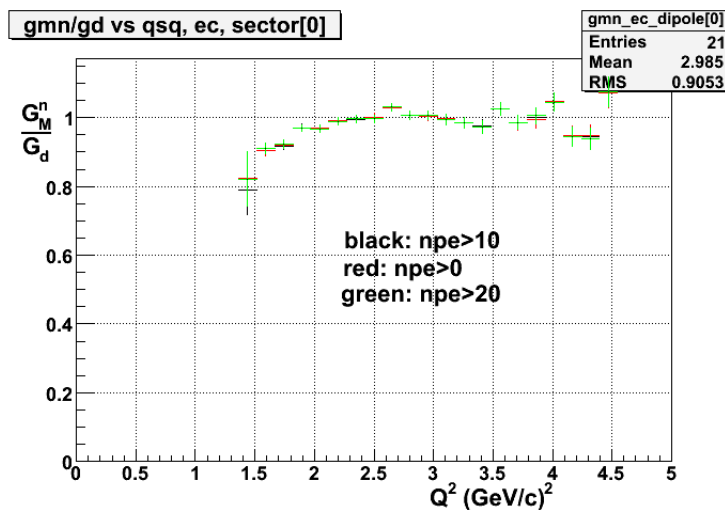


Figure E.14: A comparison of  $G_M^n$  for neutrons detected in the EC for three different choices for the cut on the number of photoelectrons in the CC.

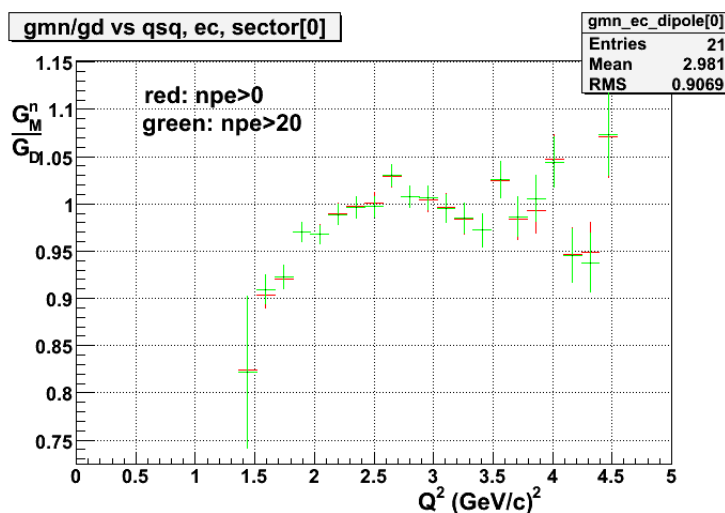


Figure E.15: A comparison of  $G_M^n$  for neutrons detected in the EC for two different choices for the cut on the number of photoelectrons in the CC with an expanded vertical scale.

✓ 16) Plot in Fig. 2.7 beta versus P. What is the maximum pion momentum your beta cut is designed for?

The cuts illustrated in Fig. 2.7 are cuts on the distribution of the difference between  $\beta$  determined from path length and time-of-flight and  $\beta$  determined from the measured momentum with the assumption that the particle is a  $\pi^+$ . These cuts do not produce a cut on the pion momentum.

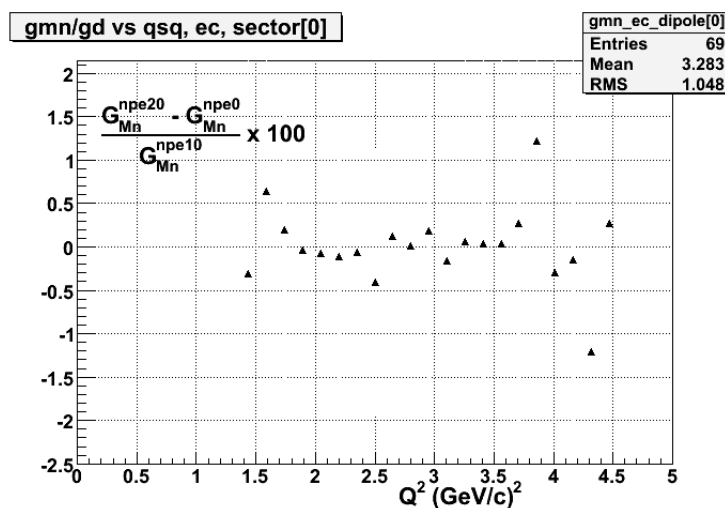


Figure E.16: The percent variation in  $G_M^n$  for different cuts on the number of photoelectrons in the CC.

✓ 17) Does CC veto for  $\pi^+$  remove  $e^+$  background? Can you check in a correlation CC/EC plot that it really does?

The source of a positron background in the calibration reaction is unclear. There is a cut requiring that all tracks emerge from the hydrogen target, and that the events have only two tracks: one negative, one positive. Subject to these constraints, the simplest reaction I can think of that might resemble the calibration reaction and have a positron is:  $e^-p \rightarrow e^-e^-e^+p$  where the proton and one of the electrons are not observed. This seems unlikely to satisfy the additional constraint that the missing mass from the two observed tracks be close to the neutron mass, but no quantitative study to prove this was made.

No CC veto was applied to candidate  $\pi^+$  events. The  $\pi^+$ 's were selected based on a cut on  $\Delta\beta$ , where  $\Delta\beta = \beta_{tof} - \beta_p$ .  $\beta_p$  is the beta determined from the measured momentum and the assumption that the particle mass is the pion mass.

The only CC information that was kept for pions in the filtered files used for the neutron efficiency analysis was the CCstat word in the EVNT bank. If CCstat  $\neq 0$ , then there is some CC information (which wasn't kept for the filtered files, though it could in principle be recovered by re-filtering the data set). Fig. E.17 shows a comparison of the reconstructed neutron momentum spectra for the usual case (no cut on CCstat) and the case where CCstat  $\neq 0$ . Fig. E.18 shows the same for the found neutron distribution.

In both cases, there are some "pions" that have something reported in the CC bank. Since the CC bank contents were not retained in the filtered files, a detailed cut on the CC information cannot be made. If we assume that any positive track with any information reported in the CC bank is a positron (regardless of the results of the  $\Delta\beta$  cut) and we exclude all CCstat  $\neq 0$  events, the resulting neutron detection

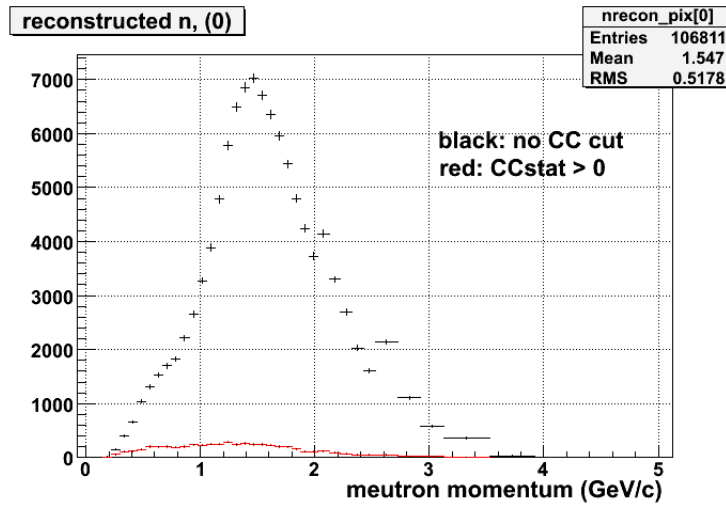


Figure E.17: Reconstructed neutron momentum distribution with and without CCstat cut.

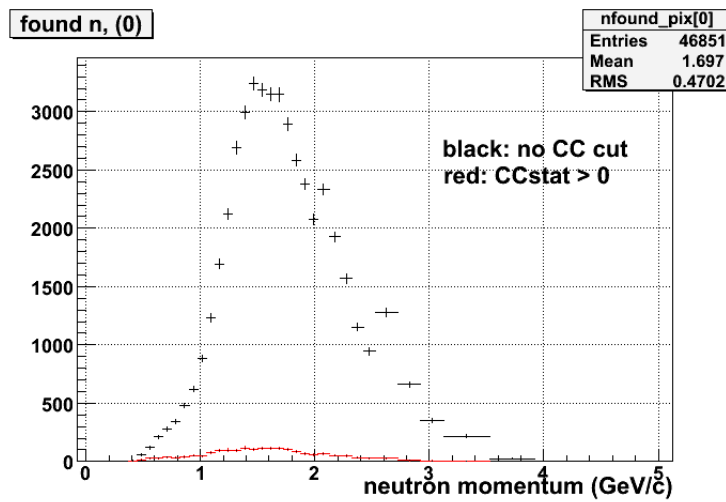


Figure E.18: Found neutron momentum distribution with and without CCstat cut.

efficiency is shown in Fig. E.19.

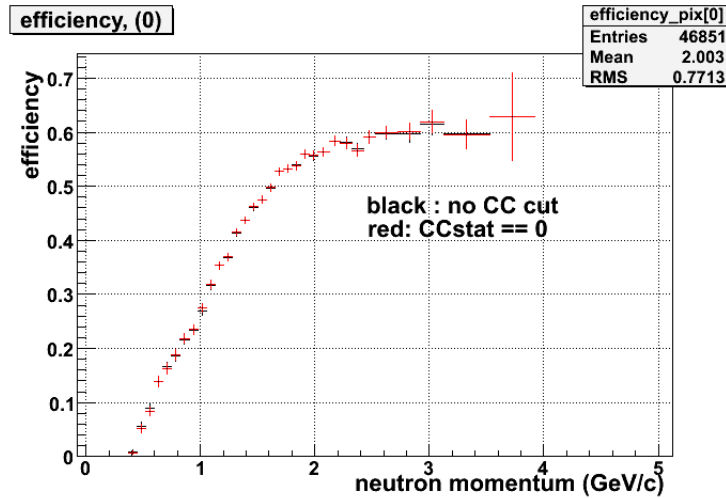


Figure E.19: EC neutron detection efficiency with and without CCstat $\neq 0$  pions.

In Fig.E.19, the black points are the EC neutron detection efficiency determined in the usual fashion, and the red points are the EC neutron detection efficiency determined with an additional cut throwing out all events where CCstat $\neq 0$  for the candidate  $\pi^+$ . The two efficiency curves are very similar: the change is not easily visible, except at a few points. The small effect seen in the efficiency histogram is smoothed out by the fitting procedure. Fig. E.20 shows the fractional change in the EC  $G_M^n$  induced by adding the "CCstat == 0" requirement to the efficiency calibration. Adding the CCstat $\neq 0$  cut changes the  $G_M^n$  determination by 0.2% at most (and much less than that in most cases).

✓ 18) Section 2.3.4.1 Delta R (and D"Delta R cut") is used but not defined by this page.

In the first paragraph of Section 2.3.4.1 we will insert the following language before the sentence that begins 'A cut rejecting ...'.

The distance  $\Delta R$  between the expected point-of-intersection on the EC plane and the observed one is defined as

$$\Delta R = |\vec{R}_{EC} - \vec{R}_{expected}| \leq 60 \text{ cm}$$

where  $\vec{R}_{EC}$  is a vector from the electron- $\pi^+$  vertex to the measured position of the neutron on the face of the EC and  $\vec{R}_{expected}$  is a vector from the same vertex to the expected point-of-intersection on the EC face.

In Section 2.3.4.1 of the analysis note it is incorrectly stated that the  $\Delta R$  cut is 30 cm. This will be corrected.

✓ 19) We expect SC neutron detection efficiency to rise at lower momenta (cross section is getting higher), why in Fig.2.17 it seems to go to zero?

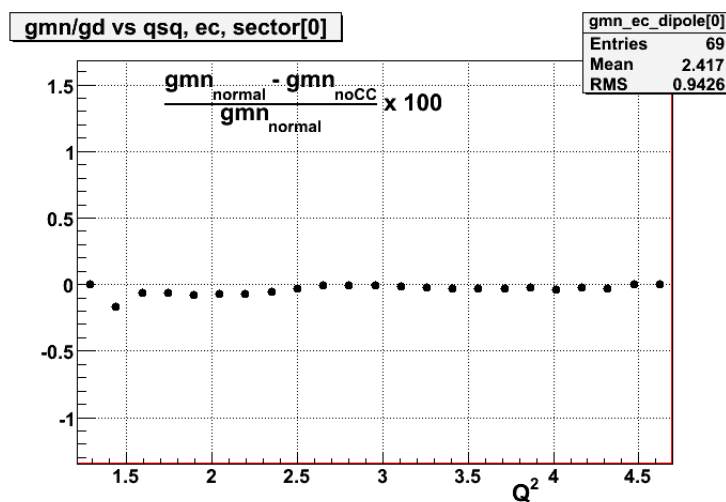


Figure E.20: Fractional change in EC  $G_M^n$  from adding CCstat == 0 cut to calibration reaction.

It is true that we expect the cross section to increase at lower neutron energy, but under normal running conditions we also require signals from the SC to be above a fixed threshold on the deposited energy to eliminate noise and background photons. For E5, this cut was set at 5 MeV electron equivalent in software (see Figure 2.15). If the neutron deposits all or most of its energy in the scintillator with no low-energy cut or discriminator thresholds set, the ‘zero-bias’ detection efficiency does increase at low neutron momentum. With a non-zero threshold the fraction of light lost below the threshold in an event gradually increases as neutron momentum decreases. The neutron detection efficiency decreases until it finally goes to zero when the maximum energy deposited by a low-momentum neutron is below the threshold. The precise value where the neutron detection efficiency goes to zero is smeared out because of different competing processes for neutrons to make light in the SC. At high neutron energy, the effect on the efficiency is small. Fig. E.21 below (from *Radiation Detection and Measurement* by G. F. Knoll) schematically shows this effect. This effect was also observed in the measured and simulated neutron detection efficiencies in CLAS-Note 2001-006 for the g2 running period.

✔ 20) You assume that the neutron detection efficiency is constant along SC paddle. Did you verify this?

While it is true that no corrections are applied for variation in efficiency along an SC paddle, this does not imply that the efficiency is assumed to be constant. The position-averaged efficiency can be properly represented as a single number as long as the position distributions are similar for the quasi-elastic neutrons of interest and for those used in calibration. (The ‘efficiency’ of a paddle is then really the ‘hit-density-weighted average efficiency along the length of the paddle’.)

Both neutron distributions are essentially axially symmetric over the range of in-

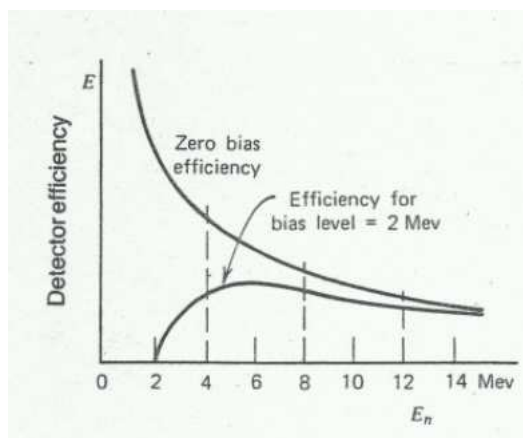


Figure E.21: Effect of discrimination level on neutron detection efficiency using proton recoil (from *Radiation Detection and Measurement* by G. F. Knoll).

terest along the paddles and both are cut by the same fiducial cuts excluding the ends of the paddles. Any slight differences in the actual position distributions of calibration neutrons compared to the quasi-elastic neutrons would not be expected to have a significant impact on the average efficiency unless the efficiency varied dramatically with position. In fact the variation in response of the paddles was expected to be modest since the energy-deposited cut, used in selecting neutron candidates, was based on the geometric average of the light reaching each end. This geometric averaging serves to remove the first order effects of light attenuation.

✓ 21) How the neutral hit in EC is identified (describe what is considered a neutral hit and how its position is measured)?

Neutral hits in the EC are identified the same way any other hit in the EC is identified. A detailed description of the hit-finding procedure can be found in the EC NIM paper ([http://www.jlab.org/Hall-B/pubs/ec\\_nim.ps](http://www.jlab.org/Hall-B/pubs/ec_nim.ps) or NIM A 460, 239 (2001)). In addition to forming a hit in the EC reconstruction, additional requirements are enforced. In either the efficiency calibration or the QE analysis, it is required that no charged tracks are found in the same sector as the candidate neutral event. Additional selection criteria are described in Sec. 2.3.4.1 for the calibration reaction, and Sec 2.6.3 for neutrons in the calibration reaction. Language will be added to section 2.6.3 to make it clear that the same energy deposit cut and edge cut used for the calibration reaction were applied for quasi-elastic neutron selection.

✓ 22) You mention many times "swimming" of the proton track through the torus magnetic field but never say how it was done practically?

Charged particle swimming is performed using the routine "swim2pln". This is part of the standard CLAS software package and can be found in the file "/trk/swim2pln.F" in any version of the CLAS software. The user supplies a magnetic-field map, an initial momentum, charge and initial vertex and the particle is propagated through the

magnetic field until it crosses a user specified plane (in our case, planes parallel to either the EC face or one of the TOF panels).

✓ 23) Can you compare your  $W/\theta_{pq}$  distributions from the event generator (Figs. 2.53 and 2.54) with similar distributions from the data. You can add plots like in Fig. 2.28 but in the same scale and with the same kinematics as in 2.53 and 2.54.

Shown in Figs. E.22 and E.23 are  $W^2$  vs.  $\theta_{pq}$  spectra for e-p coincidences for the E5 4.2-GeV and 2.6-GeV data sets, respectively.

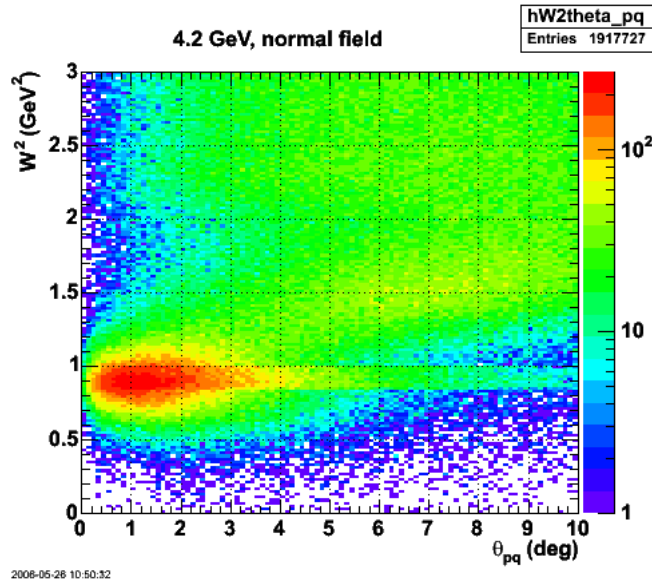


Figure E.22: A  $W^2$  vs.  $\theta_{pq}$  spectrum for e-p coincidences for the 4.2-GeV data.

✓ 24) In Fig. 2.27 can you add  $W^2$  distribution after selection of a nucleon and (separately) corresponding  $\theta_{qp}$  cut?

Shown Fig. E.24 is a comparison of  $W^2$  distributions for ep events before and after a cut requiring that  $\theta_{pq}$  be less than  $3^\circ$ . We will add this figure to the analysis note.

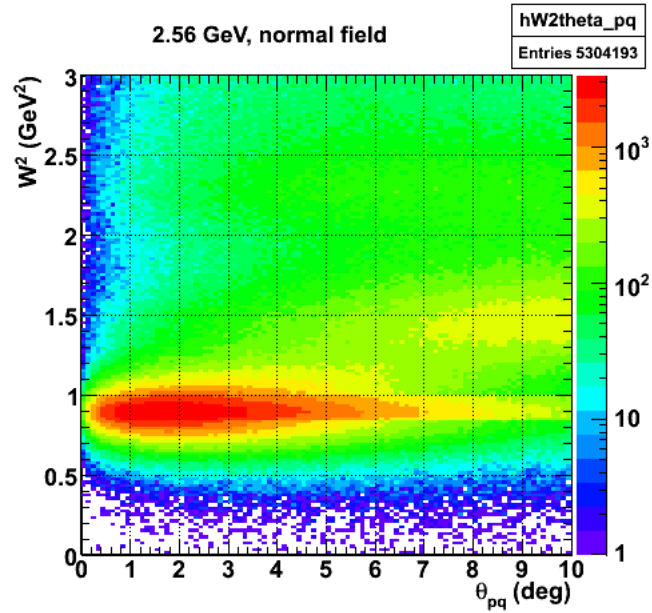


Figure E.23: A  $W^2$  vs.  $\theta_{pq}$  spectrum for e-p coincidences for the 2.6-GeV data.

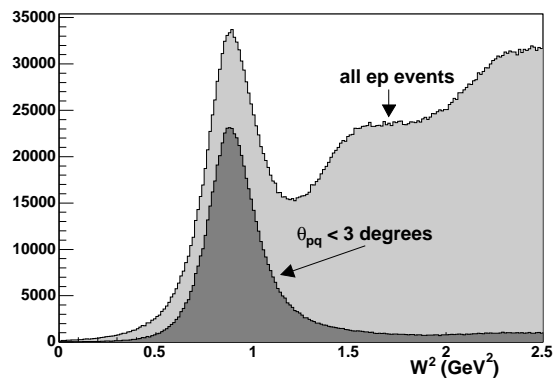


Figure E.24: Comparison of  $W^2$  spectra for ep events before and after a  $\theta_{pq} < 3^\circ$  cut.

# Appendix F

## Response to Analysis Review Committee 2

### A High Precision Measurement of the Neutron Magnetic Form Factor Using the CLAS Detector

#### Analysis Review Committee Response 2

October 19, 2007

*Jeff Lachniet, Will Brooks, Jerry Gilfoyle, Brian Quinn, and Mike Vineyard*

In order to better understand where we are in addressing the questions and comments of the review committee, the following key is being used:

- ✓ - Question/comment has been adequately addressed. (7)
- ✗ - More work is needed to address the question/comment. (0)

---

Analysis review committee members: Michail Osipenko (chair), Michel Guidal, and Henry Juengst.

Dear Michael, Will and Jeff,

first of all I apologize for lately response, but because of significant time interval between our fist discussion and the present one we had to study the analysis note from scratch. We certainly acknowledge the work done by the authors, but we feel to have still some questions about the analysis. This questions are listed below. It would be nice to have all new plots and additional information to be implemented in the new version of the analysis note.

With Best Regards,  
Mikhail and Michel.

✓1) We feel strongly that authors have to compare their proton detection efficiency against GSIM Monte Carlo simulations. In the case of neutron detection efficiency we agree with authors and do not insist on such a comparison. We do not believe that proton detection efficiency measured by means of the elastic peak can

be (much) better than GSIM extracted efficiency. In particular, this is not the case at large- $Q^2$  where your data become very important. The cross section of the elastic peak at  $Q^2 \sim 4.5 \text{ GeV}^2$  in previously studied and published CLAS data had  $\sim 10\%$  statistical error. Thus we do not understand Fig. 2.42 in the analysis note where the efficiency seem to have no statistical error. Could you give some explanation? In addition, we need to have a comparison GSIM vs. data on this efficiency.

The committee asks: We feel strongly that authors have to compare their proton detection efficiency against GSIM Monte Carlo simulations. In the case of neutron detection efficiency we agree with authors and do not insist on such a comparison. We do not believe that proton detection efficiency measured by means of the elastic peak can be (much) better than GSIM extracted efficiency. In particular, this is not the case at large- $Q^2$  where your data become very important.

Response: We are not sure whether the committee is suggesting: (i) using GSIM results to supplement our efficiency measurements to improve our results OR (ii) using our results to test GSIM as a way to tune GSIM as a service to the collaboration.

We address both interpretations below:

(i) The most important feature of this experiment for control of systematic errors was the continuous measurement of both neutron and proton efficiencies in parallel with (and under identical running conditions with) the actual data taking. It was presumably this feature which convinced the PAC that the experiment could be done with the desired accuracy.

We do not believe that any simulation can be expected to accurately predict efficiencies at the sub-percent level without being tuned to observed results. (Furthermore we don't believe we could ever convince an outside referee that a simulation is accurate at sub-percent level by dead-reckoning.) While beam intensity fluctuations, wire-by-wire gain variation, long term gain drifts, etc. are automatically included in the calibration data, they are not included in GSIM. Making GSIM accurately reproduce the observed efficiencies run-by-run would be an enormous task. In the end we would have a simulation which produces the results it has been told to produce... it can not do any better than the data to which it is calibrated. There would be no gain in tuning GSIM to produce the observed efficiencies rather than simply applying the observed efficiencies directly as we presently do.

(ii) While our data set could be used as a cross-check to test or tune GSIM, it is not uniquely suited to that task, compared to any other data set taken with an electron beam on a hydrogen target. While this might be seen as a service to the collaboration it should be noted that the publication of these much-anticipated results has already lagged significantly and there is pressure to get them out. Pushing ahead with publication would be a better service to the collaboration.

The committee asks: The cross section of the elastic peak at  $Q^2 \sim 4.5 \text{ GeV}^2$  in previously studied and published CLAS data had  $\sim 10\%$  statistical error.

Response: We are not sure to which published results the committee refers. The cross section for elastic scattering from hydrogen at these kinematics ( $E = 4.2 \text{ GeV}$ ,  $\theta$

$= 45^\circ$ ) is small, but not unusually small ( $\sim 0.014$  nb/sr). Statistics on elastic scattering at this  $Q^2$  would not be hard to accumulate if it were not for the fact that we have reached the edge of the Cerenkov coverage (at this beam energy). Figure F.1 shows the statistics for reconstructed elastic scattering events (black) and for those in which the proton is also reconstructed (red) for the 4.2-GeV runs, summed over the 6 sectors. The statistics are seen to be quite high over most of the SC paddles. Since the committee is interested in the highest  $Q^2$  point, we also show an expanded view of the lowest-numbered detectors (highest  $Q^2$ ) in Figure F.2. The statistics are seen to be over 100 per detector except for the two most forward detectors. As we explain below, binomial errors must be used to determine the resulting error on the extracted efficiencies.

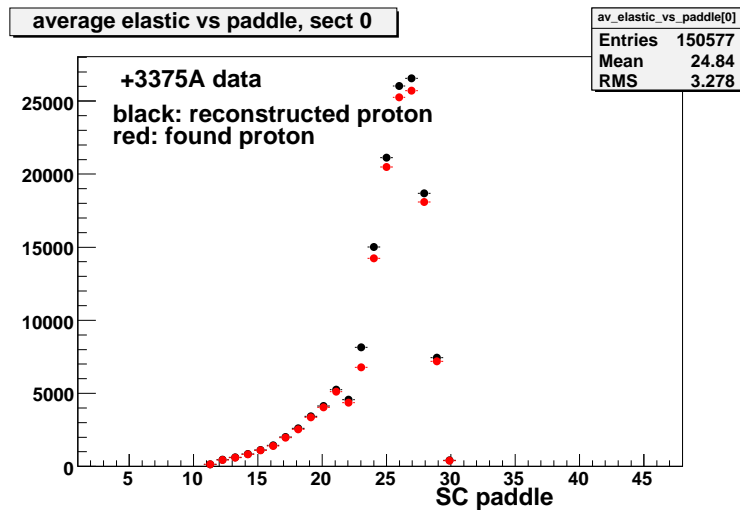


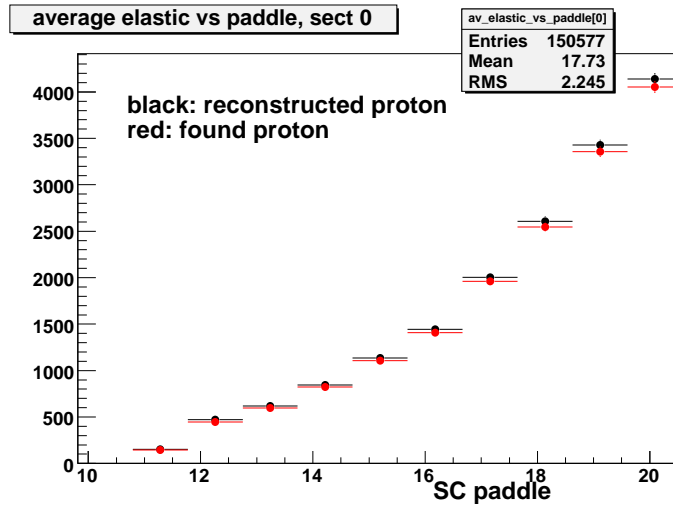
Figure F.1: Statistics of reconstructed and found proton calibration events.

Even at the edge of the electron acceptance, the statistics are not limited by elastic scattering from the proton. Quasi-elastic scattering from the neutron has a still smaller cross section and the efficiency for neutron detection is smaller. So we are more statistically limited by neutron coincidence data than by proton calibration data.

Perhaps this is an unimportant side-issue and the real question is why the errors on proton efficiency are so small. We address that next.

The committee asks: Thus we do not understand Fig. 2.42 in the analysis note where the efficiency seem to have no statistical error. Could you give some explanation?

Response: The statistical error on the proton efficiency measurements is small both because there are reasonable statistics for the calibration and because the error on a binomial distribution has been applied in calculating the error. It is important to note that the fractional error on the measurement of a high efficiency may be considerably smaller than what one might expect from  $\sqrt{N}$ . (Poisson statistics do

Figure F.2: Close-up of high  $Q^2$  region.

not apply in such a case, so  $\sqrt{N}$  is not the correct error estimate.) For example, if  $r = 1000$  events are reconstructed as elastic scattering from the hydrogen target (by detecting the electron) and  $f = 950$  protons are actually found when the predicted SC paddles are searched for a charged hit, then the estimated efficiency is clearly  $p = f/r = 95\%$ . It might be tempting to estimate the fractional error on that ratio as  $1/\sqrt{1000} = 3.2\%$  (or even as  $\sqrt{2}/\sqrt{1000} = 4.5\%$  if the errors on the numerator and denominator were treated as independent). However, since binomial statistics apply, the variance of  $f$  (if the true efficiency is  $P$ ) is

$$V = \sigma_f^2 = \left( \frac{r^2}{r-1} \right) P(1-P)$$

then, calculating the best estimate as  $p = f/r$  gives the error on  $p$  as

$$\sigma_p = \sqrt{\frac{P(1-P)}{r-1}} \sim \sqrt{\frac{p(1-p)}{r-1}} = \sqrt{\frac{0.95(1-0.95)}{1000-1}} = 0.007$$

or 0.7% which is 4.5 (or 6.5) times smaller than would be estimated from Poisson statistics. See, for example, 'Statistics for Nuclear and Particle Physicists' by Louis Lyons.

The committee asks: In addition, we need to have a comparison GSIM vs. data on this efficiency.

Response: It is not clear how this differs from the first question. We expect that GSIM could be made to reproduce our observed efficiency (with adequate simulation of observed dead/low-efficiency wires, pile-up, dead paddles, gains, etc.). But it is not clear what we would learn from such a simulation that we don't already know.

✔ 2) Both photon rejection cuts: angular cut in EC and timing cut in SC, are shown to give good results in the case of exclusive reactions where kinematics of

neutron is fixed by conservation laws, can you provide similar plots (Fig.2 of the answer and Fig.2.16 of the analysis note) for the quasi-elastic case? In the case of Fig.2 you can plot e-n missing mass (which should be almost a proton).

To demonstrate that the photon background in the neutron selection for the quasi-elastic analysis is small, we have calculated the time-of-flight for neutrons detected in the EC and SC using two different techniques and generated distributions of the difference in these times. In the first technique the TOF was calculated as the detector time minus the event time and in the second it was calculated assuming that all of the momentum of the virtual photon is transferred to the neutron. The distributions for neutrons detected in the EC for the 4.2 and 2.6 GeV data are shown in Fig. F.3 and those for SC neutrons are shown in Fig. F.4. There is little or no photon background evident in these distributions.

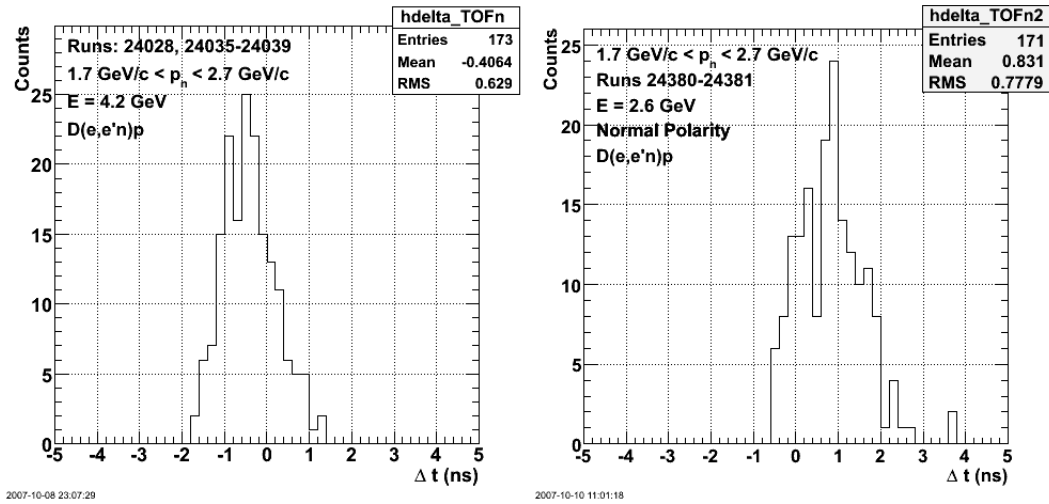


Figure F.3: Time-of-flight difference for quasi-elastic neutrons detected in the EC for 4.2 GeV (left panel) and 2.6 GeV with normal torus polarity (right panel).

The most direct evidence that the accidental coincidence rate is weak and under control in the quasi-elastic analysis is provided by rotating the reconstructed neutron momentum vector by a random multiple of  $60^\circ$  around the beam axis into a sector where the neutron is not expected to be found. The rest of the quasi-elastic analysis is carried out as usual. Any "neutrons" found in this analysis must be due to accidental coincidences. This is the same procedure that was used to show that the accidental background in the  $ep \rightarrow e'\pi^+(n)$  reaction is small (see Section 3.2.3.1 of the Analysis Note).

The results of this analysis are shown in Figs. F.5 and F.6. Figure F.5 shows the number of "found neutrons" as a function of  $Q^2$  with (red) and without (black) the  $60^\circ$  rotation of the reconstructed neutron momentum vector for neutrons in the EC (left panel) and SC (right panel). Shown in Fig. F.6 are  $\theta_{pq}$  distributions for "found neutrons" in the SC as successive cuts are applied in the quasi-elastic analysis

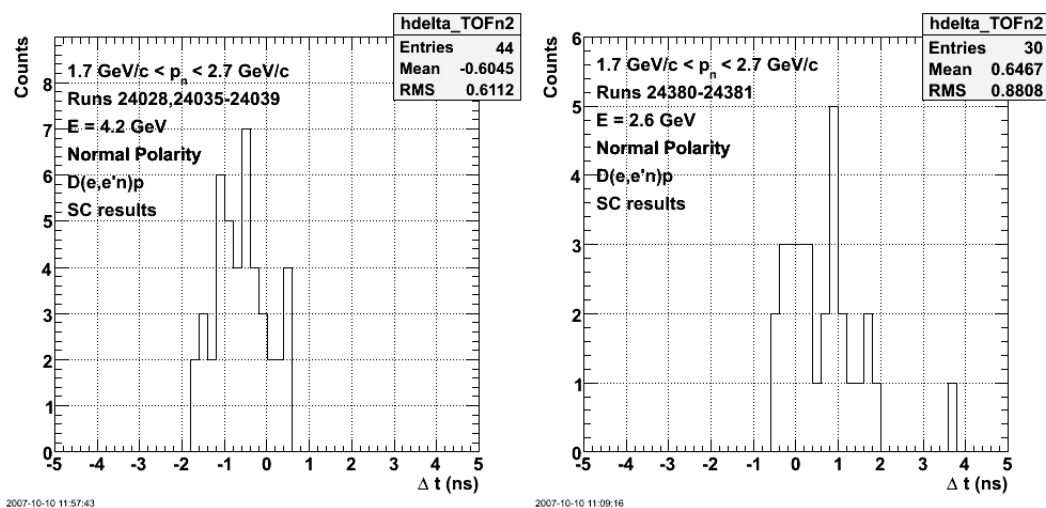


Figure F.4: Time-of-flight difference for quasi-elastic neutrons detected in the SC for 4.2 GeV (left panel) and 2.6 GeV with normal torus polarity (right panel).

with the  $60^\circ$  rotation of the reconstructed neutron momentum vector. The cuts are cumulative, so the "blue" histogram equals the "black" histogram plus the "red" cuts plus the "green" cuts plus the "blue" cuts. The few events remaining in the blue histogram are rejected for either being at a larger  $\theta_{pq}$  than is allowed for that  $Q^2$  or failing the fiducial matching cut. From this analysis it is clear that the accidental coincidence rate is low and under control.

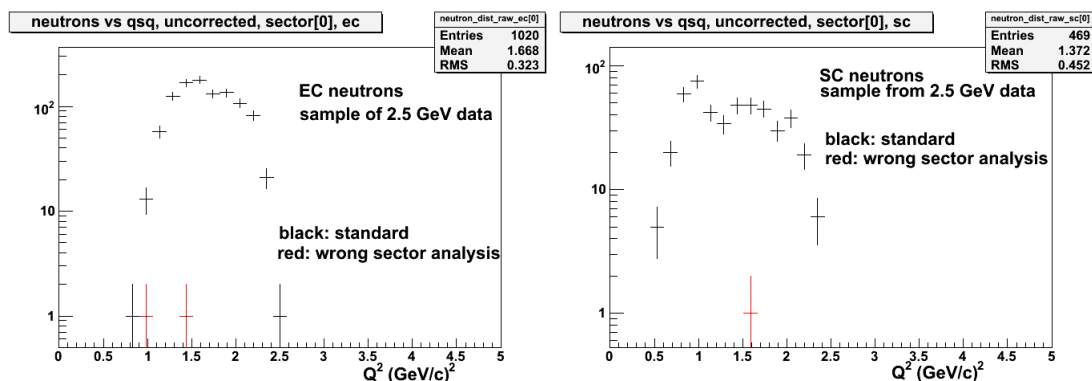


Figure F.5: Neutrons detected in the EC (left panel) and SC (right panel) with (red) and without (black) a  $60^\circ$  rotation of the reconstructed neutron momentum vector.

3) in your answer on question N6 you claim that the background of photons, included also in Fig. 2 of the answer, is small. However provided that the relation between the missing mass plot and the neutron rate include the neutron detection efficiency (which can be of a few percent) we do not have feeling that your claim is well supported. Could you do similar plot with only events selected by the neutron

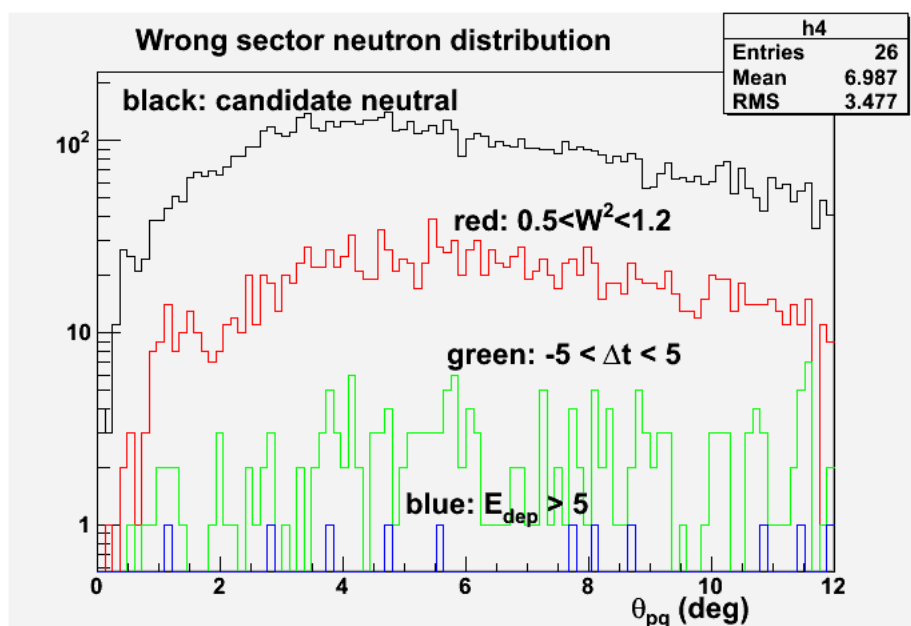


Figure F.6: Rejection of SC neutron candidates in the wrong sector by successive application of cuts.

selection cuts for a couple neutron momentum ranges (low and high)?

Missing mass distributions for the  $ep \rightarrow e'\pi^+X$  reaction with EC neutrons passing all cuts and with momentum less than and greater than 1.5 GeV are shown in Figure F.7.

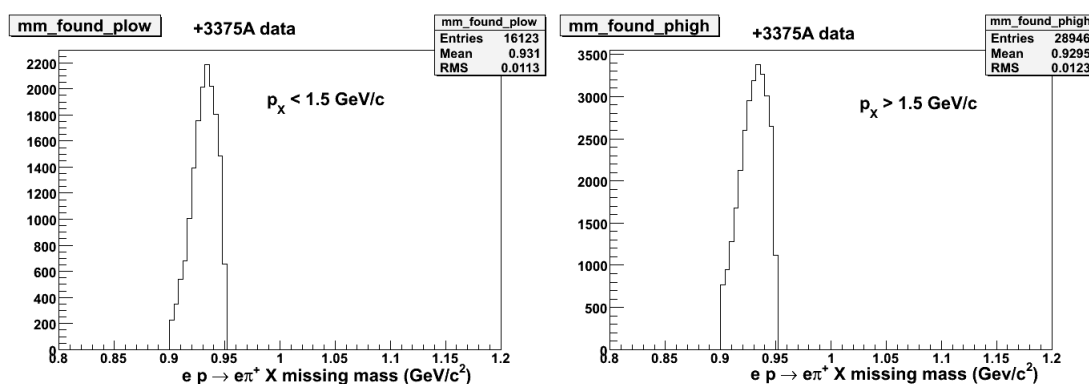


Figure F.7: Missing mass spectra for the  $ep \rightarrow e'\pi^+X$  reaction for EC neutrons passing all cuts and with momentum less than (left panel) and greater than (right panel) 1.5 GeV.

✓ 4) We suggest to add in the analysis note the plots of  $N_n/N_{p\text{stability}}$  as a function of time during the runs used in the analysis. Committee needs to see how much stable your observable is disregarding the fact that you can correct for this

effect. If there are runs where variations are too large these have to be removed.

Shown in Fig. F.8 is the neutron to proton ratio for accepted events versus run number for the runs used in the analysis of the +2250-A (left panel) and +3375-A (right panel) data. The  $\chi^2$  per degree-of-freedom is about 1.0 as expected for each distribution.

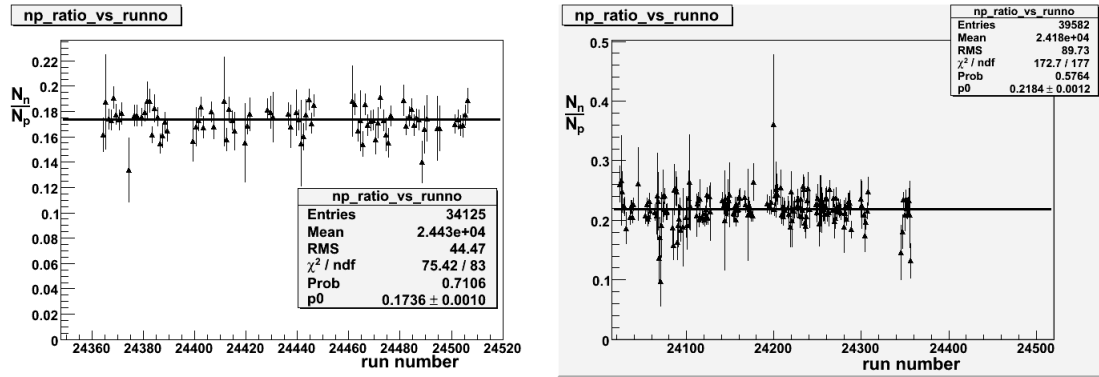
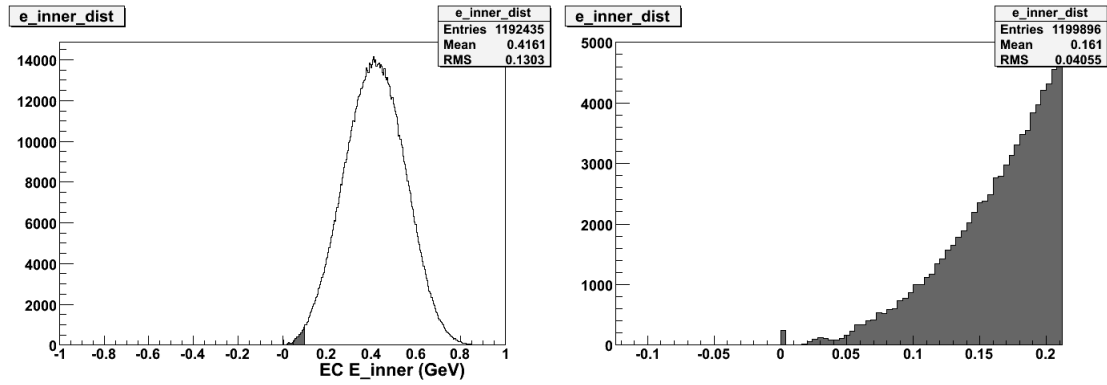
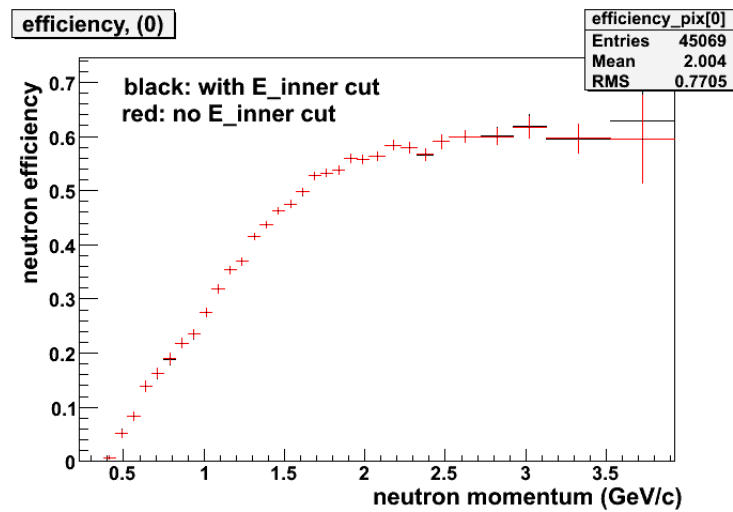


Figure F.8: The neutron to proton ratio for accepted events versus run number for the runs used in the analysis of the +2250-A (left panel) and +3375-A (right panel) data.

✓ 5) RECSIS sometimes fails to reconstruct ECinner or ECouter deposited energy even for good events (the information can be still found by searching for identical particles in the bank). This is why we were asking if after all your geometrical cuts you have electrons (e.g. with number of photo-electrons  $\geq 3$ ) with ECinner=0? Can you provide a plot (starting from negative values on the x-axis) before your cut on ECinner?

The  $E_{inner}$  distribution for electrons which pass all of the electron selection cuts (including the  $E_{inner}$  cut) is shown as the white region under the histogram in the left panel of Fig. F.9. Those electrons removed by the  $E_{inner}$  cut are shown by the gray-filled region in Fig. F.9. There is a small bump at  $E_{inner} = 0$ , as shown in the right panel of Fig. F.9, which shows a closeup of the  $E_{inner}$  distribution in the case where the  $E_{inner}$  cut has been removed, but all of the other electron selection cuts have been enforced.

Because all selected electrons are used in the calculation of the ratio of two quantities ( $e_n/e_p$  in the quasi-elastic case, or  $e\pi^+n_{found}/e\pi^+n_{reconstructed}$  in the calibration reaction case), we are not especially sensitive to the electron detection efficiency, as it tends to cancel out in the ratio. This can be seen in Fig. F.10, which shows the neutron detection efficiency in the EC (summed over all six sectors) for two cases: (a) the usual case (shown in black) where the  $E_{inner}$  cut is enforced, and (b) the case (shown in red) where the  $E_{inner}$  cut was not enforced. As can be seen, the cut has only negligibly small effects everywhere except at the statistically marginal point at the far end of the distribution. A similar insensitivity to the details of the electron selection function would be observed in other ratio-type quantities.

Figure F.9: Plots of EC  $E_{inner}$  for electrons.Figure F.10: The effect on the EC neutron detection efficiency of switching off the EC  $E_{inner}$  cut used in electron selection.

✓ 6) We do not understand whether the Fermi loss correction has been done with GSIM simulations or it is simply Monte Carlo which does not include the detector response? In particular the  $W$  vs.  $\theta_{qp}$  plots for your simulations (Fig.2.53 and Fig.2.54 of the analysis note) have much smaller peak width than similar plots in the data (Fig.22 and Fig.23 of the answer). This is disturbing in view of large disagreement between your data and the world data in the region where Fermi loss correction is maximal. Could you explain whether you did GSIM simulations and show the same plots for GSIM output?

The Fermi loss correction was NOT done with GSIM and the calculations shown in Figures 2.53 and 2.54 do not include the CLAS response. The goal here was to isolate the effect on the ratio  $R$  of the Fermi motion pushing scattered nucleons out of the CLAS acceptance. A Monte Carlo simulation was done using different Fermi momentum distributions for the struck nucleon. The different distributions give significantly different results for individual nucleons, but the effect on the ratio  $R$  is small. See Section 3.2.3.8 in the analysis note. The detector response was measured separately in the procedure described in Sections 2.3 and 2.4.

The width in  $W^2$  of the  $W^2 - \theta_{pq}$  distributions in Figs. 2.53 and 2.54 are considerably less than the widths of the data shown in Figs. 22 and 23 in our first response. This is expected since the distributions shown in the analysis note are the output of the quasi-elastic event simulation (QUEEG) and do not include the CLAS response. Again, the idea here is to isolate the effect of Fermi motion and then measure the CLAS response.

Figure F.11 shows a comparison of the  $W^2$  distributions for 4.2 GeV and 2.6 GeV between a GSIM simulation and the data. These spectra are essentially the projection of the other figures discussed above along the  $W^2$  axis to more clearly show the widths. This simulation (red histograms in each panel) used the same event generator, QUEEG, as in Figures 2.53 and 2.54 of the analysis note as input to GSIM. There is little difference in the widths of the distributions from GSIM and the data. Also, it should be pointed out that the study of the systematic uncertainties indicates that the results for  $G_M^n$  have very little sensitivity to the details of the Fermi loss correction procedure (see Section 3.2.3.8 of the analysis note).

✓ 7) Many plots requested by the committee have not been made. We repeat our requests:

a) beta vs. p neutron plot in EC (N6),

A  $\beta$  (from TOF measurements) versus reconstructed momentum spectrum for neutrons detected in the EC is shown in Fig. F.12.

b) neutron angular reconstruction quality and its correlation with Edep (N7),

Shown in Fig. F.13 are plots of  $\Delta\theta$  (left panel) and  $\Delta\phi$  (right panel) as a function of energy deposited in the EC for neutrons from the +3375-A data set. The angular difference is defined as the reconstructed angle minus the measured angle.

c) correlation plot neutron EC deposited energy and Delta R (N8),

A histogram of  $\Delta R$  versus energy deposited in the EC for neutrons is shown in

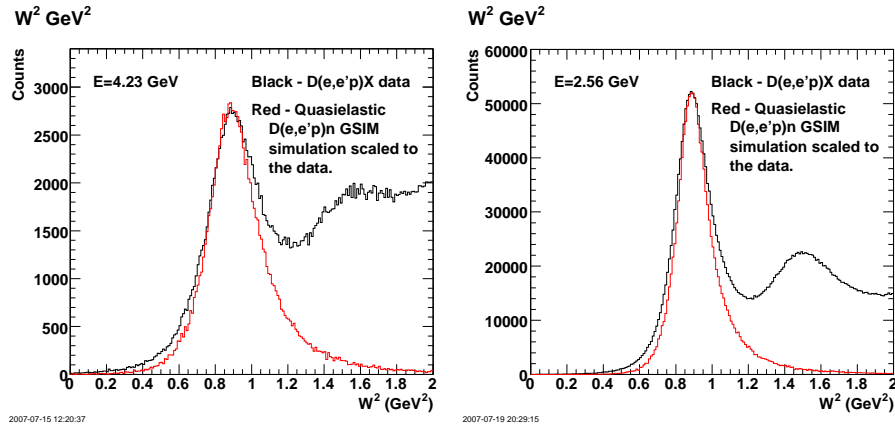


Figure F.11: Comparison of measured (black histograms) and simulated (red histograms)  $W^2$  distributions at 2.6 GeV (left-hand panel) and 4.2 GeV (right-hand panel). The simulations used the QUEEG event generator.

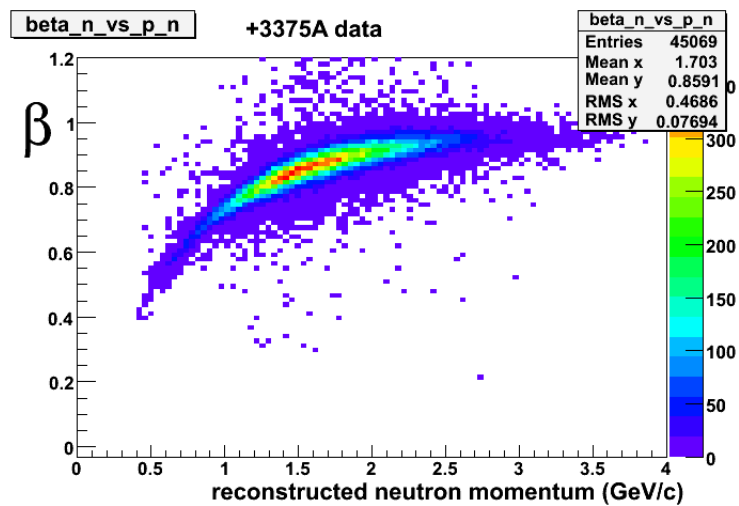


Figure F.12: A neutron  $\beta$  versus momentum spectrum.

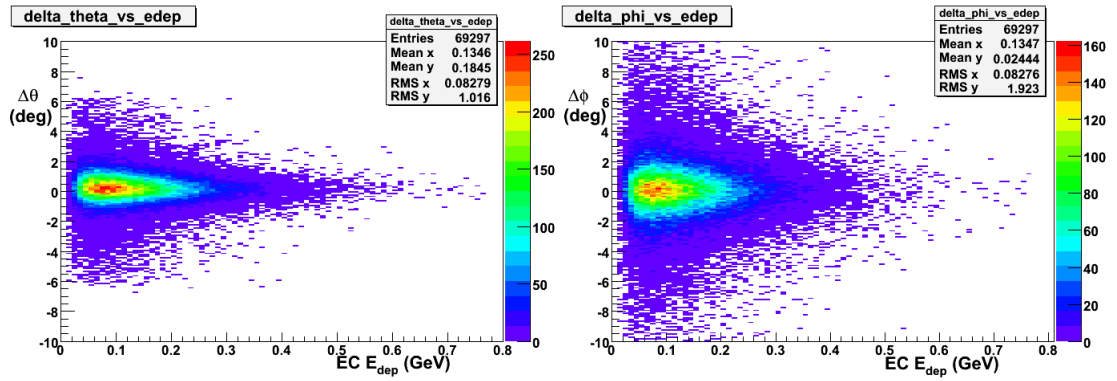


Figure F.13: Plots of  $\Delta\theta$  (left panel) and  $\Delta\phi$  (right panel) as a function of energy deposited in the EC for neutrons.

Fig. F.14.

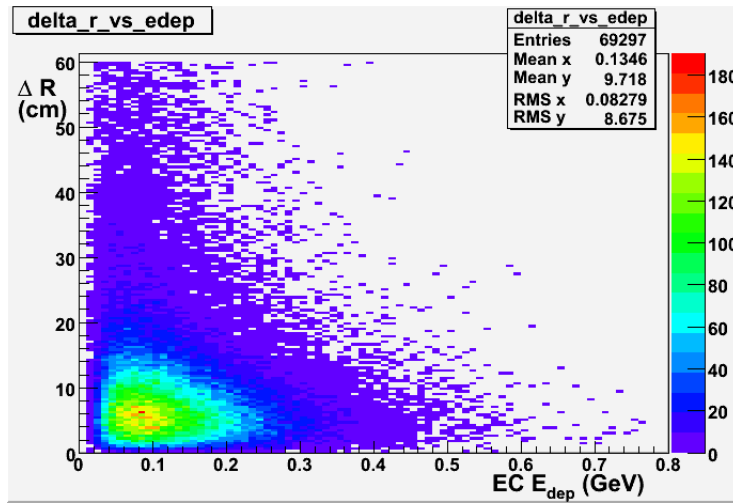


Figure F.14: A histogram of  $\Delta R$  versus energy deposited in the EC for neutrons.

d) electron EC energy deposited as in Fig. 2.5 (but from -0.2 to 0.2) sector by sector (N13),

Figure 2.5 of the analysis note doesn't show electron EC energy deposited. It shows the difference between the electron energy from the DC momentum and the sampling-fraction corrected EC energy deposit. Assuming that when the committee asks for a sector by sector version of Fig. 2.5, what they mean is a plot showing the quantity plotted in Fig 2.5, then Fig. F.15 below shows  $E - E_{dep}/f$  for each sector.

e) pion beta vs. P plot and the cut on top of it (N16),

As was described in the analysis note, the pion selection cut was on  $\Delta\beta = \beta_{tof} - \beta_{dc}$ , not on  $\beta$  directly. Shown in Fig. F.16 are  $\beta$  versus momentum spectra for  $\pi^+$  candidate events before (top panel) and after (bottom panel) the  $\Delta\beta$  cut. It was

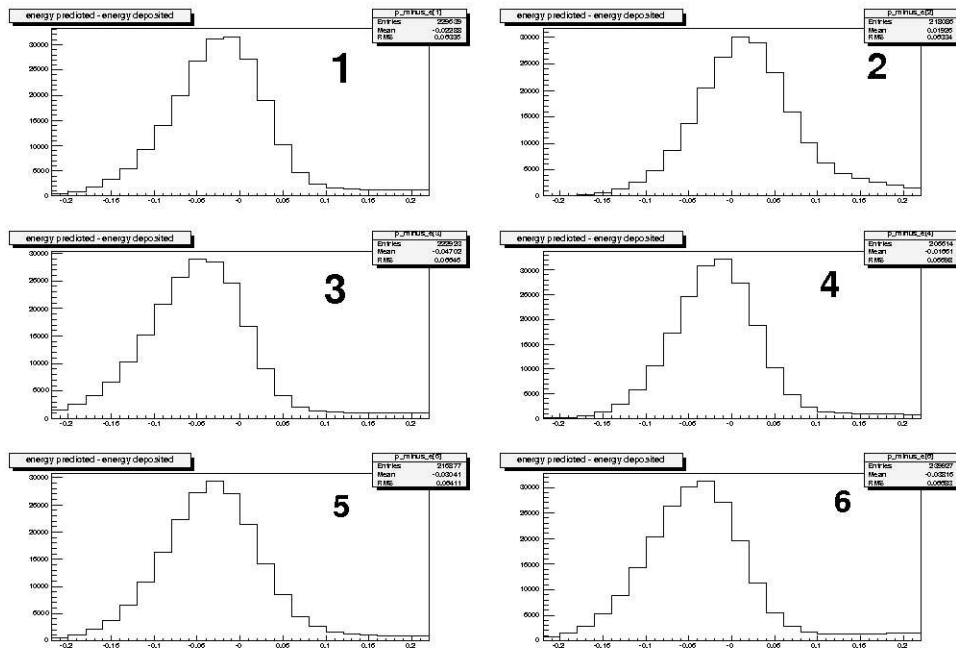


Figure F.15: The difference between electron energy (in GeV) determined from tracking and sampling-fraction corrected energy deposited in the EC for each sector.

required that these events have one negative track that satisfies the electron selection criteria and one positive track. We present the data in this fashion because straight line cuts in  $\Delta\beta$  are curved cuts in  $\beta$ , which are difficult to draw.

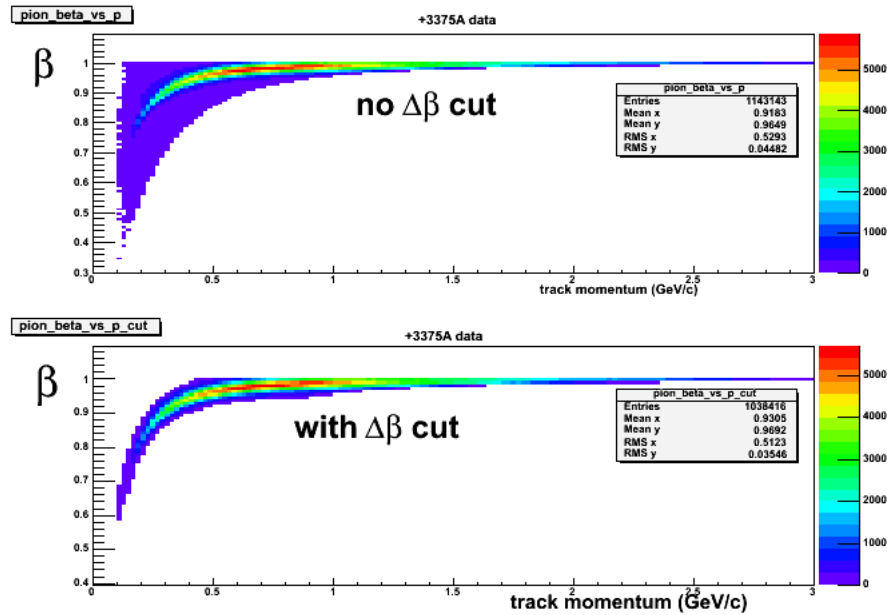


Figure F.16:  $\beta$  versus momentum spectra for  $\pi^+$  candidate events before (top panel) and after (bottom panel) the  $\Delta\beta$  cut.

f) prepare additional plots discussed in N14 with the following ranges: Fig.2.5 from -0.2 to 0.2 y axis in log scale, Fig.2.9 from -5 to 50 y axis in log scale, Fig.2.15 from -1 to 10 y axis in log scale, Fig.2.33 from -5 to 30 y axis in log scale, Fig.2.37 the same as before.

The requested distributions are shown in Figs. F.17-F.20.

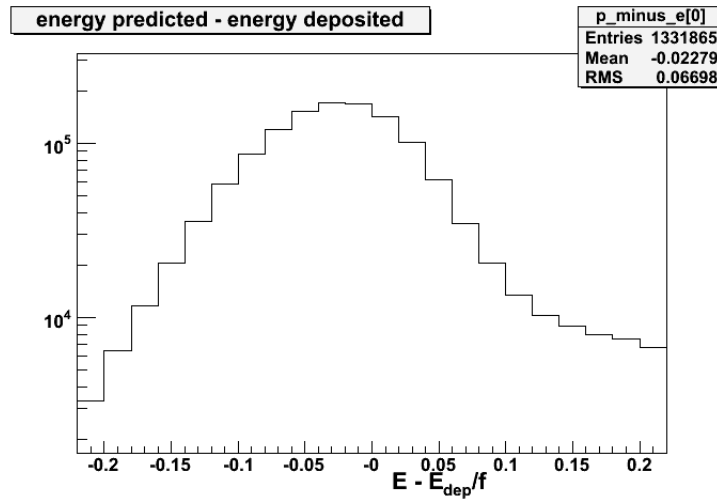


Figure F.17: The difference between electron energy (in GeV) determined from tracking and sampling-fraction corrected energy deposited in the EC.

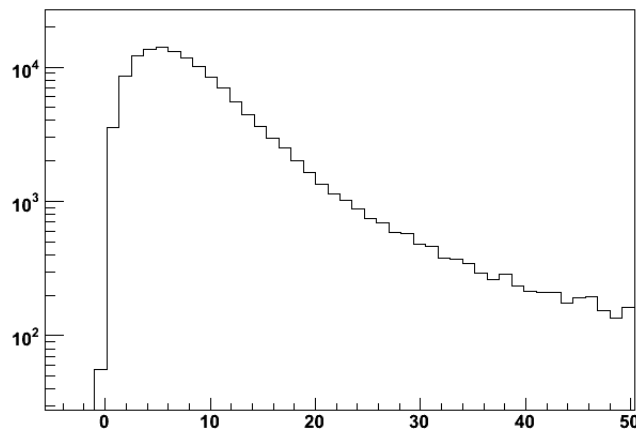


Figure F.18: The distribution of the distance  $\Delta R$  between the expected point-of-intersection and the observed hit location for neutron candidate events in the EC.

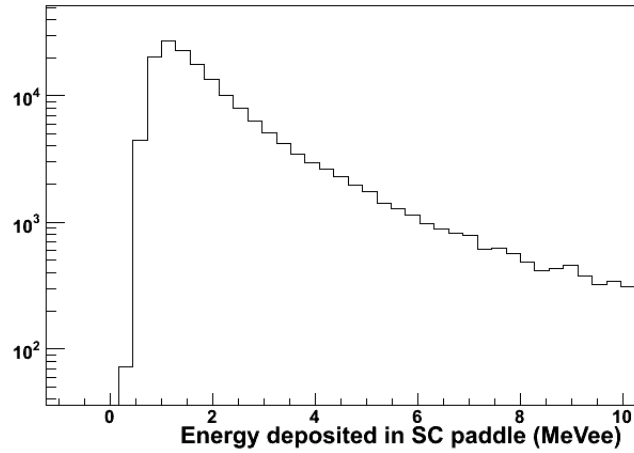


Figure F.19: The energy deposited in the SC by candidate neutron events.

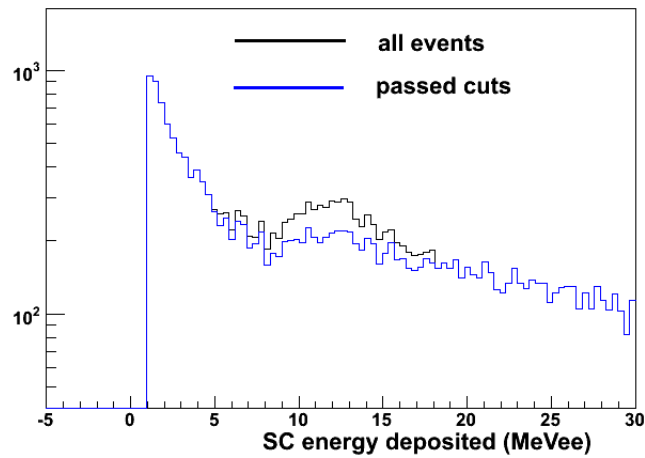


Figure F.20: Spectra of deposited energy in the SC for candidate neutral events before (black histogram) and after (blue histogram) applying DC wire-based unreconstructed proton rejection cuts.